Wissenschaftliche Mitteilungen

aus dem
Institut für Meteorologie der Universität Leipzig

ISBN **978-3-9814401-3-3**

Meteorologische Arbeiten (XX) und Jahresbericht 2014 des Instituts für Meteorologie der Universität Leipzig

Hrsg.: Armin Raabe

Leipzig 2015

Band 53

Wissenschaftliche Mitteilungen aus dem Institut für Meteorologie der Universität Leipzig Bd. 53

Wissenschaftliche Mitteilungen aus dem Institut für Meteorologie der Universität Leipzig Bd. 53

Delayed response of global ionospheric electron content to EUV variations derived from combined SolACES-SDO/EVE measurements

Christoph Jacobi[1], Claudia Unglaub[1], Gerhard Schmidtke[2], Robert Schäfer[2], Norbert Jakowski[3]

[1]*Institute for Meteorology, Universität Leipzig*
[2] *Fraunhofer-Institut für Physikalische Messtechnik (IPM), Freiburg*
[3]*German Aerospace Center, Neustrelitz*

Summary

The ionospheric response to solar EUV variability during 2011 - 2014 is shown by an EUV proxy based on primary ionization calculations using combined solar spectra from SDO/EVE and SolACES on board the ISS. The daily proxies are compared with global mean TEC analyses. At time scales of the solar rotation and longer, there is a time lag between EUV and TEC variability of about one to two days, indicating dynamical processes in the thermosphere/ionosphere systems. This lag is not seen at shorter time scales. When taking this delay into account the TEC variance at the seasonal and short-term time scale explained by EUV variations increases from 71% to 76%.

Zusammenfassung

Die ionosphärische Antwort auf Variationen des solaren EUV im Zeitraum 2011-2014 wird anhand eines Proxys dargestellt, welcher die primäre Ionisation auf der Basis gemessener solare EUV-Spektren beinhaltet. Die täglichen Werte werden mit Analysen des global gemittelten Gesamtelektronengehalts verglichen. Auf Zeitskalen der solaren Rotation und länger findet sich eine Zeitverzögerung zwischen der EUV-Variation und des derjenigen des Gesamtelektronengehalts von ein bis 2 Tagen, welche auf dynamische Prozesse im System Thermosphäre/Ionosphäre hinweist. Die Verzögerung ist auf kurzen Zeitskalen nicht zu sehen. Wenn diese Verzögerung berücksichtigt wird, erhöht sich die durch EUV-Variationen erklärte Varianz des Elektronengehalts von 71% auf 76%.

1. Introduction

The solar extreme ultraviolet (EUV) radiation varies on different time scales, including the 27-day Carrington rotation as one of the primary sources of variability at the intra-seasonal time scale. Consequences are strong changes of ionization of the Earth´s upper atmosphere, and corresponding variability of the electron density and also the Total Electron Content (TEC, frequently given in terms of TEC Units, 1 TECU = 10^{16} electrons/m^2). The majority of electrons are found in the ionospheric F layer where, according to the Chapman theory, electron production is proportional to

the ionizing EUV intensity, and electron density is approximately proportional to the electron production rate. Therefore, TEC variability is a coarse estimate for ionization as well, so that indices describing ionization may be compared against ionospheric TEC or, in turn, these indices may be used to provide a first guess of ionospheric TEC variability. Therefore, Unglaub et al. (2011, 2012) has introduced a proxy, termed EUV-TEC, which is based on the vertical and globally integrated primary ionization rates calculated from spectral EUV fluxes measured by satellite instruments such as TIMED/SEE (Woods et al., 2000, 2005). They found that, using data of about one decade, simple primary ionization calculations based on the measured spectra describe the TEC variability better than e.g. F10.7.

However, correlation of parameters describing ionospheric electron density and EUV proxies is not always strong at time scales of the solar rotation, and several studies report a delayed response of the ionospheric plasma density to solar activity changes (e.g. Jakowski et al., 1991; Astafyeva et al., 2008; Afraimovich et al., 2008; Lee et al., 2012). In most cases, TEC is reported to be delayed against the variation of the solar radiation by 1-2 days. To interpret the ionospheric delay, Jakowski et al. (1991) performed simplified theoretical studies using a one-dimensional numerical model. They found a delayed accumulation of atomic oxygen at 180 km height caused by slow diffusion of atomic oxygen that has been created via O_2 photo-dissociation. Since the major F region ionization is proportional to O, these results were consistent with the observed delayed ionospheric ionization response.

In this paper, we shall make an attempt to improve the performance of the EUV-TEC proxy after Unglaub et al. (2011, 2012) by taking into account the ionospheric delay mentioned above. We shall apply EUV spectra from combined SDO/EVE and SolACES measurements from 2011 through early spring 2014, and modify the EUV-TEC proxy through shifting the spectral contributions at the solar rotation time scale by the observed delay.

2. EUV data and analysis

The Solar Dynamics Observatory (SDO) was launched on 11 February 2010 (Pesnell et al., 2012), and data are available from 1 May 2010. The Extreme Ultraviolet Variability Experiment (EVE) onboard SDO measures the solar EUV irradiance from 0.1 to 105 nm with a spectral resolution of 0.1 nm, a temporal cadence of ten seconds, and an accuracy of 20% (Woods et al., 2012). SolACES (Schmidtke et al., 2006, 2014) is recording the short-wavelength solar EUV irradiance from 16.5 to 150 nm since 2008. The mission is extended from a period of 18 months to more than 8 years until end of 2016. SolACES is operating three grazing incidence planar grating spectrometers and two three-current ionization chambers. Re-filling the ionization chambers with different gases repeatedly and using overlapping band-pass filters the absolute EUV fluxes are derived in these spectral intervals. This provides an independent and absolute measurement of EUV fluxes that are used to calibrate the SolACES spectrometers. This way the problem of continuing efficiency changes in space-born instrumentation, which otherwise cannot be corrected without specific effort, is overcome during the mission.

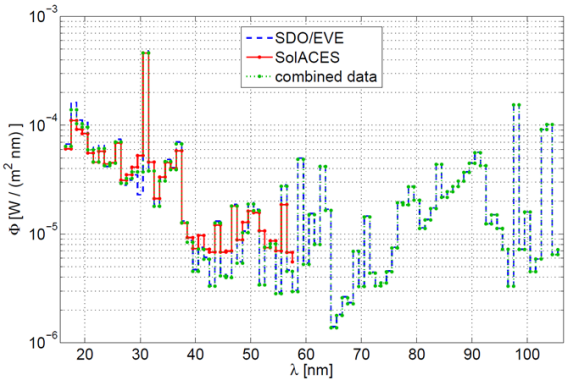

Figure 1: Example of SDO/EVE and SolACES spectra, and combined spectrum.

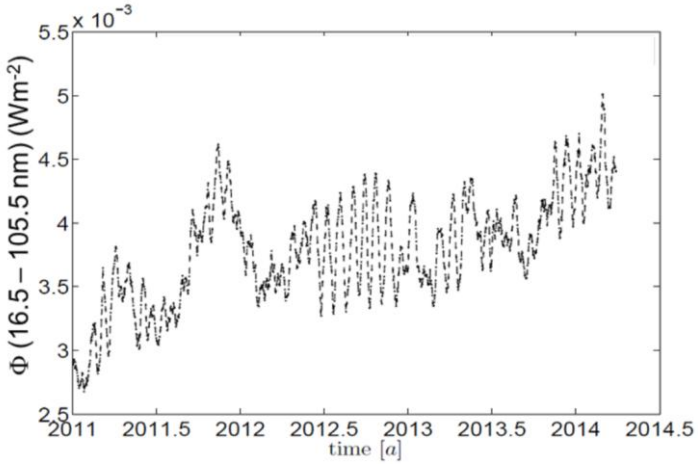

Figure 2: Solar flux between 16.5 nm and 105.5 nm from combined SDO/EVE and SolACES SSI measurements.

To calculate combined spectra, SDO/EVE version 4 daily spectra are used together with SolACES spectra. Between 16.5 and 29.5 nm the spectral fluxes are averaged, when SolACES spectra are available. A correction factor for SDO/EVE was then determined for each of these days by linearly fitting the ratio of the SDO/EVE integrated flux to the mean SDO/EVE and SolACES integrated flux between 16.5 and 29.5 nm. Thus the correction/weighting factor linearly scales from its initial value applied at 29.5 nm to unity at 105.5 nm. The correction factor changes, owing to the respective performance of the two instruments which changes with time. If no SolACES observation is available, the correction factor is derived from the fit function by interpolation to the particular day and applied to the SDO/EVE measurements between 16.5 and 29.5 nm. For wavelengths beyond 29.5 nm, the spectra solely consist of SDO/EVE-data, weighted with the correction factor. Figure 1 shows an example of SDO/EVE and SolACES spectra, with a correction factor in this case very close to unity, and the resulting combined spectrum. Figure 2 presents the time series of combined EUV fluxes integrated from 16.5 – 105.5 nm from January 2011 through March 2014. The dataset covers part of the increasing phase of solar cycle 24, and the variability of EUV is also characterized by the 27-day solar rotation, particularly well expressed during the 2nd half of 2012.

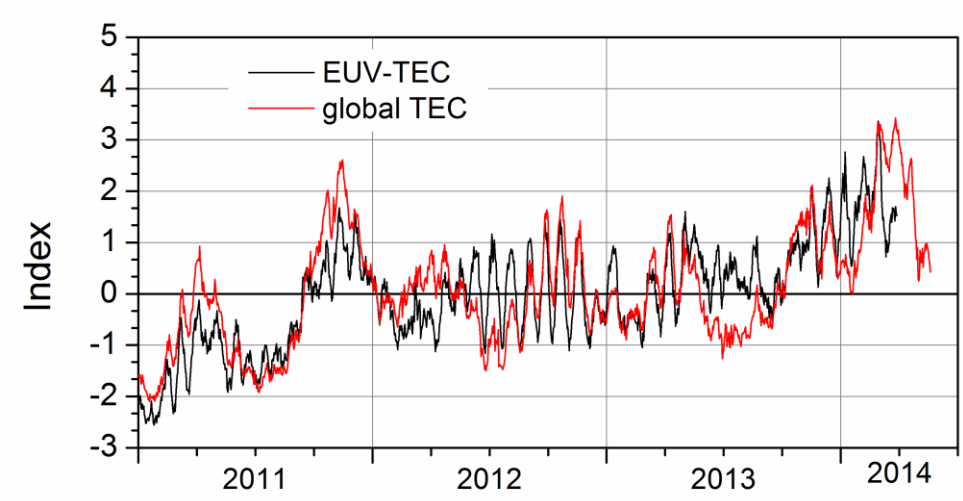

Figure 3: Times series of normalized global mean ionization rates (EUV-TEC proxy, red) and normalized global TEC (black).

We analyze the EUV-TEC proxy after Unglaub et al. (2011, 2012), based on the combined SDO/EVE-SolACES between 16.5 and 105.5 nm. EUV-TEC is calculated from the satellite-borne EUV measurements assuming a model atmosphere that consists of four major atmospheric constituents. Regional number densities of the background atmosphere are taken from the NRLMSISE-00 model (Picone et al., 2002). Daily global mean TEC values have been calculated based on IGS TEC maps (Hernandez-Pajares et al., 2009) in order to evaluate the EUV-TEC proxy, and they will be used here to analyze the ionospheric delay. The resulting ionization rates and global TEC values were normalized by subtracting the mean and dividing by the standard deviation from January 20, 2011 through March 10, 2014 (approx. Carrington rotations 2106 - 2147). The mean values and standard deviations are $1.180 \cdot 10^{19} \pm 1.23 \cdot 10^{18}$ ions/m^2 for the ionization rates, and 24.41±6.05 TECU for global TEC. The corresponding time series are shown in Figure 3. Their variability is generally similar, although not identical, and also corresponds to the one of the EUV flux in Figure 2.

In order to analyze the correlation of TEC and EUV-TEC at different time scales, we filtered the normalized data using a Lanczos bandpass filter with 100 weights. In Figure 4, EUV-TEC and TEC for several period bands are presented. The upper panel (a) shows the data for all time scales up to 3 months. The correlation coefficient between normalized TEC and EUV-TEC at these time scales is r = 0.844 (r^2 = 0.712). Other analyses (Unglaub et al., 2011) provided greater correlation coefficients, but these included the 11-year cycle. Longer time scales will not be considered here, because these are dominated by the annual cycle, which is different for TEC and solar radiation, and part of the 11-year cycle. The next two panels of Figure 4 show the EUV-TEC and TEC variations at period intervals 17-53 days (including the solar rotation) and 54-76 days. One can see from Figure 4b, which mainly exhibits the 27-day solar rotation that there is a delay of TEC frequently visible when the amplitude of the 27-day cycle is well expressed. For longer time scales (Figure 4c), the lag is also visible, but more irregular albeit larger in those cases it appears. The last panel (d) of Figure 4

shows the residuals, i.e. the differences between the curves in panel (a) and those in panels (b) and (c). Those values are representative for short-term fluctuations and long ones with time scales of 77-90 days. The variations are more irregular, and the correlation between EUV-TEC and TEC is weak at these time scales.

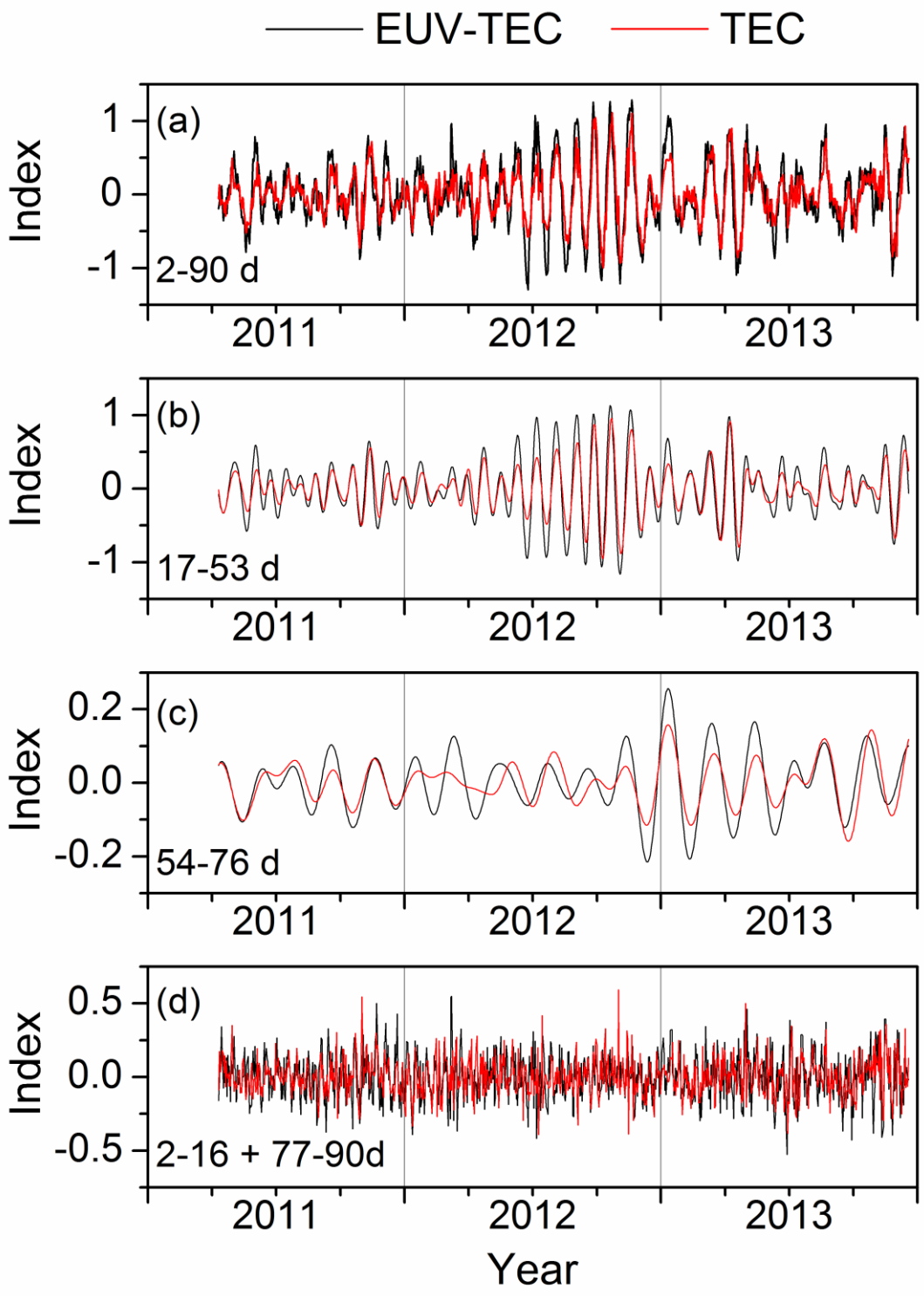

Figure 4: Time series of EUV-TEC and global TEC in different period bands (a) 0-90 days (b) 17-53 days (c) 54-76 days (d) 2-17 and 77-90 days.

To systematically investigate the delay at different time scales, we now filtered the time series and the cut-off periods of the Lanczos filter were chosen in such a way that each period band ranges over 4 days, while the centre of the period band was shifted from 4 to 88 days. For each pair of filtered time series, i.e. for each time scale (which was defined as the centre of the respective period window), the cross-correlation function was calculated. The results are shown in Figure 5. Positive values indicate that TEC variations lag EUV ones. Solid dots are added that show the time lag with maximum correlation which can, however, only be provided at an accuracy of one day. Figure 5 shows that at short time scales of few days, the correlation is weak, and the ionospheric delay is small. At time scales of the solar rotation, the strongest correlation is found and global TEC lags EUV-TEC variations by about one day. The lag increases to 2 days for time scales around 2 months, such that the lag scales with the time scale of the variation, which would be consistent with slow transport processes being responsible for ionospheric delay.

3. Considering the ionospheric delay in EUV-TEC

To improve the correlation between TEC and EUV-TEC, we constructed a new index from the original one, which takes into account the time lag at the respective time scales of the EUV variations. To this end, we filtered the EUV-TEC time series in different period windows, shifted the filtered series using the time lags taken from Figure 5, and reconstructed the EUV-TEC series from these values. Taking into account that the time resolution of the datasets allows only a first and coarse approach, we did not consider small structures in the time lag, but used a period window of 17-53 days that was shifted by 1 day and another window of 54-76 days that was shifted by 2 days.

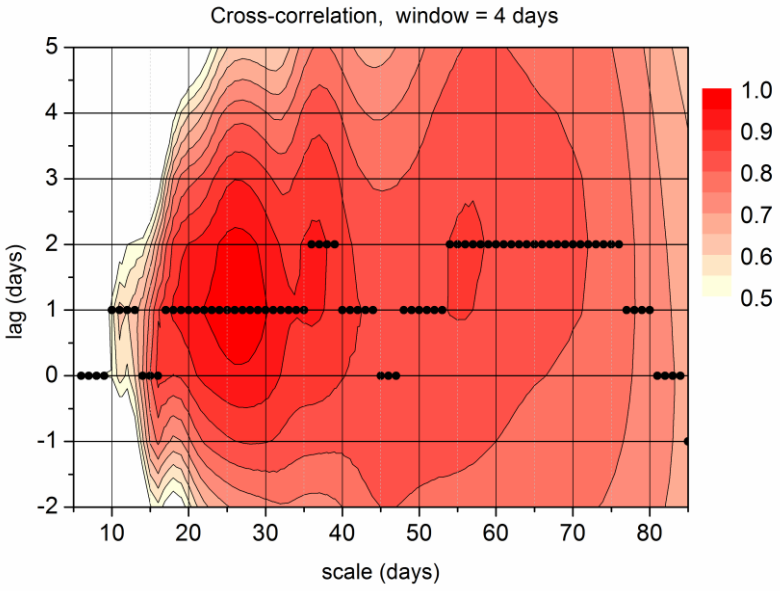

Figure 5: Cross-correlation coefficients between global TEC and EUV-TEC based on SDO/EVE and SolACES combined daily EUV spectra. The scale is the centre of the 4-day period band of the respective filter. Positive values indicate that TEC variations lag EUV ones. Solid dots show the lag with maximum correlation at an accuracy of one day.

Figure 6 shows an example of the original EUV-TEC index, the modified one, and the normalized TEC time series. The ionospheric delay between TEC and EUV-TEC is clearly visible with the original data, but vanishes if the modification is applied. Short-term variations are retained. When using the modified EUV-TEC time series, the correlation between normalized TEC and EUV-TEC increases to r = 0.874 (r^2 = 0.764), i.e. the TEC variance explained by the EUV-TEC proxy has increased by about 5%. The respective scatter plots are shown in Figure 7. One can see that after modification the scatter has decreased.

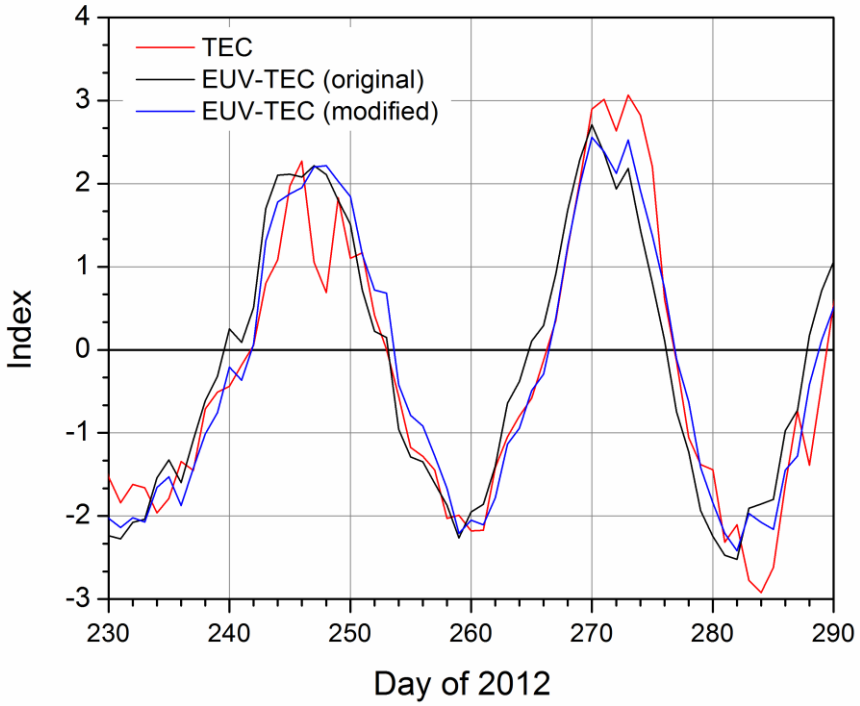

Figure 6: Example of normalized TEC, EUV-TEC, and EUV-TEC modified by shifting the filtered contributions in the 17-53 day range by 1 and in the 54-77 day range by 2 days.

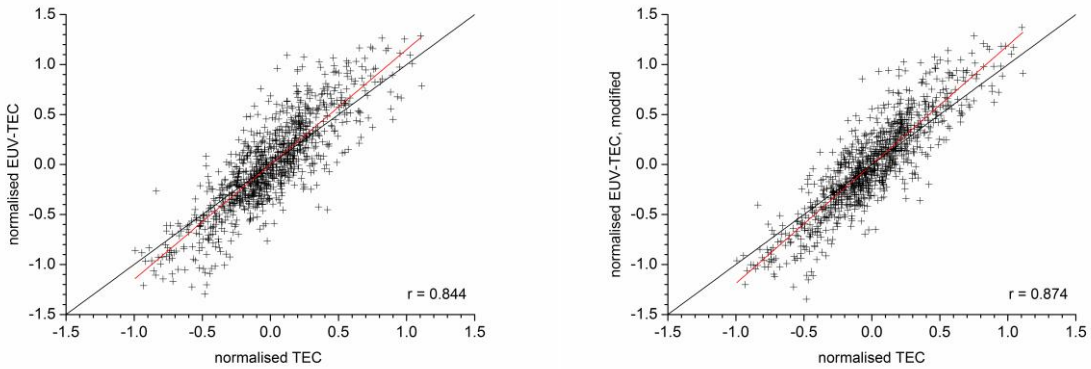

Figure 7: Normalized EUV-TEC vs. TEC. Left panel: original EUV-TEC. Right panel: Modified EUV-TEC.

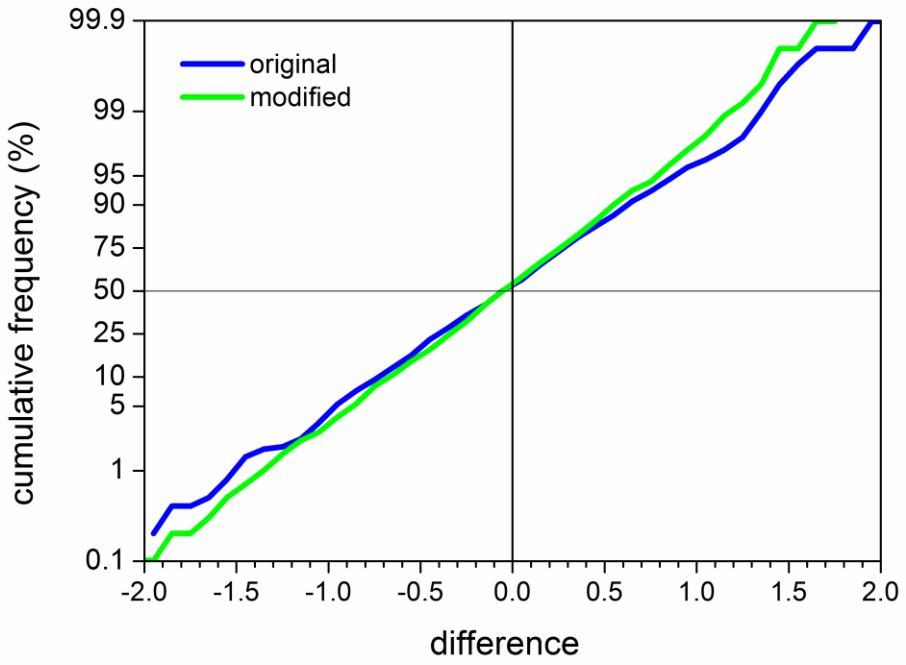

Figure 8: Cumulative frequency distribution of differences between normalized global TEC and original (blue) or modified (green) EUV-TEC index. Positive differences indicate larger normalized TEC.

To further visualize the improvement, we calculated the differences between normalized global TEC and the EUV-TEC index (at time scales to 3 months, i.e. high-pass filtered with a cut-off period of 90 days) both using the original values and the modified EUV-TEC. While the unfiltered EUV-TEC and TEC data shown in Figure 3 had been scaled to a standard deviation of 1, after the filtering their mean amplitudes differ slightly. Therefore the input data used to calculate the differences have been again scaled to a standard deviation of 1 to allow of comparability. Then the standard deviations of the differences between scaled TEC and EUV-TEC decreases from 0.56 for the original EUV-TEC to 0.50 for the modified one. Figure 8 shows the cumulative frequency distribution of the differences. One can see that the line for the original data starts at larger differences and also ends at larger differences, i.e. after modification especially the large differences between TEC and EUV-TEC appear more rarely.

4. Conclusions and outlook

When taking into account the ionospheric delay at the solar rotation time scale, proxies to describe the influence of EUV on ionization rates can be improved. It should be stated here that the ionization rates calculated by the EUV-TEC model represent only a coarse description of global TEC, and only about ¾ of the variance at the intra-seasonal time scale are explained. At the decadal time scale, the correlation increases to about r = 0.95 (Unglaub et al., 2012), but this is mainly owing to the 11-year Schwabe cycle. The EUV-TEC model also does not account for dynamics, secondary ionization, or ionization through electron precipitation at higher latitudes. It also does not take into account effects of ionospheric storms, which are a challenge for TEC forecast

(Borries et al., 2015). Nevertheless, EUV-TEC describes TEC variations better than conventional indices like F10.7 (Unglaub et al., 2011) and thus may be useful as a proxy for EUV and to replace F10.7 e.g. in models where it is used as input data. Taking into account the time delay will further improve the EUV-TEC proxy.

Obviously, the results presented here are preliminary. Further analyses will employ SDO/EVE version 5 data which recently had become available. Furthermore, the EUV spectral data set will be extended using TIMED/SEE data in order to cover a full solar cycle. We used daily EUV spectra and daily and global averaged TEC, which gives only coarse values for the time lag. TEC maps are available at higher temporal resolution, and EUV fluxes at least for some spectral bands are also available e.g. from SDO, SOHO/SEM (Judge et al., 1998) or GOES. This provides the possibility to study ionospheric delay in higher temporal resolution and spatially resolved, however, for the calculation of the EUV-TEC index spectral resolution is required, so that this would only provide guidance for further improvements.

Taking into account the ionospheric delay by simply shifting the contributions from the respective period ranges also neglects possible processes taking place during the 1-2 days such as the O production from O_2 dissociation and subsequent modifications in the EUV absorption. Further analyses will take into account possible weighting of the shifted contributions, and this also will require modeling of the photodissociation and transport processes to estimate these weights.

Acknowledgements

EVE version 4 spectra have kindly been provided by LASP, University of Colorado at Boulder. TEC data has been provided by NASA through ftp access on ftp://cddis.gsfc.nasa.gov/gps/products/ionex/.

References

Afraimovich, E.L., Astafyeva, E.I., Oinats, A.V., Yasukevich, Yu.V., Zhivetiev, I.V., 2008: Global electron content: a new conception to track solar activity. Ann. Geophys., 26, 335–344.

Astafyeva, E.I., Afraimovich, E.L., Oinats, A.V., Yasukevich, Yu.V., Zhivetiev, I.V., 2008: Dynamics of global electron content in 1998–2005 derived from global GPS data and IRI modeling. Adv. Space Res., 42, 763–769.

Borries, C., Berdermann, J., Jakowski, N., Wilken, V., 2015: Ionospheric storms - a challenge for empirical forecast of the Total Electron Content. J. Geophys Re. Space Phys., doi: 10.1002/2015JA020988.

Hernandez-Pajares, M., Juan, J.M., Sanz, J., Orus, R., Garcia-Rigo, A., Feltens, J., Komjathy, A., Schaer, S.C., Krankowski, A., 2009: The IGS VTEC maps: a reliable source of ionospheric information since 1998, J. Geod. 83, 263–275.

Jakowski., N., Fichtelmann, B., Jungstand, A., 1991: Solar activity control of ionospheric and thermospheric processes. J. Atmos. Terr. Phys., 53, 1125-1130.

Judge, D.L., McMullin, D.R., Ogawa, H.S., Hovestadt, D., Klecker, B., Hilchenbach, M., Möbius, E., Canfield, L.R., Vest, R.E., Watts, R.,Tarrio, C., Kühne, M., Wurz,

P., 1998. First Solar EUV Irradiances Obtained from SOHO by the Celias/Sem. Solar Phys., 177,161–173.

Lee, C.-K., Han, S.-C., Bilitza, D., Seo, K.-W., 2012. Global characteristics of the correlation and time lag between solar and ionospheric parameters in the 27-day period. J. Atmos. Sol.-Terr. Phys, 77, 219–224, doi:10.1016/j.jastp.2012.01.010.

Pesnell, W.D., Thompson, B.J., Chamberlin, P.C., 2012. The Solar Dynamics Observatory (SDO). Solar Phys., 275. 3-15, doi:10.1007/s11207-011-9841-3.

Picone, J.M., Hedin, A.E., Drob, D.P., 2002: NRLMSISE-00 empirical model of the atmosphere: statistical comparisons and scientific issues. J. Geophys. Res., 107, 1468, doi:10.1029/2002JA009430.

Schmidtke, G., Brunner, R., Eberhardt, D., Halford, B., Klocke, U., Knothe, W., Konz, M., Riedel, W.-J., Wolf, H. 2006: SOL-ACES: Auto-calibrating EUV/UV spectrometers for measurements onboard the International Space Station. Adv. Space Res., 37, 273-282.

Schmidtke, G., Nikutowski, B., Jacobi, Ch., Brunner, R., Erhardt, Ch., Knecht, S., Scherle, J., Schlagenhauf, J., 2014: Solar EUV irradiance measurements by the Auto-Calibrating EUV Spectrometers (SolACES) aboard the International Space Station (ISS), Solar Phys., 289, 1863-1883, doi: 10.1007/s11207-013-0430-5.

Unglaub, C., Jacobi, Ch., Schmidtke, G., Nikutowski, B., Brunner, R., 2011: EUV-TEC proxy to describe ionospheric variability using satellite-borne solar EUV measurements: first results, Adv. Space Res., 47, 1578-1584, doi:10.1016/j.asr.2010.12.014.

Unglaub, C., Jacobi, Ch., Schmidtke, G., Nikutowski, B., Brunner, R., 2012: EUV-TEC proxy to describe ionospheric variability using satellite-borne solar EUV measurements, Adv. Radio Sci., 10, 259-263.

Woods, T. N., Bailey, S., Eparvier, F., Lawrence, G., Lean, J., McClintock, B., Roble, R., Rottmann, G. J., Solomon, S. C., Tobiska, W. K., White, O. R., 2000: TIMED Solar EUV Experiment, Phys. Chem. Earth (C), 25, 393–396.

Woods, T. N., Eparvier, F., Bailey, S., Chamberlin, P., Lean, J., Rottmann, G. J., Solomon, S. C., Tobiska, W. K., Woodraska, D. L., 2005: Solar EUV Experiment (SEE): Mission overview and first results, J. Geophys. Res., 110, A01312, doi:10.1029/2004JA010765.

Woods, T.N., Eparvier, F.G., Hock, R.; Jones, A.R., Woodraska, D., Judge, D., Didkovsky, L., Lean, J., Mariska, J., Warren, H., McMullin, D., Chamberlin, P., Berthiaume, G., Bailey, S., Fuller-Rowell, T., Sojka, J., Tobiska, W.K., Viereck, R., 2012: Extreme Ultraviolet Variability Experiment (EVE) on the Solar Dynamics Observatory (SDO): Overview of Science Objectives, Instrument Design, Data Products, and Model Developments, Solar Physics, 275, 115-143, doi: 10.1007/s11207-009-9487-6.

Gravity Wave effects on a Modeled Mean Circulation

F. Lilienthal[1], **P. Šácha**[2], **Ch. Jacobi**[1]

[1] *Institute for Meteorology, Stephanstr. 3, 04103 Leipzig*
E-Mail: friederike.lilienthal@uni-leipzig.de
[2] *Charles University in Prague, Prague, Czech Republic*

Summary: Using a global circulation model of the middle atmosphere we analyze the influence of different tropospheric gravity wave amplitude distributions in the gravity wave parameterization on the mean circulation. Thereby we compare the standard configuration, which includes a simple zonal mean weighting of gravity wave amplitudes with a more realistic zonal mean weighting obtained from measurements using GPS radio occultations and a GW distribution in both latitude and longitude. The results show a stronger polar vortex and a descent of the meridional wind jet in the mesopause. Furthermore, two-dimensional weightings from the measurements are considered in order to analyze nonzonal effects resulting especially in stationary planetary waves. In this case we obtain a stronger stationary planetary wave and find enhanced equatorward wave motions in the lower stratosphere. These results give reason for further investigations about the impact of gravity waves on the Brewer-Dobson circulation.

Zusammenfassung: Mit Hilfe eines globalen Zirkulationsmodells für die mittlere Atmosphäre untersuchen wir den Einfluss verschiedener in der Troposphäre festgelegter Verteilungen der Schwerewellenamplitude in der Schwerewellenparametrisierung des Modells auf die mittlere Zirkulation. Dazu vergleichen wir den Standardfall zonal gemittelter künstlicher Wichtungen der Schwerewellenamplituden mit sowohl zonal gemittelten als auch längen-breitenabhängigen Wichtungen aus GPS-Radiookkultationensmessungen. Die Ergebnisse zeigen einen stärkeren Polarwirbel und ein Absinken des meridionalen Windjets in der Mesopause. Zusätzlich wurden zweidimensionale Wichtungen aus den GPS-Radiookkultationen ausgwertet, um den Einfluss planetarer Wellen zu analysieren. In diesem Fall lässt sich eine äquatorwärts gerichtete Verstärkung der Wellenbewegung in der unteren Stratosphäre feststellen. Diese Ergebnisse geben Anlass für weitere Nachforschungen über den Einfluss von Schwerewellen auf die Brewer-Dobson-Zirkulation.

1 Introduction

Among other processes, wave-mean flow interactions have significant impact on the middle atmosphere. One of these processes are owing to gravity waves (GW) which are atmospheric waves where the restoring force is the difference between gravity and buoyancy. GW play an important role for the atmospheric composition, circulation and dynamics. They are able to propagate from the surface to the upper atmosphere and thus exchange angular momentum between all vertical layers. Understanding GW related processes is essential for a proper description and modeling of the middle and upper atmospheric dynamics (as reviewed comprehensively by Fritts and Alexander, 2003).

The importance of GW in the atmosphere was first recognized by Hines (1960). Today's current issues about GW deal with their influence on the middle and upper atmospheric climate change and possible acceleration of the Brewer-Dobson circulation (BDC) (e.g., Garcia and Randel, 2008), their role in the formation of the quasi-biennial oscillation (Ern et al., 2014) or with their influence on the stratosphere-troposphere exchange (STE) through affecting the tropopause inversion layer in a persistent manner (Kunkel et al., 2014). But, as GWs exhibit a broad distribution of spatial and temporal scales, they need to be parameterized in most atmospheric models.
A very useful and frequently used tool to measure GW are Global Positioning System radio occultation (GPS RO) data which are obtained from the refraction properties of the atmosphere on a radio link between a low-earth orbiting (LEO) satellite and a GPS satellite. The measurements are characterized by a good vertical resolution providing atmospheric profiles with global coverage under all weather and geographical conditions (e.g., Foelsche et al., 2008).
Using potential energy from GPS RO density measurements following Šácha et al. (2014), Šácha et al. (2015) discovered a localized area of enhanced GW activity and breaking in the lower stratosphere over the Eastern Asia/North-western Pacific region. This GW hotspot is also marked as an area of specific dynamics and anomalously small annual cycle amplitude. Such a robust and localized GW breaking region can lead to the formation of planetary waves (PW) as numerically analyzed by Smith (2003) and Oberheide et al. (2006), and experimentally verified by Liebermann et al. (2013) for the mesosphere. Ortland (1997) observed equatorward propagating PWs and argued that they can play an important role in STE.
PW, such as Rossby wave modes, that are propagating poleward can also interact with the polar vortex and influence the occurrence of sudden stratospheric warmings (SSW). These SSW can lead to abrupt changes in the middle atmosphere circulation, tracer distribution and effects on tropospheric weather patterns (e.g., Manney et al., 2009).
Motivated by these findings and their possible consequences we compare the differences of GW effects on the middle atmosphere using several GW distributions in a model study. An artificial zonal mean distribution serves as a reference while zonal mean GPS based and longitudinal dependent GPS based distributions are used to show the influence of a GW hotspot area on the global mean circulation. Finally, we shall have a first look on the formation of PW and their propagation in the stratosphere.

2 Model Description and Configuration

The Middle and Upper Atmosphere Model (MUAM) is a nonlinear 3D mechanistic primitive equation global circulation model. It has a horizontal resolution of $5 \times 5.625°$ and extends in 56 vertical layers up to an altitude of 160 km in log-pressure height as described by Pogoreltsev et al. (2007) and Jacobi et al. (2015). At 1000 hPa, which is the lower boundary of the model, we introduce stationary planetary waves of wave numbers 1, 2 and 3 obtained from ERA Interim temperature and geopotential reanalysis data. Up to an altitude of 30 km the model zonal mean temperature is nudged to the reanalysis zonal mean temperature to correct the climatology in the troposphere.
Within the model, GW are parameterized after an updated linear scheme (Jacobi et al., 2006). GW amplitudes are initialized at an altitude of 10 km with an average value of

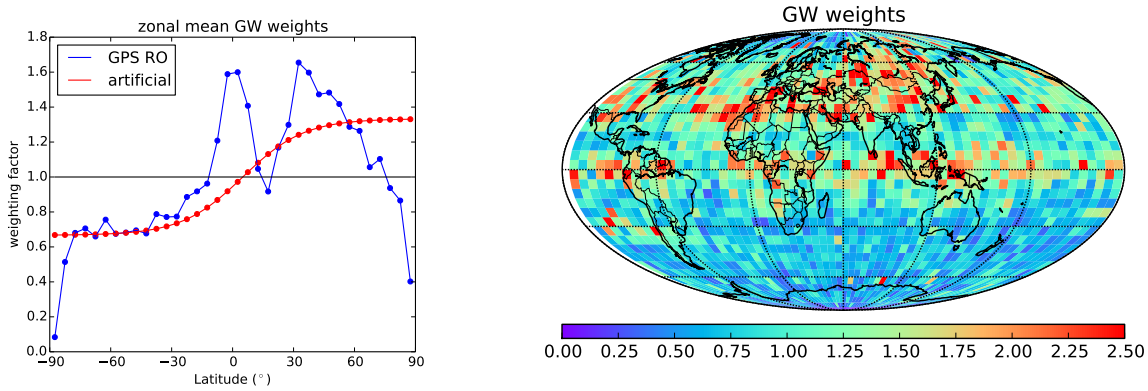

Fig. 1: Left: GW weights for the standard configuration after an artificial hyperbolic tangent of geographic latitude (red) and according to the zonal mean GPS RO potential energy (blue). Right: GW weights after GPS RO measurements, dependent on geographical latitude and longitude and interpolated to MUAM grid. All values are given for January conditions.

0.01 ms^{-1} for vertical velocity perturbation. In standard configuration these values are weighted by a hyperbolic tangent of the geographic latitude with larger amplitudes at the winter hemisphere (see Fig. 1, left). We will refer to that as the reference run. In two further runs, this artificial weighting is replaced first by a zonal mean and second by a latitudinal/longitudinal dependent weighting as shown in the two panels of Fig. 1. These data are obtained from the potential energy of disturbances, calculated from FORMOSAT3/COSMIC radio occultation density profiles between the tropopause to 35 km altitude as described by Šácha et al. (2014). Note that the tropopause is located higher at the equator (≈ 17 km) than at the poles (≈ 8 km) and that Kelvin waves are not filtered out. The GW weights are calculated from these data by dividing the potential energy at each grid point by the global mean potential energy.

As we can see in Fig. 1 (left), the zonal average of GPS RO based GW weights shows larger amplitudes than the reference weights in the equatorial region (most likely due to convective GW and due to Kelvin waves) and in the NH midlatitudes (most likely due to orographic waves). Near both poles the amplitudes on an average are many times smaller. The latitudinal-longitudinal dependent weights have a stronger contrast between small and large values of GW amplitudes which are often unevenly distributed in longitude. The distribution of the latitudinal/longitudinal dependent weights also reflects the topography of the Earth. For example, we can see in Fig. 1 (right) local areas of enhanced GW amplitudes around Himalayas and on northeastern coast of Asia. In the following we will refer to that as the GW hotspot region.

To analyze the influence of the different GW initializations on the global mean circulation we present the background January climatologies for several parameters. These are obtained by using the first 10 model days of the month January, and the zonal mean background and a stationary planetary wave of wavenumber 1 has been analyzed through least-squares fitting.

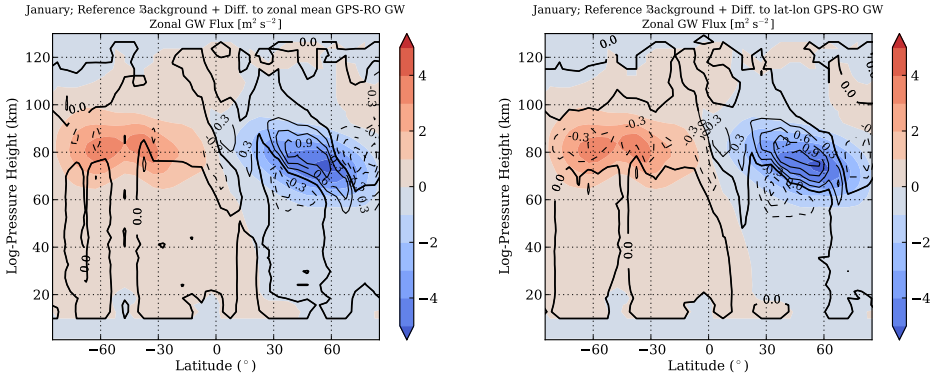

(a) GW momentum flux

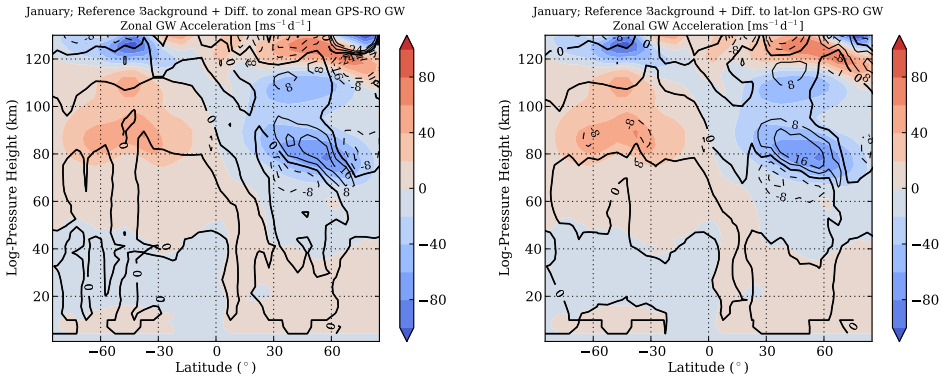

(b) GW acceleration

Fig. 2: Parameters as background reference (colors) and difference to the GW distribution from RO data as zonal mean (left) and longitudinal dependent (right) in black isolines.

3 Results

In Figs. 2 and 3 we present different atmospheric parameters as modeled by MUAM. Here, the results from the reference run are given in color coding, while the differences between the standard run and the runs with modified GW sources are added as black isolines. The respective left panels show the differences for the run with zonal mean GW, while the right panels show the results for the run with GW both dependent on latitude and longitude.

3.1 GW Parameters

In Fig. 2a we present the zonal GW momentum flux (MF) as obtained from the GW parameterization scheme in the MUAM model. The MF is positive/negative in the southern/northern hemisphere, i.e. directed in the opposite direction than the mean flow which is easterly/ westerly in the southern/northern hemisphere in January (see Fig. 3a). This also means that the mean flow is decelerated in the GW breaking region or, in other words, the mean flow is accelerated in its opposite direction, which is shown in Fig. 2b. This GW-mean flow interaction leads to the well-known zonal wind reversal above 80 km (see Fig. 3a below).

It is known from theory that GW of higher amplitudes are expected to break at lower altitude levels due to the fact that instability is reached earlier. This effect can be seen in the model simulations as well, when GW amplitudes are modified. Especially in the

area where zonal mean GPS GW amplitudes strongly exceed the artificial hyperbolic tangent (close to the equator and at 30°-60°N) we find the strongest changes in zonal GW momentum flux as shown in Fig. 2a. In both runs with GW amplitudes based on GPS RO potential energy the MF at these latitudes is larger in magnitude than in the reference run at altitudes up to approx. 70 km and weaker above that altitude. In the northern polar region where the GPS GW amplitudes become very small and are able to penetrate into higher altitudes, the MF is weaker below 70 km and stronger above that height. The same holds for acceleration of the mean flow due to GW breaking as shown in Fig. 2b.
Unexpectedly, the largest differences between the GPS zonal mean and longitudinal dependent run are found in the southern hemisphere where the maximum of GW momentum flux and its corresponding acceleration near 80 km are weakened. This effect is much stronger in the latitude/longitude dependent GW distribution. The changes generally appear to be slightly stronger in the latitude/longitude dependent GPS run than in the zonal mean GPS run.

3.2 Background Climatology

In Fig. 3a the zonal mean zonal wind is shown, while in Fig. 3b the zonal mean meridional wind is presented. The background temperature is shown in Fig. 3c. The background winds and temperatures agree with the temperature and wind patterns given in the literature (Fleming et al., 1990; Jacobi et al., 2009) which underlines the capability of the MUAM model to represent the middle atmosphere circulation.
In the zonal mean zonal wind (Fig. 3a) there are larger differences between the reference and the two GPS based runs than among the GPS based runs mutually. The reference run has lower wind speeds in the polar vortex due to the fact that GW amplitudes are larger in the polar region so that GW breaking leads to a deceleration of the polar vortex. Also the mesospheric jet is shifted more equatorward. This indicates that in both GPS RO runs the vortex is narrower. The middle atmosphere jet is also more structured in both GPS RO runs in contrast to the very symmetric looking one in the reference run.
An interesting aspect can be seen in the zonal GPS based run where up to the 30 km level in the polar region we can see weaker westerlies than in the latitude/longitude GPS and reference runs. At the lowest levels there are even prevailing easterlies in the zonal GPS run. It is surprising to see such a strong difference (extending 5 m/s) at such a low altitude taking into account that GW drag differs between runs at much higher levels (around 70 km). Furthermore, in the lower 30 km the nudging to ERA data does not seem to be prevailing in this region.
In the southern hemisphere there are only small differences and these are almost negligible below 60 km. This holds for both GPS runs.
The zonal mean meridional wind (Fig. 3b) shows considerable changes between the runs only at altitudes near the jet at about 80 km in the northern hemisphere. This jet is weakened at latitudes where the GPS zonal mean GW distribution strongly exceeds the artificial one (compare Fig. 1) and shifted slightly to lower altitudes which can be seen best at latitudes of about 40°N. In combination with the zonal mean zonal wind anomalies it seems likely that for increased amplitudes GWs begin to break earlier which leads to a stronger meridional wind below 80 km and hence to a weakening of the jet. This in turn can lead to a weakening of the middle atmosphere jet as observed in the zonal wind.

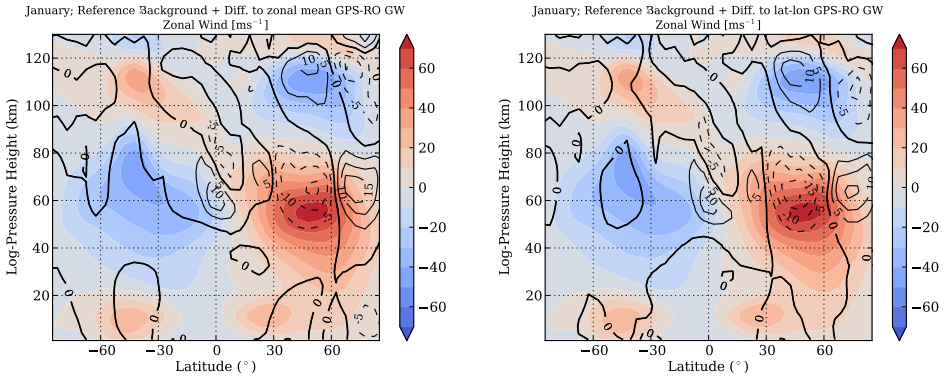

(a) Zonal wind

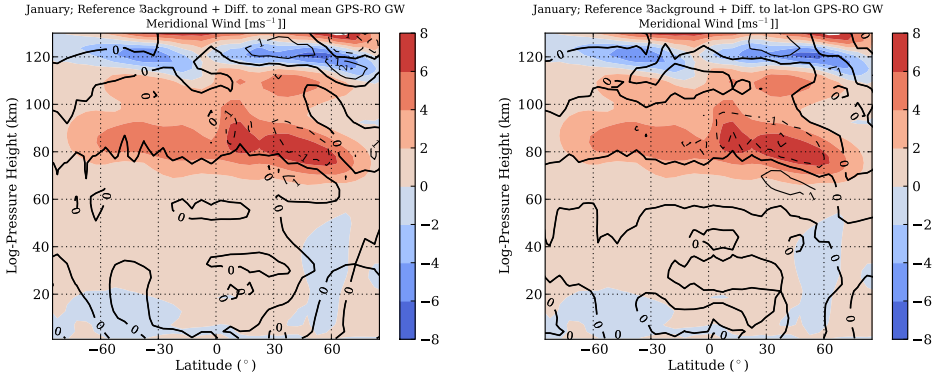

(b) Meridional wind

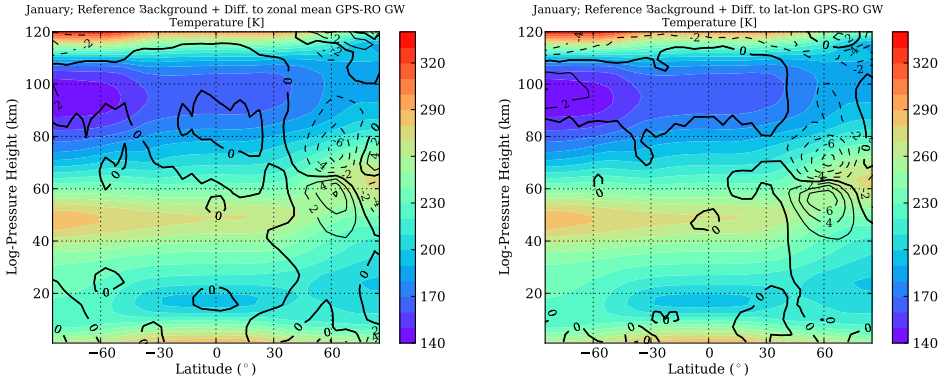

(c) Temperature

Fig. 3: Parameters as background reference (colors) and difference to the GW distribution from RO data as zonal mean (left) and longitudinal dependent (right) in black isolines.

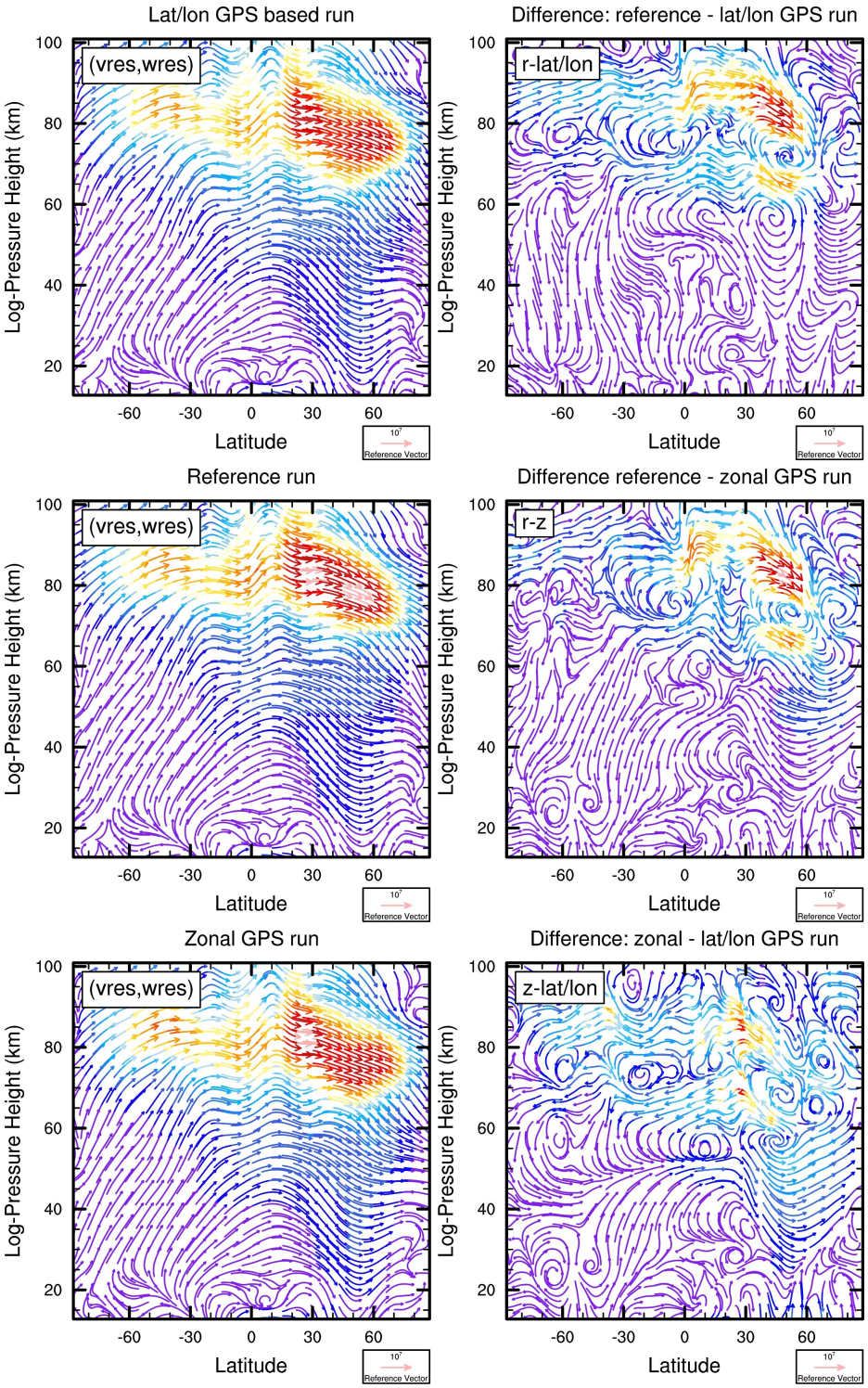

Fig. 4: Left column: Brewer-Dobson circulation vectors for a) GPS based longitudinal dependent run, b) reference run and c) GPS based zonal mean run. Right column: Differences between runs d) reference - longitudinal dependent, e) reference - zonal mean, f) zonal mean - longitudinal dependent. Residual velocity has units m/s. The intensity of circulation grows from blue to red.

Differences between the zonal mean and latitude/longitude dependent GW run are small. Qualitatively, the results show the same, however, in the latter one the effect is slightly stronger.
Between both GPS runs there are only small differences in the zonal mean temperature (Fig. 3c). The major differences between the GPS based runs and the reference run in the temperature field is a quadrupole like structure of differences centered at about 70 km and 70°N. This feature could have a physical interpretation in terms of polar vortex behaviour. As mentioned above, there is an indication from the zonal wind analysis that the vortex is broader in the reference run than in the GPS runs. When concentrating on the stratopause behaviour, we can see that in the reference run there is a sharp bend (at about 60°N) between the stratopause elevation inside the vortex and in the surf zone equatorward of the vortex. In contrast with that in both GPS runs there is a more gradual reduction of the stratopause elevation from approximately 75°N to 30°N. This could be due to the different behaviour of the BDC. In Fig. 4 the BDC, and its difference between the runs, are shown as vertical-meridional residual circulation vectors. Note that the length of the arrows has no direct physical meaning since the components of residual velocity were scaled according to Edmon Jr et al. (1980) first and then scaled by the relative ranges of the two axes of the plot(3.14 rad by 10^5 m). Finally the vectors are multiplied by a factor of 10^7 to get the reference vector.
As can be seen in Fig. 4, the BDC is characterized by an upward motion near the equator in the lower atmosphere (below 20 km) and a meridional transport from the summer pole to the winter hemisphere in higher altitudes. At about 80 km the meridional transport maximizes according to the background meridional wind shown in Fig. 3b. We find that the GPS based runs produce a stronger BDC in the northern midlatitudes (30°-60°N) around 60-70 km altitude while it is weaker higher above (see Fig. 4d and e). Also in these runs there is slightly stronger subsidence at midlatitudes below approximately 60 km. These features are even more pronounced in the latitude/longitude than in the zonal mean GPS based run (see Fig. 4f).
A further aspect is seen comparing Figs. 3c and 3a close to the surface of the northern hemisphere pole region: The regional shift from westerlies to easterlies appears to be connected to a warming by about 4 K. This could be due to subsidence. In the southern hemisphere mesopause another considerable warming of 2 K is evident in both GPS based runs, but this is stronger in the latitude/longitude dependent GPS run.

3.3 Planetary Wave Activity

Non-zonal forcing of GW in the lower atmosphere and subsequent non-zonal GW-mean flow interaction may lead to additional forcing of stationary planetary waves (PW). In Fig. 5, temperature amplitudes of the stationary PW with wavenumber $k = 1$ (SPW1) are presented for the reference run and their changes in the GPS based runs. The reference run shows a clear structure of SPW1 in the northern hemisphere region, especially for middle to high latitudes, because during winter waves are much more enhanced than during summer due to prevailing westerly winds. Additionally, northern hemisphere orography supports the enhancement of PW. Regarding the differences between the runs we find stronger amplitudes and a poleward shift of SPW1 below 60 km. Around that altitude we find only small changes but above that height amplitudes are stronger, too.

A useful tool to analyse PW activity, PW propagation and divergence and hence the regions of PW-mean flow interaction is the 2-dimensional presentation of the Eliassen-Palm (EP) flux and its divergence. EP fluxes represent the PW propagation expressed both in momentum and temperature flux, while the EP flux divergence is directly connected with the acceleration of the mean flow. In Fig. 6 we present the EP flux (arrows) and EP flux divergence (colors) for the reference run (left panel) and their changes between the GPS based longitudinal dependent run and the reference run. In the lower stratosphere (30-50 km altitude) we can observe enhanced poleward propagation above the GW hotspot region. This is in agreement with the displacement of PW shown in Fig. 5. The effect vanishes at an altitude of about 60 km. In the lower stratosphere (at about 30 km), one can see enhanced equatorward wave propagation, which leads to enhanced coupling of high, middle and lower latitude dynamics due to the GW distribution.

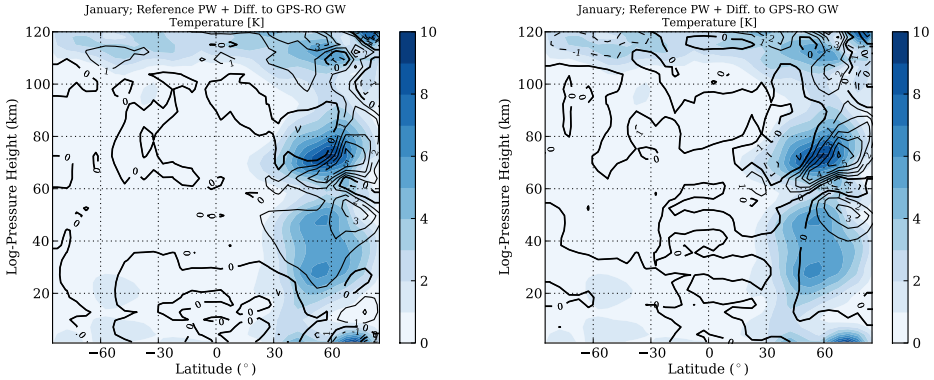

Fig. 5: Amplitudes of reference SPW1 in temperature (colors) and difference to the GW distribution from RO data as zonal mean (left) and longitudinal dependent (right) in black lines.

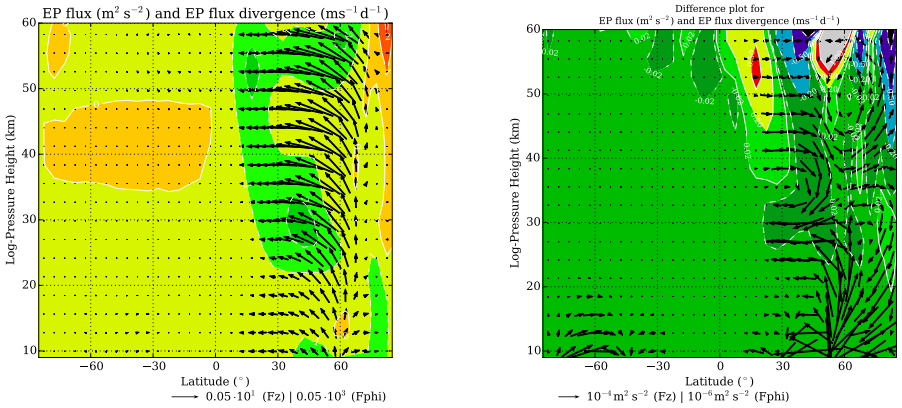

Fig. 6: Reference EP flux divergence and EP flux vectors (left) and difference to the GW distribution from RO data as longitudinal dependent and scaled by dry air density (right) for January conditions.

4 Conclusions and Outlook

In a model study we compared the influence of different distributions of GW based on artificial values and GPS RO data on the global dynamics of the middle atmosphere. While GPS retrieved zonal mean GW amplitudes are stronger than the artificial distribution at the equator and and northern midlatitudes, they are very weak at the poles. These differences lead to increased wind speeds of the polar vortex and a cooling at high latitudes as well as downward shift of the meridional wind jet.
Analyses of stationary PW indicate a stronger wave activity and an equatorward propagation of waves in the lower stratosphere, when realistic GW amplitude distributions are taken into account. Such equatorward propagating Rossby waves have been observed already by Ortland (1997) and are expected to break in tropics in the prevailing easterlies, which can lead to tropopause disruptions. This could prove to be one of the key mechanisms of STE as is suggested in the literature by the location and season of the observed STE and tropopause folds occurrence maxima (e.g. Berthet et al., 2007; Škerlak et al., 2015).
To further study the possible role of GW hotspot in PW forcing, propagation directions of the forced waves and possible interaction with stationary PW, in future we shall perform runs with artificially enhanced or distributed GW drag. We also plan to further investigate implications of localized GW activity in autumn on the evolution of the wintertime middle atmospheric circulation and structure of transport pathways in the middle atmosphere.

Acknowledgements

ECMWF reanalyses data are provided by apps.ecmwf.int/datasets/data/ and have been used in MUAM for assimilation in the troposphere.

References

Berthet, G., Esler, J. G., and Haynes, P. H., 2007: A Lagrangian per- spective of the tropopause and the ventilation of the lowermost stratosphere, J. Geophys. Res., 112, D18 102, doi:10.1029/2006JD008295.

Edmon Jr, H. J., Hoskins, B. J., and McIntyre, M. E., 1980: Eliassen-Palm cross sections for the troposphere, J. Atmos. Sci., 37, 2600–2616.

Ern, M., Ploeger, F., Preusse, P., Gille, J. C., Gray, L. J., Kalisch, S., Mlynczak, M. G., Russel, J. M., and Riese, M., 2014: Interactions of Gravity Waves with the QBO: A Satellite Perspective, J. Geophys. Res. Atmos., 119, 2329–2355, doi:10.1002/2013JD020731.

Fleming, E., Chandra, S., Barnett, J., and Corney, M., 1990: Zonal mean temperature, pressure, zonal wind and geopotential height as function of latitude, Adv. Space Res., 10, 11–59.

Foelsche, U., Borsche, M., Steiner, A. K., Gobiet, A., Pirschner, B., Kirchengast, G., and Schmidt, T., 2008: Observing upper troposphere–lower stratosphere climate with radio occultation data from the CHAMP satellite, Climate Dynamics, 31, 49–65.

Fritts, D. C. and Alexander, M. J., 2003: Gravity wave dynamics and effects in the middle atmosphere, Rev. Geophys., 41, 1003, doi:10.1029/2001RG000106.

Garcia, R. R. and Randel, W. J., 2008: Acceleration of the Brewer-Dobson circulation due to inÂcreases in greenhouse gases, J. Atmos. Sci., 65, 2731–2739.

Hines, C. O., 1960: Internal atmospheric gravity waves at ionospheric heights, Can. J. Phys., 38, 1441–1481.

Jacobi, C., Fröhlich, K., and Pogoreltsev, A., 2006: Quasi two-day-wave modulation of gravity wave flux and consequences for the planetary wave propagation in a simple circulation model, J. Atmos. Sol.-Terr. Phys., 68, 283–292.

Jacobi, C., Fröhlich, K., Portnyagin, Y., Merzlyakov, E., Solovjova, T., Makarov, N., Rees, D., Fahrutdinova, A., Guryanov, V., Fedorov, D., Korotyshkin, D., Forbes, J., Pogoreltsev, A., and Kürschner, D., 2009: Semi-empirical model of middle atmosphere wind from the ground to the lower thermosphere, Adv. Space Res., 43, 239–246.

Jacobi, C., Lilienthal, F., Geißler, C., and Krug, A., 2015: Long-term variability of mid-latitude mesosphere-lower thermosphere winds over Collm (51°N, 13°E), J. Atmos. Sol.-Terr. Phys., doi:10.1016/j.jastp.2015.05.006.

Kunkel, D., Hoor, P., and Wirth, V., 2014: Can inertia-gravity waves persistently alter the tropoÂpause inversion layer?, Geophysical Research Letters, 41, 7822–7829, doi:10.1002/2014GL061970.

Liebermann, R. S., Riggin, D. M., and Siskind, D. E., 2013: Stationary waves in the wintertime mesosphere: Evidence for gravity wave filtering by stratospheric planetary waves, J. Geophys. Res., 118, 3139–3149, doi:10.1002/jgrd.50319.

Manney, G. L., Schwartz, M. J., Krüger, K., Santee, M. L., Pawson, S., Lee, J. N., Daffer, W. H., Fuller, R. A., and Livesey, N. J., 2009: Aura Microwave Limb Sounder observations of dynamics and transport during the record-breaking 2009 Arctic stratospheric major warming, Geophysical Research Letters, 36, doi:10.1029/2009GL038586.

Oberheide, J., Liu, H.-L., Gusev, O., and Offermann, D., 2006: Mesospheric surf zone and temperaÂture inversion layers in early November 1994, J. Atmos. Sol.-Terr. Phys., 68, 1752–1763.

Ortland, D. A., 1997: Rossby wave propagation into the tropical strato- sphere observed by the High Resolution Doppler Imager, Geophysical Research Letters, 24, 1999–2002, doi:10.1029/97GL02001.

Pogoreltsev, A. I., Vlasov, A. A., Fröhlich, K., and Jacobi, C., 2007: Planetary waves in coupling the lower and upper atmosphere, Journal of Atmospheric and Solar-Terrestrial Physics, 69, 2083–2101, doi: 10.1016/j.jastp.2007.05.014.

Smith, A. K., 2003: The origin of stationary planetary waves in the upper mesosphere, J. Atmos. Sci., 60, 3033–3041.

Šácha, P., Foelsche, U., and Pišoft, P., 2014: Analysis of internal gravity waves with GPS RO density profiles , Atm. Meas. Tech., 7, 4123–4132, doi:10.5194/amt-7-4123-2014.

Šácha, P., Kuchař, A., Jacobi, C., and Pišoft, P., 2015: Enhanced internal gravity wave activity and breaking over the Northeastern Pacific / Eastern Asian region, Atm. Chem. Phys., submitted.

Škerlak, B., Sprenger, M., Pfahl, S., Tyrlis, E., and Wernli, H., 2015: Tropopause Folds in ERA-Interim: Global Climatology and Relation to Extreme Weather Events, J. Geophys. Res. Atmos., doi:10.1002/2014JD022787.

Long-period oscillations derived from mesosphere/lower thermosphere meteor radar temperature measurements

Nadja Samtleben and Christoph Jacobi

Institute of Meteorology, Stephanstr. 3 04103 Leipzig
E-Mail: Nadja.Samtleben@t-online.de

Abstract

Using measurements, derived from a meteor radar in Collm (51.3°N, 13°E), the mesopause region is analyzed with respect to the temperature distribution at an altitude of 90 km over a period of 10 years. The analyzed period lasts from 2005 till 2013. Based on these measurements, the typical temperature seasonal cycle of the mesopause region can be observed. The temperature reaches its minimum of about 130 K in summer and its maximum of about 220 K in winter. At this altitude, also strong day-to-day-fluctuations of up to 35 K exist, which are probably partly induced by planetary waves. Shorter-period oscillations with a period between 2 and 6 days have maximum amplitudes during summer, while longer-period oscillations with a period between 7 and 20 days maximize during winter. During the measurement period the amplitudes of oscillations with periods between 4 and 6 days, which may be attributed to the quasi-5-day-wave, increase with time.

Zusammenfassung

Auf der Grundlage von Messungen eines Meteorradars in Collm (51.3°N, 13°E), die in einer Höhe von 90 km erfolgten, was in etwa der Mesopause entspricht, wird die Temperatur hinsichtlich ihres Jahresganges und insbesondere ihrer Variationen in einem Messzeitraum von 10 Jahren analysiert. Der analysierte Zeitraum erstreckt sich von 2005 bis 2013. Anhand der Daten kann man den typischen Jahresgang der Temperatur in der Mesopausenregion erkennen. Die Temperatur erreicht im Sommer das Minimum bei etwa 130 K und im Winter das Maximum bei etwa 220 K. Zudem treten starke Tag-zu-Tag-Fluktuationen auf, die im Maximum 35 K betragen. Diese werden vermutlich durch planetare Wellenaktivität der Atmosphäre hervorgerufen. Hierbei spielen im Sommer die kurzwelligen und im Winter die langwelligen Oszillationen, letztere mit Perioden größer 7 Tage, die wesentliche Rolle. Ferner sind innerhalb des Messzeitraums zunehmende Amplituden von Oszillationen mit Perioden zwischen 4 und 6 Tagen (quasi 5-Tage-Welle) zu erkennen.

1. Introduction

At an altitude of 90 km the mesopause temperature shows considerable variability. This variability becomes apparent from day-to-day observations but also from inter-seasonal observations. The variability is evoked by natural incidents. One of those incidents is the impact of planetary waves (PW). The dimension of the temperature change depends on the altitude, at which the planetary waves are breaking.

There have been frequent attempts to characterize planetary wave activity and their trends in the middle atmosphere. E.g., Pogoreltsev et al. (2009) found a decrease of the winter quasi 5-, 10-, and 16-day waves in the stratosphere since the 1960s from NCEP/NCAR reanalysis. However, interannual and quasi-decadal variability of the waves is large, and the results of linear trend analyses over short time intervals of about one decade may deviate from the long-term trends. For the mesosphere/lower thermosphere (MLT), Jacobi et al. (1998, 2008) found increasing tendencies for PW in meteor radar winds, in particular for the zonal component, while for the meridional component the trends are small or negative, which overall results in only slightly positive wind trends.

To summarize, the degree of interannual variability of PW in the middle atmosphere is still subject to current research, and new data may lead to new insights into long-term tendencies of the middle atmosphere.

Therefore, in this article, temperature oscillations in the period range between 2 and 30 days are analyzed and attributed to the activity of PW in the middle atmosphere. We analyze the seasonal cycle, and the magnitude of the wave activity changes during the period from 2005 through 2013.

2. Measurements and data analysis

2.1. Calculation of the absolute temperature

The ambipolar diffusion coefficient is needed to receive the absolute values of the temperature at a height of 90 km. The ambipolar diffusion plays a vital role during the decay of the plasma tail of the meteoroids passing the atmosphere. Consequently, the ambipolar diffusion coefficient D_{amb} can be derived from the half-time decay time $\tau_{1/2}$ of the plasma tail. The process concerning the decay of the plasma tail is illustrated in equation:

$$A(t) = A_0 e^{-\frac{16\pi^2 D_{amb} t}{\lambda^2}} = A_0 e^{-ln2\frac{t}{\tau_{1/2}}}. \quad (1)$$

Here $A(t)$ is the radio wave amplitude (of wavelength λ) at time t, while A_0 is a the amplitude at $t = 0$. With the help of equation (1) the half-decay period can be calculated. The half-decay period $\tau_{1/2}$ only depends on the frequency of the meteor radar λ and the ambipolar diffusion coefficient D_{amb}, which is given in equation (2):

$$\tau_{1/2} = \frac{\lambda^2 ln2}{16\pi^2 D_{amb}}. \quad (2)$$

The ambipolar diffusion coefficient in equation (2) can be replaced by the ratio between the absolute temperature T and the local pressure p [Jones and Jones, 1990]:

$$D_{amb} = k_{amb} \frac{T^2}{p}. \quad (3)$$

The constant k_{amb} is a value, describing the properties of plasma. If the plasma consists out of many metallic ions and N_2 molecules, the constant k_{amb} reaches a value of $2.5 \cdot 10^{-4}$ $m^2 s^{-1} V^{-1}$. The pressure p in equation (3) will be replaced by a mean linear temperature gradient [Hocking, 1999]. For this purpose the Boltzmann barometric equation is necessary:

$$p = p_0 e^{-\int_0^z \frac{mg}{kT} dz'}, \tag{4}$$

where k is Boltzmann´s constant, m is mean molecular weight of the gas mixture, g is acceleration due to gravity taken as 8.5 ms^{-1} at 90 km and T is temperature. Using a linear temperature gradient (5) instead of an isothermic atmosphere (6):

$$\alpha = \frac{1}{T_0} \frac{dT}{dz}, \tag{5}$$

$$T = T_0 \left(1 + \alpha z'\right), \tag{6}$$

and inserting this into (3) one obtains:

$$ln\, D_{amb} = ln\, k_{amb} + 2 ln\, T_0 \left(1 + \alpha z\right) - ln\, p_0 + \frac{mg}{kT_0} \int_0^z \frac{1}{1 + \alpha z'} dz' \quad . \tag{7}$$

Choosing $z = 0$ at the height of the maximum meteor flux and differentiating with respect to z one obtains:

$$\frac{d}{dz} ln\, D_{amb} = 2\alpha + \frac{mg}{kT_0} . \tag{8}$$

Using the relation:

$$\frac{1}{S_m} = \frac{d}{dz} ln\, D_{amb}, \tag{9}$$

and substituting equation (9) in equation (8) and solving for T_0 results in the following equation:

$$T_0 = S_m \left(2 \frac{dT}{dz} + \frac{mg}{k} \right). \tag{10}$$

From one day of data, S_m is determined as the slope of a best-fit line. Equation (10) is defined by the height of the maximum meteor flux, which approximately can be found at an altitude of 90 km.

2.2. Filtering and determination of standard deviation

For filtering the values of the absolute temperature a Lanczos-filter [Duchon, 1979] is used. The filter is based on sinc functions (also called sigma approximations), which reduce the Gibbs phenomenon. This means that the amplitudes of strong harmonics are dampened. The sinc function is defined by:

$$sinc\ (x) = \frac{sin(\pi x)}{(\pi x)}. \tag{11}$$

For the analysis of the temperature values the number of weights was chosen as 50. The filter was applied as a bandpass filter with 2-3, 4-6, 8-12, 12-20 and 2-30 days cutoff periods, which allows us to investigate the period range of PW.

As a proxy for PW activity, the standard deviation of the daily temperatures was chosen. We calculated the standard deviation of the filtered time series in a running 91 day window, and allocated the respective results to the middle of the time interval. This resulted in a time series of daily standard deviations. Daily climatological values have been calculated by averaging the standard deviations from each day of the year over the years. Additionally, seasonal means were calculated by averaging 91 days of standard deviations.

3. Mean seasonal cycle of wave activity

Figure 1 shows the typical temperature cycle in the mesopause region with its minimum in summer and maximum in winter for 2005. In 2005 the minimum temperature in summer is 145.8 K and the maximum temperature in winter is 229.5 K. The summer in 2005 is the warmest of all summers during the measurement period under investigation.

Additionally, strong day-to-day fluctuations can be observed. During the whole measurement period the maximum fluctuation is 35 K. Compared to the difference of the summer and winter extremes, which is nearly 85 K in 2006, the day-to-day fluctuations prove to be a major component of temperature variability. These fluctuations are dominantly caused by PW, which will be demonstrated in the following. Furthermore, measurement uncertainties play a role as well.

Additionally, Figure 1 illustrates the values of the temperature profile, filtered in a range of 2-3, 4-6, 8-12 and 12-20 days. The smaller the range of days is chosen, the stronger is the filtering process. The four ranges were chosen to investigate the amplitudes of PW. Especially, those of the quasi-2-day, quasi-5-day, quasi-10-day and quasi-15-day wave are observed. These filtered values are used to calculate the standard deviations for the different ranges and the averages for each day of the year in the period from 2005 till 2013. Actually, at the beginning and the end of the time interval analyzed, additional data have been used but had been disregarded because they would have been influenced by the filter applied. The results are shown in Figure 2.

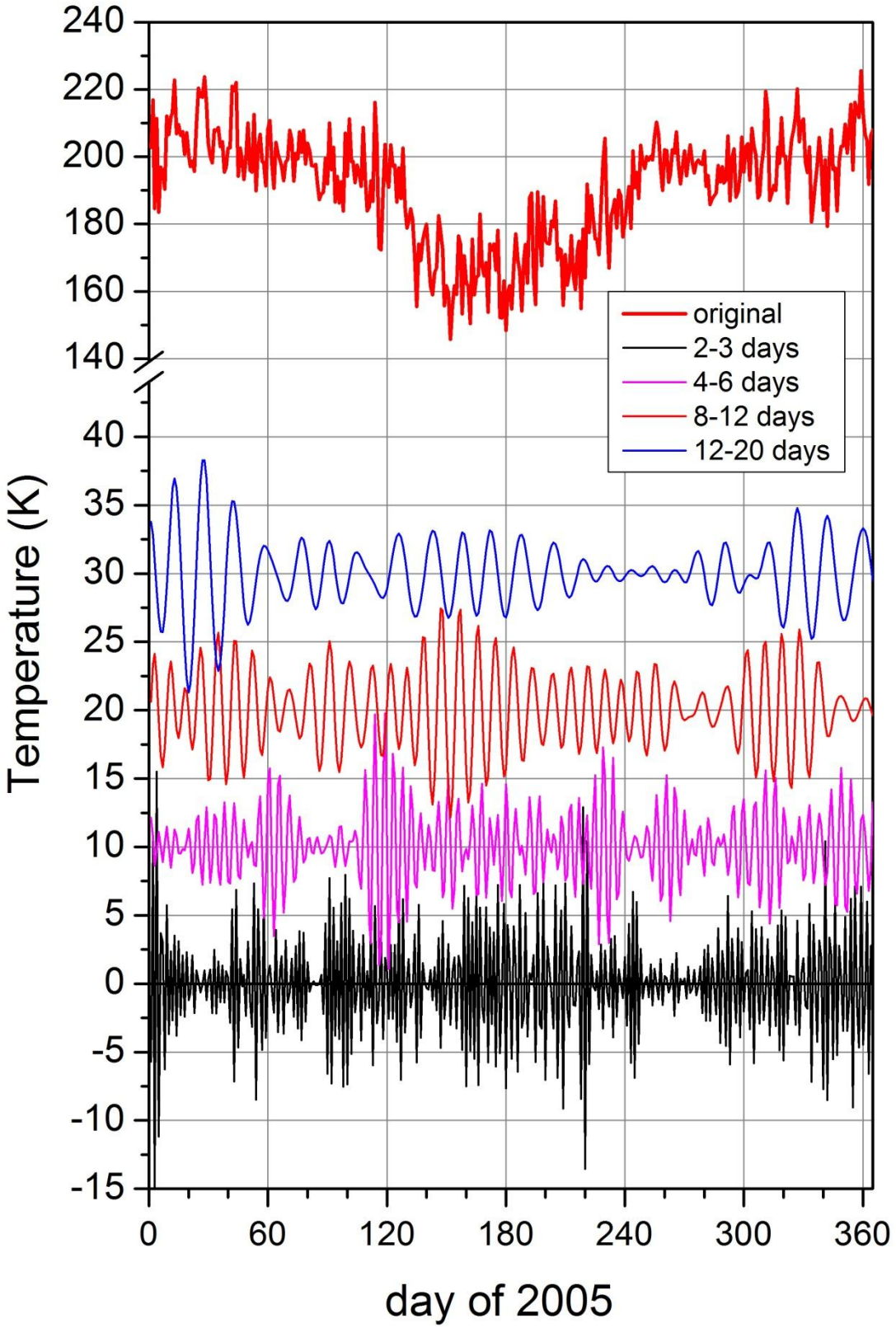

Figure 1: Example of time series of daily temperatures at 90 km over Collm in 2005. The red line shows the unfiltered data. The other curves show data filtered in the respective period ranges as given in the legend.

The standard deviation reflects the temperature fluctuation, which is assumed here to be caused by the PW. So the standard deviation is taken as proxy for seasonal PW activity and it also represents the magnitude of the wave amplitude. In general, each range, illustrated in Figure 2(a-e), demonstrates the standard deviation, which is maximal during summer and winter and minimal during the equinoxes. This means the influence of PW is stronger during solstices.

In Figure 2(a) the averaged standard deviation of the filtered data in a range between 2 and 3 days is presented. The standard deviation is larger in summer than in winter. This means that oscillations with a period between 2 and 3 days, which also includes the quasi-2-day wave, have a larger amplitude in summer than in winter. The standard deviation reaches values of about 5 K in summer, which is large in comparison to the other period ranges. The quasi-2-day wave plays an important role concerning the fluctuation of the temperature.

In Figure 2(b) the mean standard deviation of the filtered data in the range between 4 and 6 days is presented. As with the quasi 2-day oscillation shown before, the standard deviation reaches its maximum in summer. However, the maximum reaches approximately only 4 K, so the quasi-5-day wave is less dominant compared to the quasi-2-day wave. In the range between 8 and 12 days the maximum of the mean standard deviation, presented in Figure 2(c), is not reached in summer anymore but rather in winter, and it reaches nearly 3.5 K. Consequently, oscillations with periods smaller than 8 days are dominant in summer and those with periods larger than 8 days are dominant in winter. This is also confirmed by Figure 2(d), which shows the mean standard deviation of the filtered data in a range between 12 and 20 days. The mean standard deviation has its maximum in winter at about 4.25 K.

When comparing the mean standard deviation of Figure 2(c) with Figure 2(d), it can be observed, that oscillations between 12 and 20 days are more dominant in winter. So the quasi-16-day wave causes more temperature fluctuation than the quasi-10-day wave.

In the lowermost panel of Figure 2, all oscillations in a range between 2 and 30 days are taken into account. With this it can be analyzed, for which season the wave activity is strongest. The mean standard deviation reaches its maximum in winter. Consequently, the wave activity in winter is stronger than in summer.
The sum of the mean standard deviation maxima from oscillations with periods between 2 and 6 days corresponds to the maxima of the mean standard deviation of the filtered data in a range between 2 and 30 days. The sum of the mean standard deviation maxima from oscillations with periods between 8 and 20 days is 7.75 K. There are missing 3.5 K to the mean standard deviation maximum of the filtered data in a range between 2 and 30 days. Consequently, in the range between 20 and 30 days are also strong oscillations, which cause strong fluctuations.

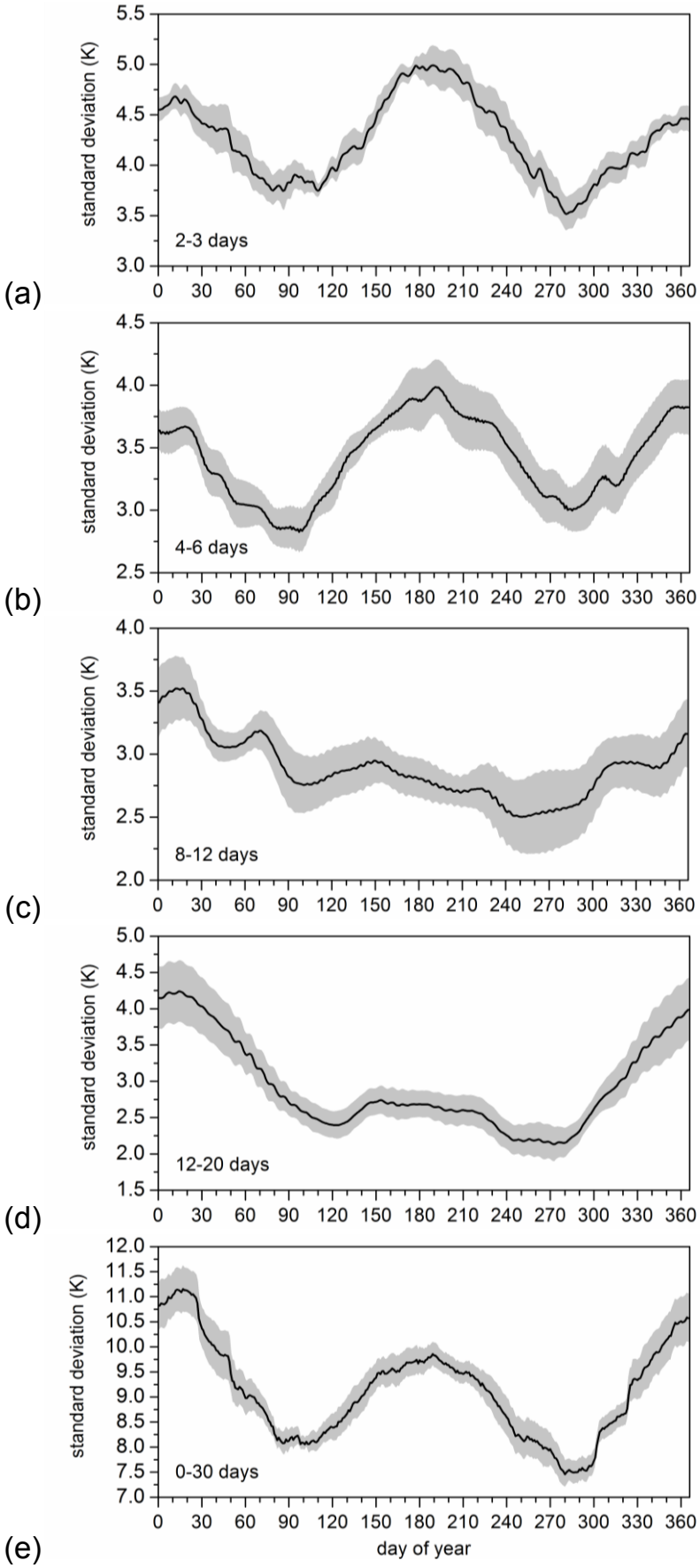

Figure 2: 2005-2013 mean standard deviation, each based on 91 days of temperatures filtered in the respective period intervals given in the legend. The greyshaded regions indicate the standard errors of the values of each day of the year.

4. Interannual variability

Due to the maximum amplitudes of oscillations during the solstices, we restrict our analysis to the interannual variability in summer and winter. Therefore, the standard deviation of the 15th of January and July of each year in different period ranges are used. These dates are chosen, because they represent the whole summer and the whole winter. As has been mentioned, during the filtering of the absolute temperature values, a time frame of 91 days was chosen. The 15th of January and July are the middle of these time frames. The standard deviation of the 15th of January represents the period from December to February and that of the 15th of July represents the period from June to August.

In Figure 3 one can see that the amplitudes of the different oscillations are different from one year to another. Consequently, the amplitude of the oscillations is not predictable from climatology alone. In contrast to the mean climatology, for some cases the standard deviations of oscillations with periods smaller than 8 days are smaller in summer than in winter. Also in some cases the standard deviations of oscillations with periods larger than 8 days are smaller in winter than in summer.

Figure 3(a) shows the individual standard deviation for a period range from 2 to 3 days. The red line represents summer (JJA – June, July, August) and the blue line represents winter (DJF – December, January, February). No clear pattern or trend can be observed. The standard deviation changes rapidly from year to year. In the period range between 4-6 days (Figure 3(b)) this is different, and a positive trend is visible. The standard deviation increases nearly from year to year, especially in summer. The wave activity in this range shows an increase of 0.2 K/year (+/- 0.05 K/year). In Figure 3(c) oscillations with periods between 8 and 12 days and in Figure 3(d) those with periods between 12 and 20 days are shown. In these cases no trend or clear variability pattern can be found.

In Figure 3(e) the standard deviation of all oscillations with periods between 2 and 30 days is presented. It can be seen that the sum of all standard deviations does not show strong variability. The standard deviation fluctuates in a specific range. One can say that in summer the impact of all oscillations causes mostly a deviation of the mesopause temperature in a range from 9 up to 10.5 K. In winter the deviation is in a range between 9 and 11K. The high value in year 2009 is neglected in this discussion, because there was a strong stratospheric warming in this year, which lead to stronger wave activity [Labitzke and Kunze, 2009; Manney et al., 2009]. This value would falsify the result. So in the end, the fluctuation of mesopause temperature due to the wave activity is nearly constant during summer and winter. During the equinoxes the range of the deviation is much smaller.

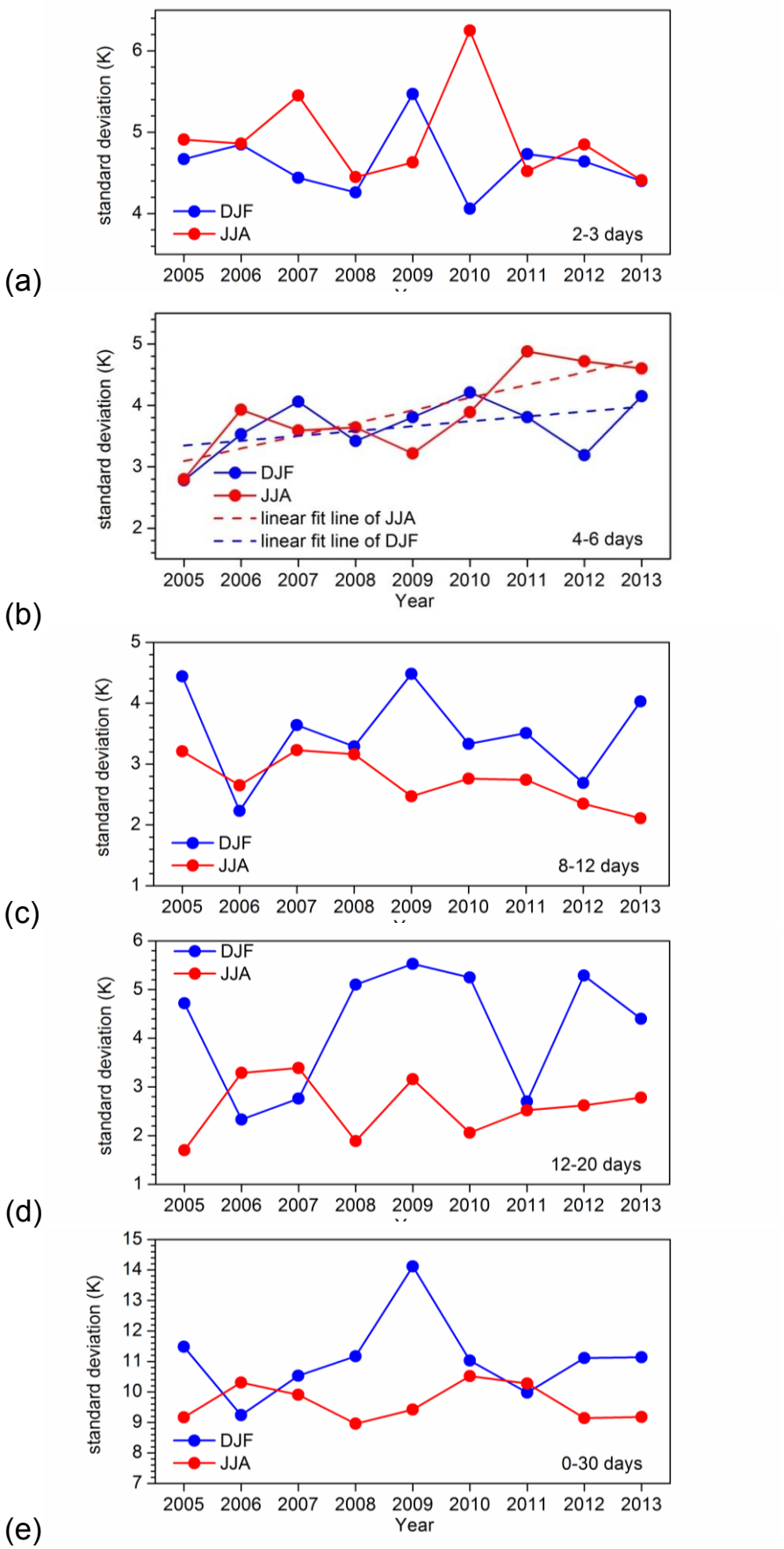

Figure 3: Seasonal mean standard deviation, each value based on 90 days of data filtered in the respective period intervals given in the legend.

5. Conclusions

On the basis of the temperature measurements one can see strong day-to-day fluctuations which are caused by PW. The amplitudes are stronger during solstices than during equinoxes. In summer (winter) oscillations with periods smaller (larger) than 8 days dominate the day-to-day variability. Except the period range between 4 and 6 days, the overall power of all oscillations was nearly constant during the measurement period. They showed a positive trend of 0.2 K/year (+/-0.05 K/year) during the last 9 years, thus, the wave activity of the quasi-5-day wave is increasing. All oscillations evoke a deviation of the mesopause temperature in a range between 9 and 11K in summer and winter.

References

Beig, G., 2011: Long-term trends in the temperature of the mesosphere/lower thermosphere region: anthropogenic influences, J. Geophys. Res., 116, doi: 10.1029/2011JA016646

Duchon, C.E., 1979: Lanczos Filtering in One and Two Dimensions, J. Appl. Meteorol., 18, No. 8, 1016–1022, doi: 10.1175/1520-0450

Hocking, W.K., 1999: Temperatures using radar-meteor decay times, Geophys. Res. Lett., 26, No. 21, 3297-3300, doi: 10.1029/1999GL003618

Jacobi, Ch., Schminder, R., and Kürschner, D., 1998: Planetary wave activity obtained from long-term (2-18 days) variations of mesopause region winds over Central Europe (52°N, 15°E), J. Atmos. Sol.-Terr. Phy., 60, 81-93, doi: 10.1016/S1364-6826(97)00117-X

Jacobi, Ch., Hoffmann, P., and Kürschner, D., 2008: Trends in MLT region winds and planetary waves, Collm (52°N, 15°E), Ann. Geophys., 26, 1221-1232, doi: 10.5194/angeo-26-1221-2008

Jones, W., and Jones, J., 1990: Ionic diffusion in meteor trails, J. Atmos. Sol.-Terr. Phy., 52, 185-191, doi: 10.1016/0021-9169(90)90122-4

Labitzke, K., and Kunze, M., 2009: Über die unerwartet warme Stratosphäre im Winter 2008/2009, Beiträge zur Berliner Wetterkarte, 27/09, SO 13/9, 8p

Manney, G.L., Schwartz, M.J., Krueger, K., Santee, M.L., Pawson, S., Lee, J.N., Daffer, W.H., Fuller, R.A., and Livesey N.J., 2009: Aura Microwave Limb Sounder observations of dynamics and transport during the record-breaking 2009 arctic stratospheric major warming, Geophys. Res. Lett., 36, L12815, doi: 10.1029/2009GL038586

Pogoreltsev, A.I., Kanukhina, A.Yu., Suvorova, E.V., and Savenkova, E.N., 2009: Variability of planetary waves as a signature of possible climatic changes, J. Atmos. Sol.-Terr. Phy., 71, 1529–1539, doi: 10.1016/j.jastp.2009.05.011

The terdiurnal tide in the MUAM circulation model

A. Krug, F. Lilienthal, Ch. Jacobi

Institute for Meteorology, Stephanstr. 3, 04103 Leipzig
E-Mail: amelie.krug@studserv.uni-leipzig.de

Summary: The terdiurnal tide (TDT) in the mesosphere and lower thermosphere has been simulated with a 3D mechanistic circulation model of the middle atmosphere. The tidal temperature amplitude shows a clear seasonal cycle with peaks in the midlatitudes and near the equator at equinox. Under solstice conditions maximum amplitudes occur at 10° in the summer hemisphere and at 30-40° latitude in the winter hemisphere. The vertical wavelengths are large at midlatitudes and small at the equator with about 15 km. These characteristics are compared with SABER/TIMED satellite data from 2002-2009. Especially for temperature amplitudes good agreement is visible. At 90 km, comparison of the zonal wind TDT with radar observations from the literature also shows that the model realistically simulates the seasonal cycle of the TDT.

Zusammenfassung: Die achtstündige Gezeit (TDT) in der Mesosphäre und unteren Thermosphäre wurde mit einem 3D mechanistischen Zirkulationsmodell der mittleren Atmosphäre modelliert. Die Amplitude der achtstündigen Gezeit in der Temperatur zeigt dabei eine klare saisonale Variabilität mit Maxima im Bereich der mittleren Breiten und des Äquators während der Äquinoktien. Die vertikale Wellenlänge ist in den mittleren Breiten groß und am Äquator mit ca. 15 km klein. Diese Strukturen werden mit SABER/TIMED Satellitenmessungen der Jahre 2002-2009 verglichen. Vor allem für die Amplituden in der Temperatur ist eine gute Übereinstimmung zu erkennen. Ein Vergleich der achtstündigen Gezeit im Zonalwind in 90 km Höhe mit Radarmessungen aus der Literatur zeigt, dass das Modell den Jahresgang realistisch simuliert.

1 Introduction

Mesosphere and lower thermosphere (MLT) large-scale dynamics are considerably influenced by atmospheric waves, including solar tides, which are inertial gravity waves with periods of a solar day or its subharmonics. Solar tides are forced by absorption of solar radiation mainly by ozone in the stratosphere and water vapor in the troposphere. Atmospheric tides propagate in each spatial direction with vertical growing amplitudes owing to the exponentially decreasing density with height. Therefore, tidal components attain large amplitudes in the MLT (Chapman and Lindzen, 1970; Andrews et al., 1987). In this article, the westward propagating TDT with a zonal wavenumber of s=3 (TW3) is presented. The TW3 generally has smaller amplitudes than the semidiurnal (SDT) and diurnal tide (DT). Beside solar heating, other formation mechanisms of terdiurnal tides have been proposed, such as gravity wave breaking (Miyahara and Forbes, 1991) and nonlinear interactions between DT and SDT (Teitelbaum et al., 1989). There have

been several studies of terdiurnal signatures in radar and satellite measurements. Beldon et al. (2006) were investigating horizontal winds, measured by a VHF meteor radar at Castle Eaton, UK (52.6° N, 2.2° W), near 90 km in 1988-2004, found a clear seasonal behavior with largest amplitudes in autumn and early winter. A similar seasonal cycle was observed by Fytterer and Jacobi (2011) and Jacobi and Fytterer (2012) over Collm (51.3° N; 13.0° E). In meteor radar measurements over Wakkanai (45.4° N; 141.7° E), however, slightly larger amplitudes were observed in winter than in summer (Namboothiri et al., 2004).

Yue et al. (2013) analyzed measurements by the Sounding of the Atmosphere using Broadband Emission Radiometry (SABER) and the TIMED Doppler Interferometer (TIDI) instruments onboard the Thermosphere-Ionosphere-Mesosphere-Energetics and Dynamics (TIMED) satellite from 2002-2009. TIDI horizontal wind measurements reveal amplitudes of more than 16 ms^{-1} at 50° N/S above 100 km and an additional peak of the meridional component in ~82 km and 10-20° N is visible. SABER temperature terdiurnal amplitudes match to the first real symmetric (3,3) mode with peaks up to 8 K above the equator and at midlatitudes. SABER/TIMED data of 2002-2011 were also analyzed by Moudden and Forbes (2013). Here, for an altitude of about 90 km, largest amplitudes were found above the equator during equinox and at 60° N during May (~7 K) and 60° S in October (up to 5 K). Generally, TDT amplitudes at midlatitudes tend to maximize during equinox and in winter. Near the equator, there is an annual cycle with largest amplitudes in summer.

Modeling of the TDT so far has mainly been focused on excitation mechanisms, in particular direct solar heating and nonlinear interaction between DT and SDT. Huang et al. (2007) developed a nonlinear numerical tidal model to investigate amplitude features of the TDT excited by nonlinear interaction between DT and SDT. The results suggest that the migrating TDT can be significantly excited by this mechanism in the MLT region. Du and Ward (2010) analyzed CMAM Global Circulation Model results with regard to correlations between TDT and DT/SDT on the short-term or seasonal time scale. Correlation analysis indicated that nonlinear forcing is unlikely to be the source of the migrating TDT in the CMAM. Akmaev (2001) concluded from circulation model calculations that nonlinear interaction makes a contribution to the excitation of the TDT at 95-100 km, particularly during equinox. Smith and Ortland (2001) performed similar calculations as well as numerical runs in which the SDT forcing was removed from the model in order to exclude nonlinear forcing as possible TDT source. The results indicate that the direct solar heating is the main driver of the TDT at middle and high latitudes, while nonlinear interactions contribute to the TDT at low latitudes.

In this paper we use the Middle and Upper Atmosphere Model (MUAM; Pogoreltsev et al., 2007) to simulate TDT amplitudes and phases. The remainder of this paper is organized as follows: In the following section 2 the model is described, in section 3 the seasonal cycle of the tidal amplitudes in temperature and zonal wind at an approximate height of 90 km are presented. Furthermore, altitude-latitude cross sections of terdiurnal amplitudes and phases in zonal wind and in temperature are shown under equinox and solstice conditions. Tidal structures in temperature are compared with observations, in particular with SABER/TIMED temperature measurements between 2002-2009, as presented in Pancheva et al. (2013). Section 4 concludes the paper.

2 Model description

MUAM (Pogoreltsev et al., 2007) is a 3D nonlinear mechanistic grid point model which generates atmospheric circulation self-consistently. The horizontal resolution in latitude and longitude is $5° \times 5.625°$. In the vertical, a log-pressure height $z = -H \ln(p/p_0)$ with a constant scale height H of 7 km and a reference pressure $p_0 = 1000$ hPa is used. Throughout the middle atmosphere, log-pressure heights and geometric heights do not differ much. The 56 vertical layers extend to an altitude of about 160 km. For time integration an Euler backward scheme after Matsuno (1966) is included with 16 time steps per hour.

As lower boundary condition we assimilate zonally averaged geopotential and temperature fields, and additionally, monthly averaged amplitudes and phases of the first three harmonics as stationary planetary waves, both taken from ERA-Interim Reanalysis data

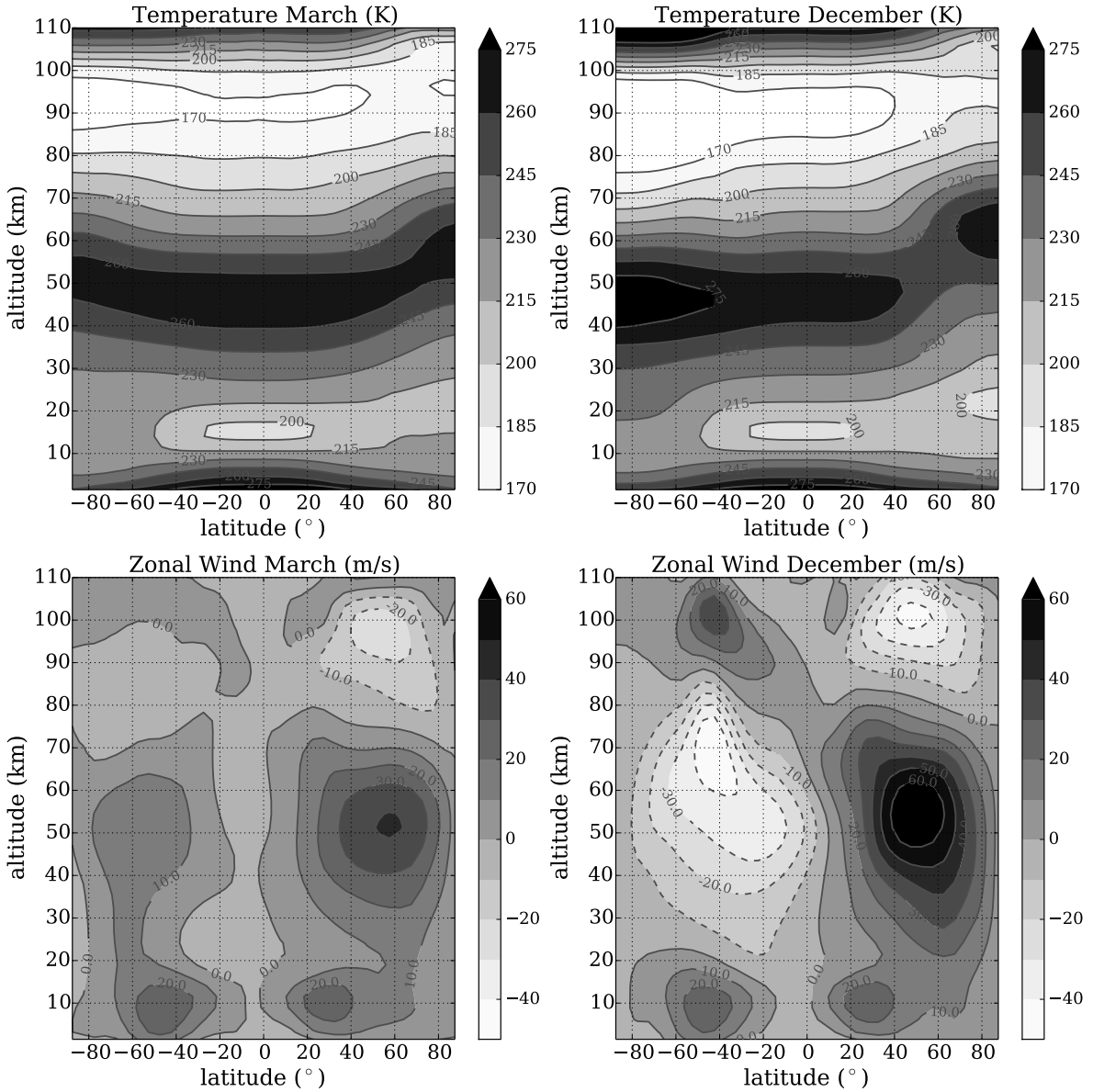

Fig. 1: MUAM zonal mean background temperature (upper row) and zonal wind (lower row) in March and December.

(Dee et al., 2011) at 1000 hPa. We further nudge zonally averaged ERA-Interim Reanalysis temperature data up to 30 km log-pressure height. Here, a 11-year monthly mean of 2000 to 2010 is applied.

Heating of the atmosphere due to absorption of solar radiation by ozone and molecular oxygen are included according to Strobel (1978) and Mlynczak and Solomon (1993). Heating rates of CO_2 are adjusted according to Liou (1992) and water vapor is included after Freidenreich and Ramaswamy (1999). EUV-heating rates are parameterized after Richards et al. (1994) and Roble (1995). Infrared cooling of CO_2 in the 15μm band in the stratosphere and lower mesosphere is calculated after Fomichev et al. (1998), cooling of water vapor after Chou et al. (1993). Ozone infrared cooling, which is mainly dominant at the lower mesosphere near the stratopause in the 9,6 μm band, is applied after Fomichev and Shved (1985). More specific information may be found in Lange (2001), section 2.1.2 and Fröhlich et al. (2003).

In MUAM, water vapor and ozone fields are prescribed. While water vapor is given as a simple zonal mean distribution, we use monthly means of ozone data by Stratosphere-troposphere Processes and their Role in Climate Project (SPARC; Randel and Wu, 2015) up to a height of 50 km log-pressure. That means that no secondary ozone maximum is considered. CO_2 is included by monthly means of measurements by Mauna Loa Observatory (Dlugokencky et al., 2014). For the presented climatology, measurements of ozone and CO_2 in 2005 are used.

The model is initialized with a global uniform temperature profile and zero wind. In a 120 model day spin-up phase, the mean wind fields are built up. In the course of this, solar heating rates are averaged over longitudes, so that no tides are forced. After that phase, during another 210 days the tides are formed by allowing longitudinal dependent solar heating. Thereafter, for each model run, additional 30 model days are simulated for January and July conditions with declination set to the respective month. Here, we analyze the TW3 in temperature and zonal wind from these 30 model days here.

The model results for zonal mean background temperature and zonal wind are shown in Figure 1. Altitude is given in geometric heights. Modeled background fields well represent the mean climatology of the middle atmosphere as, e. g., given by the COSPAR International Reference Atmosphere (CIRA; Chandra et al., 1990). In March zonal wind reverses in an altitude of ~70-80 km and reaches 40 ms^{-1} in 50 km altitude at ~60° N. In December, the wind reversal occurs slightly higher at 80-90 km. Wind speeds range from more than 40 ms^{-1} westward to ~70 ms^{-1} eastward.

3 Model results for the terdiurnal tide

To give an overview of the seasonal and latitudinal behavior, modeled tidal amplitudes in temperature and zonal wind are shown in Figure 2 at 90 km. At low latitudes, amplitudes are large during summer and the equinoxes. This pattern is also seen by Pancheva et al. (2013) but for higher altitudes. At lower midlatitudes amplitudes are increased in winter (~1 K). Weaker peaks are visible in June-July and August-September in the Northern Hemisphere (NH) and April/September in the Southern Hemisphere (SH) (~0.75 K). The SH winter maximum has also been modeled by Yue et al. (2013), while the pattern in the NH has not been modeled by them. The equinox maxima, however, has been observed by Pancheva et al. (2013) using SABER data. On the right panel in Figure 2

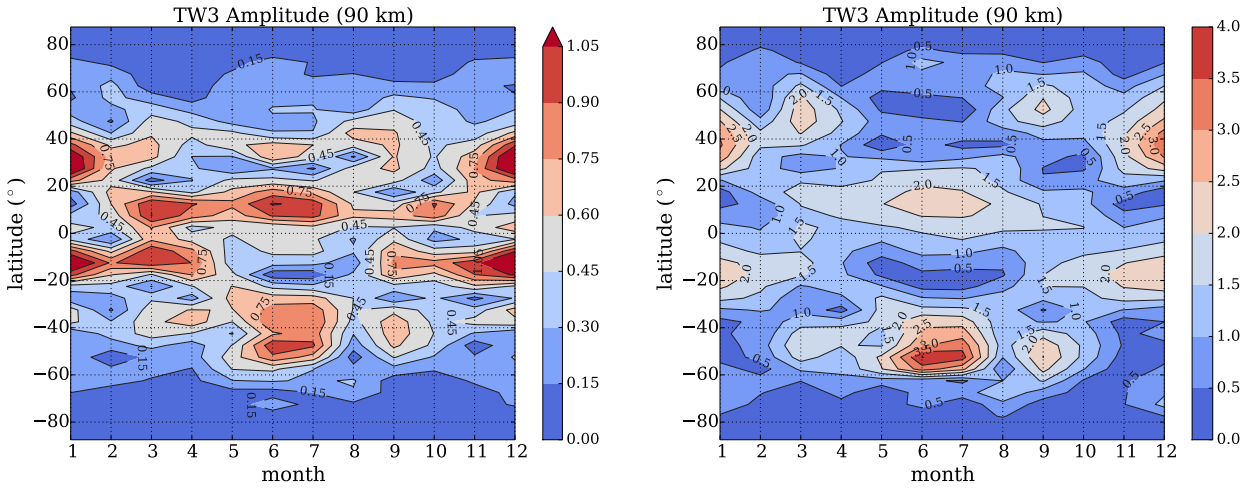

Fig. 2: Latitude-time cross section of the terdiurnal amplitudes in temperature (left, in K) and zonal wind (right, in ms^{-1}*) at 90 km modeled with MUAM.*

terdiurnal zonal wind amplitudes are presented. Similar to temperature amplitudes, peaks in winter and, for the NH, during equinox are visible at midlatitudes and in summer at low latitudes. This is in good agreement with TIDI TW3 amplitudes presented in Yue et al. (2013). The equinox and winter maxima at NH midlatitudes have also been registered by radar (Beldon et al., 2006; Fytterer and Jacobi, 2011). The equinox maxima, which are clearly observed in satellite and ground-based data, are not observed in other models like TIME-GCM (Yue et al., 2013) or the extended Canadian Middle Atmospheric Model (CMAM; Du and Ward, 2010). We may conclude that the seasonal cycle of the TW3 amplitudes in temperature and zonal wind can be well reproduced by MUAM. However, modeled amplitudes are smaller than the observed ones by a factor of two at most.

In the following, we directly compare our modeled TDT amplitudes with SABER analyses by Pancheva et al. (2013). The modeled tidal amplitudes during equinox and solstice are presented in Figure 3 as black solid lines. SABER TW3 amplitudes from Pancheva et al. (2013) are given in the figure as color coding. In order to allow comparability with SABER observations that are only available up to 50° latitude, only the region from 50° S to 50° N is shown here. During equinox (upper row) maxima in the midlatitudes (~3-5 K) and above the equator (~6 K) are visible. In June the tidal amplitude shows peaks at 10° N (~7 K), 30° N (~4 K) and 40° S (~5 K). The amplitude maximizes at 10° S (~9 K) and 30° N/S (~5 K) in December.

By comparing MUAM results with SABER measurements, the good general correspondence between the latitudinal distribution of observed and modeled amplitudes is striking. The observed amplitudes are slightly higher (~2 K), but the latitudinal and seasonal structures are well reproduced by MUAM. Even the weak peak around 85-90 km above the equator is evident in MUAM, though the modeled amplitudes are about 3 K too small. Pancheva et al. (2013) claim that this peak corresponds to a trapped phase above the equator. This can be seen in Figure 4, which presents a altitude-latitude cross section of the tidal phase structure in SABER/TIMED measurements (color shaded) and MUAM (black solid lines).

Observed tidal phase shows large vertical wavelengths above the equator and small ones in midlatitudes (e. g. from 70 km to 95 km at 40° S in March). Overall, a negative phase gradient can be seen, which implies upward propagating energy. This is similar to MUAM results. However, the modeled phases have shortest vertical wavelengths above the equator with ca. 15 km in March and from 90 to 100 km above the equator in October or at 10° S in June. In contrast, vertical wavelengths at midlatitudes are large. The modeled phases in the NH and SH in summer and winter are similar, as is the case with the amplitudes during solstice.

The modeled TW3 zonal wind amplitudes in March and December are displayed in Figure 5. In March maximum values with up to 9 ms^{-1} are reached in the midlatitudes and above the equator. In the SH peaks are slightly shifted to low and high latitudes in December. Like TW3 temperature phases, shown in Figure 4, TW3 zonal wind phases have large wavelengths above the equator and smaller ones in the midlatitudes.

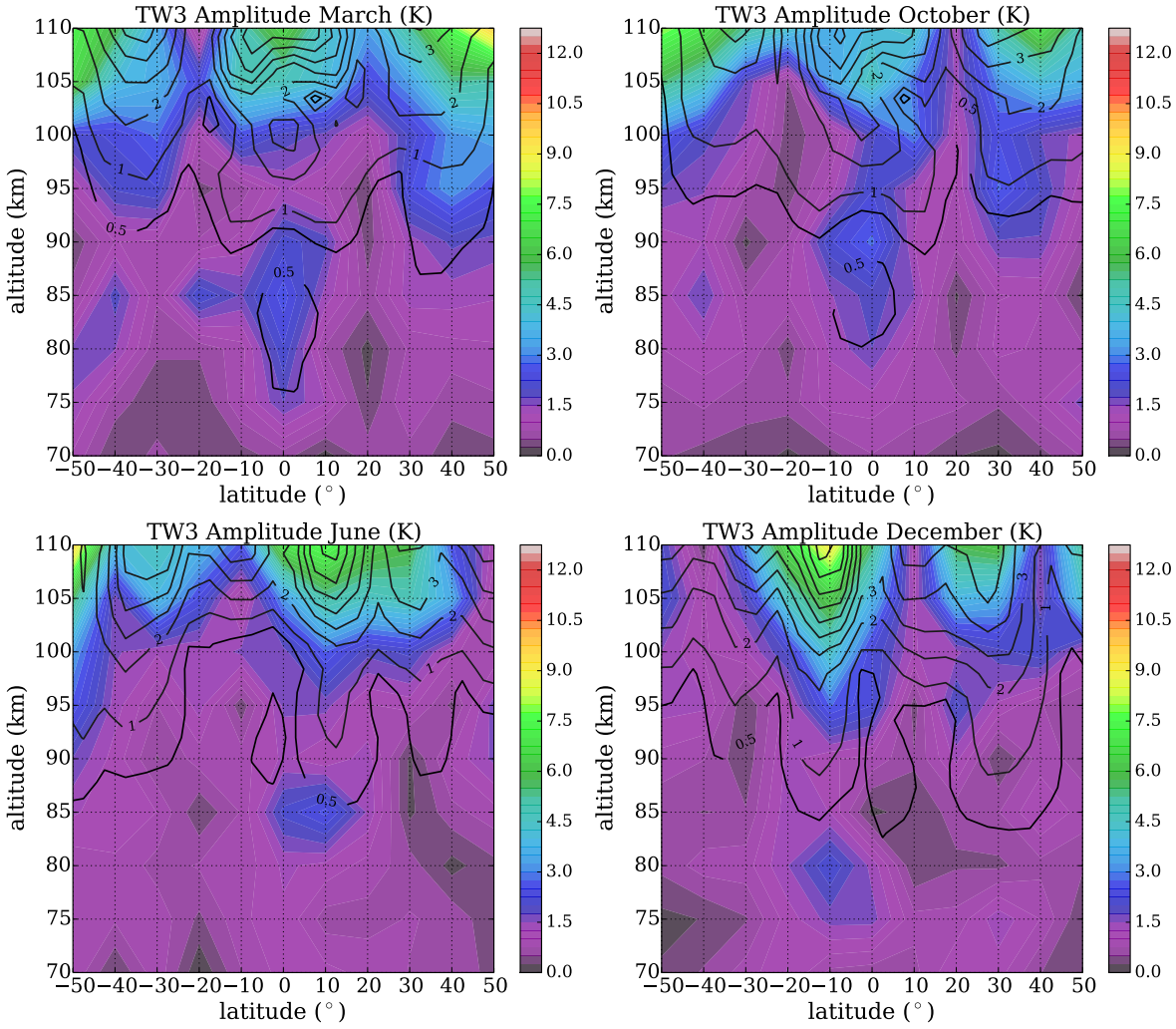

Fig. 3: Terdiurnal temperature amplitudes for equinox (upper row) and solstice (lower row) conditions modeled with MUAM. Corresponding SABER amplitudes from Pancheva et al. (2013) are added in color.

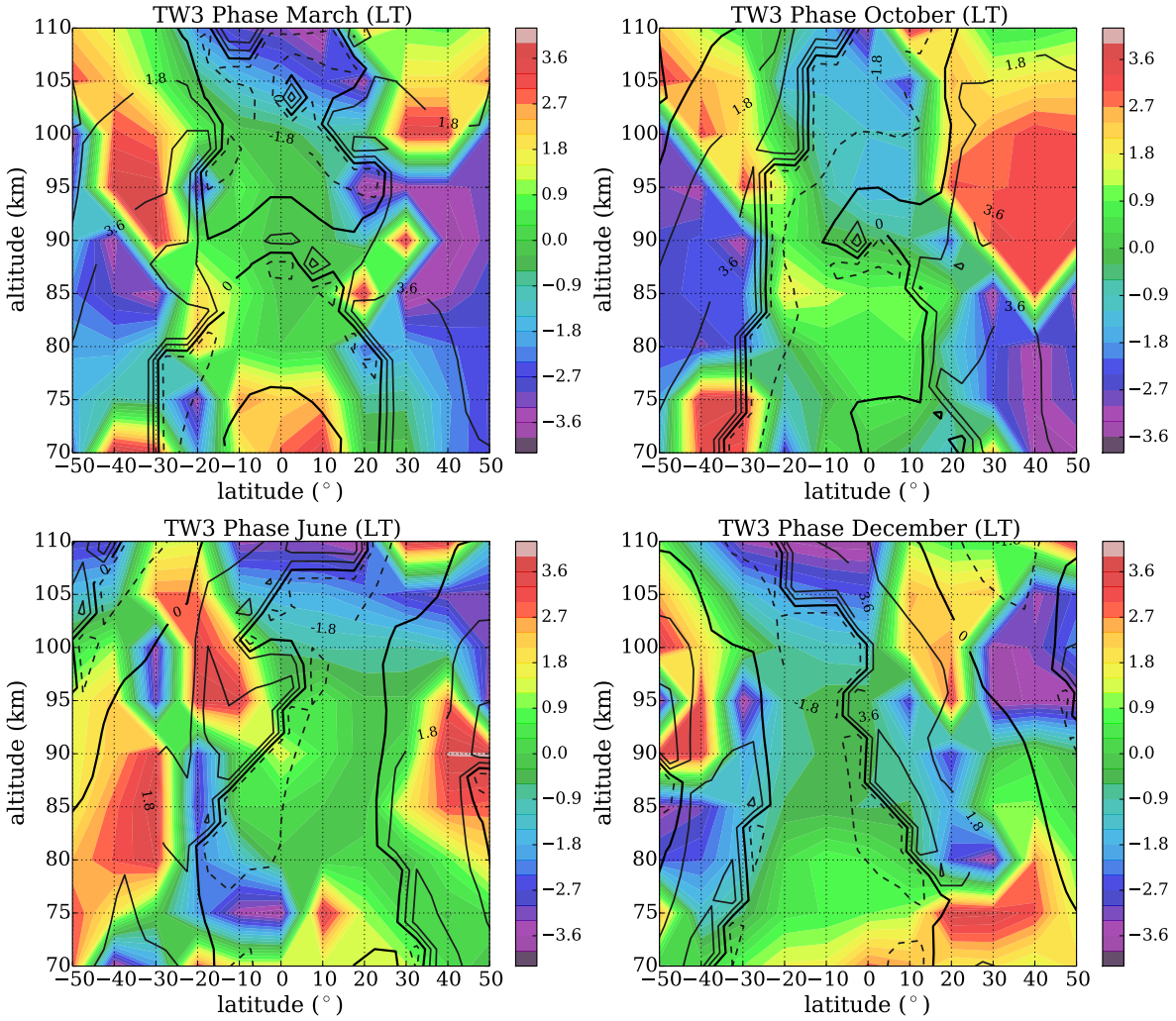

Fig. 4: As in Figure 3, but for the terdiurnal temperature phases.

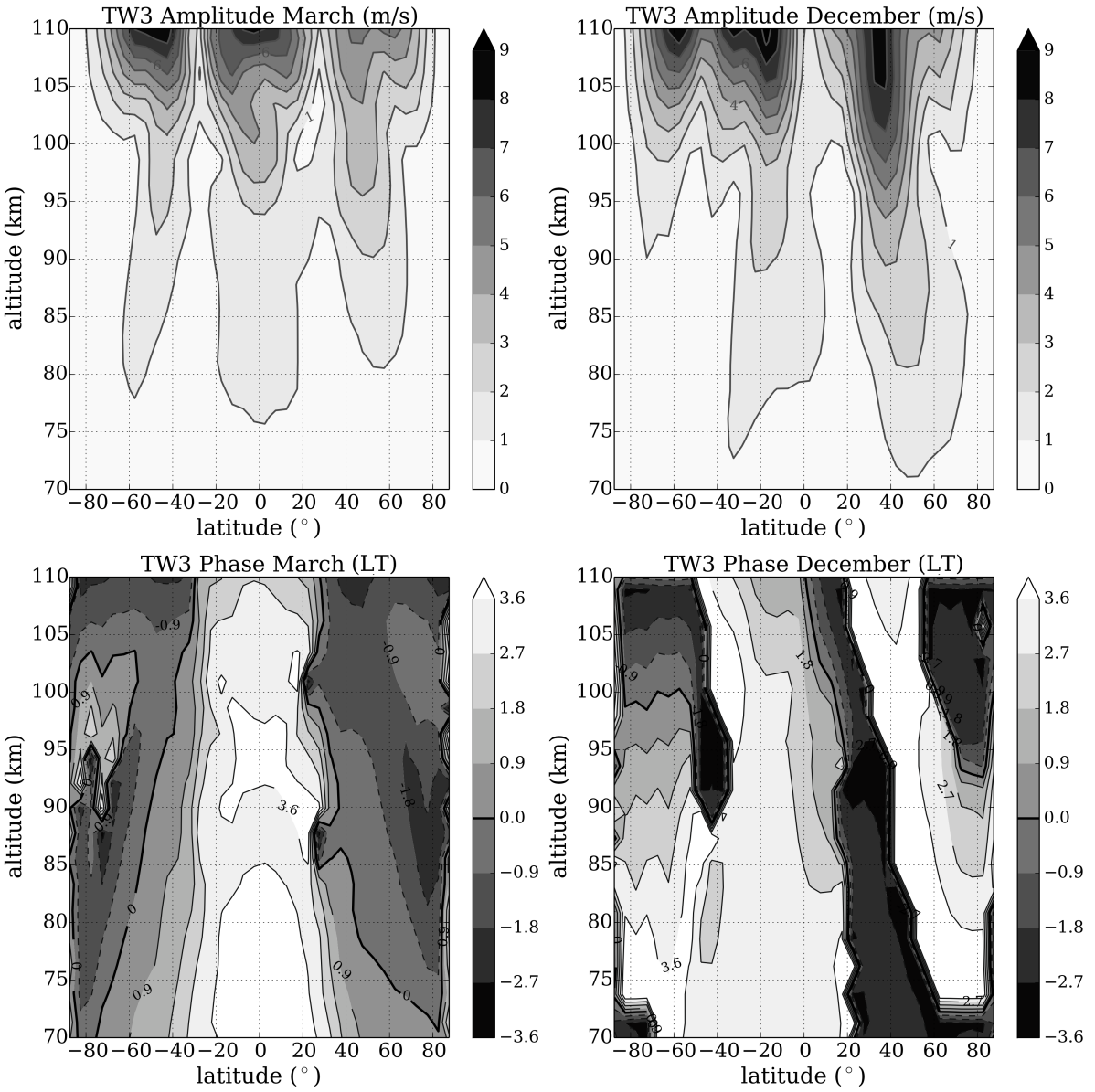

Fig. 5: Terdiurnal zonal wind amplitudes (upper row) and phases (lower row) for March and December modeled with MUAM.

4 Conclusions

We have analyzed the TW3 amplitudes and phases as simulated by the Middle and Upper Atmosphere Model. For modeling the TW3 realistically, lower atmosphere circulation has been included by assimilating 11-year mean ERA-Interim Reanalysis data from 2000-2010. For appropriate heating rates ozone and CO_2 fields according to measurements in 2005 were included.

The seasonal cycle of TW3 temperature and zonal wind amplitudes are shown at an altitude of ~90 km. Good agreement with SABER and TIDI measurements (Yue et al., 2013; Pancheva et al., 2013) is visible. In particular, the midlatitude peak during equinox, which is well expressed in satellite but also in radar observations, is reproduced by MUAM.

Additional to latitude-time cross sections, the tidal structures in temperature are presented for equinox and solstice conditions between 50° N/S in an altitude from 70 km to 110 km. Largest amplitudes are found in December at 10° S and ~110 km with more than 9 K. Another peak occurs at 30° N in December. Amplitudes in June are similar to those in December mirror inverted to the equator. Under solstice conditions tidal amplitude maximizes above the equator and at midlatitudes with up to 6 K. Modeled TW3 phases have shortest vertical wavelengths above the equator from ~87 km to 100 km in March and from 90 to 100 km in October or at 10° S in June. In contrast, vertical wavelengths at midlatitudes are large.

These results were compared with SABER/TIMED satellite data (2002-2009). Observed tidal phases show larger vertical wavelengths above the equator. One reason might be that equatorial waves like the quasi-biennial oscillation or Kelvin-waves are not excited in the presented model run. Good agreement in latitudinal structure and maximum values of TW3 amplitudes was found. Even the weak peak at ~85 K above the equator could be reproduced, however, the modeled amplitudes are too weak here.

Generally, the modeled amplitudes are smaller than observed. This might be due to a too strong dissipative damping in the modeled mesosphere and thermosphere. Further experiments will take that into account.

Acknowledgements

The authors are grateful to D. Pancheva for providing SABER/TIMED terdiurnal amplitudes and phases in SABER/TIMED measurements. The work has partly been supported by DFG under grant JA 836/30-1.

References

Akmaev, R. A., 2001: Seasonal variations of the terdiurnal tide in the mesosphere and lower thermosphere: a model study, Geophysical Research Letters, 28, 3817–3820, doi: 10.1029/2001GL013002.

Andrews, D. G., Holton, J. R., and Leovy, C. B., 1987: Middle Atmosphere Dynamics, Academic Press Inc. (London) Ltd., 150-169.

Beldon, C. L., Muller, H. G., and Mitchell, N. J., 2006: The 8-hour tide in the mesosphere and lower thermosphere over the UK, 1988-2004, Journal of Atmospheric and Solar-Terrestrial Physics, 68, 655–668, doi: 10.1016/j.jastp.2005.10.004.

Chandra, S., Fleming, E. L., Shoeberl, M. R., and Barnett, J. J., 1990: Monthly mean global climatology of temperature, wind, geopotential height and pressure for 0–120 km, Advances in Space Research, 10, 3–12, doi: 10.1016/0273-1177(90)90230-W.

Chapman, S. and Lindzen, R., 1970: Atmospheric tides - thermal and gravitational, D. Reidel Publishing Company (Dordrecht, Holland), iX, p. 200.

Chou, M.-D., Ridgway, W. L., and Yan, M. M.-H., 1993: One-Parameter Scaling and Exponential-Sum Fitting for Water Vapor and CO_2 Infrared Transmission

Functions, Journal of the Atmospheric Sciences, 50, 2294–2303, doi:10.1175/1520-0469(1993)050<2294:OPSAES>2.0.CO;2.

Dee, D. P., Uppala, S. M., Simmons, A. J., Berrisford, P., Poli, P., Kobayashi, S., Andrae, U., Balmaseda, M. A., Balsamo, G., Bauer, P., Bechtold, P., Beljaars, A. C. M., van de Berg, L., Bidlot, J., Bormann, N., Delsol, C., Dragani, R., Fuentes, M., Geer, A. J., Haimberger, L., Healy, S. B., Hersbach, H., Hólm, E. V., Isaksen, L., Kållberg, P., Köhler, M., Matricardi, M., McNally, A. P., Monge-Sanz, B. M., Morcrette, J.-J., Park, B.-K., Peubey, C., de Rosnay, P., Tavolato, C., Thépaut, J.-N., and Vitart, F., 2011: The ERA-Interim reanalysis: configuration and performance of the data assimilation system, Quarterly Journal of the Royal Meteorological Society, 137, 553–597, doi: 10.1002/qj.828, Path: http://apps.ecmwf.int/datasets/data/interim_full_moda/?levtype=pl.

Dlugokencky, E., Lang, P., Masarie, K., Crotwell, A., and Crotwell, M., 2014: Atmospheric Carbon Dioxide Dry Air Mole Fractions from the NOAA ESRL Carbon Cycle Cooperative Global Air Sampling Network, 1968-2013, Version: 2014-06-2, Path: ftp://aftp.cmdl.noaa.gov/data/trace_gases/co2/flask/surface/.

Du, J. and Ward, W. E., 2010: Terdiurnal tide in the extended Canadian Middle Atmospheric Model (CMAM), Journal of Geophysical Research, 115, doi:10.1029/2010JD014479, doi: 10.1029/2010JD014479.

Fomichev, V. and Shved, G., 1985: Parameterization of the radiative flux divergence in the 9.6 μm O_3 band, Journal of Atmospheric and Terrestrial Physics, 47, 1037 – 1049, doi: 10.1016/0021-9169(85)90021-2.

Fomichev, V. I., Blanchet, J.-P., and Turner, D. S., 1998: Matrix parameterization of the 15 μm CO_2 band cooling in the middle and upper atmosphere for variable CO_2 concentration, Journal of Geophysical Research: Atmospheres, 103, 11 505–11 528, doi: 10.1029/98JD00799.

Freidenreich, S. M. and Ramaswamy, V., 1999: A new multiple-band solar radiative parameterization for general circulation models, Journal of Geophysical Research: Atmospheres, 104, 31,389–31,409, doi:10.1029/1999JD900456.

Fröhlich, K., Pogoreltsev, A., and Jacobi, Ch.., 2003: The 48 Layer COMMA-LIM Model: Model description, new aspects, and Climatology, Rep. Inst. Meteorol. Univ. Leipzig, 30, 157–185.

Fytterer, T. and Jacobi, Ch.., 2011: Climatology of the 8-h tide over Collm (51.3°N;13°E), Wiss. Mitteil. Inst. f. Meteorol. Univ. Leipzig, 48, 23–32.

Huang, C., Zhang, S., and Yi, F., 2007: A numerical study on amplitude characteristics of the terdiurnal tide excited by nonlinear interaction between the diurnal and semidiurnal tides, Earth, Planets and Space, 59, 183–191.

Jacobi, C. and Fytterer, T., 2012: The 8-h tide in the mesosphere and lower thermosphere over Collm (51.3°N;13°E), 2004-2011, Advances in Radio Science, 10, 265–270, doi:10.5194/ars-10-265-2012, doi: 10.5194/ars-10-265-2012.

Lange, M., 2001: Modellstudien zum CO_2-Anstieg und 0_3-Abbau in der mittleren Atmosphäre und Einfluss des Polarwirbels auf die zonale Symmetrie des Windfeldes in der Mesopausenregion, (Dissertation) University of Leipzig, p. 124.

Liou, K.-N., 1992: Radiation and Cloud Processes in the Atmosphere: Theory, Observation and Modeling, Oxford Monographs on Geology and Geophysics.

Matsuno, T., 1966: Numerical Integrations of the Primitive Equations by a Simulated Backward Difference Method, Journal of the Meteorological Society of Japan, 44, 76–84.

Miyahara, S. and Forbes, J. M., 1991: Interactions between gravity waves and the diurnal tide in the mesosphere and lower thermosphere, Journal of the Meteorological Society of Japan, 69, 523–531.

Mlynczak, M. G. and Solomon, S., 1993: A detailed evaluation of the heating efficiency in the middle atmosphere, Journal of Geophysical Research: Atmospheres, 98, 10 517–10 541, doi: 10.1029/93JD00315.

Moudden, Y. and Forbes, J. M., 2013: A decade-long climatology of terdiurnal tides using TIMED/SABER observations, Journal of Geophysical Research: Space Physics, 118, 4534–4550, doi:10.1002/jgra.50273.

Namboothiri, S. P., Kishore, P., Murayama, Y., and Igarashi, K., 2004: MF radar observations of Terdiurnal Tide in the mesosphere and lower thermosphere at Wakkanai (45.4°N, 141.7°E), Japan, Journal of Atmospheric and Solar-Terrestrial Physics, 66, 241–250, doi: 10.1016/j.jastp.2003.09.010.

Pancheva, D., Mukhtarov, P., and Smith, A. K., 2013: Climatology of the migrating terdiurnal tide (TW3) in SABER/TIMED temperatures, Journal of Geophysical Research: Space Physics, 118, 1755–1767, doi: 10.1002/jgra.50207.

Pogoreltsev, A. I., Vlasov, A. A., Fröhlich, K., and Jacobi, Ch., 2007: Planetary waves in coupling the lower and upper atmosphere, Journal of Atmospheric and Solar-Terrestrial Physics, 69, 2083 – 2101, doi: 10.1016/j.jastp.2007.05.014.

Randel, W. and Wu, F., 2015: A stratospheric ozone profile data set for 1979–2005: Variability, trends, and comparisons with column ozone data, Journal of Geophysical Research, 112, doi: 10.1029/2006JD007339, Path: ftp://sparc-ftp1.ceda.ac.uk/sparc/ref_clim/ randel/o3data/.

Richards, P. G., Fennelly, J. A., and Torr, D. G., 1994: EUVAC: A Solar EUV Flux Model for aeronomic calculations, Journal of Geophysical Research: Space Physics, 99, 8981–8992, doi:10.1029/94JA00518. (Correction, 1994. J. Geophys. Res. 99, 13283).

Roble, R. G., 1995: Energetics of the Mesosphere and Thermosphere, Geophysical Monographs, 87, 1–21, doi:10.1029/GM087p0001.

Smith, A. K. and Ortland, D. A., 2001: Modeling and Analysis of the Structure and Generation of the Terdiurnal Tide, Journal of the Atmospheric Sciences, 58, 3116–3134, doi: 10.1175/1520-0469(2001)058%3C3116:MAAOTS%3E2.0.CO;2.

Strobel, D. F., 1978: Parameterization of the atmospheric heating rate from 15 to 120 km due to O_2 and O_3 absorption of solar radiation, Journal of Geophysical Research: Oceans, 83, 6225–6230, doi: 10.1029/JC083iC12p06225.

Teitelbaum, H., Vial, F., Manson, A. H., Giraldez, R., and Massebeuf, M., 1989: Non-linear interation between the diurnal and semidiurnal tides: Terdiurnal and diurnal secondary waves, Journal of Atmospheric and Terrestrial Physics, 51, 627–634, doi: 10.1016/0021-9169(89)90061-5.

Yue, J., Xu, J., Chang, L. C., Wu, Q., Liu, H.-L., Lu, X., and Russell III, J., 2013: Global Structure and seasonal variability of the migrating terdiurnal tide in the mesosphere and lower thermosphere, Journal of Atmospheric and Solar-Terrestrial Physics, 105-106, 191–198, doi: 10.1016/j.jastp.2013.10.010.

Three-dimensional radiative effects in Arctic boundary layer clouds above ice edges

M. Schäfer[+], E. Bierwirth[+,*], A. Ehrlich[+], E. Jäkel[+], and M. Wendisch[+]

+) Leipzig Institute for Meteorology, Stephanstr.3, 04103 Leipzig, E-Mail: michael.schaefer@uni-leipzig.de

*) now at: PIER-ELECTRONIC GmbH, Nassaustr. 33–35, 65719 Hofheim-Wallau, Germany

Abstract

Based on airborne spectral imaging observations, three-dimensional (3-D) radiative effects between Arctic boundary layer clouds and highly variable Arctic surfaces have been identified and quantified. A method is presented to discriminate sea ice and open water in cloudy conditions based on airborne upward radiance measurements in the visible spectral range. This separation simultaneously reveals that the transition of radiance between open water and sea ice is not instantaneous in cloudy conditions but horizontally smoothed. In general, clouds reduce the nadir radiance above bright surfaces in the vicinity of open water, while the nadir radiance above open sea is enhanced compared to situations with clouds located above sea ice surfaces. With the help of the observations and 3-D radiative transfer simulations, this effect was quantified. This affected distance ΔL was found to depend on both cloud and sea ice properties. For a low level cloud at 0-200 m altitude, as observed during the Arctic field campaign Vertical Distribution of Ice in Arctic Clouds (VERDI) in 2012, an increase of the cloud optical thickness from $\tau = 1$ to $\tau = 10$ leads to a decrease of ΔL from 600 to 250 m. An increase in cloud base altitude or cloud geometrical thickness results in an increase of ΔL. Furthermore, the impact of these 3-D-radiative effects on a retrieval of cloud optical properties was investigated. The enhanced brightness of a dark pixel next to an ice edge results in uncertainties of up to 90 % in retrievals of τ and up to 30 % in retrievals of the effective radius r_{eff}. With the help of ΔL quantified here, an estimate of the distance to the ice edge is given where the retrieval uncertainties due to 3D-effects are negligible.

Zusammenfassung

Mit Hilfe flugzeuggetragener abbildender spektraler Beobachtungen wurden 3-D Strahlungseffekte zwischen arktischen Grenzschichtwolken sowie der hochvariablen arktischen Bodenoberfläche identifiziert und quantifiziert. Eine Methode zur Differenzierung von Meereis und offener Wasserflächen, auf Grundlage flugzeuggetragener Messungen der aufwärtsgerichteten Strahldichte im sichtbaren Spektralbereich, während bewölkter Bedingungen wird vorgestellt. Diese Differenzierung zeigt gleichzeitig auf, dass die Strahldichtereduzierung beim Übergang vom Meereis zu den offenen Wasserflächen nicht unmittelbar erfolgt, sondern horizontal geglättet ist. Allgemein verringern Wolken in der Umgebung von Eiskanten die Nadir-Strahldichte über den hellen Eisflächen und erhöhen sie über dunklen Meeresoberflächen. Mit Hilfe von 3-D Strahlungstransferrechnungen wurde dieser Effekt quantifiziert. Die Reichweite dieses Effektes wird sowohl von den

Wolken- als auch den Oberflächeneigenschaften beeinflusst. Für eine flache Wolke zwischen 0 und 200 m, so wie sie während der arktischen Feldkampagne Vertical Distribution of Ice in Arctic Clouds (VERDI), 2012 beobachtet werden konnte, führt eine Erhöhung der wolkenoptischen Dicke von $\tau = 1$ zu $\tau = 10$ zu einer Verringerung in ΔL von 600 zu 250 m. Zudem führt eine Erhöhung der Wolkenhöhe und ihrer geometrischen Dicke zu einer Zunahme von ΔL. Anschließend wurde der Einfluss dieser 3-D Strahlungseffekte auf die Ableitungsergebnisse von τ untersucht. Die Aufhellung eines dunkleren Pixels neben der Eiskante führt zu Unsicherheiten von bis zu 90 % bei der Ableitung von τ. Beim effektiven Radius zu bis zu 30 %. ΔL ist ein Maß mit Hilfe dessen die Entfernung zur Eiskante bestimmt werden kann, ab welcher die Unsicherheiten bezüglich der 3-D Effekte vernachlässigt werden können.

1. Introduction:

As shown by observations and simulations, the Arctic climate changes faster and stronger than the global climate (e. g., Sanderson et al., 2011; Overland et al., 2011). Among others, clouds play a major role in projections of the future Arctic climate. Therefore, understanding the effects of clouds in the Arctic is of utmost importance. Depending on the time of year and their altitude, Arctic clouds may exert either a net warming or cooling effect. However, the low Sun in summer combined with usually high surface albedo lead to a dominance of the terrestrial (infrared) radiative warming of low clouds (Intrieri et al., 2002b; Wendisch et al., 2013). In this regard, surface albedo (sea ice coverage) is a major parameter determining whether a change of cloud amount in future climate is associated with a warming or cooling effect.

While in most cases, Arctic stratus is nearly homogeneous from a microphysical point of view, the ice-covered surface areas are often inhomogeneous. The sea ice has irregular top and bottom surfaces and is broken into distinct pieces, called floes (Rothrock and Thorndike, 1984). Often leads, cracks, or polynias are present especially in the transition zone between sea ice and open water, which often is dominated by scattered ice floes. The albedo contrast in such areas is the highest we can observe on Earth. For open water the albedo is generally low (0.042 at 645 nm wavelength; Bowker et al., 1985) while above the ice/snow covered ocean the albedo is high at visible wavelengths (0.91 at 645 nm wavelength; Bowker et al., 1985). Using Advanced Very High Resolution Radiometer (AVHRR) data from the polar-orbiting satellites NOAA IO and NOAA-11, Lindsay and Rothrock (1994) analyzed the albedos of 145 different 200 km^2 cells in the Arctic. The mean values for the cloud-free portions of individual cells range from 0.18 to 0.91 and were found to be highly variable during the monthly and annual cycle (Lindsay and Rothrock, 1994).

Retrievals of cloud optical properties at visible wavelengths are strongly biased by bright surfaces (Krijger et al., 2011). Most satellite retrievals simply exclude such areas from analysis. Only pixels identified as ice-free are used. This might become ambiguous in case of clouds that cover both ice floes and open water. However, even when ice and ice-free areas are perfectly separated by the retrieval algorithms, still 3-D radiative effects may affect the cloud retrieval over ice-free pixels close to the ice edge. Lyapustin (2001) and Lyapustin and Kaufman (2001) investigated the impact of the strong contrast of the surface albedo between open sea and adjacent sea-ice on the retrieval of Arctic cloud properties. Adjacency effects were found to reduce surface

contrasts by decreasing the top-of-atmosphere radiance over bright pixels and increasing the brightness of dark pixels which becomes important for remote-sensing applications developed for use with both dark or bright targets.

In Sect. 2, we present airborne observations using imaging spectrometer measurements of reflected radiance to quantify the 3-D radiative effects of clouds above heterogeneous Arctic surfaces. A robust algorithm separating sea ice and open water surfaces when covered by clouds is introduced in Sect. 3 and applied to the measurements. Observations and simulations of the 3-D radiative effects are analyzed in Sect. 4. A critical distance from the ice edge is defined to quantify the horizontal range of the effects for variations in cloud optical thickness τ, cloud altitude, cloud vertical extent, r_{eff}, and surface albedo. In Sect. 5 we finally investigate how these 3-D radiative effects bias 1-D retrievals of τ and r_{eff}. The whole study presented here in this article is based on the findings from Schäfer et al. (2015).

2. Airborne measurements of reflected (nadir) spectral radiance:

The measurements used in this study were performed during the international field campaign Vertical Distribution of Ice in Arctic Clouds (VERDI), which took place in Inuvik, Northwest Territories, Canada, in April and May 2012. The instruments were installed on Polar 5, an aircraft used for scientific research by the Alfred Wegener Institute Helmholtz Centre for Polar and Marine Research (AWI), Bremerhaven. Most flights were performed over the Beaufort Sea, partly covered by sea ice interspersed with open leads and polynias which grew bigger towards the end of the campaign.

The measurement strategy during VERDI was aimed at combining remote sensing and in situ cloud observations. Therefore, the same clouds were subsequently sampled by a set of remote-sensing and in situ instruments on board of Polar 5. The aircraft was equipped with an active [as the Airborne Mobile Aerosol Lidar (AMALi; Stachlewska et al., 2010)] and several passive remote-sensing systems. Passive radiation measurements were carried out with the imaging spectrometer AisaEAGLE (manufactured by Specim Ltd. in Oulu, Finland; Schäfer et al., 2013), the Spectral Modular Airborne Radiation Measurement System (SMART-Albedometer; Wendisch et al., 2001), and a tracking Sun photometer. The configuration was similar to that during the aircraft campaign SoRPIC (Solar Radiation and Phase Discrimination of Arctic Clouds), as described by Bierwirth et al. (2013). Additionally, dropsondes were used at selected waypoints to sample profiles of meteorological parameters over the whole distance between the ground and the aircraft. In this study, data from the AMALi and dropsondes were used to determine the cloud-top altitude and geometrical thickness, those of the SMART-Albedometer to verify and validate the radiance measurements of AisaEAGLE. To analyze the 3-D radiative effects of ice edges in a cloudy atmosphere, we focus on measurements by the imaging spectrometer AisaEAGLE. With 1024 spatial pixels, the single-line sensor provides a sufficiently high horizontal resolution to observe ice edges in detail. The flight altitude was about 3 km above ground which is about 2 km above cloud top for typical boundary layer clouds. For this geometry, the width of one AisaEAGLE pixel at cloud top is 3.5 m and the length is 4.2 m with an exposure time 10 ms and flight speed of 65 ms^{-1}. Each spatial pixel consists of 488 spectral pixels to detect spectra of radiance in the wavelength range from 400 to 970 nm with 1.25 nm full width at half maximum. For

radiance measurements, Schäfer et al. (2013) estimated an uncertainty of ± 6 %. Assuming a fixed effective radius, those detected spectra of radiance can then be used to retrieve τ. During all 15 flights of VERDI, 130 recordings (25 h, 11 min, 29 s) of cloud-top and surface reflectance were collected with AisaEAGLE. 78 % of the observation time was spent above clouds. However, for 86 % of the cloud observations a cloud retrieval as described by Bierwirth et al. (2013) could not be applied as the surface albedo did not fulfill the constraint of being relatively dark, related to the differences in the contrast between cloud and ground being larger than the measurement uncertainties. Either snow-covered ice almost eliminated the contrast between cloud and surface, or a mixture of ice and open water made a cloud retrieval impossible. The latter occurred in 42 % of all observations and is for three measurements exemplary analyzed in more detail in this paper. The goal is to quantify how strong cloud retrievals are biased above such heterogeneous surfaces.

3. Identification of ice and open water:

The MODIS (Moderate-Resolution Imaging Spectroradiometer) image shown in Fig. 1a illustrates the difficulties of cloud remote sensing in areas with sea ice and snow cover. On 17 May 2012, an optically thin stratus cloud was situated above the Beaufort Sea. However, in areas where sea ice is located below the cloud, no visible contrast between sea ice and cloud remains. From the visible wavelength range, a retrieval of τ is not possible in those areas; it can only be performed above water surfaces. Fig. 1b shows the calculated nadir radiance at 645 nm for clouds with different values of τ over a dark ocean surface (blue lines) and a bright sea-ice surface (red lines). The calculations were performed for different solar zenith angles (SZA) of 45°, 60°, and 75° (average range during VERDI measurements).

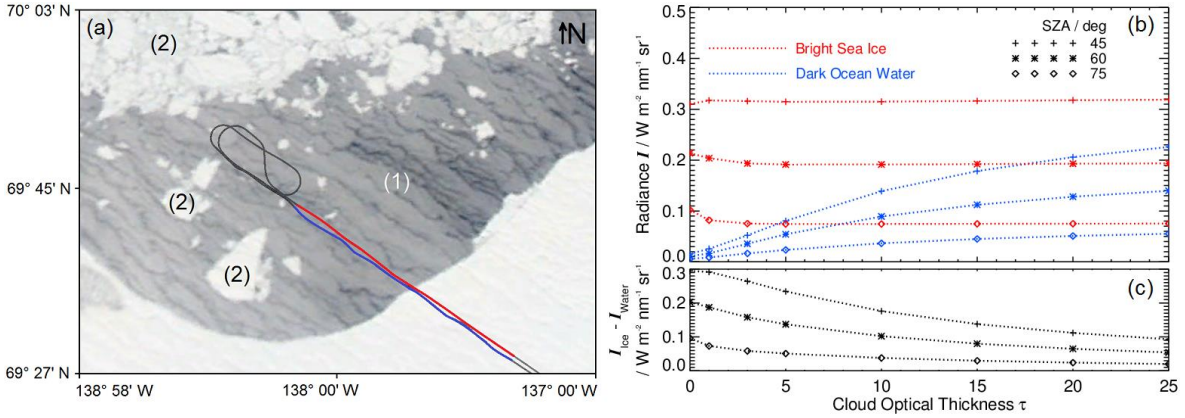

Figure 1: (a) VERDI flight track and true-color MODIS image (Aqua; 250m resolution) of 17 May 2012. Numbers (1) and (2) label open ocean and sea ice, respectively. (b) Simulated nadir radiance at 645 nm calculated for different τ ranging from 0 to 25 and cloud particles with a fixed r_{eff} = 15 µm. The calculations were performed for different SZA of 45, 60, and 75° over a sea-ice surface and an ocean surface. (c) Difference between the simulated nadir radiance over sea ice surface and ocean surface from (b).

The wavelength of 645 nm is chosen with respect to the sensitivity of τ in this spectral range (Nakajima and King, 1990). The sensitivity of the nadir radiance with respect to

τ above sea ice is not significant and below measurement uncertainty of AisaEagle. For the same clouds placed above a dark ocean surface, the reflected radiance exhibits a strong function of τ, which is used for the tau-retrieval applied to data of AisaEagle.

In order to select the dark-surface pixels for which a cloud retrieval can be applied, a sea-ice mask has to be derived. Fig. 1b clearly shows that even for optically thick clouds the nadir reflected radiance is significantly larger (> 25 % at τ = 25 and SZA = 60°) above bright sea ice than over a dark ocean surface. This gap can be used as a threshold to distinguish between measurements of clouds above the dark ocean surface and a bright sea ice surface. To define this threshold it has to be considered that the differences between the reflected radiance measured above a dark ocean surface or a bright sea ice surface is smaller for larger solar zenith angles and decreases with increasing τ. However, the differences are still significant at large solar zenith angles of SZA = 60° and τ = 25. For VERDI, where SZA was in the range of 55° to 75° for most of the observations, the threshold is defined as the center value between the two simulations:

$$I_{\text{thresh}} = 0.5 \cdot (I_{\text{ice}} + I_{\text{water}}) \quad (1)$$

To test this threshold, we analyzed a section of a VERDI flight on 17 May 2012 (Fig. 1). The flight was divided into a remote-sensing leg A at 2920 m altitude (red in Fig. 1) and an in situ leg B inside the cloud at 150 m altitude (blue in Fig. 1). The solar zenith angle was 58°. We estimate τ from the MODIS image to be in the range of 5. There, $I_{\text{ice}} = 0.20$ W m^{-2} nm^{-1} sr^{-1} and $I_{\text{water}} = 0.06$ W m^{-2} nm^{-1} sr^{-1} in the simulation shown in Fig. 1b gives a threshold of 0.13 W m^{-2} nm^{-1} sr^{-1}. Fig. 2 shows a histogram of the measured radiances at 645 nm of leg A (solid black line in Fig. 1a).

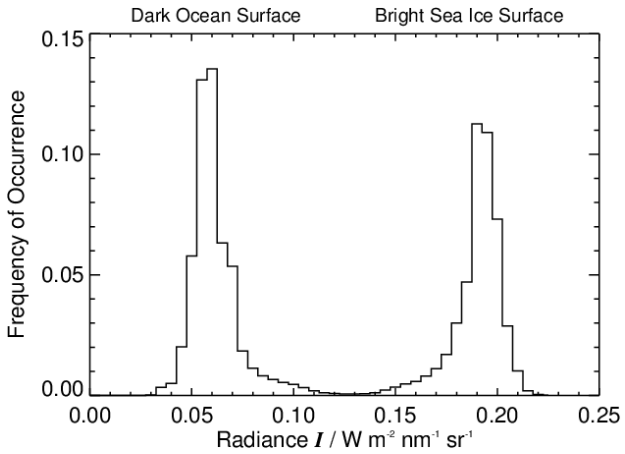

Figure 2: Fraction of occurrence of the measured radiance at 645 nm, given in the example of Fig. 4a. The bin size is 0.005 W m^{-2} nm^{-1} sr^{-1}.

There are two maxima with a distinct separation which correspond to measurements above sea ice and ocean water. The minimum between the two maxima can be used as an alternative estimate of the threshold for the ice mask. In this particular case, the threshold estimated from the frequency distribution is 0.13 W m^{-2} nm^{-1} sr^{-1} which confirms the theoretical value derived above. Using those methods to estimate the threshold, ice masks were created to identify measurements of clouds above sea ice for which the cloud retrieval by Bierwirth et al. (2013) cannot be applied.

Fig. 3a shows a long ice edge and Fig. 3b an accumulated ice floe field observed on 17 May 2012 around 17 UTC (SZA=58°). For those two cases there was a cloud layer between the ground and the aircraft. Fig. 3c shows ice floes without clouds above. The corresponding ice masks are shown on the right panel in Fig. 3d-f. In those images, all pixels identified as sea ice are shown as red areas. The clear-sky case presented in Fig. 3c was measured on 14 May 2012 around 21:00 UTC. Due to lower SZA = 52° compared to the previous cases, different maximum values of the reflected radiance were measured.

Fig. 3g-i shows the corresponding frequency distributions for the three cases (solid black lines). All frequency distributions are normalized by their maximum. In each case two maxima of the distribution are separated by the defined threshold value, located at the minimum between the two maxima. For cloudy cases in Fig. 3g and 3h, the dark-surface peak is broadened asymmetrically towards higher radiance values while the bright-surface peak is broadened towards lower radiance values, which both indicate the horizontal photon transport. For the clear-sky case in Fig. 3i, the frequency distributions representing dark ocean and sea ice surfaces are clearly separated due to less radiative 3-D effects.

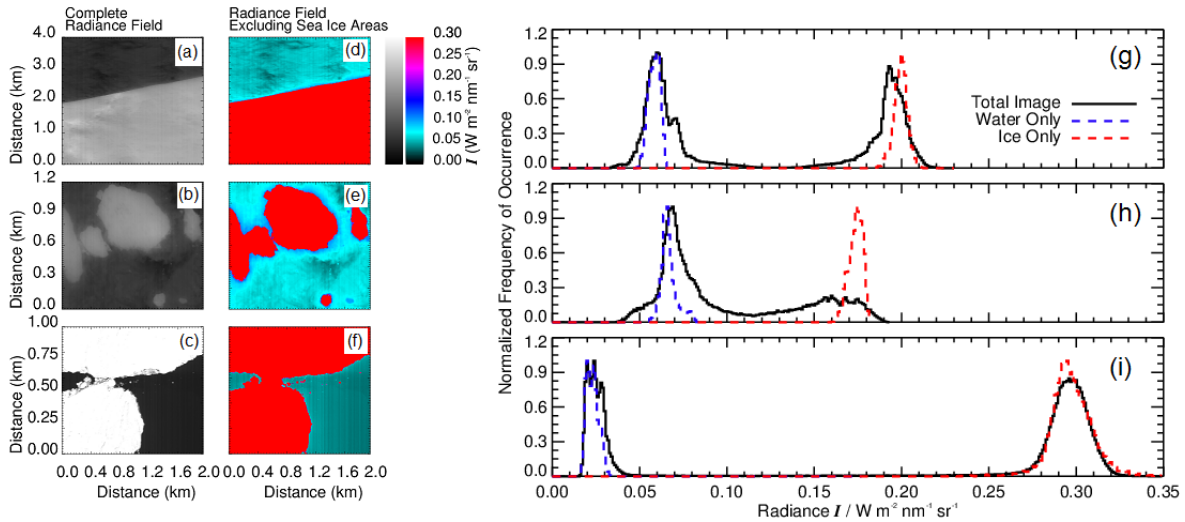

Figure 3: Left Side, Panel (a), (b), (c): Fields of radiances at 645 nm, measured with the imaging spectrometer AisaEAGLE. Measurements from 17 May 2012. Left side, panel (d), (e), (f) The same as on the left side in color-scale and with ice mask overlay. Right side, Panel (g), (h), (i): Normalized distributions of the frequency of occurrence of the radiance measured during the three cases presented on the left side. Additionally included are frequency distributions over sea ice and ocean water only.

To highlight this more clearly, frequency distributions for a selection of pixel far from the ice edge are included in Fig. 3g,h,i, separated into dark ocean water pixel (dashed blue lines) and bright sea ice pixel (dashed red lines). For the clear-sky case in Fig. 3i, these selective frequency distributions are almost congruent with the single peaks of the entire frequency distribution. In Fig. 3g and h, the selective frequency distributions are not congruent with original peaks. The measured reflected radiance over ocean water is enhanced, while it is reduced over sea ice. This particular enhancement and reduction of the measured reflected radiance is related to 3-D radiative effects in clouds and may influence cloud retrievals based on 1-D

simulations. In the following we will investigate those 3-D effects by analyzing the reflected radiance and their influence on the retrieved τ.

4. 3-D radiative effects of clouds near ice edges:
4.1. Measurements from VERDI:

In the vicinity of sea-ice areas close to the detected ice edge enhanced reflected radiance, i. e. narrow bright bands, are observed (Fig. 3d,e). Horizontal photon transport in the layer between surface and cloud is smoothing the abrupt decrease of the surface albedo from large values above sea ice to low values above the open water, while for measurements without clouds (Fig. 3f) we could not find similar areas with enhanced reflected radiance above the water close to the ice edge. Fig. 4 illustrates the measured nadir radiance as function of the distance to the ice edge for the three scenes in Fig. 3.

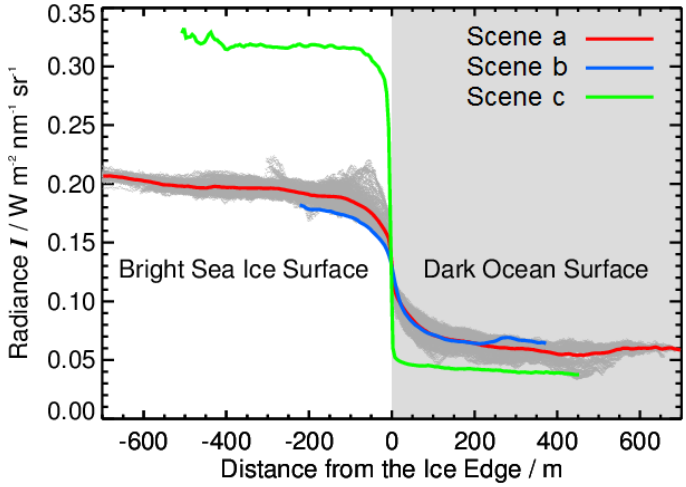

Figure 4: Averaged radiance (color coded) at 645 nm wavelength measured perpendicular to the scenes shown in Fig. 3a-c. Additionally included are all radiance values used for the average of the scene from Fig. 3a (gray shaded).

For the case of the straight ice edge (Fig. 3a) the distances presented here are almost in line with the flight track which was perpendicular to the ice edge. The spatial range of 1400 m perpendicular to the ice edge corresponds to 1418 m distance along the flight track. With a frame rate of 30 Hz and an aircraft speed of 65 ms^{-1} this results in 700 measurements along the 1418 m for each of the 1024 spatial pixels. This large amount of data provides good statistics for the mean radiance illustrated as solid red line in Fig. 4. In general, the nadir reflected radiance is decreased by about two thirds from 0.20 W m^{-2} nm^{-1} sr^{-1} above bright sea ice to about 0.06 W m^{-2} nm^{-1} sr^{-1} above dark ocean surface. For scene (a) and (b) the decrease does not occur sharply over the ice edge, but gradually starts at about 400 m distance from the ice edge above the ice itself and ends at 400 m distance from the ice edge over open water. In the cloud free case the asymptotic values above sea ice and water are reached much closer to the ice edge at about 50 m. Over the water-covered area, there is an enhancement of the measured reflected radiance close to the ice edge and a reduction of the measured reflected radiance above the ice itself next to the edge. We define a critical distance ΔL_{crit} where

the radiance is reduced by 94 % of the difference between the average radiance above ice and open water, I_{ice} and I_{water}:

$$I_{meas}(water) = I(water) + 0.06 \cdot [I(ice) - I(water)]. \quad (2)$$

With this criterion (corresponding to measurement uncertainty), the enhancement of the nadir radiance over the water surface extends to a distance of 200 m from the ice edge. Applying the same criterion for the reduced nadir radiance above sea ice, the affected area extends 200 m over the sea ice. Above open water, all measurements within that transition zone cannot be used for the retrieval of τ as the enhanced radiance will positively bias it.
Furthermore, we define a second distance ΔL where the radiance $I_{meas}(water)$ is enhanced by 6 % of the average radiance above open water.

$$I_{meas}(water) = I(water) + 0.06 \cdot I(water). \quad (3)$$

Using this criterion, the defined distance to the ice edge is independent of the radiance measured above the ice surface, which may reduce sources of uncertainties in the 1-D cloud retrieval. For the case of the measured radiance in Fig. 4, ΔL yields 300 m. For the isolated ice floes of the second scenario in Fig. 3b, the values of the averaged nadir radiance (solid blue line) in Fig. 4b are comparable to the values from the first scenario in Fig. 3a. Over open water, the values are almost identical, while they are lower over sea ice by 10 % (0.02 W m^{-2} nm^{-1} sr^{-1}). This asymmetry compared to the straight ice edge might result from the shape of the ice edge. It will be discussed in Sect. 4.2.1 more deeply. Furthermore, Fig. 4 shows a similar analysis (solid green line) for the cloud-free scenario on 14 May 2012 (Fig. 3f). Here, the decrease of the nadir radiance over the ice edge is significantly sharper than for the cloud-covered scenes.

4.2. Simulations:
4.2.1. Model:

To better quantify these observations of 3-D radiative effects at ice edges, we applied a 3-D radiative transfer model. The simulations will be used to determine ΔL as a function of different cloud properties. We expect that the interaction between clouds and sea ice surface varies with varying τ, geometrical thickness and cloud base altitude.

The radiative transfer simulations are performed with the open-source Monte Carlo Atmospheric Radiative Transfer Simulator (MCARaTS) which is a forward-propagating Monte Carlo photon-transport model (Iwabuchi, 2006; Iwabuchi and Kobayashi, 2008). It traces individual photons on their path through the 3-D atmosphere. To reduce the computational effort for radiance simulations, MCARaTS uses several variance reduction techniques, such as a modified local estimation method or a truncation approximation for highly anisotropic phase functions (Iwabuchi, 2006). The input to the radiative transfer model (RTM) contains the optical properties of atmospheric contributions as clouds and trace gases (e.g., extinction coefficients, single-scattering albedos, phase functions) at 645 nm (the common cloud retrieval wavelength in the visible wavelength range; Nakajima and King, 1990) and the 2-D

surface albedo. The model requires a predefined albedo field. For this purpose we create a field of 20 000 m by 20 000 m with a pixel size of 50 m by 50 m (400 pixels in both horizontal dimensions). Depending on the given sea-ice distribution, the albedo of individual pixels is set to sea-ice albedo (0.910 at 645 nm; Bowker et al., 1985) or water albedo (0.042 at 645 nm; Bowker et al., 1985). 2.2×10^9 photons were used in each single model run which resulted in a noise level of the 3-D simulations similar to the measurement uncertainties of AisaEAGLE.
Other input parameters for the model are adapted to the measurement conditions on 17 May 2012 around 17:00 UTC with a solar zenith angle of 58°. The extraterrestrial solar spectrum was taken from Gueymard (2004). The output altitude for the nadir radiance at 645 nm is 2920 m (10 000 ft flight altitude). To represent the observed clouds in an idealized way, a horizontally and vertically homogeneous liquid water cloud was assumed between 0 and 200 m altitude. The simulations were performed for $\tau = 1$, $\tau = 5$ and $\tau = 10$ as 3-D effects are assumed to be larger for clouds of high τ. As a reference a clear-sky scenario was also simulated to quantify the 3-D effects between sea ice and atmosphere in absence of any cloud. The effective radius of the liquid water droplets was set to $r_{\mathrm{eff}} = 15$ μm. The microphysical properties of the liquid water clouds are converted to optical properties by Mie calculations. Furthermore, profiles of the atmospheric pressure, temperature, density, and gases are taken from profiles given by Anderson et al. (1986). Gas absorption was modeled by LOWTRAN (Low Resolution Transmission Model parametrization, Pierluissi and Peng, 1985), as adapted from SBDART (Santa Barbara DISORT Atmospheric Radiative Transfer, Ricchiazzi and Gautier, 1998).

4.2.2. Results:

Comparable to Fig. 3a , the most general case of an ice edge is an infinite straight ice edge. Fig. 5 illustrates the results of the 3-D simulation. Additionally, results of a 1-D model that uses the independent pixel approximation (IPA) are included as grey lines. The IPA simulations were performed with the same 3-D model, but with a homogeneous surface albedo – either dark ocean water or bright sea ice. All other parameters remain the same as in the 3-D simulations. The results were averaged along the ice edge direction.

Similar to the observations, the nadir radiance from the 3-D simulations decreases above the sea ice and increases above the ocean surface the closer the pixel is located to the ice edge. In the clear sky simulations this effect is only small as 3-D and IPA simulations are almost identical. This indicates that the 3-D effect is dominated by horizontal photon transport between sea ice and clouds and the scattering processes by the cloud particles into the observation direction.

In general, Fig. 5 shows that with increasing τ the slope of the decrease of the nadir radiance next to the ice edge is flattened. This results from the reduction in contrast between the ocean and sea ice surface by the overlying clouds with lower absolute difference between nadir radiance above sea ice and open water for higher τ.
To compare the results to the measurements in Fig. 3, we use the distance ΔL defined by Eq. (3). For the radiance values I(water) above water, the IPA values from the 1-D simulation are applied. For the cases presented in Fig. 5, ΔL decreases from 600 m to 400 m and to 250 m (at τ = 1/5/10). The decrease of ΔL suggests that the area in which

the cloud retrieval is biased is smaller for optically thick clouds. This is related to the decrease of the contrast, Δ(IPA), between the radiances calculated with IPA over a bright sea ice surface and over a dark ocean water surface. Δ(IPA) decreases from 0.22 W m^{-2} nm^{-1} sr^{-1} for the clear sky case to 0.11 W m^{-2} nm^{-1} sr^{-1} for $\tau = 10$. If Δ(IPA) is smaller, the radiance reaches the threshold difference of 6 % · I(water) in closer vicinity to the ice edge.

However, the critical distance ΔL_{crit}, as defined by Eq. (2) in Sect. 4.1, increases with increasing τ from 50 m at $\tau = 1$ to 150 m at $\tau = 5$ and to 250 m at $\tau = 10$. Additionally, we investigated the impact of r_{eff} on our results. For simulations with r_{eff} = 10/15/20/30 µm, ΔL was almost identical (not shown). This indicates that a variation of r_{eff} does not need be considered when estimating the 3-D radiative effects described here. Furthermore, the exact albedo value of the ice and water surface only has an effect on the magnitude of the simulated nadir radiance, but not on the distance ΔL (not shown). With those findings the distance ΔL discussed here can be used as a general critical distance to quantify horizontal photon transport in case of heterogeneous surfaces beneath homogeneous clouds.

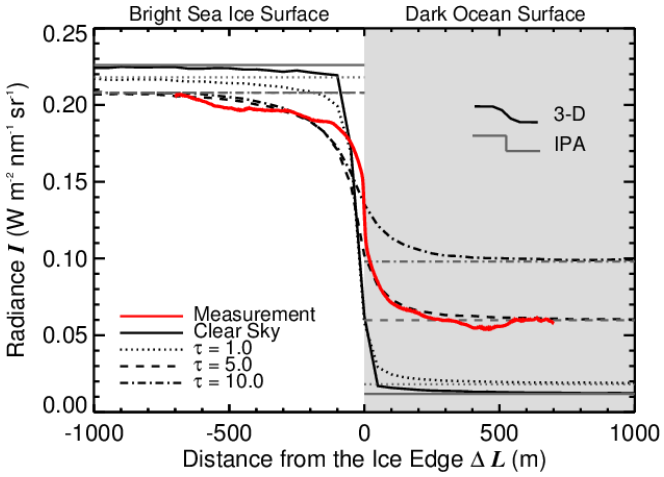

Figure 5: Simulated mean radiance across an ice edge for clear-sky conditions as well as for ground overlying clouds with cloud tops at 200 m and τ = 1/5/10. The effective radius of the cloud particles is r_{eff} = 15 µm. The white area illustrates the bright sea ice, the grey area the dark ocean water. Included are the results of the 3-D and IPA simulation as well as the average of the reflected radiance measured perpendicular to the ice edge in Fig. 3a.

Other important aspects which influence our results are the cloud altitude and cloud geometrical thickness. The horizontal photon transport as a process of isotropic surface reflections and scattering in the cloud layer will change if the cloud geometry changes. Depending in what altitude the photons are scattered by the cloud into the observation direction, the horizontal photon transport will be increased (high cloud) or decreased (low cloud). Figure 6 shows the simulated upward radiance for clouds of different altitude (Fig. 6a) and clouds of different vertical thickness (Fig. 6b).

For an increasing altitude of a cloud with a thickness of 500 m, ΔL increases from 700 m/1000 m (at τ = 1/5) for a cloud base at 0 m to 3200 m/4000 m for a cloud base at 1500 m. Similarly, ΔL increases with increasing vertical thickness; 1100 m/300 m (at τ = 1/5) for 200 m cloud thickness and 3200 m/2100 m for 1500 m

cloud thickness. In comparison to the influence of a different τ (Fig. 6 shows results for τ = 1/5), the cloud altitude and cloud geometrical thickness have similar significance for Δ*L* and cannot be neglected. Indeed, for distances larger than Δ*L*, the cloud altitude and cloud geometrical thickness do not affect the value of the maximum/minimum nadir radiance above sea ice/ ocean water. The IPA value is the same for each cloud altitude and only a function of τ. The increase of Δ*L* with increasing cloud base altitude follows a linear function and can be parameterized by

$$\Delta L(h_{\text{cloud}}) = A \cdot h_{cloud} + B. \quad (4)$$

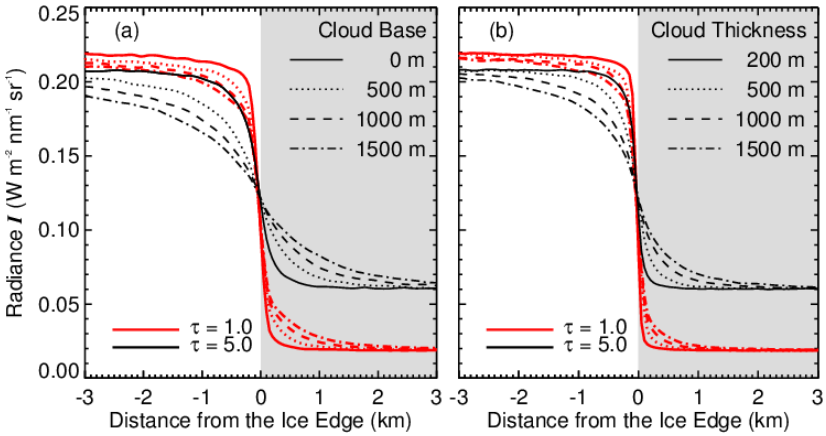

Figure 6: Simulated reflected radiance for clouds at different altitudes and with different geometrical thickness for the passage from a highly reflecting region to a darker region. The white area illustrates the ice stripe. (a) The cloud geometrical thickness is 500m. (b) Ground touching cloud with cloud base at 0 m.

For the parameters A and B, the linear regression yields A = 2.00/1.66 and B = 1000 m/730 m for clouds with τ = 1/5. This shows that the influence of the 3-D effects are much larger for clouds in higher altitudes and lower τ. Comparing the results for τ = 1/5 indicates that the slope decreases with increasing τ. This proves that the influence of cloud geometry on the 3-D effects is decreasing with increasing τ. The cloud base of all boundary layer clouds observed during VERDI ranged between 0 and 650 m which agrees with the climatology presented by Shupe et al. (2011). To demonstrate the potential effects of clouds with higher cloud base, the following simulations will cover two clouds, one similar to the observed case (ground overlying cloud with cloud top at 200 m) and one with cloud base/ top at 500 m/1000 m.

5. Retrieval of cloud optical thickness τ and effective radius r_{eff}:

All simulations in Sect. 4.2 have shown that the nadir radiance in open water areas close to sea ice can be enhanced drastically. For a classic cloud retrieval this enhancement suggests that τ and r_{eff} will be overestimated in this area when a surface albedo of water is assumed. To quantify the magnitude of this overestimation, a cloud retrieval based on forward simulations is applied to the radiance field of a 3-D simulation where the cloud optical properties are known exactly. To study a simple case, in the 3-D simulation a homogeneous cloud with τ = 10 and r_{eff} = 15 µm placed above an ice edge at an altitude of 500 to 1000 m.

The retrieval is performed over the ocean surface only. The forward simulations of the radiance look-up table are based on 1-D simulations of clouds between 500 and 1000 m altitude. τ and r_{eff} are varied between 1 and 25 µm and 10 and 25 µm, respectively; see Fig. 7a. The retrieval grid is constructed from the simulated nadir radiance at 645 nm wavelength on the abscissa and the ratio of the nadir radiance at 1525 and 579 nm wavelength on the ordinate. This wavelength and the wavelength ratio were chosen by following the method presented by Werner et al. (2013) which creates a more unambiguous retrieval grid than the classic two wavelength method by Nakajima and King (1990).

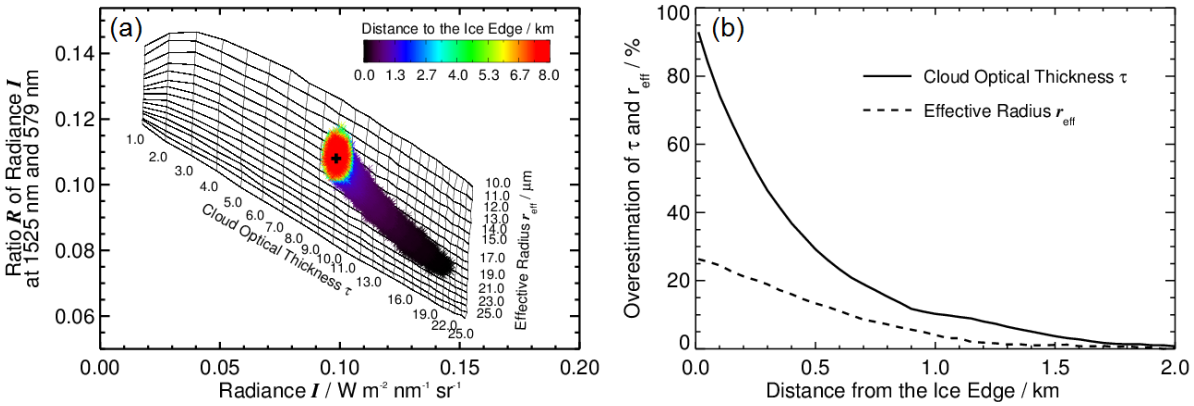

Figure 7: a) Retrieval grid using nadir radiance at 645 nm and the ratio of the nadir radiance at λ1/λ2 = 1525 nm/579 nm. The radiance of the 3-D simulation is illustrated by color-coded dots as a function of distance to the ice edge. The black cross marks the exact cloud properties (τ = 10, r_{eff} = 15 µm) for the cloud at 500 to 1000 m altitude. b) Overestimation of τ and r_{eff} as a function of the distance to the ice edge. The model cloud at an altitude of 500 to 1000 m had τ = 10 and r_{eff} = 15 µm.

The nadir radiance of the 3-D simulation is plotted in Fig. 7a as dots color-coded with the distance to the ice edge. The exact result of a cloud with τ = 10 and r_{eff} = 15 µm is marked with a black cross. The results imply a significant overestimation of τ and r_{eff} at distances below 2 km from the ice edge (dark blue dots). The overestimation increases with decreasing distance to the ice edge. As expected, for distances larger than 2 km from the ice edge (light blue to red dots) the radiance is close to the IPA value (black cross). Small deviations are results of noise in the 3-D simulations. For the range below ΔL = 2 km, the mean τ and r_{eff} derived from the retrieval are shown as a function of distance to the ice edge in Fig. 7b. The graph shows that the overestimation of τ increases up to 90 % while r_{eff} is biased by up to 30 % close to the ice edge. Both values are valid only for the cloud used in the simulations (τ = 10 and r_{eff} = 15 µm). For a lower τ, the effect will be lower. Using this simulations shown here and assuming a horizontally homogeneous cloud, Fig. 7b offers a possibility to correct the retrieved τ and r_{eff} for this overestimation.

6. Summary and conclusions:

Airborne measurements of reflected solar radiance with the imaging spectrometer AisaEAGLE were performed during the international field campaign VERDI in Inuvik, Canada, in spring 2012. In particular, measurements above clouds in situations

with heterogeneous surface albedo were analysed in order to retrieve τ. Due to the high contrast in the surface albedo of sea ice and open water, the data revealed a distinct difference between radiance reflected above water and sea ice surfaces. This transition was used to distinguish between areas of both surfaces. Threshold radiance values with good agreement could be derived from measurements and radiative transfer simulations and were found to be robust for the separation of the surfaces. However, radiative transfer simulations showed that for clouds with a bright sea-ice surface albedo, a retrieval of cloud microphysical (τ, r_{eff}) and macrophysical properties (cloud inhomogeneities) is not possible from the visible wavelength range. The differences of the reflected nadir radiance by clouds of different τ above bright sea ice are far below the measurement uncertainties of AisaEAGLE.

With focus on cloud retrievals for areas with open water below clouds, we found that reflected radiance is enhanced in the vicinity of ice edges. Those narrow bright bands are related to 3-D effects and result from isotropic reflection on the bright sea ice. In this study, this 3-D radiative effect was quantified using reflected radiance measurements from VERDI and 3-D radiative transfer simulations with MCARaTS. A critical distance ΔL was defined to characterize the 3-D effect. It can be used to estimate where the retrieval of τ and r_{eff} is influenced by 3-D effects.

From the two measurement cases presented here, with $\tau = 5$ and cloud base and cloud top at 0 and 200 m, respectively, a ΔL of 400 m was observed. This value could be confirmed by radiative transfer simulations adapted to the cloud and ice situation of the observations. Further simulations have been performed to identify the most important cloud parameters determining the magnitude of the 3-D effect. Therefore, 3-D radiative transfer simulations were performed for a clear-sky case and clouds with $\tau = 1/5/10$ located above a straight ice edge.

It was found that for adjacent sea ice and ocean water the reflected radiance is reduced above the sea ice and enhanced above the ocean surface. The reduction/ enhancement is not symmetric to the ice edge. The enhancement of the reflected radiance above ocean water is stronger than its reduction over sea ice. For the case of the straight ice edge the critical distance ΔL_{crit} was found to be in the range of ΔL_{crit} = 50 m/150 m/250 m for $\tau = 1/5/10$. However, the minimum distance ΔL to the ice edge where a 1-D cloud retrieval can be applied is decreasing with increasing τ. The values are in a range of ΔL = 600 m/400 m/250 m for $\tau = 1/5/10$.

The cloud altitude and cloud geometrical thickness were found to be parameters significantly influencing ΔL. The distance ΔL increases linearly with increasing cloud base altitude (at $\tau = 1/5$ from 700/1000 to 3200 m/4000 m for 500 m thick cloud and cloud base at 0 m/1500 m) as well as with increasing cloud geometrical thickness (for $\tau = 1/5$ from 1100/300 to 3200 m/2100 m for 200 m/1500 m thick cloud). Therefore, the cloud base altitude and cloud geometrical thickness have to be known exactly, while performing 3-D radiative transfer simulations of clouds above ice edges.

The results from the simulations suggest that using a 1-D cloud retrieval, for ocean areas located close to sea ice edges, τ and r_{eff} will be overestimated the closer the pixel is located to the ice edge. This overestimation was calculated for a liquid water cloud with $\tau = 10.0$ and $r_{eff} = 15$ µm. In that case the overestimation of the retrieved τ reaches up to a distance of 2 km from the ice edge. The maximum overestimation was found with 90 % directly beside the ice edge. For r_{eff} an overestimation of 30 % was

found up to a distance of 1.5 km from the ice edge. Further investigations on this and the application of our findings to satellite retrieval of cloud properties in Arctic regions will be part of future studies on the topic of 3-D radiative effects.

7. References:

Anderson, G., Clough, S., Kneizys, F., Chetwynd, J., and Shettle, E., 1986: AFGL Atmospheric Constituent Profiles (0-120 km), Tech. Rep. AFGL-TR-86-0110, AFGL (OPI), Hanscom AFB, MA 01736.

Bierwirth, E., Ehrlich, A., Wendisch, M., Gayet, J.-F., Gourbeyre, C., Dupuy, R., Herber, A., Neuber, R., and Lampert, A., 2013: Optical thickness and effective radius of Arctic boundary-layer clouds retrieved from airborne nadir and imaging spectrometry, Atmos. Meas. Tech., 6, 1189–1200, doi:10.5194/amt-6-1189-2013.

Bowker, D., Davis, R., Myrick, D., Stacy, K., and Jones, W., 1985: Spectral Reflectances of Natural Targets for Use in Remote Sensing Studies, NASA RP-1139, NASA Langley Research Center, Hampton (VA), USA.

Gueymard, C. A., 2004: The sun's total and spectral irradiance for solar energy applications and solar radiation models, Sol. Energy, 76, 423–453.

Intrieri, J. M., Fairall, C. W., Shupe, M. D., Persson, P. O. G., Andreas, E. L., Guest, P. S., and Moritz, R. E., 2002a: An annual cycle of Arctic surface cloud forcing at SHEBA, J. Geophys. Res., 107, SHE 13-1-SHE 13-14, doi:10.1029/2000JC000439.

Intrieri, J. M., Shupe, M. D., Uttal, T., and McCarty, B. J., 2002b: An annual cycle of Arctic cloud characteristics observed by radar and lidar at SHEBA, J. Geophys. Res., 107, SHE 5-1-SHE 5-15, doi:10.1029/2000JC000423.

Iwabuchi, H., 2006: Efficient Monte Carlo methods for radiative transfer modeling, J. Atmos. Sci., 63, 2324– 2339.

Iwabuchi, H. and Kobayashi, H., 2008: Modeling of radiative transfer in cloudy atmospheres and plant canopies using Monte Carlo methods, Tech. Rep. 8, 199 pp., FRCGC.

Krijger, J. M., Tol, P., Istomina, L. G., Schlundt, C., Schrijver, H., and Aben, I., 2011: Improved identification of clouds and ice/snow covered surfaces in SCIAMACHY observations, Atmos. Meas. Technol., 4, 2213–2224, doi:10.5194/amt-4-2213-2011.

Lindsay, R. W. and Rothrock, D. A., 1994: Arctic sea–ice albedo from Avhrr, J. Climate, 7, 1737–1749, doi:10.1175/1520-0442(1994)007<1737:ASIAFA>2.0.CO;2.

Lyapustin, A., 2011: Three-dimensional effects in the remote sensing of surface albedo, IEEE T. Geosci. Remote, 39, 254–263.

Lyapustin, A. and Kaufman, Y., 2001: Role of adjacency effect in the remote sensing of aerosol, J. Geophys. Res., 106, 11909–11916.

Nakajima, T. and King, M.,1990: Determination of the optical thickness and effective particle radius of clouds from reflected solar radiation measurements. Part I: Theory, J. Atmos. Sci., 47, 1878– 1893.

Overland, J. E., Wood, K. R., and Wang, M., 2011: Warm Arctic–cold continents: impacts of the newly open Arctic Sea, Polar Res., 30, 15787, doi:10.3402/polar.v30i0.15787.

Pierluissi, J. and Peng, G.-S., 1985: New molecular transmission band models for LOWTRAN, Opt. Eng., 24, 541–547.

Ricchiazzi, P. and Gautier, C., 1998: Investigation of the effect of surface heterogeneity and topography on the radiation environment of Palmer Station, Antarctica, with a hybrid 3-D radiative transfer model, J. Geophys. Res., 103, 6161–6178.

Rothrock, D. A. and Thorndike, A. S., 1984: Measuring the sea ice floe size distribution, J. Geophys. Res., 89, 6477–6486.

Sanderson, M. G., Hemming, D. L., and Betts, R. A., 2011: Regional temperature and precipitation changes under high-end (4 degrees C) global warming, Philos. T. R. Soc. A., 369, 85–98, doi:10.1098/rsta.2010.0283.

Schäfer, M., Bierwirth, E., Ehrlich, A., Heyner, F., and Wendisch, M., 2013: Retrieval of cirrus optical thickness and assessment of ice crystal shape from ground-based imaging spectrometry, Atmos. Meas. Tech., 6, 1855–1868, doi:10.5194/amt-6-1855-2013.

Schäfer, M., Bierwirth, E., Ehrlich, A., Jäkel, E., and Wendisch, M., 2015: Observations and simulations of three-dimensional radiative interactions between Arctic boundary layer clouds and ice floes, Atmos. Chem. Phys. Discuss., 15, 1–49, doi:10.5194/acpd-15-1-2015.

Shupe, M. D., Walden, V. P., Eloranta, E., Uttal, T., Campbell, J. R., Starkweather, S. M., and Shiobara, M., 2011: Clouds at Arctic atmospheric observatories. Part I: Occurrence and macrophysical properties, J. Appl. Meteorol. Clim., 50, 626–644, doi:10.1175/2010JAMC2467.1.

Stachlewska, I. S., Neuber, R., Lampert, A., Ritter, C., and Wehrle, G., 2010: AMALi – the Airborne Mobile Aerosol Lidar for Arctic research, Atmos. Chem. Phys., 10, 2947–2963, doi:10.5194/acp-10-2947-2010.

Wendisch, M., Müller, D., Schell, D., and Heintzenberg, J., 2001: An airborne spectral albedometer with active horizontal stabilization, J. Atmos. Ocean. Tech., 18, 1856–1866, 2001.

Wendisch, M., Pilewskie, P., Jäkel, E., Schmidt, S., Pommier, J., Howard, S., Jonsson, H. H., Guan, H., Schröder, M., and Mayer, B., 2004: Airborne measurements of areal spectral surface albedo over different sea and land surfaces, J. Geophys. Res., 109, D08203, doi:10.1029/2003JD004392.

Wendisch, M., Yang, P., and Ehrlich, A., 2013: Amplified climate changes in the Arctic: Role of clouds and atmospheric radiation, vol. 132, 1–34, Sitzungsberichte der Sächsischen Akademie der Wissenschaften zu Leipzig. Mathematisch-Naturwissenschaftliche Klasse, S. Hirzel Verlag, Stuttgart/Leipzig.

Werner, F., Siebert, H., Pilewskie, P., Schmeissner, T., Shaw, R. A., and Wendisch, M., 2013: New airborne retrieval approach for trade wind cumulus properties under overlying cirrus, J. Geophys. Res., 118, 1–16, doi:10.1002/jgrd.50334.

Characterization and calibration of a Full Stokes polarization camera

T. Carlsen[1], A. Ehrlich[1], M. Wendisch[1]

1) Leipzig Institute for Meteorology, Leipzig University, Stephanstr. 3, 04103 Leipzig, E-Mail: tim.carlsen@uni-leipzig.de

Summary: Initially unpolarized solar radiation is polarized in the atmosphere due to scattering processes at molecules and aerosols. Therefore, the measurement of the polarization state of solar radiation is of vital importance in remote sensing. A SALSA Full Stokes polarization camera measuring the complete Stokes vectors in real time is characterized within this work. The main focus lies on the radiometric calibration as well as the determination and validation of the calibration matrix based on a Data Reduction method. One main issue is the temporal instability of the calibration matrix, which gives rise to the need of a thorough calibration process. In accordance with theoretical expectations and model simulations, the SALSA Full Stokes polarization camera provides reliable measurement results under the condition of Rayleigh scattering.

Zusammenfassung: Die beim Eintritt in die Atmosphäre unpolarisierte solare Strahlung wird durch Streuprozesse an Molekülen oder Aerosolpartikeln polarisiert. Die Messung des Polarisationszustandes der solaren Strahlung spielt deshalb in der Fernerkundung eine wichtige Rolle. Die vorliegende Arbeit charakterisiert eine SALSA Full Stokes Polarisationskamera, die den kompletten Stokes-Vektor in Echtzeit misst. Das Hauptaugenmerk liegt dabei auf der radiometrischen Kalibrierung sowie der Bestimmung und Validierung der Kalibrationsmatrix über die Methode der Datenreduktion. Die zeitliche Instabilität der Kalibrationsmatrix stellt ein großes Problem dar und stellt Anforderungen an den Umfang der Kalibrierung. Mit der SALSA Full Stokes Polarisationskamera sind zuverlässige Messungen unter einer rayleighstreuenden Atmosphäre möglich, die in Übereinstimmung mit den theoretischen Erwartungen und Modellsimulationen stehen.

1. Motivation

The radiative effect of aerosols on the climate is a major element of uncertainty in investigations of the Earth's climate change (IPCC, 2013). Therefore, the precise characterization of aerosol properties as well as the spatial extent and temporal variability of aerosol concentrations is of upmost importance. Due to its interaction with aerosols, the polarization state of solar radiation changes. Consequently, measurements of the polarization state have the ability to provide a deeper insight into aerosol

characteristics. Aerosol optical properties and their effects on climate have been investigated by either active instruments in terms of a lidar (Bösenberg and Matthias, 2003) or passive instruments in terms of sun photometers. Sun photometers measure the radiance not only in sun direction but are applied to mechanically scan the entire sky (Holben et al. 1998, Dubovik and King 2000, Bayat et al. 2013). This scanning technique is very time-consuming and requires clear-sky conditions for reliable measurements. Nevertheless, it is a suitable technique to measure aerosol properties. Imaging polarization measurements cover a wide range of observed scattering angles and are applied for atmospheric observations on satellites (Goloub et al., 2000) as well as with ground-based all-sky cameras (Kreuter and Blumthaler, 2013). The principle behind polarized all-sky imaging is based on the usage of different polarization filters that are mechanically placed into the optical path in order to measure the Stokes vector. Such imaging techniques using filters are too slow for ground-based observations during conditions with fast-moving clouds.
Since 2012, the Institute for Meteorology at Leipzig University owns a SALSA Full Stokes polarization camera made by Bossa Nova Technologies. The major advantage of this camera is the imaging technique. Due to the implemented measurement principle involving two ferroelectric liquid crystals (FLCs) and one fixed polarizer, the complete Stokes vector of the incident radiation can be measured in real time. Compared to a previous version introduced by Lefaudeux et al. (2008), the SALSA camera used here additionally measures circularly polarized components of radiation. In the following, the characterization and calibration of the polarization camera is presented.

2. Polarimetry Using the Full Stokes Polarization Camera

The SALSA polarization camera from Bossa Nova Technologies (Serial number: UOL-612-SAL-1, dimensions: 80 mm × 80 mm × 100 mm) is a passive polarimeter as it measures the radiation of an external source. It is a division-of-time polarimeter.

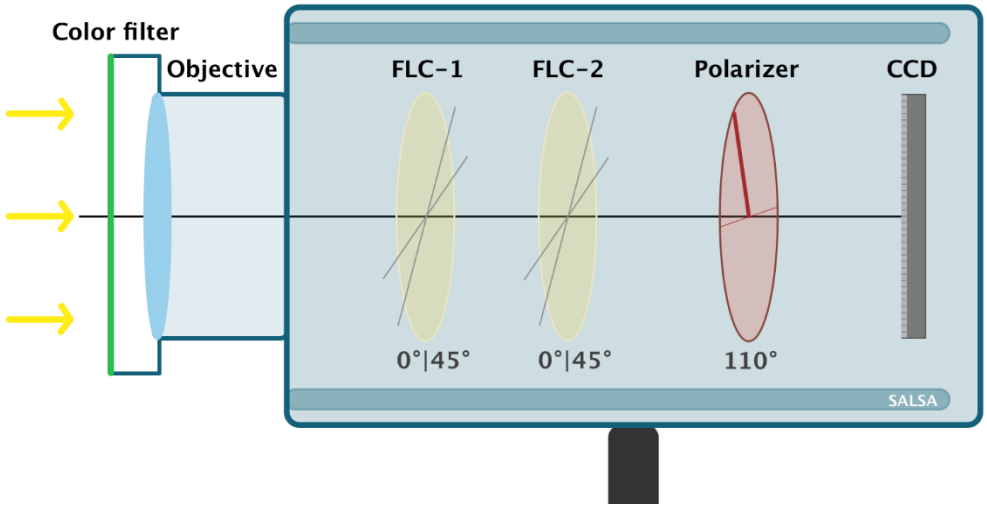

Fig. 1: Schematic set-up of the SALSA Full Stokes polarization camera

To measure the Stokes vector $\vec{S}$, 4 consecutive measurements are needed. Within the compact camera (see Fig. 1), the incident radiation initially passes through a color filter

before entering the objective (type: NMV-5M23 by Navitar, focal length: 5 mm, manual focus, iris aperture). The polarization state analyzer (PSA) consists of two FLCs and a fixed linear polarizer (transmission axis relative to horizontal: 110°). The liquid crystals each act as a programmable phase shifter, the first with a retardation close to $\lambda/2$, the second with a retardation close to $\lambda/4$. The angle of the optical axes of the FLCs with respect to the horizontal can be switched between 0 and 45 degrees. After passing the PSA, the radiation eventually reaches the CCD sensor (type: Basler avA1900-50gm, 1920×1080 pixel). During the entire work, the green color filter is used due to its higher transmission (type: HOYA G(X1) 52 mm). The intensity of the radiation I impinging on the CCD sensor can be described using the Stokes formalism as

$$\begin{aligned} I(\alpha,\theta_1,\theta_2) = \frac{1}{2}\Big\{ & S_0 + S_1\Big[\cos 2\alpha\left(\cos^2 2\theta_2 \cos 4\theta_1 + \sin 2\theta_2 \cos 2\theta_2 \sin 4\theta_1\right) \\ & + \sin 2\alpha\left(\sin 2\theta_2 \cos 2\theta_2 \cos 4\theta_1 + \sin^2 2\theta_2 \sin 4\theta_1\right)\Big] \\ & + S_2\Big[\cos 2\alpha\left(\cos^2 2\theta_2 \sin 4\theta_1 - \sin 2\theta_2 \cos 2\theta_2 \cos 4\theta_1\right) \\ & + \sin 2\alpha\left(\sin 2\theta_2 \cos 2\theta_2 \sin 4\theta_1 - \sin^2 2\theta_2 \cos 4\theta_1\right)\Big] \\ & + S_3\Big[\cos 2\alpha \sin 2\theta_2 - \cos 2\theta_2 \sin 2\alpha\Big]\Big\}, \end{aligned} \tag{1}$$

where θ_1 and θ_2 are the angles of the FLCs with respect to the x axis. α is the angle between the transmission axis of the linear polarizer and the x axis. The 4 components of the incident Stokes vector are denoted by S_i. The PSA runs through 4 different configurations for each measurement. With the known angles of the axes of the FLCs, Eq. (1) simplifies to:

$$I_1 = I(\alpha, 0°, 0°) = \frac{1}{2}\Big[S_0 + \cos 2\alpha S_1 - \sin 2\alpha S_3\Big], \tag{2a}$$

$$I_2 = I(\alpha, 45°, 0°) = \frac{1}{2}\Big[S_0 - \cos 2\alpha S_1 - \sin 2\alpha S_3\Big], \tag{2b}$$

$$I_3 = I(\alpha, 0°, 45°) = \frac{1}{2}\Big[S_0 - \sin 2\alpha S_2 + \cos 2\alpha S_3\Big], \tag{2c}$$

$$I_4 = I(\alpha, 45°, 45°) = \frac{1}{2}\Big[S_0 + \sin 2\alpha S_2 + \cos 2\alpha S_3\Big]. \tag{2d}$$

In solving this set of linear equations, the 4 unknown Stokes parameters of the incident radiation are derived:

$$S_0 = I_1 + 2I_3 - 2I_4 + I_2 + \frac{\sin 2\alpha}{\cos 2\alpha + \sin 2\alpha}\Big[I_3 - I_1 + I_4 - I_2\Big], \tag{3a}$$

$$S_1 = \frac{1}{\cos 2\alpha}\Big[I_1 - 2I_3 + 2I_4 - I_2\Big], \tag{3b}$$

$$S_2 = \frac{1}{\sin 2\alpha}\Big[I_4 - I_3\Big], \tag{3c}$$

$$S_3 = \frac{1}{\cos 2\alpha + \sin 2\alpha}\Big[I_3 - I_1 + I_4 - I_2\Big]. \tag{3d}$$

The Stokes components depend only on the 4 measured intensities. Therefore, with 4 images taken at each measurement it is possible to determine the full Stokes vector of the incident radiation.

3. General Camera Characteristics

3.1 Linearity

One great advantage of CCDs is the very linear response to the incident light intensity. In order to characterize the linearity, the radiation of an integrating sphere with variable aperture was measured. The measured intensity (corresponding to the first Stokes parameter S_0) showed a linear behaviour with respect to both the intensity of the incident radiation and the exposure time (linear correlation coefficients greater than 0.99).

3.2 Dark Current

At temperatures above absolute zero, the thermal movement of charge carriers is sufficient to excite electrons to the conduction band. Independent from any incident radiation, a certain statistically distributed dark current is measured by the CCD. The SALSA polarization camera is not cooled actively to reduce dark current. At each measurement, the dark current is subtracted immediately by means of offset maps. They consist of the dark signal measured at different gain factors at the laboratories of Bossa Nova Technologies. Several dark measurements proved the validity of this dark-frame subtraction. The CCD itself is divided into 4 separate taps. The images are therefore grabbed separately through 4 different electronic channels which allows fast image acquisition. Each tap has a different black level. Dark measurements lead to the registration of 6 digital counts for three of the 4 taps and one digital count for the fourth. This dark current is negligible compared to the maximum of 4095 counts and justifies the usage of offset maps. Furthermore, the measured dark current is independent of exposure time, gain factor and temperature (tested at $-3\ °C$ and at room temperature). Nevertheless, a similar test needs to be done for considerable higher temperatures in the future, as the exponential increase of thermally excited electrons in the conduction band might invalidate the offset maps.

3.3 Read-out Noise

Fast image acquisition can lead to a loss of electrons or an erroneous assignment of the electrons to the false pixel. Conversely, a slow read-out process poses problems due to the non-ideal insulation between different pixels. Read-out noise is independent of exposure time and measured signal. For the SALSA camera a read-out noise close to 8 digital counts was quantified.

3.4 Field of View

One main characteristic of each camera is its field of view. For achieving a sharp image on the CCD, the following trigonometric relation is valid in the internal coordinate system of the camera (CVZA: camera viewing zenith angle):

$$\mathrm{CVZA} = \arctan\frac{d}{f}\ . \tag{4}$$

Therein, the focal length of the camera is 5 mm, d denotes the distance of the image point to the center of the sensor. For the dimensions of the CCD in the SALSA camera (width: 10.56 mm, height: 5.94 mm), the field of view of the camera is

$93.12° \times 61.42° \times 100.93°$ (values corresponding to the horizontal, vertical and diagonal dimension). The maximum angular resolution is $0.046°$ per pixel.

4. Calibration of the Camera

If the polarization elements of the PSA were ideal, the Stokes parameters could be directly derived from the 4 frames at each measurement (compare Eq. (3a) to Eq. (3d)). However, due to depolarization, dispersion and manufacturing defects at the FLCs as well as the linear polarizer and polarization effects at the objective lens, the single elements do not affect incoming radiation in an ideal way. It is therefore of vital importance to determine the calibration matrix, which transfers the data of the 4 frames into the Stokes vector. The first part of this chapter deals with the implemented calibration. Furthermore, polarimetric measurements require a thorough radiometric calibration. Therefore, the second part of this chapter describes the correction of the photoresponse non-uniformity of each pixel of the sensor and the absolute calibration transferring the dimensionless signal by means of a calibration factor into the physical unit of a spectral radiance I ($\mathrm{Wm^{-2}sr^{-1}nm^{-1}}$).

4.1 Determination of the Calibration Matrix

The key factor for a correct measurement is the connection of the intensities of the 4 frames from the different configurations of the PSA with the incident, unknown Stokes vector:

$$\vec{X} = \begin{pmatrix} I_{\mathrm{frame1}} \\ I_{\mathrm{frame2}} \\ I_{\mathrm{frame3}} \\ I_{\mathrm{frame4}} \end{pmatrix} = \mathcal{C} \cdot \vec{S}_{\mathrm{in}} \ . \tag{5}$$

Matrix C is the real PSA matrix. Its inverse, C^{-1}, is the calibration matrix. The calibration matrix is determined by means of the Data Reduction Method (DRM). Each state i of the PSA is characterized by an own Mueller matrix:

$$\vec{S}^{\,i}_{\mathrm{out}} = \begin{pmatrix} S^i_{0,\mathrm{out}} \\ S^i_{1,\mathrm{out}} \\ S^i_{2,\mathrm{out}} \\ S^i_{3,\mathrm{out}} \end{pmatrix} = \begin{pmatrix} m^i_{00} & m^i_{01} & m^i_{02} & m^i_{03} \\ m^i_{10} & m^i_{11} & m^i_{12} & m^i_{13} \\ m^i_{20} & m^i_{21} & m^i_{22} & m^i_{23} \\ m^i_{30} & m^i_{31} & m^i_{32} & m^i_{33} \end{pmatrix} \vec{S}_{\mathrm{in}} \ . \tag{6}$$

As the camera sensor is insensitive to polarization, just the first row of the Mueller matrix is relevant, reducing Eq. (6) to:

$$\vec{S}^{\,i}_{0,\mathrm{out}} = m^i_{00} S_{0,\mathrm{in}} + m^i_{01} S_{1,\mathrm{in}} + m^i_{02} S_{2,\mathrm{in}} + m^i_{03} S_{3,\mathrm{in}} \ . \tag{7}$$

The aim of the calibration process is to determine the elements of the first row of the Mueller matrix for each of the 4 configurations of the PSA. For each configuration, the following system of equations in matrix form is given:

$$\begin{pmatrix} S^0_{0,\mathrm{out}} \\ S^1_{0,\mathrm{out}} \\ S^2_{0,\mathrm{out}} \\ \vdots \\ S^N_{0,\mathrm{out}} \end{pmatrix}_i = \left[\left(\vec{S}_{\mathrm{in}}\right)^T\right] \begin{pmatrix} m^i_{00} \\ m^i_{01} \\ m^i_{02} \\ m^i_{03} \end{pmatrix} = \begin{pmatrix} S^0_{0,\mathrm{in}} & S^0_{1,\mathrm{in}} & S^0_{2,\mathrm{in}} & S^0_{3,\mathrm{in}} \\ S^1_{0,\mathrm{in}} & S^1_{1,\mathrm{in}} & S^1_{2,\mathrm{in}} & S^1_{3,\mathrm{in}} \\ S^2_{0,\mathrm{in}} & S^2_{1,\mathrm{in}} & S^2_{2,\mathrm{in}} & S^2_{3,\mathrm{in}} \\ \vdots & \vdots & \vdots & \vdots \\ S^N_{0,\mathrm{in}} & S^N_{1,\mathrm{in}} & S^N_{2,\mathrm{in}} & S^N_{3,\mathrm{in}} \end{pmatrix} \begin{pmatrix} m^i_{00} \\ m^i_{01} \\ m^i_{02} \\ m^i_{03} \end{pmatrix}, \tag{8}$$

where $\left[\left(\vec{S}_{in}\right)^T\right]$ is a $N \times 4$-matrix consisting of 4 generated Stokes parameters for each of the N measurements during the calibration process. The first row of the Mueller matrix is calculated for each state i of the PSA via:

$$\begin{pmatrix} m^i_{00} \\ m^i_{01} \\ m^i_{02} \\ m^i_{03} \end{pmatrix} = \left[\left(\vec{S}_{\mathrm{in}}\right)^T\right]^+ \begin{pmatrix} S^0_{0,\mathrm{out}} \\ S^1_{0,\mathrm{out}} \\ S^2_{0,\mathrm{out}} \\ \vdots \\ S^N_{0,\mathrm{out}} \end{pmatrix}_i, \tag{9}$$

where $\left[\left(\vec{S}_{in}\right)^T\right]^+$ denotes the Moore-Penrose pseudoinverse of $\left[\left(\vec{S}_{in}\right)^T\right]$. The PSA matrix C consists of the first rows for each state of the PSA:

$$\vec{X} = \begin{pmatrix} I_{\mathrm{frame1}} \\ I_{\mathrm{frame2}} \\ I_{\mathrm{frame3}} \\ I_{\mathrm{frame4}} \end{pmatrix} = \mathcal{C} \cdot \vec{S}_{\mathrm{in}} = \begin{pmatrix} m^1_{00} & m^1_{01} & m^1_{02} & m^1_{03} \\ m^2_{00} & m^2_{01} & m^2_{02} & m^2_{03} \\ m^3_{00} & m^3_{01} & m^3_{02} & m^3_{03} \\ m^4_{00} & m^4_{01} & m^4_{02} & m^4_{03} \end{pmatrix} \cdot \vec{S}_{\mathrm{in}}\ . \tag{10}$$

Finally, the PSA matrix C is regularly inverted. This way, the calibration matrix C^{-1} (or Data Reduction Matrix) transfers the 4 measured intensities of the 4 frames into the unknown Stokes vector $\vec{S}_{in}$:

$$\vec{S}_{\mathrm{in}} = \mathcal{C}^{-1} \begin{pmatrix} I_{\mathrm{frame1}} \\ I_{\mathrm{frame2}} \\ I_{\mathrm{frame3}} \\ I_{\mathrm{frame4}} \end{pmatrix}. \tag{11}$$

As the retardance of the individual FLCs is wavelength dependent, each color filter of the camera has its own calibration matrix. Within this work, the green wavelength channel is analyzed.

Figure 2 shows the schematic of the calibration process. An integrating sphere generates unpolarized radiation which is incident on the Polarization State Generator (PSG) consisting of a linear polarizer and a Fresnel rhomb. Both the polarizer and the Fresnel rhomb are rotatable around the propagation direction of the radiation. Within the calibration process, 1729 different polarization states were generated with the PSG and measured by the camera (lens, filter, PSA and CCD). The Fresnel rhomb was rotated

from 0° to 90° (increments of 5°). For each position of the Fresnel rhomb, the linear polarizer was rotated from 0° to 180° (increments of 2°).

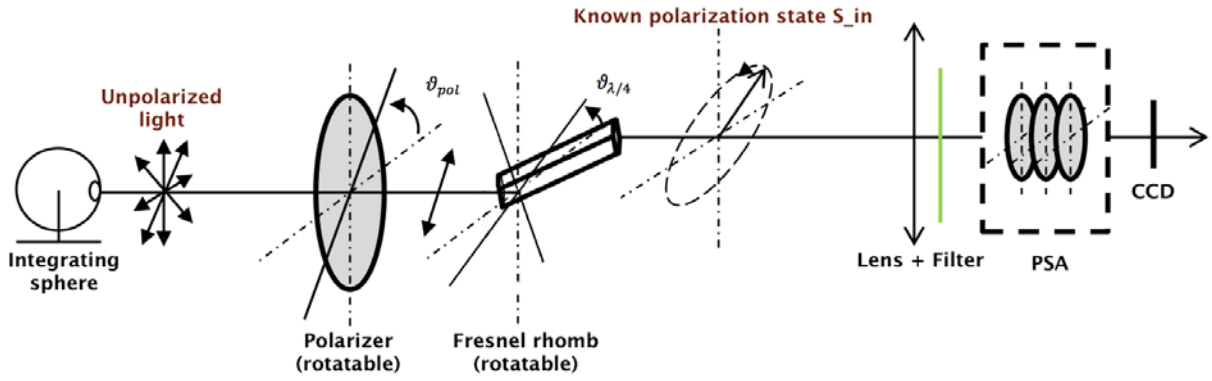

Fig. 2: Schematic of the calibration set-up (Vedel et al., 2011, modified figure 1)

The best way to visualize the generated polarization states is to use the Poincaré sphere. In a Cartesian coordinate system, the normed Stokes parameters S_1, S_2 and S_3 correspond to the x, y and z axis. For completely polarized radiation, all generated polarization states lie on the surface of a sphere with radius 1, called Poincaré sphere (see Fig. 3). All generated polarization states lie along the black paths. The dashed path visualizes the number of states on one path (one line connects two states). As illustrated in Fig. 3, the polarization states used for the calibration cover most parts of the Poincaré sphere. However, Fig. 3 also shows the view on the pole region (right part), where a huge concentration of generated polarization states is obvious. In this region, all polarization states are very similar to each other and provide just very little new information about the calibration matrix. A better coverage of the Poincaré sphere during the calibration process would allow more accurate measurements of random polarization states and should thereby be optimized during future calibrations. The calibration analyzed here still has a sufficient number of different polarization states in the equatorial region.

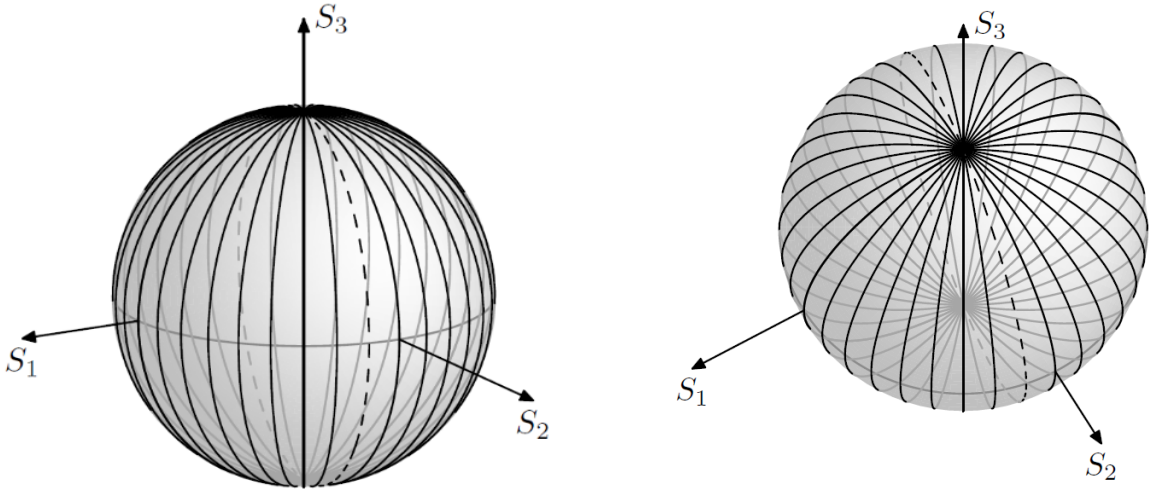

Fig. 3: Generated polarization states on Poincaré sphere (Jonsson, 2014), left: view on equator, right: view on pole

The DRM leads for 1729 generated polarization states to the calibration matrix shown in Eq. (12). For comparison, Eq. (13) shows the calibration matrix as determined in the laboratories of the manufacturer (Bossa Nova Technologies, 2012). The signs of the matrix elements in the second and third row were changed with respect to the calibration report due to a different definition of the coordinate systems.

$$\mathcal{C}^{-1} = \begin{pmatrix} 0,400021 & 0,141730 & 0,398747 & 0,059502 \\ 0,947775 & -1,226719 & 1,049670 & -0,770726 \\ 1,246871 & -0,342375 & 0,503146 & -1,407641 \\ 0,352059 & -0,175396 & -0,505731 & 0,329069 \end{pmatrix}, \tag{12}$$

$$\mathcal{C}^{-1}_{\text{BossaNova}} = \begin{pmatrix} 0,372054 & 0,171512 & 0,375346 & 0,089320 \\ 0,714034 & -1,042598 & 0,928807 & -0,587025 \\ 1,146722 & -0,257262 & 0,408144 & -1,286936 \\ 0,409610 & -0,207622 & -0,448940 & 0,249989 \end{pmatrix}. \tag{13}$$

The corresponding matrix elements of the two calibration matrices show significant deviations between 6.2 % and 33 %. This illustrates that the camera calibration has to be repeated regularly.

4.2 Radiometric Calibration

Each pixel of the CCD has its specific sensitivity due to fabrication tolerances, contamination with dust particles or optical effects at the edge of the objective lens. This photoresponse non-uniformity needs to be corrected via a radiometric calibration.

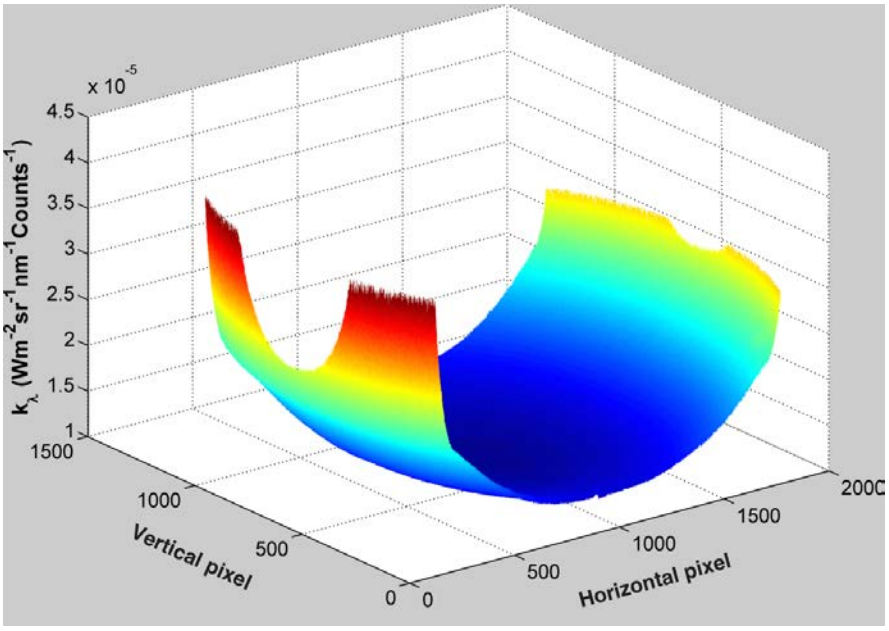

Fig. 4: Pixel-dependent illustration of the calibration factor k_λ

Therefore, the measured, uniform radiance of an integrating sphere I_λ is put in relation to the Stokes parameter S_0 determined for each pixel (x, y) by means of the calibration matrix (see Eq. (12)):

$$k_\lambda(x,y) = \frac{I_\lambda}{S_0(x,y)} \,. \tag{14}$$

The calibration factor $k_\lambda(x,y)$ corrects the different pixel sensitivities and transforms the dimensionless signal into the physical unit of a spectral radiance ($Wm^{-2}sr^{-1}nm^{-1}$). Figure 4 shows the calibration factor for an exposure time of 10 ms and gain factor 0 dB. Regions of higher sensitivity are found close to the center of the image with considerably smaller values of k_λ. This vignetting effect is typical for digital cameras and is corrected by applying the calibration factors k_λ.

5. Validation of Calibration Results

The distinct deviations of the calibration matrix elements from the manufacturer's calibration rises the need for a thorough analysis. At first, the Stokes parameters calculated by means of the calibration matrix are compared to the theoretical expectations. Secondly, temporal stability and warm-up time of the camera are investigated. The intensity of incident radiation was found to have no significant effect on the measured degree of linear polarization (DOLP).

5.1 Quality of the Calibration Matrix

Throughout the process of calibration, the theoretical Stokes vectors of the generated polarization states were already determined and can be used for the analysis. Figure 5 shows the deviations between measured and theoretical Stokes parameters S_1 for all 1729 generated polarization states.

$$\vec{S}_{\text{diff}} = \vec{S}_{\text{measured}} - \vec{S}_{\text{theoretic}} = \begin{pmatrix} \text{Dev}S_0 \\ \text{Dev}S_1 \\ \text{Dev}S_2 \\ \text{Dev}S_3 \end{pmatrix}. \tag{15}$$

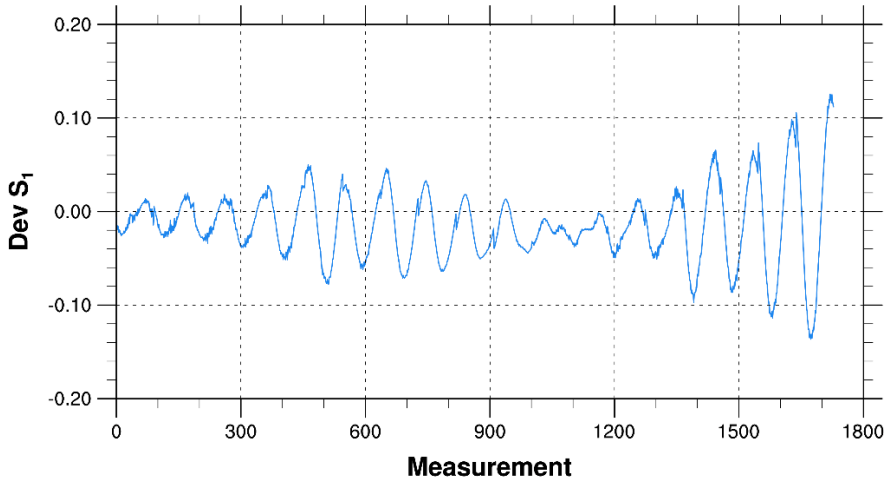

Fig. 5: Quality of the calibration matrix: standard deviation for S_1

Within Fig. 5, a pronounced periodicity of the deviations is obvious. This is due to a certain periodicity in the generated polarization states as for one position of the Fresnel

rhomb the polarizer passes through all possible positions. As the calibration matrix is the result of an error reduction, some measurements are closer to the theoretical expectations than others. The remaining Stokes parameters as well as the degree of polarization (DOP), DOLP and degree of circular polarization (DOCP) show similar behaviours (not shown here). Standard deviations can be used as a quantitative measure of the quality of the calibration matrix. Table 1 lists the standard deviations for all Stokes parameters and the different degrees of polarization when using both our calibration matrix and the manufacturer's calibration matrix. Additionally, the standard deviations as listed in the calibration report by Bossa Nova Technologies are given for comparison. Our own calibration matrix leads to maximum deviations of 5.5 % (S_2). The DOLP can be determined with deviations of ± 4.5 %. The measurement uncertainties are approximately 5-times higher than the specifications stated in the calibration report. The manufacturer's calibration matrix is based upon approximately 2000 different polarization states (15 % more than used in our calibration). Naturally, the number of generated polarization states used during the calibration has an influence on the measurement uncertainties. If just parts of the 1729 generated polarization states are used in order to determine the calibration matrix, different matrix elements are derived with different standard deviations (see Fig. 6). The higher the number of used polarization states, the more precise are subsequent measurements. Lower numbers of polarization states correspond to a worse coverage of the Poincaré sphere and lead to strongly increased uncertainties. The aim of future calibrations should therefore be to produce both a high number and preferably a sufficient variety of different polarization states in order to measure random polarization states with high precision.

Table 1: Standard deviations when using our own calibration matrix and the Bossa Nova Technologies matrix (in brackets: values from calibration report).

Standard deviation	**LIM calibration matrix**	**Bossa Nova Technologies calibration matrix**
$\sigma(S_0)$	$5.3881 \cdot 10^{-17}$	$5.1720 \cdot 10^{-17}$
$\sigma(S_1)$	0.0415	0.0942 (0.01153)
$\sigma(S_2)$	0.0547	0.0692 (0.00950)
$\sigma(S_3)$	0.0231	0.0416 (0.00630)
$\sigma(DOP)$	0.0216	0.0694
$\sigma(DOLP)$	0.0451	0.0749 (0.00923)
$\sigma(DOCP)$	0.0231	0.0416

When the Bossa Nova Technologies calibration matrix is applied to the polarization states generated in the laboratory, Stokes parameters S_1 and S_2 can only be measured with deviations of up to ± 9.4 % and ± 6.9 %, respectively (see Tab. 1). Thus, the uncertainties are one order of magnitude higher than stated in the calibration report, indicating a temporal instability of the calibration matrix. If the calibration matrix is applied to measurements which were taken three months earlier (144 different

polarization states), the measured Stokes parameters are not reliable any longer (standard deviations of up to 14 %). It cannot be ruled out that the calibration of the camera changes over time due to external influences.

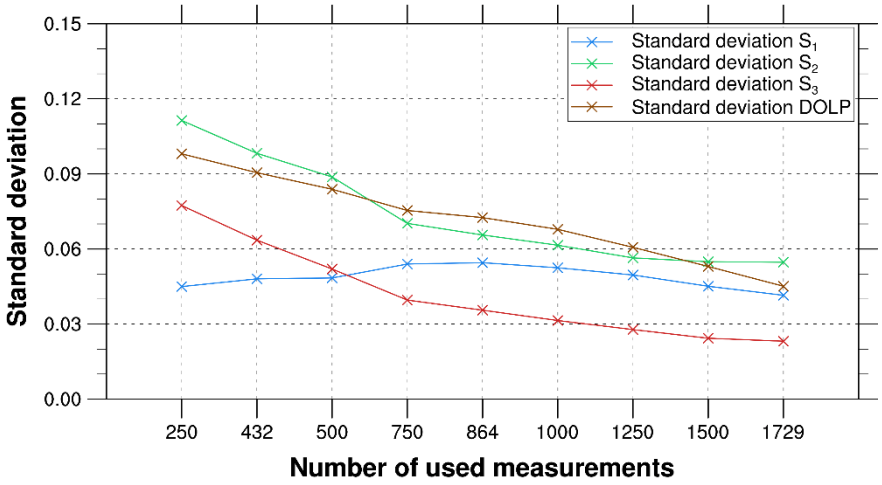

Fig. 6: Dependence of the number of used polarization states during calibration process on measurement uncertainties

5.2 Warm-up Time of the Camera

Polarized radiation ($DOLP = 1.0$) was generated by an integrating sphere and a linear polarizer (13 different positions) and measured with the camera at different times after starting the camera in order to investigate the temporal behaviour of the camera. The DOLP was measured at 13 different time steps (from 5 minutes to 4 hours after turning on the camera, see Fig. 7).

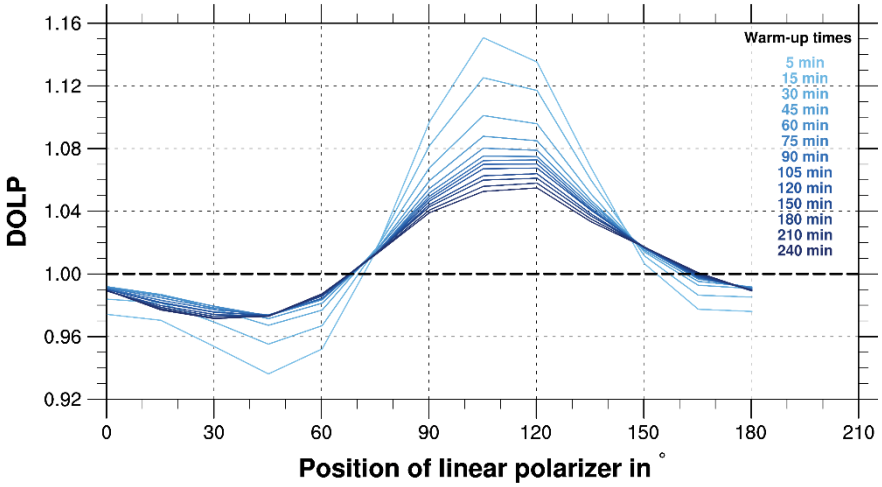

Fig. 7: Temporal evolution of DOLP measurements after camera power-on

Directly after turning on the camera, the DOLP varies between 0.94 and 1.15. Deviations of that magnitude are not acceptable for atmospheric applications of the camera. Typically, aerosol polarimetric effects are in the same order of magnitude and thus are not observable by the camera early after switching it on. However, the deviations become smaller while the camera is running. 45 minutes after power-on, the DOLP varies between 0.97 and 1.09 if the polarizer is rotated along its axis. The most precise measurements were taken after 4 hours. It should be noted that improvements became

slower with increasing runtime of the camera. Nevertheless, the camera needs a certain time after power-on in order to reach a permanent regime and measure in a reliable way. A time of 45 minutes is proposed in consideration of acceptable measurement uncertainties below 5 %.

6. Field Measurement

The sun is known to emit unpolarized radiation. Within the atmosphere, the polarization state of solar radiation changes due to numerous scattering processes. Figure 8 shows radiative transfer simulations with the MYSTIC model by Emde et al. (2010) for a molecular atmosphere. The simulated intensity shows a minimum at a viewing direction of 90° with respect to the sun. This is due to the minimum of the phase function at scattering angles of 90°. At this viewing angle, the DOP shows a pronounced maximum of approximately 65 %. On the other hand, radiation is completely unpolarized when looking into the direct sun. In order to test the camera for atmospheric applications, we performed a field measurement on 18th June 2013. The day featured a cloudless sky and therefore Rayleigh scattering conditions. Only at the end of the measurement, some altocumulus and cirrus fibratus affected the observations.

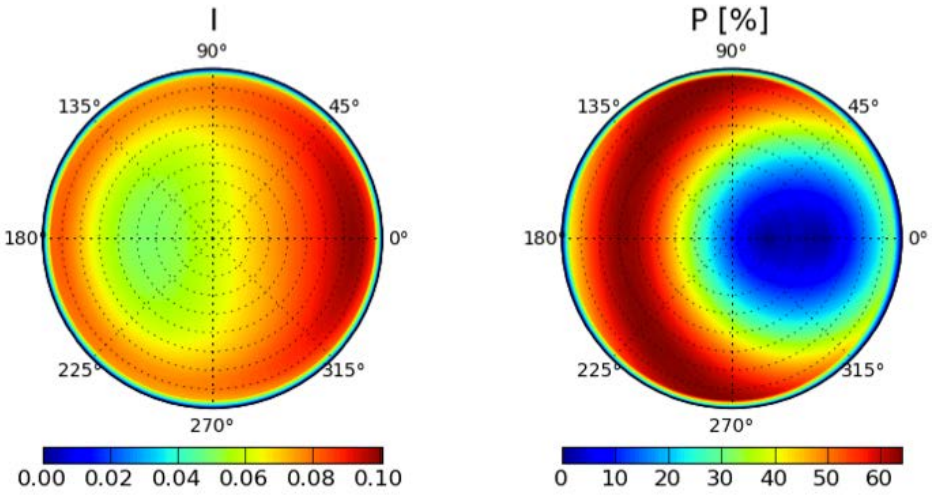

Fig. 8: Simulated intensity I and simulated degree of polarization P for molecular atmosphere (Rayleigh scattering), zenith angle: 30°, *azimuth angle:* 0°, *wavelength:* 350 *nm, surface albedo:* 0 *(Emde et al., 2010)*

The measurements were taken on the roof of the Leipzig Institute for Meteorology. The SALSA camera was mounted on a tripod and the green color filter was used. In order to cover large parts of the sky, 6 images were taken during 20 minutes starting at 2:45 p.m. (UTC). During that time, the solar zenith angle increased from 49.5° to 51.6°, the solar azimuth angle changed from 256.7° to 259.7°.

Throughout the analysis, we consecutively applied the dark current correction, the calibration matrix and the radiometric calibration to the measured signal. With help of Eq. (4) and the roll, pitch and yaw angles of the camera, each pixel of the images was related to a certain viewing angle. Afterwards, the Cartesian coordinates were transformed into polar coordinates similar to Ehrlich et al. (2012), who corrected airborne downward looking camera measurements for aircraft alignments. The

coordinate system was rotated in order to have the sun on the left side (solar azimuth angle: 270°). At pixels with more than one value from different measurements, the arithmetic mean was calculated. Figure 9 shows the polar coordinate system (all 6 images combined) and visualizes the DOLP depending on the viewing angle of the camera. The ring of high DOP values is clearly visible. The maximum DOP is 52.5 % which is smaller than the 65 % simulated by Emde et al. (2010). This can be attributed to the very idealized simulation conditions: the atmosphere was not ideally molecular due to an Aerosol Optical Depth of 0.38 at the measurement station IFT-Leipzig (AERONET, 2013) and the beginning evolution of clouds. Furthermore, the simulation was computed for a single wavelength at 350 *nm*, whereas the camera integrated over the wavelength range of the green color filter. Also, the surface albedo in reality is not zero which increases the influence of multiple scattering and decreases the DOP. A quantitative comparison is therefore not feasible. Nevertheless, a qualitative agreement between the measurements of the SALSA camera and the simulations by Emde et al. (2010) is clearly visible.

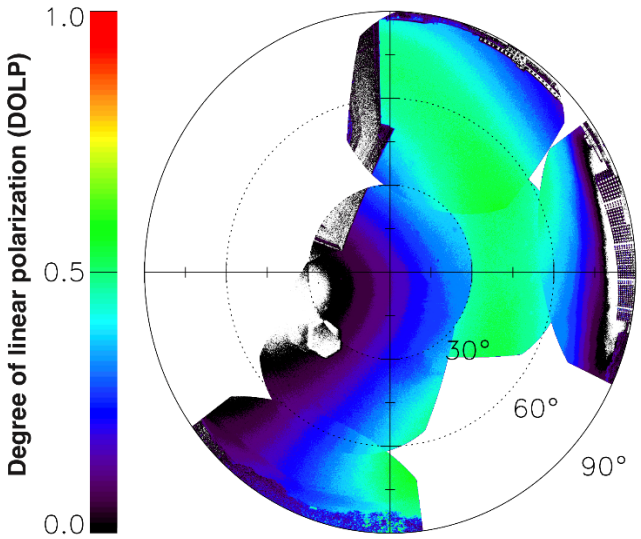

Fig. 9: Measured DOLP on 18th June 2013 in Leipzig, solar zenith angle: 50°, *solar azimuth angle:* 270°

7. Summary and Outlook

The SALSA polarization camera, a robust camera with fast image acquisition due to the use of two FLCs and a CCD with 4 separate electronic channels, was introduced and characterized by laboratory and field measurements. The SALSA polarization camera is suitable for field measurements. The qualitative agreement between the field measurement and the model simulations by Emde et al. (2010) indicates that the camera can be applied for atmospheric observations. The valid dark current correction, small read-out noise, linearity of the CCD and the independence of the intensity of incident radiation favour a high measurement accuracy. Within this work, the necessity of a thorough radiometric and polarimetric calibration became evident. One major problem is the apparent temporal instability of the calibration matrix. Already three months after

the last calibration, a measurement of the four Stokes parameters showed standard deviations of up to 14 %. Future calibrations should concentrate both on a high number and on a great variety of the generated polarization states. Furthermore, the warm-up time of the camera of about 45 minutes needs to be considered.
The findings of this work revealed sensible parts of the calibration process and allow the operation of the SALSA polarization camera in future field measurements. Future research subjects may include the derivation of aerosol properties under cloudless conditions as well as cloud detection and the retrieval of cloud properties such as effective radii.

References

AERONET, 2013: AERONET data of the station IFT-Leipzig from 18th June 2013. Aerosol Robotic Network of NASA/GSFC, Principal Investigator: Dr. Albert Ansmann, Leibniz Instititute for Tropospheric Research Leipzig.

Bayat, A., Khalesifard, H.R., Masoumi, A., 2013: Retrieval of aerosol single-scattering albedo and polarized phase function from polarized sun-photometer measurements for Zanjan's atmosphere, Atmos. Meas. Tech., 6, 2659-2669

Bösenberg, J. and Matthias, V., 2003: EARLINET: a European aerosol research lidar network to establish an aerosol climatology, MPI-Report 348, Hamburg, Germany

Bossa Nova Technologies, 2012: Calibration report – SALSA camera, Serial: UOL-612-SAL-1

Dubovik, O. and King, M., 2000: A flexible inversion algorithm for retrieval of aerosol optical properties from Sun and sky radiance measurements, Journal of Geophysical Research, 105(D16), 20673-20696

Ehrlich, A., Bierwirth, E., Wendisch, M., Herber, A., Gayet, J.-F., 2012: Airborne hyperspectral observations of surface and cloud directional reflectivity using a commercial digital camera, Atmos. Chem. Phys. 12, 3493-3510

Emde, C., Buras, R., Mayer, B., Blumthaler, M., 2010: The impact of aerosols on polarized sky radiance: model development, validation, and applications, Atmos. Chem. Phys. 10

Goloub, P., Herman, M., Chepfer, H. Riedi, J., Brogniez, G., Couvert, P., Séze, G., 2000: Cloud thermodynamical phase classification from the POLDER spaceborn instrument, Journal of Geophysical Research, 105(D11), 14747-14759

Holben, B., Eck, T.F., Slutsker, I., Tanré, D., Buis, J.P., Setzer, A., Vermote, E., Reagan, J.A., Kaufman, Y.J., Nakajima, T., Lavenu, F., Jankowiak, I., Smirnov, A., 1998: AERONET – A Federated Instrument Network and Data Archive for Aerosol Characterization, Remote Sens. Environ., 66, 1-16

IPCC, 2013: Boucher, O., Randall, D., Artaxo, P., Bretherton, C., Feingold, G., Forster, P., Kerminen, V.-M., Kondo, Y., Liao, H., Lohmann, U., Rasch, P., Satheesh, S.K., Sherwood, S., Stevens, B., Zhang, X.Y.: Clouds and Aerosols, In Climate Change 2013: The Physical Science Basis, Contribution of Working Group I to the Fifth Assessment Report of the Intergovernmental Panel on Climate Change [Stocker, T.F., Qin, D., Plattner, G.-K., Tignor, M., Allen, S.K., Boschung, J., Nauels, A., Xia, Y., Bex, V., Midgley, P.M. (eds.)], Cambridge University Press, Cambridge, United Kingdom and New York, NY, USA

Jonsson, F., 2014: C program, Visualization of Stokes parameter on Poincaré sphere, available under: http://www.jonsson.eu/programs/ansic/poincare/ (9th February 2014)

Kreuter, A. and Blumthaler, M., 2013: Feasibility of polarized all-sky imaging for aerosol characterization, Atmos. Meas. Tech., 6, 1845-1854

Lefaudeux, N., Lechocinski, N., Breugnot, S., Clemenceau, P., Bossa Nova Technologies, 2008: Compact and robust linear Stokes polarization camera, SPIE conference, Polarization: Measurement, Analysis, and Remote Sensing VIII, 6972

Vedel, M., Breugnot, S., Lechocinski, N., Bossa Nova Technologies, 2011: Full Stokes polarization camera, SPIE Proc., Vol. 8160-33, SPIE Optical Engineering + Applications

Retrieval of optical and microphysical cloud properties using ship-based spectral solar radiation measurements over the Atlantic ocean

M. Brückner[a,b]

[a]*Leibniz Institute for Tropospheric Research (TROPOS), Permoserstr. 15, 04318 Leipzig, Germany*

[b]*Leipzig Institute for Meteorology (LIM), University of Leipzig, Stephanstr. 3, 04103 Leipzig, Germany*

Summary. In this paper spectral solar zenith radiances are analyzed which were obtained from ship–based measurements over the Atlantic ocean. In combination with high–resolution lidar and microwave remote sensing optical and microphysical cloud properties were retrieved using spectral radiation data. To overcome problems of existing transmissivity–based cloud retrievals, a new retrieval algorithm is introduced which circumvents retrieval ambiguities and reduces the influence of measurement uncertainties. The method matches radiation measurements of ratios of spectral transmissivity at six wavelengths with modeled transmissivities. The new retrieval method is fast and accurate, and thus suitable for operational purposes. It is applied to homogeneous and inhomogeneous liquid water and cirrus clouds. The results from the new algorithm are compared to observations of liquid water path obtained from a microwave radiometer, yielding an overestimation for thick liquid water clouds but a slight underestimation for thin clouds.

Zusammenfassung. In dem vorliegenden Artikel werden abwärtsgerichtete spektrale Strahldichten analysiert, die mithilfe schiffsgebundener Beobachtungen über dem Atlantischen Ozean gemessen wurden. In Verbindung mit hochauflösenden Lidar und Mikrowellenradiometer Fernerkundungsverfahren werden optische und mikrophysikalische Wolkeneigenschaften aus spektralen Daten abgeleitet. Um Probleme bereits existierender Verfahren, die auf Transmissionen basieren, zu beseitigen, wird ein neuer Fernerkundungsalgorithmus vorgestellt, der nicht nur Zweideutigkeiten in der Bestimmung der Parameter umgeht, sondern auch den Einfluss von Messunsicherheiten verringert. Die Methode vergleicht gemessene spektrale Transmissionsverhältnisse bei sechs Wellenlängen mit modellierten Verhältnissen. Die neue Fernerkundungsmethode ist schnell und exakt, sodass sie für operative Zwecke geeignet ist. Sie wird für homogene und inhomogene Wasserwolken als auch für Cirren angewendet. Die Ergebnisse des neuen Ableitungsverfahrens werden mit Beobachtungen des Flüssigwasserpfades eines Mikrowellenradiometers verglichen. Daraus ergibt sich eine Überschätzung des Flüssigwasserpfades unter dicken Wolken, jedoch eine leichte Unterschätzung für dünne Wolken.

Introduction

The most important microphysical parameters describing the radiative energy effects of clouds are the cloud optical thickness τ and the droplet effective radius r_{eff} (ratio of the third moment of the cloud droplet size distribution to its second moment). To investigate cloud properties of marine clouds different remote sensing methods are used on the basis of satellite, airborne, and ship-based radiation measurements. Long–term global cloud data such as the International Satellite Cloud Climatology Project (ISCCP, Rossow and Schiffer, 1991) are based on space–borne observations of cloud reflectivity. In non-absorbing water vapor wavelength regions (visible) cloud reflectivity primarily depends on τ , whereas due to the proportionality of the liquid/ice absorption coefficient and r_{eff} (in the solar spectral region) cloud reflectivity primarily depends on r_{eff} in liquid water/ice absorbing wavelength regions (near-infrared). This is the basis of most satellite–based cloud retrievals (e.g., Nakajima and King, 1990). The cloud reflectivity is mostly determined by the upper cloud layers in these reflectivity-based retrievals (Platnick et al., 2003). Platnick (2000) modeled photon transport through cloud layers using vertical weighting functions to quantify the relative contributions of distinct cloud layers to the retrieval of r_{eff} . These simulations show that the upper part of the cloud is weighted stronger than lower cloud parts using reflectivity. In contrast, transmissivity is mostly determined by the center layers of the cloud.

However, transmissivity principally contains less information on r_{eff} as reflectivity. This is due to the competing effects of absorption and forward scattering. With increasing r_{eff} forward scattering increases; however, in this case also cloud droplet absorption increases in the near–infrared wavelength region. Furthermore, transmissivity has a non–monotonic behavior with regard to τ . This causes ambiguous retrieval results in contrast to using reflectivity, which is a monotonic function of τ (Kikuchi et al., 2006). For optically thin clouds ($\tau < 5$) an increase in τ results in an increased number of scattered water droplets in the upward looking sensor field–of–view and thus larger transmissivity. As the cloud becomes optically thicker, zenith radiance decreases and attenuation dominates which enhances the uncertainty of r_{eff} retrievals.

Different ground–based retrievals were developed to obtain τ and r_{eff} . A number of studies obtain simultaneously τ and r_{eff} using zenith radiance measurements (Rawlins and Foot, 1990; Kikuchi et al., 2006; McBride et al., 2011, 2012; Chiu et al., 2012). The basic principle of these transmissivity–based methods is to combine a non–water absorbing wavelength with a liquid–water/ice absorbing wavelength.

McBride et al. (2011) introduced a method for retrieving τ and r_{eff} with enhanced sensitivity to r_{eff} using the spectral slope of transmissivity between 1565 nm and 1634 nm in combination with transmissivity at a visible wavelength. This spectral method agreed with the common two–wavelength approach for τ retrievals but improved results for r_{eff} for $\tau > 25$. Furthermore, the comparison of retrieved τ , r_{eff} and liquid water path (LWP) agree well with satellite and ship–based microwave observations. More recently, almost parallel but independent from this work (Brückner et al., 2014), LeBlanc et al. (2014) introduced a new retrieval method for τ , r_{eff} , and additionally cloud phase using ground–based spectral transmissivity. Using multiple spectral variations in zenith radiance due to

absorption and scattering of liquid water and ice clouds, they found a closer fit by a weighted least–squares retrieval between observed and modeled transmissivity compared to existing retrieval methods.
This paper is concerned with a ground–based retrieval of τ , r_{eff} and LWP of marine clouds by analyzing spectral zenith radiance measurements. A new retrieval technique is developed which is similar to LeBlanc et al. (2014). Data used in this paper are based on spectral zenith radiance measurements with the COmpact RAdiation measurement System (CORAS). The measurements are complemented with data collected with different active and passive remote sensing instruments. The data set was gathered during three Atlantic ocean transfers of the Research Vessel (RV) Polarstern in the framework of the German Leibniz–network OCEANET–project (autonomous measurement platforms for material and energy exchange between ocean and atmosphere). The measurements benefit from the regular transfers of RV Polarstern between the polar regions on both hemispheres and provides the opportunity to observe clouds in three climate zones (tropics, subtropics, and mid–latitudes).This paper summarizes the results presented in Brückner et al., (2014) and Brückner (2015).

Instrumentation

The OCEANET-Atmosphere container consists of several instruments. A microwave radiometer HATPRO (Humidity and Temperature PROfiler) provides atmospheric vertical profiles of temperature, humidity and liquid water path (Zoll, 2012). A full sky imager (Kalisch and Macke, 2008) determines the cloud coverage and cloud type. For daytime every 15 seconds a picture is taken. Pyrano- and Pyrgoemeter were used to obtain the solar and terrestrial downward broadband irradiance (Macke et al., 2010). A multi wavelength Raman lidar Polly^{XT} (Althausen et al., 2009) measured vertical profiles of the particle extinction coefficient and aerosol microphysical properties. Spectral radiation measurements were performed with the COmpact RAdiation measurement System (CORAS). This instrument consists of two optical inlets to measure downward spectral irradiance and radiance; both inlets were mounted on the roof of the container. Here, only data from spectral zenith radiance were used. The inlets are connected via optical fibers to a system of spectrometers. For measurements in the visible to near infrared (VNIR: 350-1000 nm) and shortwave infrared (SWIR) spectral range (950-2200 nm). The spectral resolution is 2-3 nm in VIS and 15 nm in NIR. The OCEANET-container was located on the helicopter deck of RV Polarstern.

Multi-Wavelength Cloud Retrieval

To retrieve microphysical properties from spectral radiation measurements simulated radiances are required over ranges of τ , r_{eff} and solar zenith angles θ_0 to calculate lookup tables (LUT). The plane–parallel radiative transfer model package libRadtran version 1.6beta (Mayer and Kylling, 2005) was used to calculate the zenith radiance $I^{\downarrow}_{\lambda,\mathrm{mod}}$ at sea level z_0. The spectral transmissivity T at sea level z_0 was calculated using

$$T^{\downarrow}_{\lambda,\mathrm{mod/obs}} = \frac{\pi I^{\downarrow}_{\lambda,\mathrm{mod/obs}}(z_0)}{\mu_0 F^{\downarrow}_{\lambda}(z_{\mathrm{TOA}})}, \quad 1)$$

where the indices 'mod' refers to the model results and 'obs' to the observations. To consider the current position of the sun the cosine of solar zenith angle μ_0 is used along the cruise track and the incoming solar irradiance $F^{\downarrow}_{\lambda}$ at the top of atmosphere (TOA).

Examples of modeled spectral transmissivity derived with Eq. (1) are shown in Figure 1 assuming a liquid water cloud based on McBride et al. (2011), for different values of τ and two values of r_{eff} (5 μm: solid lines and 25 μm: dashed lines). The shaded areas illustrate constant values of τ. The calculations were performed for θ_0 = 40° and a surface albedo typical for ocean. For the liquid water cloud largest transmissivity occurs at values of 4 < τ < 5 and decreases with increasing τ. At wavelengths shorter than about 1100 nm scattering dominates. Larger droplets with larger asymmetry factors result in enhanced forward scattering and thus in larger transmissivity. However, with increasing r_{eff} transmissivity decreases because of increasing cloud droplet absorption at wavelengths larger than about 1400 nm. The crossover between these competing effects occurs at wavelengths between 1100 nm and 1400 nm depending on the magnitude of cloud droplet absorption (McBride et al., 2011). Especially in the wavelength region between 1560 nm and 1670 nm the differences between 5 μm and 25 μm are largest and result in an enhanced sensitivity with respect to r_{eff}.

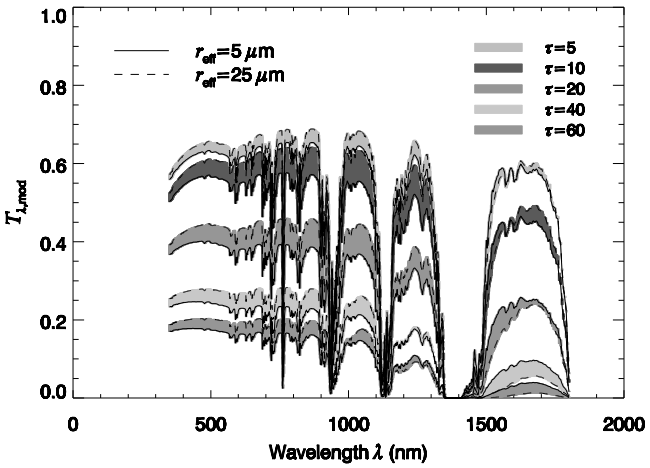

Fig. 1: Modeled spectral transmissivity for different values of r_{eff} (solid lines for r_{eff} = 5 μm, dashed lines for r_{eff} = 25 μm) and τ (gray shaded areas) at θ_0 = 40° and assuming an ocean surface albedo for a liquid water cloud according to McBride et al., (2011). Figure adopted from Brückner et al., (2014).

In this paper a new spectral cloud retrieval is proposed that uses the information of ratios of transmissivity at different wavelengths. A similar approach using ratios of reflected spectral radiances was reported for airborne measurements (Werner et al., 2013). Obviously, the wavelengths for the retrieval should exclude regions with significant molecular absorption. The systematic search for suitable wavelengths for the ratios of transmissivity was done separately for the VIS and NIR wavelength region to avoid a

mixture of the two CORAS spectrometers and resulting systematic measurement uncertainties. Furthermore, the retrieval sensitivity affected by measurement uncertainties is reduced. Not each wavelength combination is useful to provide an optimum of information to retrieve τ and r_{eff} (Coddington et al., 2012).
To retrieve τ and r_{eff}, and, additionally dealing with the ambiguity problem for transmissivity, at least three independent measurement points are required, which are sensitive to these parameters. The ratio $T_1 = T_{450} / T_{680}$ discriminates between thin and thick clouds (thin clouds transmissivity increases with τ , thick clouds vice versa), where the two ratios in the NIR wavelength region are used to retrieve r_{eff}, $T_2 = T_{1670} / T_{1560}$, and ratio $T_3 = T_{1050} / T_{1250}$ overcomes the ambiguity problem.

Figure 2 show the results of simulated ratios of transmissivity for different combinations of τ and r_{eff} for a liquid water cloud situated in 2−4 km. Isolines of constant r_{eff} (solid lines) and τ (dashed lines) are plotted. The new multi–wavelength approach circumvents the ambiguity regarding τ. The combination of three transmissivity ratios allows to ambiguously retrieve τ and r_{eff}. Adding the ratio $T_1 = T_{450} / T_{680}$ provides improved sensitivity to thin clouds. The two branches of the surface represent thick clouds, where T_2 and T_3 dominates (τ > 10), and thin clouds, where T_1 reaches values larger than 1 with decreasing τ (insert in Figures 2), while the other two ratios vary only slightly. The knee of the surface, where the two branches separate, conforms to the largest values of transmissivity and depends only slightly on θ_0.
To retrieve microphysical properties from observations the best match between the modeled and observed transmissivity is inferred by finding the minimum of a cost function $f(\tau, r_{eff})$:

$$(\tau_{retr}, r_{eff,retr}) = \min\,[\,f(\tau, r_{eff})], \quad (2)$$

with:

$$f(\tau, r_{eff}) = \sqrt{\sum_{n=1}^{3} \left[T_{n,obs} - T_{n,mod}(\tau, r_{eff})\right]^2}, \quad (3)$$

where

$$T_1 = \left(\frac{T_{450}}{T_{680}}\right); \quad T_2 = \left(\frac{T_{1670}}{T_{1560}}\right); \quad T_3 = \left(\frac{T_{1050}}{T_{1250}}\right), \quad (4)$$

which is the sum of the difference between the three observed and modeled transmissivity ratio $T_{n,obs/mod}$ for the entire range of τ and r_{eff}.

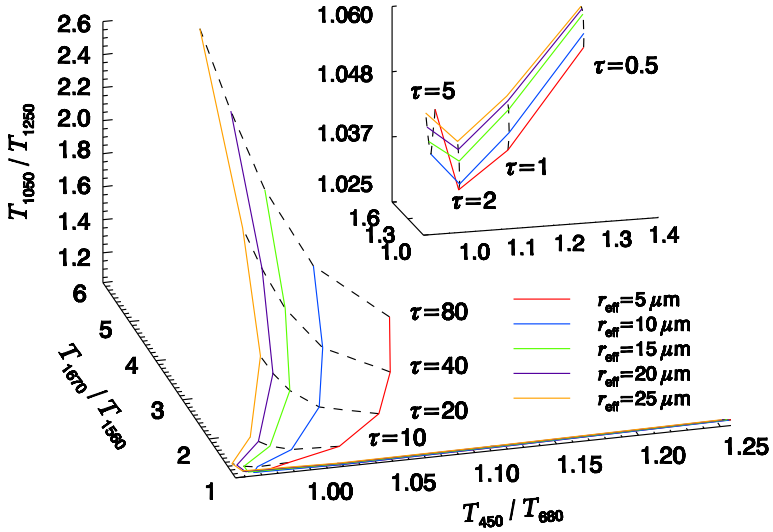

Fig. 2: Retrieval grid using modeled ratios of transmissivity for a solar zenith angle of θ_0 = 40° and an assuming ocean surface albedo. Dashed isolines represent different values of τ and colored lines indicate different values of r_{eff} for a liquid water cloud for τ > 10 with zoom into axis for thin clouds with τ < 5 in the upper right part (Brückner et al., 2014).

Case Studies

During three Atlantic transfer cruises of RV Polarstern (ANT-XXVII/4, ANT-XXVIII/5 and ANT-XXIX/1) data were collected between Cape Town (South Africa) – Bremerhaven (Germany) and Punta Arenas (Chile) – Bremerhaven (Germany), respectively. Individual case studies from the OCEANET–transects are presented to exemplify the new multi–wavelength cloud retrieval.

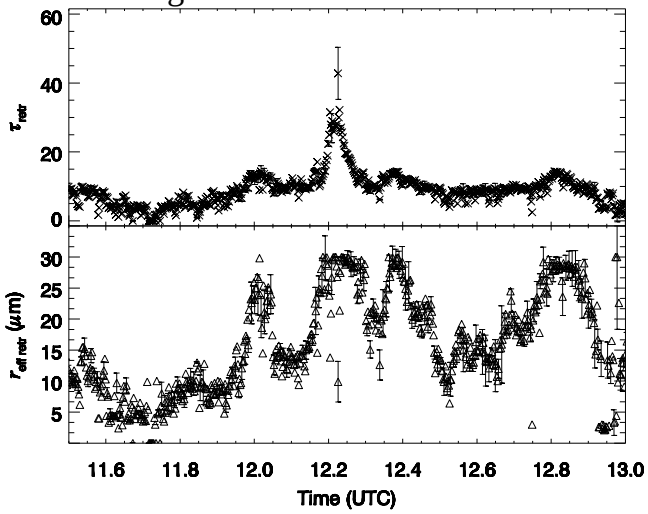

Fig. 3: Time series of τ (upper panel) and r_{eff} (lower panel), based on retrievals using data from CORAS. The distance covered in the depicted times series is about 2.8 km (Brückner et al., 2014).

A liquid water cloud was observed on November 19, 2012 around 15°S and 0°E during ANT-XXIX/1. In Figure 3 retrieval results of τ and r_{eff} are shown. The mean retrieved cloud optical thickness is 9.1 ± 0.5. The mean effective radius is 16.1 ± 1.7 μm. The retrieved r_{eff} is more variable with values ranging between 2 − 30 μm and shows higher uncertainties with up to ±7.1 μm compared to τ. Considering a threshold of an uncertainty of ±1 in τ, and according to the suggested one from McBride et al. (2011), an uncertainty of ±2 μm in r_{eff} , the new retrieval results in 87% and 78% valid retrievals for τ and r_{eff}, respectively. The uncertainty of the measurements increases for thicker clouds because the attenuation of the spectral radiance is stronger and, therefore, the contribution of the signal–to–noise ratio to the uncertainty increases. For selected time periods (e.g., between 12.2−12.3 UTC) r_{eff} reaches values up to 30 μm. Unfortunately, the simulations were limited to $r_{eff} < 30$ μm because this suffices for most non–precipitating liquid water clouds and more specifically measurement uncertainties are too high for $r_{eff} > 30$ μm. Obviously r_{eff} is larger than 30 μm but the extrapolation to larger r_{eff} is not a suitable method for these complex LUTs. Possible reasons for $r_{eff} > 30$ μm could be the presence of overlying cirrus above the low–level stratocumulus or precipitating clouds. The former can be excluded since there was no evidence of high cirrus in satellite images or atmospheric soundings for that measurements example (not shown). While the HATPRO rain sensor did not detect precipitation at the surface during the time period, it is possible that evaporating drizzle in the atmosphere cause these large r_{eff} values. Wood (2000) suggest, based on theoretical analysis and synergetic ship–based observations of low–level liquid water clouds, that drizzle droplets near the cloud base can significantly increase r_{eff} . The high variability is caused by entrainment of thermal energy and water vapor into the cloud from the sublayer below, cloud droplets can grow or evaporate in the downdrafts and thus causes the variability in the droplet effective radius.
Using the retrieved values of τ and r_{eff}, the liquid water path (LWP) is calculated. LWP is approximated using the following equation where ρ is the density of liquid water, with:

$$LWP = \frac{5}{9} \cdot \rho \cdot \tau \cdot r_{\text{eff}} \quad . \quad 5)$$

Wood and Hartmann (2006) determined the LWP for adiabatic clouds where the liquid water content increases linearly with altitude above cloud height.

A comparison between the retrieved LWP from the microwave radiometer HATPRO and the LWP retrieved from the spectral transmissivity measurements is presented in Figure 4a for November 19, 2012. For the analyzed time period the mean LWP and standard deviation was 87 ± 49 gm^{-2} for HATPRO and 97 ± 11 gm^{-2} for the spectral cloud retrieval. CORAS overestimates the LWP for values > 80 gm^{-2} but underestimates the LWP for values < 80 gm^{-2} compared to HATPRO which is shown in the scatter plot in Figure 4b. The black dashed line is the one–to–one line. The uncertainty of the spectral radiance measurements increases in thicker clouds and, therefore, the number of valid retrievals decreases. Larger values of retrieved r_{eff} cause an overestimation of CORAS derived LWP. However, drizzle–sized droplets can lead to a wrong estimate of the liquid water distribution and, therefore, lead to an overestimation of LWC in the microwave radiometer retrievals (Löhnert et al., 2001). Furthermore, deviations in the CORAS LWP

retrieval might come from the approximation of the plane–parallel cloud model in the radiative transfer model. Boers et al. (2006) suggested a sub–adiabatic cloud model which parametrizes the vertical variation of cloud optical and microphysical properties. In this cloud model τ and r_{eff} are explicit functions of the geometrical thickness z and the droplet number concentration N of the cloud. The major source of uncertainty in the LWP retrieval is the sub–adiabatic behavior of the cloud, which is described as the sub–adiabatic fraction *Fr*. Due to turbulent entrainment and mixing processes in the cloud, *Fr* typically ranges between 0.3−0.9 (Boers et al., 2006). For oceanic clouds Boers et al. (1998a) found a typical value of $Fr = 0.6$. The shape of the vertical LWC profile varies between a linear and a C–shaped profile and is characterized by factor α, which determines the vertical weight of the liquid water distribution for a given value of *Fr* (Boers et al., 2006). The smaller the value of α, the closer the LWC profile approaches linearity. For a given τ and r_{eff} the deviation from adiabatic clouds ($Fr = 1$) lead to an increase of geometrical thickness of the cloud but a decrease in cloud base droplet number concentration. To quantify the influence of different cloud models on the retrieved cloud properties, further investigations based on satellite or synergetic observations are needed.

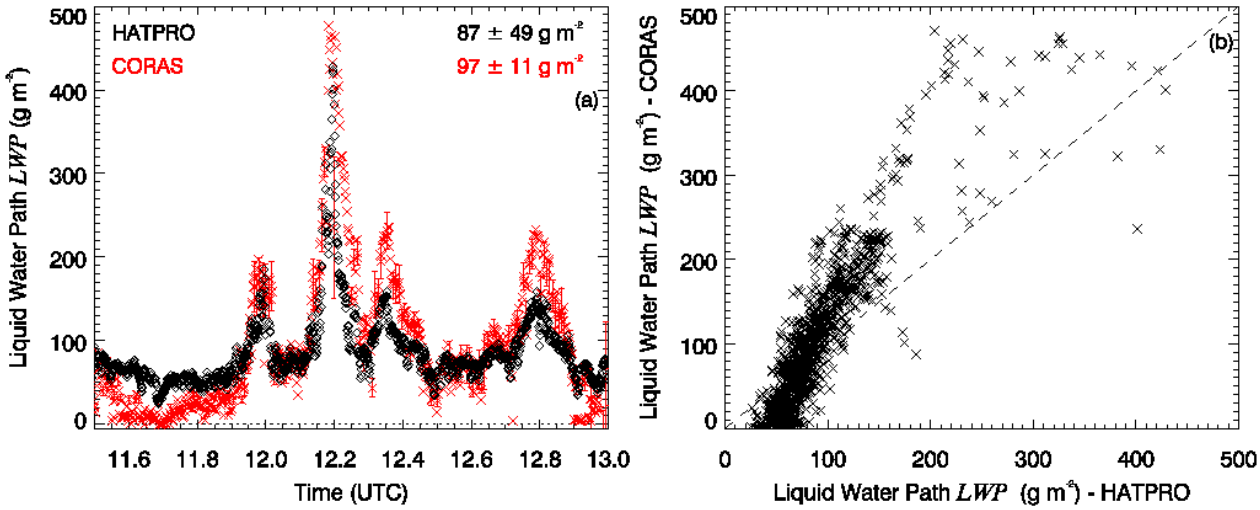

Fig. 4: (a) Time series of LWP as retrieved from HATPRO (black diamonds) and CORAS (red crosses) data at 11.5 - 13.0 UTC on November 19, 2012 around 15°S and 0°E from ANT-XXIX/1.(b) Scatter plot of the retrieved LWP from HATPRO and CORAS (Brückner et al., 2014).

The comparison of the retrieval methods by McBride et al. (2011), hereafter named the slope method, and the multi–wavelength method are shown in Figure 6 for a time period from November 14, 2012 around 0°N and 11°E from ANT-XXIX/1. During this period low–level boundary layer clouds with a cloud base height of about 1 km were observed which is shown in the time series of backscatter coefficient from ceilometer data (Figure 5d). The geometrical thickness of the cloud ranges between 500−800m. Cloud top heights were lower than the freezing level obtained from atmospheric sounding indicating a liquid water cloud. Ceilometer, as well as the lidar did not detect higher level cirrus. In Figure 5a–b the retrieval of τ and r_{eff} from the new multi–wavelength method (red symbols) and

the slope method (blue symbols) is presented. The retrieved τ from both methods show similar results with mean values of 16.3 and 14.3 for the multi–wavelength and slope method, respectively. The mean difference between both approaches is 2.5 for the entire time series, while the differences in r_{eff} are larger with a mean difference of 4.4 μm. The multi–wavelength method retrieves smaller values of r_{eff} with 14.0 μm compared to 17.0 μm from the slope method. But in general, the agreement is within the uncertainties of the retrieved cloud properties from both methods. This is also evident in the time series plot of HATPRO LWP and the derived LWP shown in Figure 5c. Both retrievals match the LWP observations from the microwave radiometer, except the later period where it starts to rain. Only around 8.6–8.68 UTC, the LWP derived from the multi–wavelength method matches more closely the LWP from HATPRO, because the slope method retrieves larger values of τ. Mean values of LWP and standard deviations are 139.8 ± 26.3 gm^{-2} for HATPRO, 126.9 ± 10.6 gm^{-2}, and 142.5 ± 17.7 gm^{-2} for the multi–wavelength and slope method, respectively.

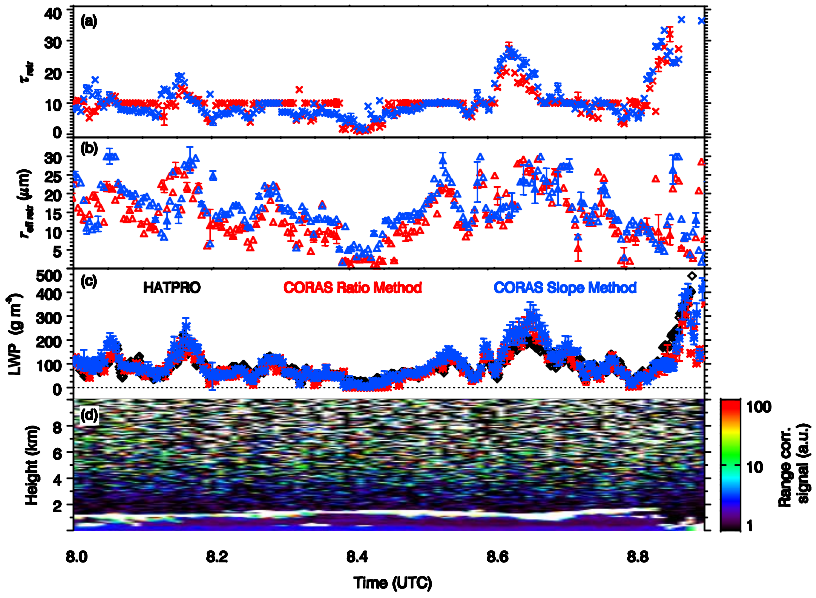

Figure 5: Time series of τ (a) and r_{eff} (b) at 8.0 - 9.0 UTC on November 14, 2012 around 0°N and 11°E from ANT-XXIX/1, based on two retrieval methods using data from CORAS. Retrieval results from the new multi–wavelength method are shown with red symbols, results from the slope method by McBride et al. (2011) in blue symbols. (c) Time series of LWP as retrieved from HATPRO (black diamonds), CORAS with multi–wavelength method (red crosses) and CORAS with slope method by McBride et al. (2011) (blue crosses). (d) Time series of vertical backscatter coefficient in arbitrary units (a.u.) obtained from ceilometer. The distance covered in the depicted times series is about 18 km (Brückner et al., 2014).

The uncertainties of τ, r_{eff}, and LWP from the multi–wavelength and slope methods along the time series from November 14, 2012 are shown in Figure 6. The retrieval uncertainty thresholds of ±1 in τ , and ±2 μm in r_{eff} are plotted with black dashed lines in Figure 6a,b. The uncertainties of the slope method were calculated as reported by McBride et al. (2011), but using the measurement uncertainty of CORAS spectrometers of 5.1% in the VIS wavelength region and 2.2% uncertainty in normalized transmissivity used for the spectral slope fit. Uncertainties of LWP were calculated using error propagation of uncertainties of τ and r_{eff} from both methods. As shown in Figure 6a, the multi–wavelength method does not significantly reduce the uncertainty in τ, since both methods (valid retrieval multi–wavelength method: 82%; valid retrievals slope method: 78%) stay below the threshold. Uncertainties increase around 8.18 UTC and 8.6 UTC as τ increases for both methods. Due to the use of ratios of transmissivity, the uncertainty in r_{eff} is significantly reduced for the multi–wavelength method. 80% of the retrievals passes the 2 μm threshold, whereas 66% valid retrievals were observed for the slope method. Uncertainties in r_{eff} under thicker clouds are reduced, which is also obvious in the LWP uncertainty shown in Figure 6c.

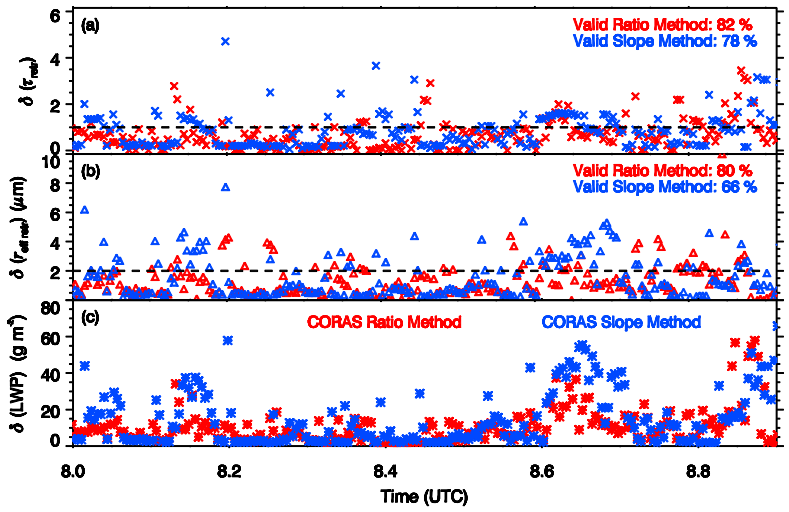

Figure 6: Time series of calculated uncertainties of (a) τ , (b) r_{eff}, and (c) LWP at 8.0 - 9.0 UTC on November 14, 2012 around 0°N and 11°E from ANT-XXIX/1. Uncertainties from the new multi–wavelength method are shown with red symbols, uncertainties from the slope method by McBride et al. (2011) in blue symbols. Black dashed lines in (a) and (b) shows the uncertainty threshold of 1 in τ, and 2 μm in r_{eff} used to define valid retrievals (Brückner et al., 2014).

Summary and Conclusions

The retrieval of optical thickness τ and droplet effective radius r_{eff} of clouds using observed and simulated spectral zenith radiances requires a different treatment of physical principles compared to the well–known reflectivity–based counterpart as performed by satellites and aircraft measurements. However, zenith radiances which can be converted to spectral transmissivity contains relatively less information on r_{eff} compared to reflectivity. Due to competing effects of cloud droplet absorption and forward scattering, the sensitivity to this parameter is reduced. Furthermore, transmissvity is not a unique function of τ, which causes retrieval ambiguities. Existing transmissvity–based cloud retrievals already achieved reasonable results for τ ranging from 10 to 40, however, large uncertainties remain for optically thin clouds with $\tau < 5$. Also the sensitivity to r_{eff} could be enhanced by using spectral features of asymmetry factor and spectral coalbedo within the NIR spectral wavelength region. To infer microphysical properties from spectral transmissivity measurements, simulated zenith radiances were calculated using a plane–parallel (1D) radiative transfer model. In this paper a new cloud retrieval using ratios of spectral cloud transmissivity is introduced. The six–wavelength approach uses the information of three ratios of spectral transmissivity (wavelength combinations: 450 nm/680 nm, 1050 nm/1250 nm, 1670 nm/1560 nm) to retrieve simultaneously cloud optical thickness and effective radius. The combination of these transmissivity ratios overcomes the limitations of existing retrievals concerning thin liquid water clouds ($\tau < 5$). Furthermore, the retrieval ambiguity with regard to τ is circumvented by separating very thin and thick clouds. Using ratios of transmissivity in certain wavelength regions, reduces the measurement uncertainties significantly compared to methods using absolute values. The multi–wavelength method benefits from the spectral features of zenith radiance depending on the scattering and absorption properties from liquid water droplets and ice crystals and thus is applicable to liquid water and ice clouds. The retrieval is fast and accurate and thus suitable for operational purposes and the huge variety of measurements obtained during three cruises. Compared to the slope method by McBride et al. (2011), the computational time was reduced by a factor of 15.

The spectral cloud retrieval was applied to observations on board of RV Polarstern during three Atlantic transfers of the OCEANET–project. Primarily, the new cloud retrieval was applied to homogenous water clouds. For the presented case study of a homogenous liquid water cloud the mean τ and r_{eff} were calculated with 9.1 ± 0.5 and 16.1 ± 1.7 μm, respectively. The variability of r_{eff} is caused by complex mixing of thermal energy and water vapor from layers above and beneath the cloud. Larger variability in the r_{eff} retrieval occur for thicker clouds when zenith radiance is more attenuated. Considering an uncertainty threshold of ± 1 in τ and ± 2 μm in r_{eff}, the new multi–wavelength retrieval results in 87% and 78% valid retrievals for τ and r_{eff}, respectively. Measurement uncertainties increase for thicker clouds ($\tau > 40$) as the attenuation of spectral radiance is increased. For a number of measurements r_{eff} reaches values up to 30 μm which represents the upper retrieval limit. Possible reasons for cloud particles with $r_{eff} > 30$ μm were discussed. In warm marine stratocumulus clouds a large number of drizzle droplets near the cloud base was found which can significantly increase r_{eff} and could explain these

observations reported here. From the retrieved microphysical properties the LWP was calculated using an adiabatic approximation where r_{eff} increases above the cloud base height. The comparison with the LWP from microwave radiometer HATPRO shows an overestimation of the LWP by CORAS for clouds with LWP > 80 gm^{-2} and an underestimation for values of LWP < 80 gm^{-2}. Due to the increased attenuation of spectral zenith radiance in optical thick clouds, the CORAS retrieval results are larger and associated with larger uncertainties. For the analyzed homogeneous cloud scene a mean LWP of 87± 49 gm^{-2} for HATPRO and 97±11 gm^{-2} for CORAS was derived.
A comparison between the new multi–wavelength cloud retrieval and the slope method (McBride et al., 2011) yields similar results for τ and r_{eff}, while the mean temporal deviation for τ was smaller (2.5) than for r_{eff} (4.4 μm). Both methods exhibit good agreement with the HATPRO LWP retrieval. Propagating the measurement uncertainties through both approaches, it was found that the multi–wavelength retrieval slightly reduce the uncertainties with regard to τ (slope method: 78%, multi–wavelength method: 82%) considering an uncertaintiy threshold of ±1, and significantly reduce the r_{eff} uncertainties. 80% of the retrievals passes the uncertainty threshold (±2 μm), whereas only 66% valid retrievals were obtained with the slope method. In conclusion, the new multi–wavelength retrieval yields comparable values of τ and r_{eff} with regard to the existing slope method, but reduces the retrieval uncertainties by using ratios instead of absolute values. In conjunction with the notable reduction of the computational time, this method is more suitable for the observations on the ship and more adjustable to different cloud scenes, in particular for clouds with $\tau < 5$.

Acknowledgments

The author thank the scientist and crew from the RV Polarstern and the Alfred Wegener Institute for Polar and Marine Research (AWI) for their permanent support and the opportunity to perform measurements during the Atlantic transfer cruises ANT-XXVII/4, ANT-XXVIII/5 and ANT-XXIX/1.

References

Althausen, D., Engelmann, R., Baars, H., Heese, B., Ansmann, A., Müller, D., and Komppula, M.: Portable Raman lidar PollyXT for automated profiling of aerosol backscatter, extinction, and depolarization, J. Atmos. Oceanic Techno. 26, 2366–2378, doi:10.1175/2009JTECHA1304.1, 2009.

Boers, R., Jensen, J. B., and Krummel, P. B.: Microphysical and radiative structure of marine stratocumulus clouds over the Southern Ocean: Summer results and seasonal differences, Q.J.R. Meteorol. Soc., 124, 151–168, 1998a.

Boers, R., Acarreta, J. R., and Gras, J. L.: Satellite monitoring of the first indirect aerosol effect: Retrieval of the droplet concentration of water clouds, J. Geophys. Res., 111, D22 208, DOI: 10.1029/2005JD006838, 2006.

Brückner, M., Pospichal, B., Macke, A., and Wendisch, M.: A new multispectral cloud retrieval method for ship-based solar transmissivity measurements, J. Geophys. Res. Atmos., 119, 1–17, DOI: 10.1002/2014JD021775, 2014.

Brückner, M.: Retrieval of optical and microphysical cloud properties using ship-based spectral solar radiation measurements over the Atlantic ocean, PhD Thesis, University of Leipzig, 2015.

Chiu, J. C., Marshak, A., Huang, C.-H., V´arnai, T., Hogan, R. J., Giles, D.M., Holben, B. N., O'Connor, E. J., Knyazikhin, Y., and Wiscombe, W. J.: Cloud droplet size and liquid water path retrievals from zenith radiances measurements: examples from the Atmospheric Radiation Measurements Program and the Aerosol Robotic Network, Atmos. Chem. Phys., 12, 10 313–10 329, DOI: 10.5194/acp-12-10313-2012, 2012.

Coddington, O., Pilewskie, P., and Vukicevic, T.: The Shannon information content of hyperspectral shortwave cloud albedo measurements: Quantification and practical applications, J. Geophys. Res., 117, D04 205, DOI: 10.1029/2011JD016771, 2012.

Kalisch, J. and Macke, A.: Estimation of the total cloud cover with high temporal resolution and parameterization of short-term fluctuations of sea surface insulation, Meteorol. Z. 17, 603-611, 2008.

Kikuchi, N., Nakajima, T., Kumagai, H., Kuroiwa, H., Kamei, A., Nakamura, R., and Nakajima, T. Y.: Cloud optical thickness and effective particle radius derived from transmitted solar radiation measurements: Comparison with cloud radar observations, J. Geophys. Res., 111, D07 205, DOI: 10.1029/2005JD006363, 2006.

LeBlanc, S. E., Pilewskie, P., Schmidt, K. S., and Coddington, O.: A generalized method for discriminating thermodynamic phase and retrieving cloud optical thickness and effective radius using transmitted shortwave radiance spectra, Atmos. Meas. Tech. Discuss., 7, 5293–5346, DOI: doi:10.5194/amtd-7-5293-2014, 2014.

Löhnert, U., Crewell, S., Simmer, C., and Macke, A.: Profiling cloud liquid water by combining active and passive microwave measurements with cloud model statistics, J. Atmos. Oceanic Technol., 18, 1354–1366, 2001.

Macke, A., Kalisch, J., Zoll, Y., and Bumke, K.: Radiative effects of the cloudy atmosphere from ground and satellite based observations, EPJ Web of Conferences 9, 83-94, 2010.

Mayer, B. and Kylling, A.: Technical note: The libRadtran software package for radiative transfer calculations – description and example of use, Atmos. Chem. Phys. 5, 1855-1877, 2005.

McBride, P. J., Schmidt, K. S., Pilewskie, P., Kittelman, A. S., and Wolfe, D. E.: A spectral method for retrieving cloud optical thickness and effective radius from surfacebased transmittance measurements, Atmos. Chem. Phys., 11, 7235–7252, DOI: 10.5194/acp-11-7235-2011, 2011.

McBride, P. J., Schmidt, K. S., Pilewski, P., Walther, A., Heidinger, A. K., Wolfe, D. E., Fairall, C.W., and Lance, S.: CalNex cloud properties retrieved from ship-based spectrometer and compariosions with satellite and aircraft retrieved cloud properties, J. Geophys. Res., 117, D00V23, DOI: 10.1029/2012JD017624, 2012.

Nakajima, T. and King, M.: Determination of the optical thickness and effective particle radius of clouds from reflected solar radiation measurements. Part I: Theory, J. Atmos. Sci., 47, 1878–1893, 1990.

Platnick, S.: Vertical photon transport in cloud remote sensing problems, J. Geophys. Res., 105, 22 919–22 935, 2000.

Platnick, S., King, M., Ackerman, S., Menzel, W., Baum, B., Riedi, J., and Frey, R.: The MODIS cloud products: Algorithms and examples from TERRA, IEEE Trans. Geosci. Remote Sens., 41, 459–473, 2003.

Rawlins, F. and Foot, J. S.: Remotely sensed measurements of stratocumulus properties during FIRE using the C130 aircraft multi-channel radiometer, J. Atmos. Sci., 47, 2488– 2504, 1990.

Rossow, W. and Schiffer, R.: ISCCP cloud data products, Bull. Amer. Meteorol. Soc., 72, 2–20, 1991.

Werner, F., Siebert, H., Pilewskie, P., Schmeissner, T., Shaw, R. A., and Wendisch, M.: New airborne retrieval approach for trade wind cumulus properties under overlying cirrus, J. Geophys. Res. Atmos., 118, 3634–3649, DOI: 10.1002/jgrd.50334, 2013.

Wood, R.: Stratocumulus clouds, Mon. Wea. Rev., 140, 2373–2423, 2012.

Wood, R. and Hartmann, D. L.: Spatial variability of liquid water path in marine low cloud: The importance of mesoscale cellular convection, J. Climate, 19, 1748–1764, 2006.

Zoll, Y.: Bestimmung des Flüssigwasserpfades auf See mit Hilfe der passiven Mikrowellenradiometrie, Ph.D. Thesis, Christian-Albrechts-University of Kiel, 2012.

Power curves of whole wind farms under real operating conditions

Armin Raabe[1], Robert Wagner[1], Janek Zimmer[2]

[1]*Leipzig Institute for Meteorology (LIM), University Leipzig, Germany*
[2]*Engineering Consultancy Load and Energy Management Leipzig (LEM), Germany*

Summary

The time-variable production of wind energy must be included into the time-variable energy consumption schemes. This interactive process depends on a precise prediction of weather conditions, particularly of the wind speed (u), and knowledge of the behavior of the consumers. Parallel to the wind speed prediction the wind energy production depends on the technical parameter of the wind turbines, e.g. characterized by a power curve $p(u)$. As we show here, the power curve of a wind farm, consisting of a number of wind turbines, and an individual power curve of a single wind turbine are different. To systematize the relation between wind speed and energy production the power curve is here approximated using an analytic function. This function fits in our case the predicted wind speed with the predicted or actual energy production of a wind farm. Using this function the behavior of wind farms under real operation conditions are shown. The potential of these wind farm power curves are discussed. These curves are used for the power prediction in a power forecast system based on a neural network. The neural network uses the analytic function to systematize the energy output of the wind farms under different wind field conditions. These analytic power curves are helpful tools to characterize the behavior of a wind farm in a good agreement with the measured power output. Additionally, the analysis of some wind parks shows great differences in the expected power output, depending on the wind direction, the position of each wind turbine and the location of the wind farms in their surroundings.

Zusammenfassung:

Die zeitlich variable Produktion von Windenergie muss in das zeitlich variable Energienutzungsverhalten integriert werden. Dieser Wechselwirkungsprozess schließt eine präzise Wettervorhersage, speziell der Windgeschwindigkeit, und die Kenntnis des Verhaltens der Konsumenten ein. Neben der Windfeldvorhersage hängt die Windenergieproduktion auch von den technischen Parametern der Windenergieanlagen ab, die durch eine Leistungskurve $p(u)$ charakterisiert werden kann. Hier wird gezeigt, dass sich die Leistungsabgabe ganzer Windparks von denen einzelner Anlagen stark unterscheidet. Um diesen Zusammenhang zwischen Windgeschwindigkeit und Energieproduktion zu systematisieren, werden hier die Leistungskurven durch eine analytische Funktion approximiert. Diese Funktion stellt in unserem Fall einen

Zusammenhang zwischen der prognostizierten Windgeschwindigkeit und der prognostizierten bzw. tatsächlich eingetretenen Energieproduktion her. Mit dieser Funktion wird das Verhalten von Windparks unter realen Betriebsbedingungen gezeigt. Zusätzlich wird das Potenzial der Windpark-Leistungskurven diskutiert. Diese Kurven werden für die Leistungsvorhersage in einem Energieprognosesystem auf Basis eines neuronalen Netzes verwendet. Das neuronale Netz nutzt die analytische Funktion, um den Energieertrag der Windparks unter verschiedenen Windfeldbedingungen zu systematisieren. Die Analyse einiger Windparks zeigt große Unterschiede zwischen der erwarteten Ausgangsleistung in Abhängigkeit von der Windrichtung, von der Position jeder Windkraftanlage und der Lage des Windparks in seiner Umgebung.

1. Introduction / Motivation

The part of wind power plants at the electricity market increases year by year and the operators of the electricity networks need a more accurate forecast of this highly variable power production for a better management of the electricity market and to reduce the number of necessary reserve power plants (Klobasa and Obersteiner, 2006). Therefore, it's necessary to reduce the forecast error. This can be achieved on different ways. One option is the improvement of numerical weather prediction (NWP) models and their better modification to the application in the wind power forecast. This will happen probably in some years together with the ongoing improvement in the computer capacity. Another maybe less burdensome way to improve the prognosis quality is a better knowledge about the behavior of the wind turbines in a complex wind farm.

As is well known, the power production of each wind turbine is related to the wind velocity by their individual power curve. These power curves are known mostly very precisely because they have to be determined for every different type of wind turbines before commissioning. The determination of the power curves is prescribed explicit in the engineer standard ICE 61400-12-1 (ICE, 2005). This process includes a lot of detail requirements like the positioning of a meteorological mast for the measurement of the wind speed and wind direction near the wind turbine, the calibration of the associated anemometers and other things (for further details see ICE 61400-12-1). In addition, the surrounding conditions of the test field are regulated by the standard; it demands a free and undisturbed wind field around the wind turbine (Mellinghoff, 2013). Due to all these requirements the determination of such a power curve is very expensive and time-consuming. An isolated location of the tested wind turbine, which is demanded by the standard, is not the case in practice where often many wind turbines, frequently in addition different types, standing together in big wind farms. So every wind turbine shows an individual behavior. Additionally, obstacles in the surrounding area could affect the regional wind field (Milan et al., 2013). Thus, the operating conditions differ dramatically from the test conditions and an individual wind power plant executes a lot

of interactions with neighboring wind turbines and the surrounding area. This tends to result in a difference between the real and the tested power curves, which can be a source of wrong power predictions despite wind energy appraisals.

Furthermore, it can be noticed that virtually no wind farm resembles another one. Hence, it is nearly impossible to describe the behavior and power performance of every single wind turbine in such a complex configuration. However, the power output of each single wind turbine is quite uninteresting for the most fields of application because usually the whole wind farm is connected to only one electric power transformation substation. Thus, the launched power is a superposition of the individual performance of all single wind turbines. All this leads to the fact that network operators are only interested in the power production of the whole wind park and the individual power curve of a single wind turbine is not essential. Therefore, we create an alternative form of a so called analytic power curve which can describe the behavior of a whole wind farm with the aim to improve the numerical wind power forecast, especially that with neural networks.

2. The analytic power curve model

The relationship between wind velocity and power output of a wind turbine is associated with a power curve. Usually, these power curves show in the range of 3 to 12 m/s an increase in the power output following the dependence on the wind velocity to the power of three (u^3) until the maximum installed power is reached. Compared to this, the power curve of a whole wind farm is in principle similar, but their slope is much smoother, resulting from shadowing effects. The aim of this work was the derivation of an analytic function, which can describe the observed power output of whole wind farms as a function of the wind velocity as accurately as possible. For this we have adapted a sigmoid function in the following form

$$\frac{P(u)}{P_{\max}} = \left[\exp\left(\frac{u_0 - u}{L_u} \right) + 1 \right]^{-1} \qquad (1)$$

with the produced power $P(u)$ depending on the wind velocity u and P_{max} as the maximum installed power of the whole wind farm. Additionally, there are two individual constants u_0 and L_u, which differ according to the examined wind farm. In this case, L_u represents the slope and u_0 the turning point of the function $P(u)$. Both parameters, L_u and u_0 must be selected individually by a numerical algorithm. An example of such a power curve is shown in Fig. 1. The replacement power curve according to TR5 FGW (FGW, 2013) follows an “ideal” function $P(u^3)$. The power curve of an individual wind turbine is close to this function, whereas the power curve of a wind farm differs from the individual power curve, but can be approximated by use of eq. (1).

One advantage of these analytic power curves is the closer concordance to the real performance of a wind farm compared to the sum of single wind turbines. This fact can be used for a better wind power prediction because the analytic power curve can consider the highly complex interaction between the single wind turbines and the impacts resulting from the environment in an easy way.

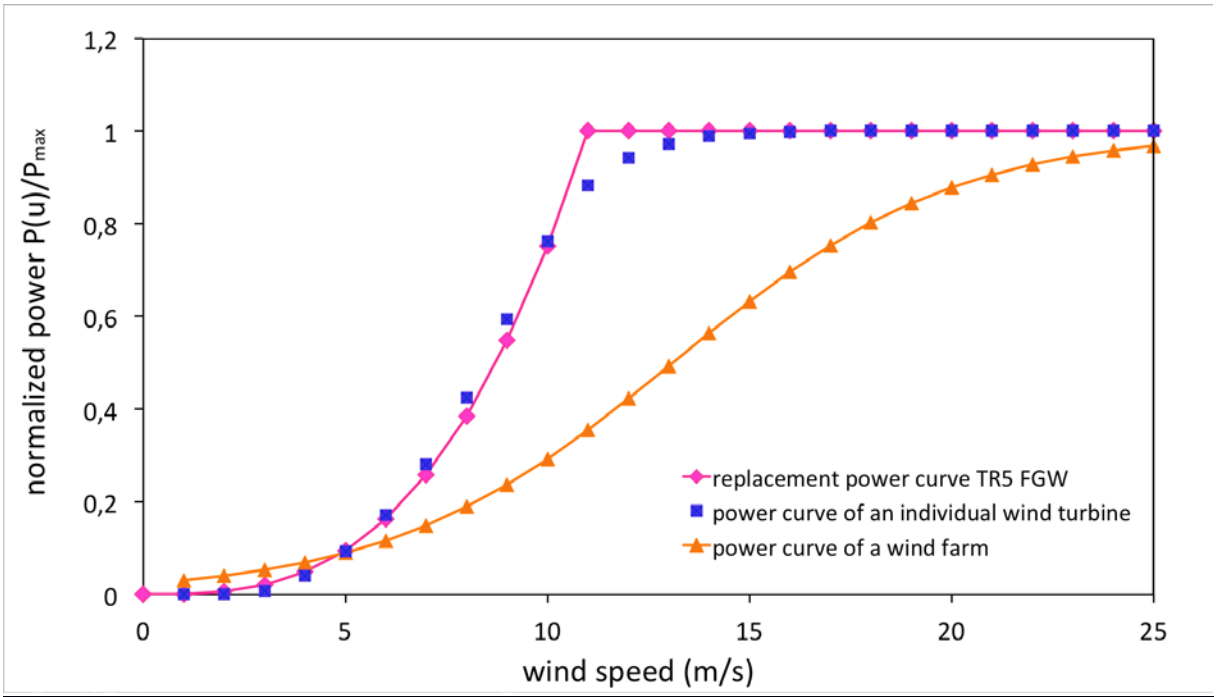

Figure 1: *An example of the difference between the power curves of a single wind turbine and a power curve as realized by a wind farm (see Fig. 4).*

3. Data and properties of analytic wind farm power curves

The following analysis is based on predicted wind speeds. This is caused by a lack of observed wind speed data at the locations of the wind farms, which could be used for the determination of a connection between power and wind speed like in a measured power curve.

For an examination of the analytic power curves we investigate four different wind farms in Northern and Eastern Germany, which can be described below for legal reasons only as wind farm 1, 2, 3 and 4 (WF1-WF4). The used datasets comprise the meteorological variables of NWP models (time – 6h) and the predicted power output as well as the effectively measured power output (data from 2011 and 2012). The underlying NWP models are WRF (Skamarock et al., 2008) and UKMO (Met Office UK, 2015). These are tuned to predict the wind speed for the hub height of each wind turbine, which is installed in the wind farm.

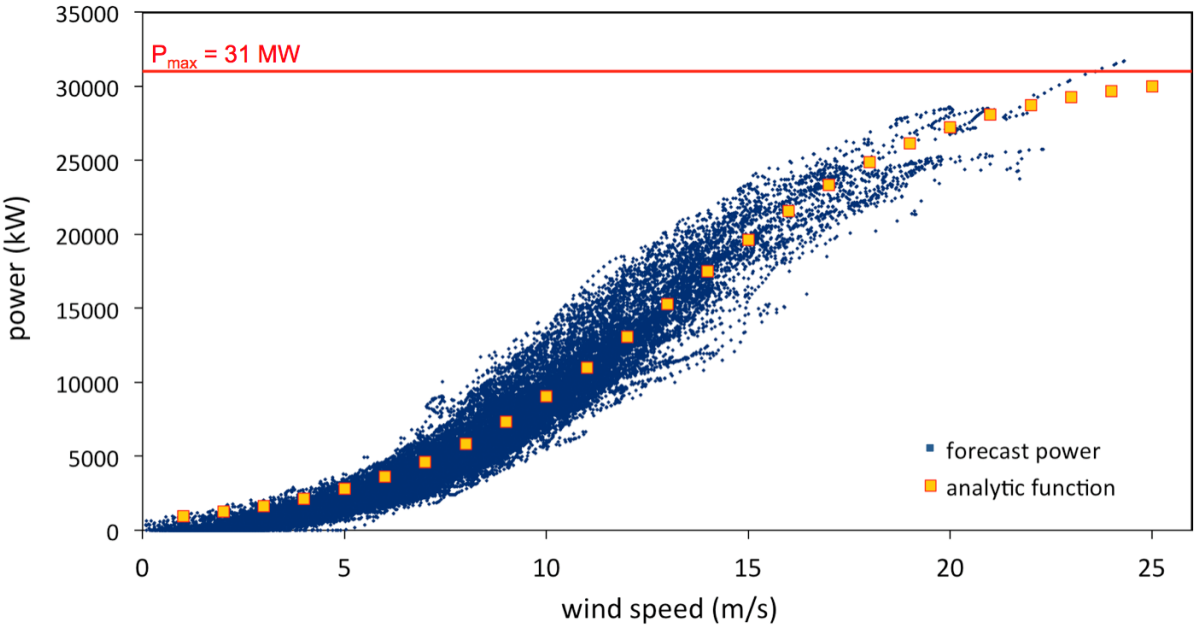

Figure 2: *Forecast of the power output of a wind farm (WF1) with an installed power of 31 MW (red line) using a neural network basing on the Time-6h predicted wind speed (blue dots). The yellow dots represent the mean analytic power curve of this wind farm with the found parameters* $L_u = 3{,}6$ *and* $u_0 = 13{,}3$.

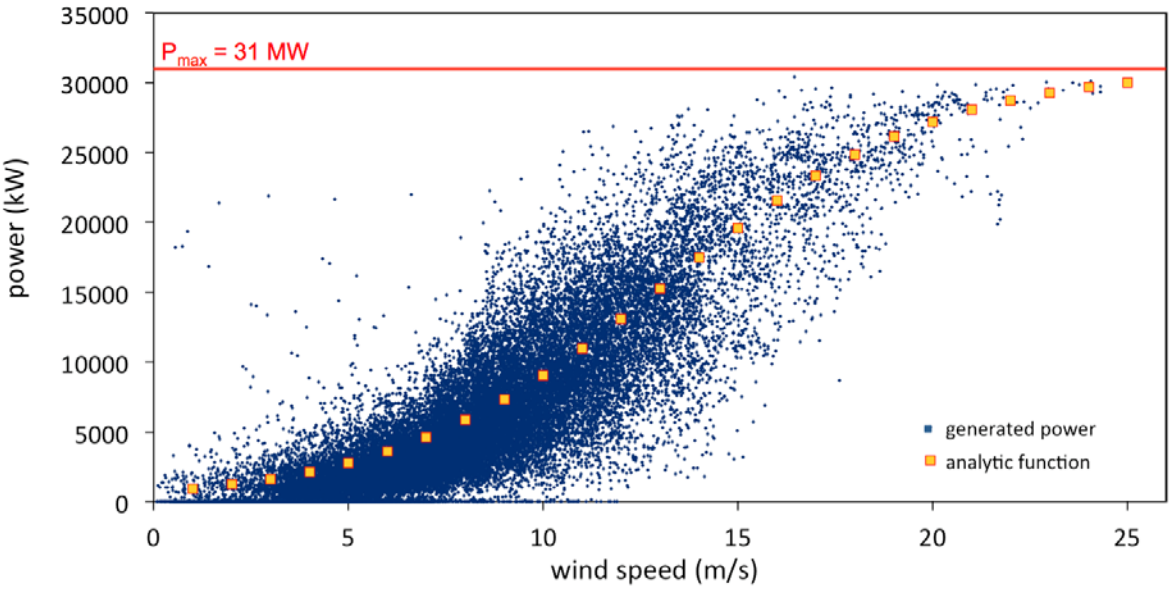

Figure 3: *Comparison of the generated power of WF1 and the Time-6h predicted wind speed.*

First, we adjust equation (1) for the predicted power output of single wind farms versus the predicted wind speed. An example of this is shown in Fig. 2. The small blue dots represent the variance of the predicted power output of wind farm WF1 versus the predicted wind speed for the selected period of two years. The related mean analytic power curve is reflected by the curve with the yellow dots.

It can be seen that this curve lies near of the center of the scatter plot (wind speed > 5m/s), which indicates in first instance a useful result. Figure 3 shows the observed power in comparison to the predicted wind speed. The single points of the generated power are arranged around the analytic function, which is characterized by the two parameters u_0 and L_u. The relatively broad range of deviation indicates that not only the wind velocity drives the power output but also the wind direction. For a precise wind power prediction this fluctuation range is might be too large and therefore it is necessary to consider more details than just the wind velocity in forecast models.

With the method described above, the parameters of the analytic function are determined for three different wind farms (see Tab. 1). Each wind farm can be described by its own analytic power curve, which differ more or less from that curve which represents a single wind turbine (Fig. 4).

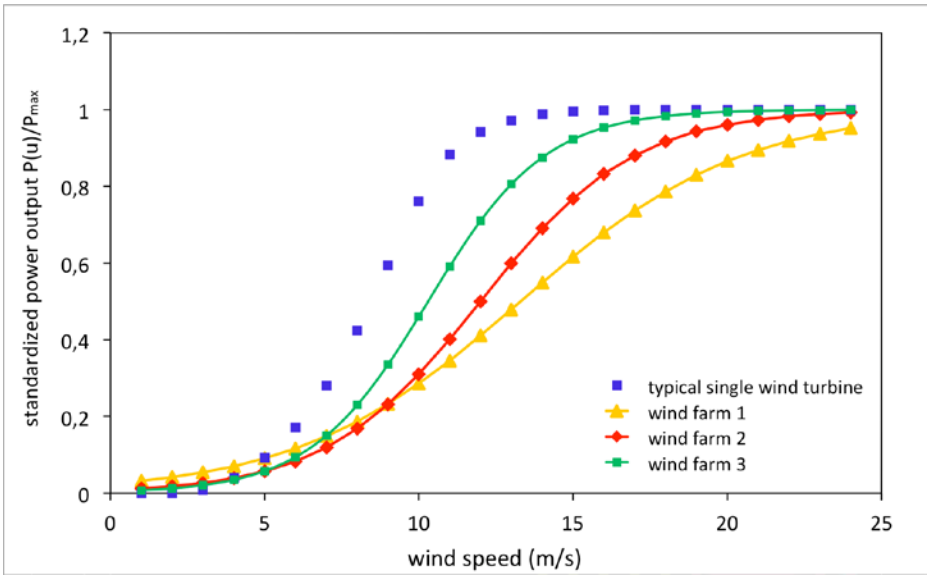

Figure 4: *Analytic power curves of different wind farms compared to that of a single wind turbine. Note that the power output is standardized to the maximum installed power of each wind farm or wind turbine respectively.*

Another advantage of these analytic power curves is their simple adjustment on different environment conditions. Thus, it is not only possible to adjust these curves to different wind farms, but also to different operation conditions of the same farm. This flexibility can help to improve the quality of power predictions. Therefore, we analyze in a next step the power output for all of our example wind farms according to the wind direction, because it can strongly affect the efficiency of a wind farm by shadowing effects. Reasons for that could be obstacles in the surrounding area or the placement of the wind turbines to each other, which is typically optimized only for the main wind direction at the corresponding location (Kiranoudis et al., 2001).

Table 1: *Overview of the computed values of the parameters L_u and u_0 for the analytic power curves of three wind farms. The analysis was executed both for all wind directions together and for a separation into sectors of 90 degree.*

wind farm	wind direction	u_0 (m/s)	L_u (m/s)
WF1 (P_{max} = 31MW)	all	13.8	3.6
	north	12.8	3.3
	east	14.7	4.5
	south	13.4	3.7
	west	13.1	3.4
WF2 (P_{max} =13MW)	all	12.0	2.5
	north	11.7	2.3
	east	11.4	2.1
	south	11.9	2.6
	west	12.1	2.4
WF3 (P_{max} =10 MW)	all	10.3	1.9
	north	9.9	1.9
	east	11.2	2.0
	south	10.5	1.9
	west	10.0	1.9

For this analysis, we split up the power output by wind directions, more precisely into four sections of 90 degree (North: 315-45°, east: 45-135°, south: 135-225° and west: 225-315°) and adjust equation (1) for every sector of flow direction. The results with the values found for the parameters u_0 and L_u are shown in Tab. 1. It can be seen that there are great spreads between the different wind farms among themselves on the one hand and also within the wind farms by separation into flow directions on the other hand. The differences inside the wind farms are considerable and a utilization of the analytic power curve only for all wind directions together will possibly lead to a noteworthy prediction error. This problem is illustrated once more in detail in the following Fig. 5, where the impact of the flow direction on the power output is shown at the example of WF1. To obtain a better comprehensibility, the analytic power curves of each wind direction were plotted as a difference from the mean analytic power curve, which represents the behavior of the wind farm for all wind directions together. In Fig. 5 can be clearly seen that the power output of WF1 varies depending on the flow direction up to 3500 kW, which corresponds to over 10 percent of the installed capacity (31 MW). In this case, the output is reduced strongly for an easterly flow and less severe for a southerly flow, whereas the wind farm shows an above-average power production for westerly and northerly winds. This leads to the recognition that the wind farm was designed in an advantageous way because east and south winds are far less frequent and strong then northerly and westerly winds at the location of this wind farm in Northern Germany.

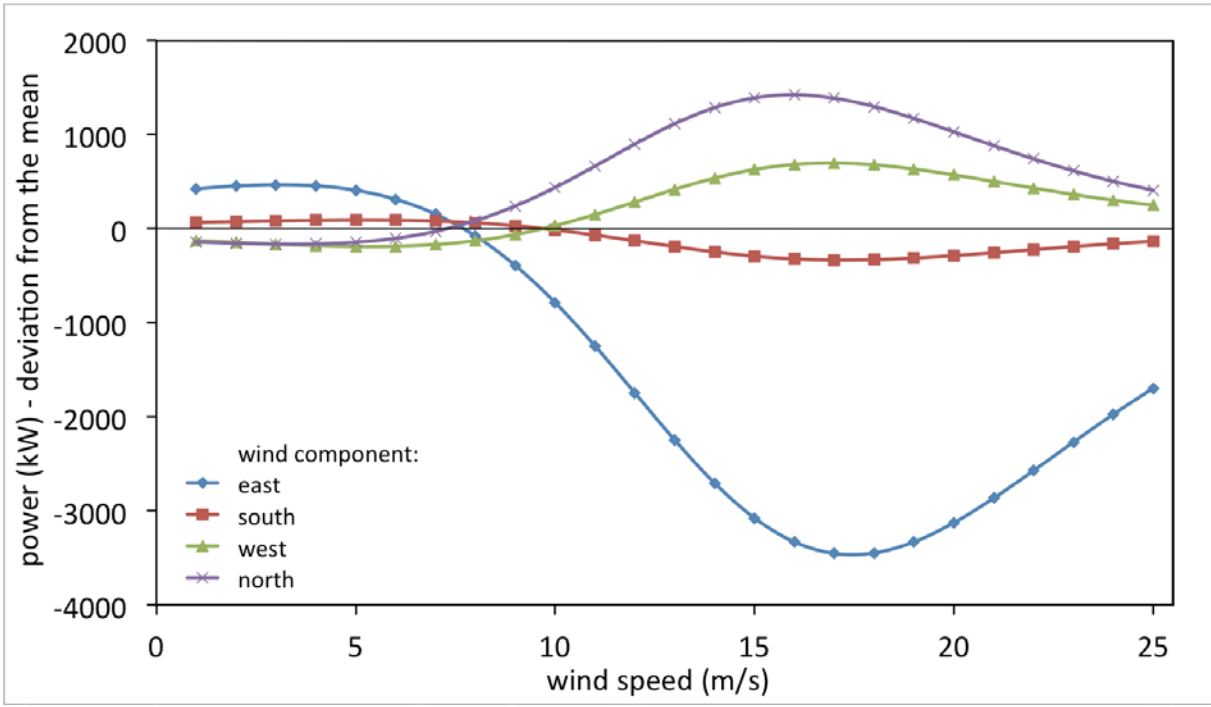

Figure 5: *Differences in the power output on several flow directions using the example of wind farm 1 (31MW). Shown is for all four wind components the deviation of their analytic power curves from the mean power curve which includes all wind directions. (Please note, the u > 20 m/s parts of the analytic curves are not represented by enough data, see Fig. 3).*

4. Improvement of the wind power forecast due to analytic power curves

To improve the influence of the analytic power curve model (PC) to the wind power prediction we compare here a power output model, based on a neural network (NN, see More and Deo, 2003; Artipoli, Durante, 2014), with the prediction, which only use the PC-Module.

Both models need information of the meteorological conditions, especially the wind velocity and wind direction, which are the main drivers of the power production and could be forecast by numerical weather prediction (NWP) models. On base of these data and further information about the technical details of the wind farm, it is possible to develop a power production forecast. Such a neural network, as an example of a statistical approach, does not need any detailed information about the wind turbines and their environment. The NN establish an arbitrary link between the data from the NWP models and the power production of the wind farm (More and Deo, 2003). For this, the computation is relatively easy and fast compared to an explicit modeling.

A schematic illustration of the structure and the principle of operation of a neural network, used by LEM (see Heinrich, 2005) can be seen in Fig. 6. In principle, a neural network consists of connected neurons, which are arranged in the simplest case in three layers: input, hidden and output layer. Figure 6 illustrates a special form of neural

networks, an easy feed-forward network. The process of the creation of wind power predictions with neural networks can be described in the following way: The input values from a NWP model and optional some characteristics of the wind farm were weighted according to their importance (they are known from a training process; see section below). Now, the transfer function generates from the weighted input values the effective input of the neuron. If a certain threshold is reached, the neuron will be activated. Afterwards, the output of the neurons will be weighted again and at the end of the process the network will create the power prediction for this wind farm.

To achieve this aim, a learning and training phase is necessary. Such a training phase needs historical datasets to identify certain patterns and to use them on the later forecast (More and Deo, 2003). This training process is difficult, if the wind farm is re-edified and there is not enough time for a learning phase of the NN-system. This results from the aim to integrate the wind farms into the power supply as soon as possible. At the end of such a learning phase the NN knows enough about the individual properties of the wind farm to create such a prediction. This prediction takes into account the relation between the wind field and the power output, which is realized as a wind farm power curve (see Fig. 4) as well as their variability with wind direction (Fig. 5).

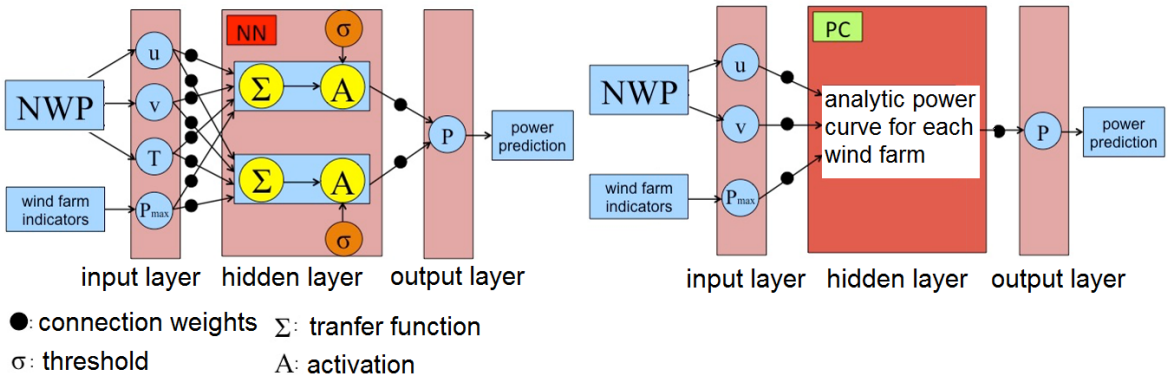

Figure 6: *Schematic illustration of a feed-forward neural network which is used in a wind power prediction (left). To demonstrate the effect of a good knowledge of the wind farm power curve, which are describable by the analytical predetermined functions, the hidden layer of NN is replaced by a power curve module (right).*

NWP *(numerical weather prediction) as the meteorological input (among others):*
U, V wind speed components, wind direction, T air temperature (air density)
Wind farm indicators:
Rated nominal power P_{max}, hub heights, power production time series

If the NN starts with the learning phase, it could be helpful to know more about the properties of such a wind farm. One option could be to replace the power curve of an individual wind turbine by the power curve of a whole wind farm. To demonstrate the effect of learning by the NN, in our example the NN-hidden layer is replaced by an analytical PC-model, which use information of the wind farm power curve.

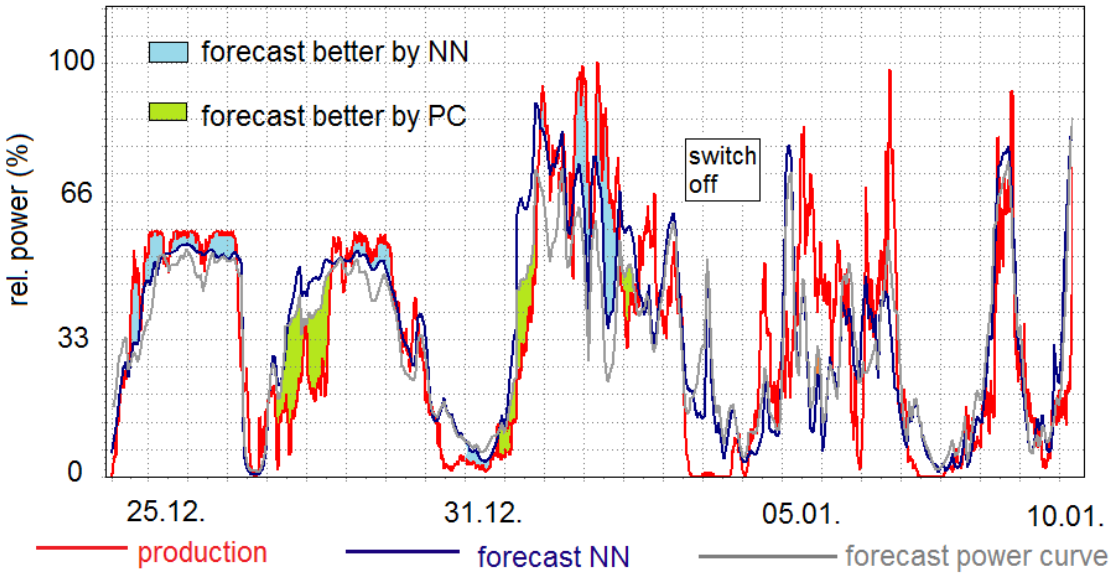

Figure 7: *Power production compared to the forecast using NN (neural network) or only the power curve model (PC). The NN learns to include the systematic variability of the power production by wind direction in most cases. During some episodes, the use of the analytical functions of the power curve for the forecast exhibit a smaller error. But with advancing training of the NN, these differences decrease.*

As can be seen in Fig. 7, during the learning phase of the NN in some cases it would be better to use such an analytic relation for the prediction. However, we know this wind farm power curves only after some time of operation of the wind farm. On the other hand, if it is known that the correlation between predicted wind speed and actual output power for wind farms always behaves according to such a pattern which differs significantly from the characteristics of the individual wind turbine, then this is a help for training of NN.

5. Conclusions

In this study we have investigated the applicability of an analytic form of wind power curves, which describes the wind speed dependent power output of a wind farm. This function is characterized by two individual parameters (L_u and u_0), which describes the individual wind farm under operational conditions. The wind farm power curve differs significantly from the individual power curve of a single type of wind turbine, according to the engineer standard IEC 61400-12-1, whose expressiveness is limited when the wind turbine is only used in wind farms. The implication of these analytic power curves in power forecast models for instance in neural networks leads to an improvement of the forecasting quality. Notably neural networks are susceptible to prediction errors during new situations or rare events, which were perhaps underrepresented in the training process. The availability of an analytic power curve, which describes invariant characteristics of the wind farm within their surroundings, can serve in these cases as a “reinsurance” which helps to reduce forecast errors.

References

Artipoli, G., Durante, F., 2014: Physical modeling in wind energy forecasting, DEWI-Magazin, No. 44, 10-15.

Heinrich, I., 2005: Arbeitsweise künstlicher neuronaler Netze und ihre Anwendung in Energieprognosesystemen. VDI/VDE-GMA-Fachausschuss FG/FA 1.10, Frankfurt am Main, 27. Juni, 2005.

IEC 61400-12-1:2005: Ed.1: Wind turbines – Part 12-1: Power performance measurements of electricity producing wind turbines (Deutsche Fassung EN 61400-12-1:2006)

Kiranoudis, C. T., Voros, N. G., Maroulis, Z. B., 2001: Short-cut design of wind farms. *Energy Policy*, *29*(7), 567-578.

Klobasa, M., Obersteiner, C., 2006: Technical constraints on and efficient strategies for the integration of wind energy. *Energy & environment*, *17*(6), 885-906. doi: 10.1260/095830506779398867

Met Office UK, 2015: http://www.metoffice.gov.uk/research/modelling-systems/unified-model/weather-forecasting

Mellinghoff, H., 2013: Development of power curve measurement standards, DEWI-Magazin No. 43, 45-48.

Milan, P., Wachter, M., Peinke, J., 2013: Turbulent character of wind energy, Physical Review Letters, 138701.

More, A., Deo, M.C., 2013: Forecasting wind with neural networks. *Marine Structures*, Vol. 16, 35-49. doi:10.1016/S0951-8339(02)00053-9

Skamarock, W.C., Klemp, J.B., Dudhia J., Gill D.O., Barker D.M., Duda M.G., Huang X.-Y., Wang W., Powers J.G., 2008: A description of the Advanced Research WRF version 3. NCAR Tech. Note NCAR/TN-475+STR, 113 pp.

TR5 FGW, 2013: Bestimmung und Anwendung des Referenzertrages, Techn. Richtlinie 5, FGW e.V.

Wissenschaftliche Mitteilungen aus dem Institut für Meteorologie der Universität Leipzig Bd. 53

Tomografische Rekonstruktion der Raumtemperaturverteilung aus einer Raumimpulsantwort

M. Bleisteiner[+], M. Barth*, A. Raabe*, P. Holstein[**]

[+]) Fachgebiet Audiokommunikation, TU Berlin, Einsteinufer 17, 10587 Berlin,
E-Mail: marcus.bleisteiner@gmail.com
**) Institut für Meteorologie, Universität Leipzig, Stephanstr. 3, 04103 Leipzig*
E-Mail: raabe@uni-leipzig.de
***) SONOTEC Ultraschallsensorik Halle GmbH, Nauendorfer Str. 2, 06112 Halle (Saale)*

Summary

Temperature can be estimated by acoustic propagation time measurements along known sound paths. By using a multitude of known sound paths in combination with a tomographic reconstruction technique a spatial and temporal resolution of the temperature field can be achieved. Based on it, this article focuses on an experimental method in order to determine the spatially differentiated development of room temperature with only one loudspeaker and one microphone. The theory of geometrical room acoustics is being used to identify sound paths under consideration of reflections. The propagation time along a specific sound path is derived from the room impulse response. Temporal variances in room impulse response can be attributed primarily to a change in air temperature and airflow. It is shown that in the absence of airflow a three-dimensional acoustic monitoring of the room temperature can be realized with a fairly limited use of hardware.

Zusammenfassung

Die Temperatur kann mithilfe von akustischen Laufzeitmessungen auf definierten Schallstrecken ermittelt werden. Der Einsatz multipler Schallstrecken, in Verbindung mit einem tomografischen Rekonstruktionsverfahren, erlaubt eine räumliche Auflösung der genannten klimatologischen Größe. Aufbauend darauf, befasst sich dieser Artikel mit einer experimentellen Methode zur Erfassung der räumlich und zeitlich aufgelösten Entwicklung der Raumtemperatur mit lediglich einem Lautsprecher und einem Mikrofon. Die Theorie der geometrischen Raumakustik wird genutzt, um Schallstrecken, unter der Berücksichtigung von Reflexionen, zu identifizieren. Die zu den Ausbreitungswegen gehörenden Laufzeiten werden aus einer gemessenen Raumimpulsantwort abgeleitet. Zeitliche Varianzen in Raumimpulsantworten sind in erster Linie auf die Veränderung der Lufttemperatur und von Strömungsverhältnissen zurückzuführen. Es wird gezeigt, dass bei Abwesenheit von Raumluftströmungen, eine dreidimensionale, akustische Überwachung der Raumtemperatur mit einem sehr geringen Einsatz an Messtechnik realisiert werden kann.

1. Einleitung

Die Schallausbreitungsgeschwindigkeit in der Atmosphäre wird maßgeblich von der Temperatur und von Strömungen beeinflusst (Bohn, 1988). Lediglich die Luftfeuchtigkeit führt proportional zur Sättigung zusätzlich zu einer geringfügigen Erhöhung der Schallausbreitungsgeschwindigkeit. Unter der Annahme der Abwesenheit des vektoriellen Einflusses durch Strömungen, kann mithilfe einer akustischen Laufzeitmessung zwischen einem Lautsprecher und einem Mikrofon die mittlere Temperatur auf dieser Schallstrecke mit bekannter Länge ermittelt werden (Kaimal und Businger, 1963). Durch Betrachtung vieler, in der Ebene oder im Raum verteilter Schallstrecken gelingt eine mehrdimensionale, örtlich aufgelöste Temperaturerfassung. Hierfür wird ein tomografisches Verfahren verwendet, das die auf den Einzelstrecken erfassten Schalllaufzeiten in räumlich verteilte Temperaturfelder überführt. Bei bisherigen Anwendungen dieser Messmethode wurde eine Vielzahl von Schallsendern und Empfängern eingesetzt. Diese wurden so um ein Untersuchungsgebiet angeordnet, dass eine möglichst homogene Überdeckung des Messgebietes mit Schallwegen erreicht werden konnte. Anfänglich wurde diese Messmethode für mikrometeorologische Fragestellungen zur Aufzeichnung von Lufttemperaturfeldern über strukturierten atmosphärischen Unterlagen eingesetzt (Wilson und Thomson, 1994., Tetzlaff u.a., 2002) später dann im Rahmen der Verfahrensentwicklung auf kleinere Raumbereiche z.B. in einem Windkanal (Holstein et. al., 2004, Barth und Raabe, 2011).
Der vorliegende Artikel beschreibt eine experimentelle Methode, die ebenfalls eine Erfassung der Temperaturverteilung im Raum ermöglicht. Dabei werden aber lediglich ein Lautsprecher und ein Mikrofon verwendet. Als weitere, virtuelle Schallquellen werden mehrfache Reflexionen des einzelnen Schallemitters an Raumbegrenzungsflächen hinzugezogen. Nach der Theorie der geometrischen Raumakustik ergibt sich, abhängig von der Position des Senders und des Empfängers, eine Vielzahl von Schallstrecken, die eine Untersuchungsumgebung hinreichend abdecken können. Der theoretische Verlauf der Schallstrecken wird mit einem Spiegelschallquellenmodell nach Allen und Berkley (1979) bestimmt. Alle Reflexionen eines Impulses, der von einer Schallquelle ausgeht, überlagern seinen Direktschall und ergeben die Impulsantwort eines Raumes. Entsprechen die Positionen für den Sender und den Empfänger bei der Messung der Raumimpulsantwort denen des Spiegelschallquellenmodells, können aus dieser die Laufzeiten, die zu den modellierten Schallstrecken gehören, abgeleitet werden. Hierfür wird ein statistisch aufbereitetes Reflektogramm verwendet. Jede Nichtlinearität durch eine globale bzw. partielle Temperaturänderung im Raum erzeugt bei der Schallausbreitung, aufgrund von Modulationen durch das Ausbreitungsmedium, zeitliche Varianzen, die im Reflektogramm abgebildet werden (Vorländer und Kob, 1997, Svensson und Nielsen, 1999).
Das Verfahren bei der experimentellen Messmethode, das im Folgenden vorgestellt wird, wurde im Zuge einer Abschlussarbeit entwickelt (Bleisteiner, 2014). Aufgrund einer Einschränkung durch die Messhardware, wurde eine Erfassung der Temperaturverteilung relativ zu einem Ausgangszustand bzw. -zeitpunkt in einem quaderförmigen Raum umgesetzt. Der Artikel stellt eine Ausführung der

entscheidenden, oben genannten theoretischen Hintergründe dar, um mit einem geringen Hardwareeinsatz eine örtlich differenzierte, akustische Überwachung der Raumtemperaturentwicklung zu ermöglichen. Weiterhin wird die praktische Umsetzung beschrieben, die den Bau und die Validierung eines spezialisierten Messlautsprechers, den Einsatz der verwendeten Messtechnik, sowie den Messalgorithmus beinhaltet. Anhand einer Beispielmessung in einem realen Raum wird das Potential der Messmethode gezeigt. Abschließend wird das System bewertet und Erweiterungsmöglichkeiten werden aufgeführt.

2. Theoretische Hintergründe

Das präsentierte Verfahren beruht auf der Verknüpfung einer akustischen Laufzeiterfassung auf modellierten Schallstrecken, unter der Berücksichtigung von Reflexionen an Begrenzungsflächen (Wände), mit einer anschließenden tomografischen Rekonstruktion der räumlichen Temperaturverteilung. Die Laufzeiten werden dabei aus der Impulsantwort des zu vermessenden Raumes abgeleitet, die mittels der Korrelationsmesstechnik bestimmt wird.

2.1 Korrelationsmesstechnik und Raumimpulsantwort

Mit der Korrelationsmesstechnik können sowohl Laufzeiten zwischen einem Sender und einem Empfänger, als auch die Übertragungseigenschaften eines LTI-Systems, in Form einer Impulsantwort, ermittelt werden. Zur Ermittlung einer Raumimpulsantwort kann dabei ein zeitlich ausgedehntes, breitbandiges Anregungssignal verwendet werden, dessen Autokorrelationsfunktion impulsförmig ist (Vorländer, 1994). Ein entscheidender Vorteil einer längeren, breitbandigen Anregung ist, dass ein System mit deutlich mehr Energie angeregt werden kann und dadurch eine besser zu verwertende Impulsantwort entsteht. In der Praxis wird ein LTI-System mit einem Signal angeregt, worauf an dessen Ausgang das Faltungsprodukt des Signals mit der Impulsantwort anliegt. Durch eine Kreuzkorrelation mit dem Anregungssignal erhält man die reine Impulsantwort. Aufgrund von Nichtlinearitäten der Messkette, macht es jedoch Sinn, mit einer Aufnahme des Anregungssignals zu korrelieren, welche unter Freifeldbedingungen entstanden ist (Tervo, 2011).
Ein geeignetes Signal für die Korrelationsmesstechnik ist eine Maximallängenfolge, bzw. MLS (Maximum Length Sequence). Hierbei handelt es sich um eine binäre Pseudozufallsfolge, deren Konstruktion und Eigenschaften in Lüke (1992) dargelegt werden. Eine MLS hoher Ordnung besitzt eine Autokorrelationsfunktion, die einem idealen Impuls recht nahe kommt. Die MLS-Methode kann zudem gewährleisten, dass selbst bei ungünstigen Störsignalpegeln verwertbare Messergebnisse zu erwarten sind (Dunn und Hawksford, 1993).

2.2 Spiegelschallquellenverfahren

Die Spiegelschallquellenmethode ist ein Standardverfahren der akustischen Simulation, um Raumimpulsantworten zu modellieren. Dabei werden sowohl die Schalllaufwege, als auch die dazugehörigen Laufzeiten, durch die strikte Beachtung des geometrischen Reflexionsgesetzes, berechnet (Möser, 2012). Dies geschieht unter der Angabe der Raumgeometrie, sowie der Position des Schallemitters und des

Schallempfängers. Die Ordnung *M*, besagt dabei, wie oft ein Schallereignis bei der Bildung der Schallstrecke an den Raumbegrenzungsflächen reflektiert wird. Niedrige Ordnungen führen zu diskreten frühen Reflexionen in der Raumimpulsantwort. Für die mathematische Bestimmung einer Raumimpulsantwort mithilfe von Spiegelschallquellen wird in Dokmanic et. al. (2013) von einer Impulsfolge der Form

$$h_m(t) = \sum_i \alpha_i \delta(t - \tau_i) \tag{1}$$

ausgegangen. Dabei wird ein um τ_i verzögerter Impuls δ aufgrund von Absorptionsvorgängen an Raumbegrenzungsflächen durch α_i in seiner Amplitude verringert. Um die Verzögerungen τ_i, welche äquivalent zur Schalllaufzeit einer individuellen Reflexion an einer bestimmten Raumbegrenzungsfläche sind, zu erhalten, wird die originale Schallquelle *S* an der entsprechenden Fläche gespiegelt. Somit erhält man die Spiegelschallquelle $\tilde{S}_i$ welche δ um α_i verringert wiedergibt. An dem Ort des Empfängers *R* ergibt sich die Impulsfolge h_m aufgrund der verschiedenen Abstände von *S* und $\tilde{S}_i$ zu *R*. Mehrfachspiegelungen von *S* an (unterschiedlichen) Raumbegrenzungsflächen ergeben Reflexionen höherer Ordnung. Die Raumimpulsantwort ist die Summe aus dem Direktschall, der von S ausgeht, und allen Signalen der Spiegelschallquellen, die entsprechend der Ordnung *M* geometrisch bestimmt wurden.
Eine Spiegelschallquelle erster Ordnung wird mit

$$\tilde{S}_i = S + 2\langle P_i - S, n_i \rangle n_i \tag{2}$$

bestimmt. Bei n_i handelt es sich um den Normalenvektor der i-ten Raumbegrenzungsfläche und P_i ist ein beliebiger Punkt auf dieser Fläche. Die Laufzeit einer Reflexion ist folglich

$$\tau_i = \frac{\left\| \tilde{S}_i - R \right\|}{c}, \tag{3}$$

wobei *c* die Schallausbreitungsgeschwindigkeit ist.
Spiegelschallquellen höherer Ordnung werden in Bezug auf eine Spiegelschallquelle der Ordnung $M = M - 1$ errechnet. Damit gilt für Spiegelschallquellen zweiter Ordnung

$$\tilde{S}_{ij} = \tilde{S}_i + 2\langle P_j - \tilde{S}_i, n_j \rangle n_j \tag{4}$$

wobei zudem

$$\left\| S - \tilde{S}_{ij} \right\| = \left\| \tilde{S}_i - \tilde{S}_j \right\| \tag{5}$$

erfüllt werden muss.
Die Konstruktion von Spiegelschallquellen kann sehr gut visualisiert werden, wozu die Abb. 1 dient.

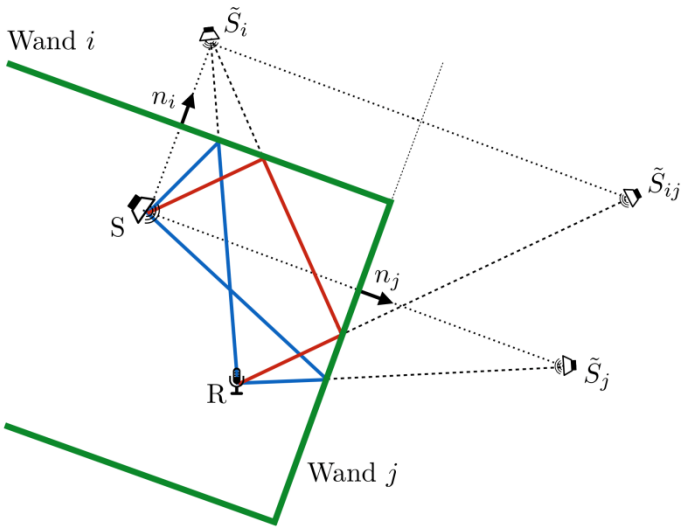

Abb. 1: Spiegelschallquellenmodell mit Reflexionen erster und zweiter Ordnung (Bleisteiner, 2014)

2.3 Akustische Laufzeittomographie

Die Laufzeit akustischer Signale in ruhender Luft hängt maßgeblich von der Temperatur entlang des bekannten Ausbreitungsweges ab. Ein Zusammenhang zwischen Schallgeschwindigkeit c und Lufttemperatur T kann unter Berücksichtigung der spezifischen Feuchte q geschrieben werden als

$$c = \sqrt{\gamma \cdot R_s \cdot T_{av}} \quad \text{mit} \quad T_{av} = (1 + 0{,}513 \cdot q) \cdot T \tag{6}$$

Hierbei wird T_{av} mit akustisch virtuelle Temperatur bezeichnet. In Analogie zur virtuellen Temperatur werden durch Verwendung dieser Größe alle Einflüsse des variablen Wasserdampfgehaltes berücksichtigt. Bei dieser Art der Betrachtung können die Werte für $\gamma = 1{,}4$ (Verhältnis der spezifischen Wärmkapazitäten bei konstantem Druck und konstantem Volumen für trockene Luft) und $R_s = 287{,}05$ J kg^{-1} K^{-1} (spezifische Gaskonstante für trockene Luft) unabhängig von der vorherrschenden Feuchte verwendet und als konstant angesehen werden.
Die Laufzeit eines akustischen Signals τ entlang eines Weges l lässt sich mit Hilfe des räumlich variablen Schallgeschwindigkeitsfeldes (bzw. dessen Kehrwerten, den Langsamkeiten s) schreiben als

$$\tau = \int_l \frac{1}{c(r)} dl = \int_l s(r) dl \tag{7}$$

Wird nun ein Untersuchungsgebiet entlang verschiedener Wege durchschallt, lassen sich räumliche Verteilungen der Langsamkeiten und hieraus die akustische virtuelle Temperatur ableiten. Hierfür werden tomographische Rekonstruktionstechniken eingesetzt. Im Folgenden soll nur ein kurzer Überblick gegeben werden, ausführliche Informationen zum hier verwendeten Verfahren der akustischen Laufzeittomographie

sind z. B. in Barth (2009) und für dreidimensionale Anwendungen in Barth und Raabe (2011) gegeben.
Für die vorgestellten Analysen fand ein iteratives algebraisches Verfahren, die simultane iterative Rekonstruktionstechnik (SIRT), Verwendung. Voraussetzung für die Anwendung eines solchen Verfahrens ist die Untergliederung des Messgebietes in diskrete Teilgebiete, in denen die gesuchte Größe jeweils als konstant angenommen wird. Für ein Gebiet aus *J* Zellen kann die Laufzeit des i-ten Schallstrahles in der Form

$$\tau_i = \sum_{j=1}^{J} s_j \cdot l_{ij} \tag{8}$$

angegeben werden, wobei s_j die Langsamkeit in der *j*-ten Zelle und l_{ij} die Länge des *i*-ten Schallstrahls in der *j*-ten Zelle darstellen.
Mit Hilfe des SIRT-Algorithmus wird eine Lösung für die Verteilung der Langsamkeiten s_{ij} bei bekannten Schallstrahlabschnitten und gemessenen Schalllaufzeiten in einem iterativen Prozess bestimmt. Dabei werden folgende Berechnungsschritte ausgeführt

1. Festlegung einer Startverteilung für die Langsamkeiten
2. Berechnung von Laufzeitwerten aus den vorgegebenen Langsamkeiten und den bekannten Schallwegen durch das Gitter
3. Bestimmung von Differenzen zwischen berechneten und gemessenen Laufzeiten für alle Schallwege und Berechnung von Korrekturwerten für die Verteilung der Langsamkeiten im Gitter entsprechend dieser Differenzen
4. Anpassung der Verteilung der Langsamkeiten entsprechend der berechneten Korrekturwerte
5. Wiederholung der Schritte 2 bis 4 bis zum Erreichen eines Abbruchkriteriums (z.B. festgelegte Anzahl an Iterationen)

Im Ergebnis erhält man eine Verteilung der Langsamkeiten, die sich entsprechend des oben angegebenen Zusammenhangs in eine Verteilung der akustisch virtuellen Temperatur überführen lässt.

3. Praktische Umsetzung

Aufbauend auf den theoretischen Grundlagen aus Abschnitt 2 wurde eine experimentelle Messmethode entwickelt, die bestimmten Anforderungen genügen sollte: Die akustische Erfassung der räumlichen Verteilung und des zeitlichen Verlaufs der Lufttemperatur soll mit lediglich einem Lautsprecher und einem Mikrofon erfolgen, die in einem Raum positioniert werden. Mit dem System soll ein Messintervall von wenigen Sekunden, eine hohe Temperaturauflösung, sowie Robustheit gegenüber Störschall erreicht werden.

3.1 Experimentelles Verfahren

Unter der Verwendung eines Spiegelschallquellenmodells werden aus den bekannten Positionen des Schallsenders und -empfängers sowie der Geometrie des Raumes theoretische Schallstrecken sowie dazugehörige Laufzeiten berechnet. Das Modell gibt zudem Auskunft darüber, welche Raumbegrenzungsflächen bei einer Reflexion

beteiligt sind und an welchen Punkten der Schall reflektiert wird. Dies ist die Voraussetzung für die örtliche Diskretisierung des Raumes zur Rekonstruktion der räumlichen Verteilung der Lufttemperatur. In der Abb. 2 ist exemplarisch die Schallstreckenverteilung eines Spiegelschallquellenmodells zweiter Ordnung in einem quaderförmigen Raum zu sehen. Basierend auf der räumlichen Verteilung der Schallstrecken kann auch die Güte der Raumabdeckung für die tomografische Rekonstruktion eingeschätzt werden. Die korrespondierenden Laufzeiten werden für jeden Schallpfad unter Annahme einer homogenen Temperaturverteilung abgeschätzt.

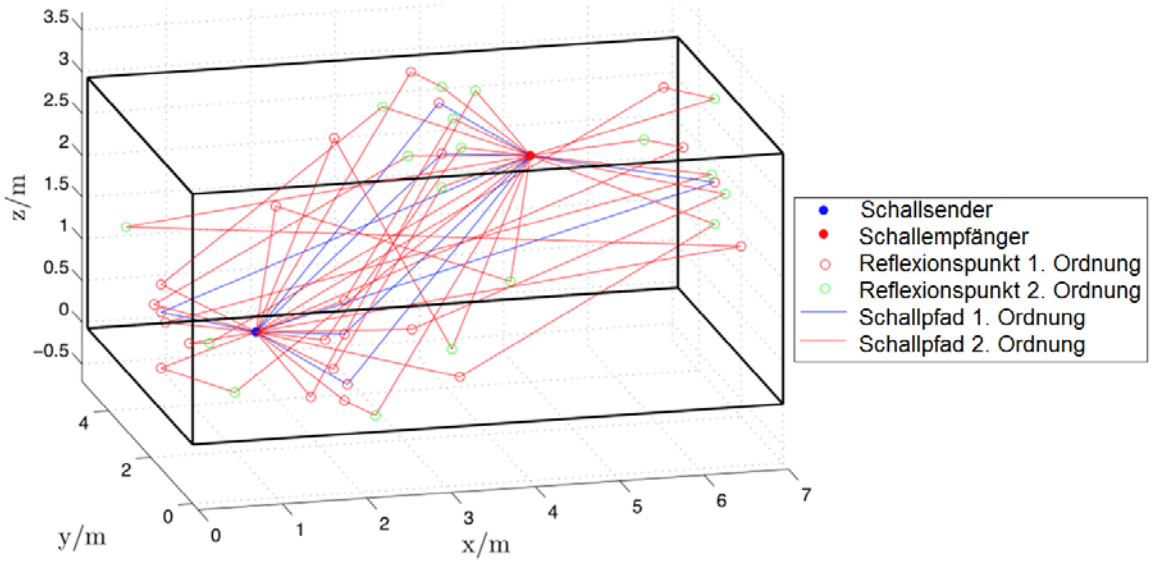

Abb. 2: Dreidimensionale Darstellung der Schallstreckenverteilung eines Spiegelschallquellenmodells zweiter Ordnung (Bleisteiner, 2014)

Die gemessenen Schalllaufzeiten werden aus dem Reflektogramm des Raumes abgeleitet, dem eine Impulsantwort zugrunde liegt, welche auf denselben geometrischen Voraussetzungen basiert wie das Spiegelschallquellenmodell. Somit ist die wesentliche Aufgabe bei der Messmethode, Reflexionen im Reflektogramm zu detektieren und deren Laufzeiten der entsprechenden modellierten Schallstrecke zuzuordnen. Dafür werden die aus dem Modell berechneten Laufzeiten verwendet, mit deren Hilfe ein Kurzzeitanalysefenster bei der zu erwartenden Reflexion gesetzt wird. Die theoretischen Schalllaufzeiten für alle Schallwege von Reflexionen erster und zweiter Ordnung aus dem Spiegelschallquellenmodell (vgl. Abb. 2) sind als rote Linien in Abb. 3 eingetragen. Um diese Laufzeiten werden die Kurzzeitfenster zentriert. Die Stelle des Maximums im Reflektogramm (blaue Linien in Abb. 3) innerhalb des Fensters repräsentiert die gemessene Laufzeit, welche per peak picking ermittelt wird.

Bevor das Reflektogramm analysiert wird, wird dieses mit einer Statistik zweiter Ordnung aufbereitet, um Reflexionen eindeutiger als solche zu identifizieren. Statt des energiebasierten Signals wird die Signalform (Kurtosis bzw. Wölbung) des Reflektogramms in Form einer Kurtosis-Analyse betrachtet. Damit werden Reflexionen niedriger Ordnung hervorgehoben. Der Schalldruck einer Reflexion kann als stochastische Funktion mit Normalverteilung modelliert werden und die Kurtosis

stellt ein Maß für den Grad der Normalverteilung dar. Für eine praktische Implementierung nach Usher (2010) werden hierfür zwei gleitende Kurzzeitfenster mit den Längen l_k und m_k verwendet, wobei $l_k << l_m$ gilt. Beide Fenster sind um das Sample n des Datenvektors x zentriert. Die Berechnung des aufbereiteten Reflektogramms erfolgt durch

$$k_{n,l,m} = \frac{(\mu_{n,l_k} - \mu_{n,m_k})^4}{\sigma^4_{n,m_k}}. \tag{9}$$

Dabei sind μ_{n,l_k} und μ_{n,m_k} die Mittelwerte der beiden Fenster und bei σ_{n,m_k} handelt es sich um die Standardabweichung der Werte im Fenster mit der Länge m_k. Die Abb. 3 zeigt das Reflektogramm eines realen Raumes, bevor und nachdem es der Kurtosis-Anlyse unterzogen wurde.

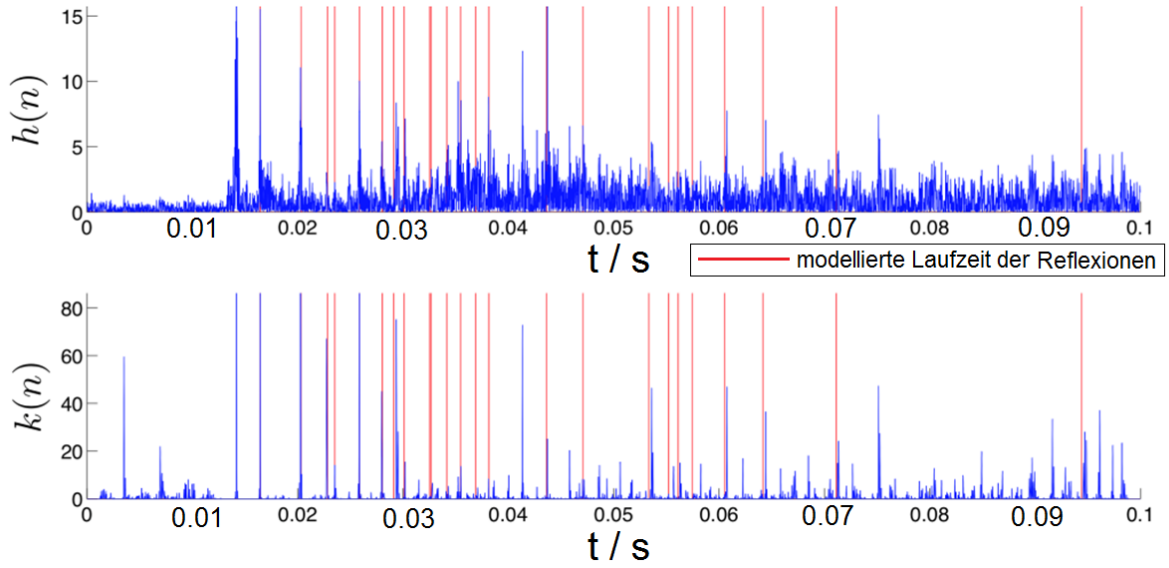

Abb. 3: Wirkung der Kurtosis-Analyse auf ein Reflektogramm (Bleisteiner, 2014)

Bei der softwaretechnischen Umsetzung des Messverfahrens wurden neben dem eigentlichen Messverfahren mehrere Algorithmen zu Vermeidung der Registrierung von fehlerhaften Laufzeiten implementiert, die beispielsweise auf geometrische Ungenauigkeiten zurückzuführen sind (Bleisteiner, 2014).

3.2 Messtechnik

Zur Bestimmung der Raumimpulsantwort mit der Korrelationsmesstechnik werden im Kontext der vorgestellten Messmethode spezifische Anforderungen an den Messlautsprecher gestellt. Im Idealfall sollte dieser eine maximal breitbandige Monopol-Punktquelle darstellen. Solch ein Lautsprecher existiert in der Realität nicht (Masiero et. al., 2011), jedoch ist mit dem Bau eines spezialisierten Versuchslautsprechers eine Schallquelle entstanden, die sich als geeignet herausgestellt hat, was theoretisch in Bleisteiner (2014) ausgeführt und messtechnisch evaluiert wurde. Es handelt sich dabei um einen kleinen tropfenförmigen Breitbandlautsprecher mit einem speziell angepassten Gehäuse

(Gehäuseinnenvolumen: 0,25 Liter) und dem 2-Zoll-Treiber Visaton FRS 5 XTS (VISATON, 2014), in Anlehnung an Masiero et. al. (2011).
Als Schallempfänger wird für das Messsystem das 1/4-Zoll-Elektret-Kondensatormokrofon AVM MI-17 (AVM, 2014) eingesetzt. Der Wandler ist als Druckempfänger mit einer Freifeldentzerrung ausgelegt. Weiterhin wird das Anregungssignal vom Leistungsverstärker Kemo M032S (Kemo, 2014) verstärkt, der sich, bei genügend Ausgangsleistung, durch kompakte Ausmaße und einen geringen Energiebedarf auszeichnet, wodurch das Messsystem sehr mobil realisiert werden konnte.
Eine besondere Rolle spielt die eingesetzte Messkarte DT 9847-1-1 (Data Translation, 2014) in Verbindung mit der Software. Dabei ist positiv hervorzuheben, dass der DA/AD-Wandler eine Digitalisierungsrate von 216 kHz aufweist, womit eine hohe zeitliche Abtastung und damit eine hohe Temperaturauflösung erreicht wird. Allerdings gewährleistet die Messkarte keine Synchronität zwischen Sende- und Empfangskanal, was beim triggern jeder Einzelmessung zu einem unbestimmten Sampleversatz führt. Dass die tatsächlichen Schalllaufzeiten im Reflektogramm abgebildet werden, setzt aber eine samplegenaue Synchronität des Eingangs und Ausgangs voraus. Dieser Umstand ist die Ursache, dass lediglich relative Temperaturwerte bezüglich eines (bekannten) Anfangswertes erfasst werden können. Um dennoch die korrekten Laufzeiten aus dem Reflektogramm ableiten zu können, wird eine Methode angewandt, welche sich die theoretische Laufzeit des Direktschalls zwischen dem Lautsprecher und dem Mikrofon zu Nutze macht (Bleisteiner, 2014).
Der komplette Messalgorithmus wurde in der Entwicklungsumgebung Matlab® (The MathWorks, 2014) umgesetzt. Hierbei wurden Funktionen und Skripte implementiert, womit eine Messung vorbereitet, durchgeführt und ausgewertet wird. Vor der Messung müssen verschiedenen Parameter, wie beispielsweise die Raumgeometrie oder die Messdauer initial angegeben werden. Im Anschluss werden die Programmteile für die eigentliche Messung, Datenaufzeichnung, -analyse und -darstellung ausgeführt. Das Messverfahren wird ausführlich in Bleisteiner (2014) dargestellt.

4 Beispielmessung

Die experimentelle Messmethode wurde in einer kleinen Sporthalle der Firma Sonotec Ultraschallsensorik Halle GmbH (SONOTEC, 2014) am 17.07.2014 erprobt. Der Raum erfüllt die Forderung eines quaderförmigen Aufbaus, wodurch das Spiegelschallquellenmodell auf den realen Raum angewandt werden kann.

4.1 Aufbau und Durchführung

Ein Lautsprecher und ein Mikrofon wurden mithilfe der Visualisierung des Spiegelschallquellenmodells (vgl. Abb. 2) derart in der Untersuchungsumgebung positioniert, dass sich eine gute Abdeckung des Raumes mit Schallstrecken und eine voneinander abweichende Laufzeit für jede Reflexion ergab. Zusätzlich wurden sieben Referenzsensoren zur Erfassung von Temperatur und Feuchte (testostor 171-3: Testo, 2014) im Raum verteilt. Mit den Daten der konventionellen Sensoren werden die Ergebnisse der akustischen Messung verglichen.

Die Sporthalle wurde für die tomografische Rekonstruktion in jeder Dimension in drei Abschnitte unterteilt. In den so definierten 27 Teilvolumen wurde jeweils die Temperatur relativ zum Ausgangszustand registriert. Das Messintervall betrug 10 s. Während der Messung, deren Ablauf in Tab. 1 skizziert ist, wurde die Messgröße aktiv beeinflusst. An einem unteren Eck im Raum wurden mehrere elektronische Heizgeräte platziert. Diese hatten eine Leistung von insgesamt 8,5 kW.

Tab. 1: Zeitlicher Ablauf der Messung

Uhrzeit	**Vorgang**
12:15:00	Messstart, Einschalten der Wärmequellen
14:15:00	Ausschalten der Wärmequellen
15:15:00	Messstop

4.2 Ergebnisse

Zunächst werden in Abb. 4 die lokalen Temperaturänderungsverläufe aller Tomografie-Zellen gezeigt, in denen sich auch ein Referenzsensor befand und zusammen mit den Daten der konventionellen Temperaturfühler aufgetragen. Das bedeutet, dass die tomographisch rekonstruierte mittlere Temperaturänderung eines Volumens mit einer punktuellen Erfassung im selben örtlichen Bereich verglichen wird.
Gut auszumachen ist bei allen Plots in Abb. 4 die zeitliche Verzögerung bei den konventionellen Thermometern, die mit der Trägheit der NTC-Fühler zu begründen ist. Die leichte Welligkeit aller Kurven rührt von der Regelung der Heizgeräte, welche nicht zu jeder Zeit ihre volle Leistung abgeben. Ob die jeweiligen Temperaturänderungsverläufe miteinander vergleichbar sind, hängt stark von der Positionierung der Referenzsensoren ab. Sind diese eher im Zentrum einer Tomografie-Zelle angebracht, kann eine recht gute Übereinstimmung festgestellt werden (vgl. Abb. 4 a) bis d)). Wenn sich die Thermometer allerdings an einer Raumbegrenzungsfläche mit einer von der Luft abweichenden Temperatur befinden, weichen die Verläufe zum Teil erheblich voneinander ab. Die Referenzsensoren bei Abb. 4 e) und f) befanden sich unmittelbar über dem Hallenboden und bei Abb. 4 g) an einer Außenwand. In jedem Fall führte eine geringere Temperatur der Raumbegrenzungsfläche zu einer Beeinflussung der angrenzenden Luftschicht und somit zu einem abweichenden Verlauf der relativen Temperatur der Punktmessungen im Vergleich zum Verlauf der akustisch tomografisch rekonstruierten Werte.

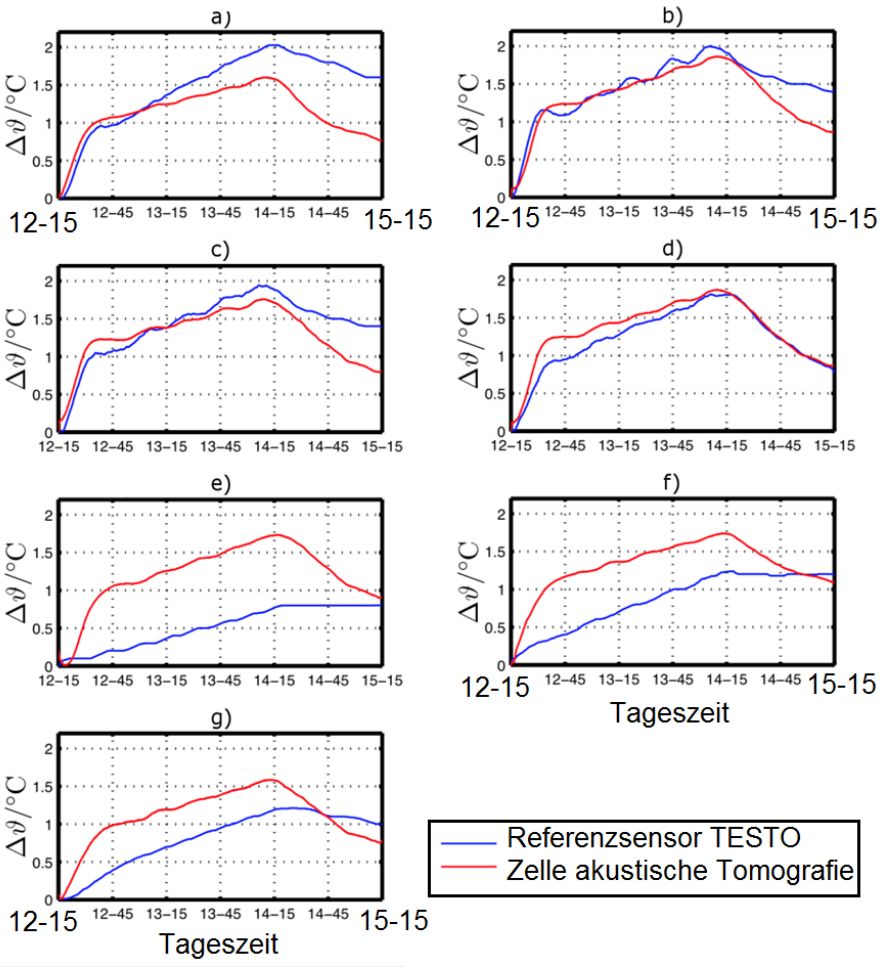

Abb. 4: Vergleich von Temperaturänderungsverläufen an verschiedenen Stellen im Raum (Bleisteiner, 2014)

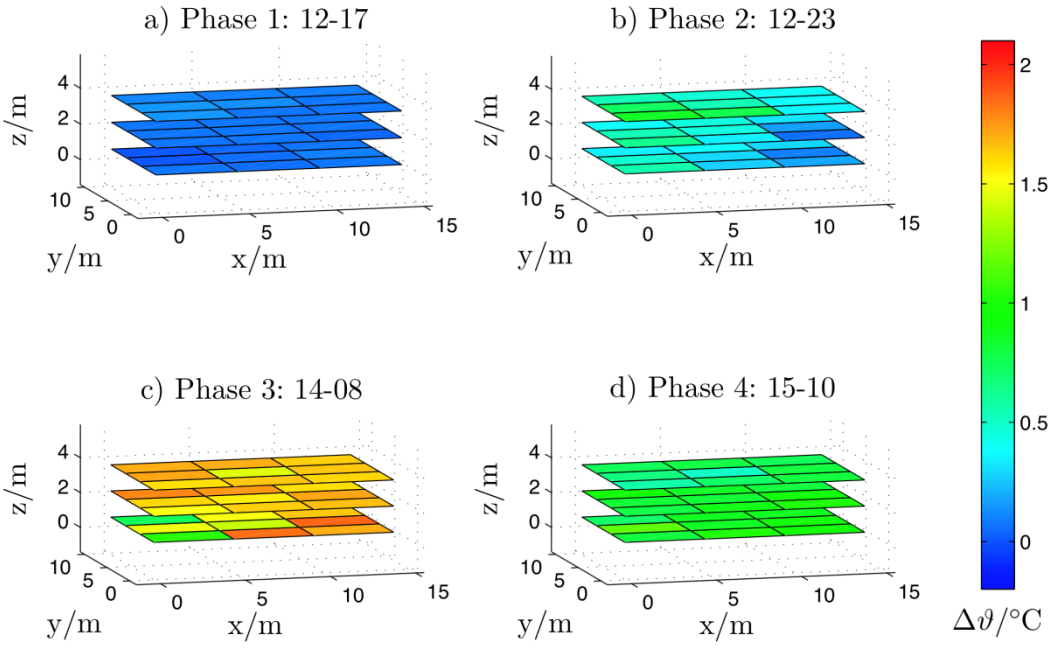

Abb. 5: Phasen der relativen Temperaturverteilung während der Messdauer, die Heizquellen befinden sich in der Raumecke bei (x,y,z) = (0,0,0) m (Bleisteiner, 2014)

In Abb. 5 wird die Temperaturänderungsverteilung zu verschiedenen Uhrzeiten dargestellt. Ein jeweiliger Plot ist repräsentativ für eine von vier Phasen, die sich während der Messdauer ausprägen.

Die vier Phasen lassen sich folgendermaßen beschreiben und erklären:

1. Homogene Verteilung der Temperatur zu Beginn der Messung (Ausgangszustand), die einer initialen Referenzmessung entspricht
2. Lokale Erwärmung im Bereich der Wärmequellen bzw. darüber (Aufsteigen der warmen Luft)
3. Diffuse und unrealistische Temperaturverteilung aufgrund einer stark ausgeprägten Konvektionsströmung, die zu einer Umwälzströmung im gesamten Raum führt (Rietschel und Fitzner, 2004). Der vektorielle Einfluss durch Strömungen wird beim derzeitigen Entwicklungsstand des Messsystems nicht berücksichtigt. Der theoretische Fehler der durch die auftretende Strömungsgeschwindigkeit verursacht wird, entspricht in etwa den Abweichungen im Temperaturfeld in Abb. 5, Phase 3 (Bleisteiner, 2014).
4. Nachdem sich die Raumluft nach dem Abschalten der Wärmequellen beruhigt hat, stellt sich wieder eine homogene Verteilung bei einer höheren mittleren Temperatur ein.

5 Schlussfolgerungen und Ausblick

Im Sinne einer Machbarkeitsstudie ist es gelungen, eine experimentelle Messmethode für eine örtlich differenzierte Überwachung der Raumtemperatur zu entwickeln. Dabei konnte die Hardware mit lediglich einem Lautsprecher und einem Mikrofon auf ein Minimum reduziert werden. Hierfür wurde die Technik der akustischen Laufzeittomographie mit Methoden der geometrischen Raumakustik kombiniert. Das ist die Voraussetzung für eine schnelle Integrierbarkeit des Messsystems in einer Messumgebung und erlaubt den Betrieb als mobiles System. Als Anwendung ist die Überwachung von technischen Betriebsräumen oder das Einmessen von klimatisierten Räumen vorstellbar. Ein Messintervall von wenigen Sekunden, abhängig von der Länge des Anregungssignals und der Leistung des eingesetzten Computers, ist dabei realistisch. Damit können plötzliche Temperaturschwankungen schnell festgestellt werden, insbesondere da bei einem akustischen System prinzipbedingt keine Sensorträgheit zu verzeichnen ist (Foken, 2006). Durch die Eigenschaften der verwendeten Anregungssignale (MLS) ist zudem unter schwierigen akustischen Bedingungen eine Datenerhebung möglich.
Das Messsystem sollte für realistische Szenarien noch um die Berücksichtigung bzw. Erhebung von Raumluftströmungen erweitert werden, da diese zum gegenwärtigen Entwicklungsstand erhebliche Unsicherheiten verursachen können. Für die reine Temperaturerhebung gilt es, den vektoriellen Einfluss durch Luftbewegungen herauszurechnen. Denkbar wäre es, der Forderung nach reziproken Schallstrecken in Barth und Raabe (2011) nachzukommen, oder Strömungen als systematische Fehler zu betrachten (Vecherin et. al., 2013). Eine weitere Einschränkung ist die idealisierte Form des Raumes als Quader, die durch die Implementierung eines komplexeren Spiegelschallquellenmodells beseitigt werden könnte. Eine weitere Verbesserung der

Messmethode würde durch die numerische Bestimmung einer idealen Sender- und Empfängerposition erreicht werden. Dadurch ergäbe sich eine optimierte Verteilung der Schallstrecken im Raum, wie auch eine bessere Verteilung der Reflexionen im Reflektogramm. Prinzipiell erlaubt das Messprogramm auch den Einsatz konventioneller Audiokarten, was dazu führen würde, dass das System sehr kostengünstig aufgebaut werden könnte. Letztlich würde eine Anregung des Raumes im Ultraschallbereich zur Erhebung der Impulsantwort den Einsatzbereich dahingehend erweitern, dass das System keine wahrnehmbaren akustischen Emissionen erzeugt.

Literatur

Allen, J. B., Berkley, D. A., 1979: Image method for efficiently simulating small-room acoustics. *The Journal of the Acoustical Society of America*, Vol. 65, 943–950.

AVM Mess- und Prüfgerätefür Akustik und Vibration, 2014: Forststr. 32, 64572 Büttelborn - Germany, E Mail: bertram.schapal.avm@t-online.de, URL: http://www.avm-akustik.de/.

Barth, M., 2009: Akustische Tomographie zur zeitgleichen Erfassung von Temperatur- und Strömungsfeldern. Wiss. Mitt. Inst. F. Meteorol. Univ. Leipzig, 44.

Barth, M., Raabe, A., 2011: Acoustic tomographic imaging of temperature and flow fields in air. *Meas. Sci. Technol.*, 22, 1-13 (doi: 10.1088/0957-0233/22/3/035102)
Bleisteiner, M., 2014: Ableitung von Raumtemperaturverteilungen aus Schallreflexionsmessungen. *Masterarbeit, Fachgebiet Audiokommunikation, TU-Berlin*, URL: https://www2.ak.tu-berlin.de/~akgroup/ak_pub/abschlussarbeiten/2014/BleisteinerMarcus_MasA.pdf.

Bohn, D. A., 1988: Environmental Effects on the Speed of Sound. *Journal of the Audio Engineering Society*, Vol. 36, No. 4, pp. 223–231.

Data Translation GmbH, 2014: Im Weilerlen 10, 74321 Bietigheim-Bissingen, Deutschland, URL: www.datatranslation.de/.

Dokmanic, I., Parhizkar, R., Walther, A., Lu, Y. M., Vetterli, M., 2013: Acoustic echoes reveal room shape. *Proceedings of the National Academy of Sciences*, Vol. 110, No. 30, pp. 12186–12191.

Dunn, C., Hawksford, M. J., 1993: Distortion immunity of MLS-derived impulse response measurements. *Journal of the Audio Engineering Society*, Vol. 41, No. 5, pp. 314–335.

Foken, T., 2006: *Angewandte Meteorologie*. Springer Vlg.

Four Audio GmbH & Co. KG, 2014: Bergdriesch 24-26, 52062 Aachen, Deutschland, E-Mail: info@four-audio.com, URL: http://www.four-audio.com/de/produkte/monkey-forest.html.

Holstein, P., Raabe, A., Müller, R., Barth, M., Mackenzie, D., Starke, E.,2004: Acoustic tomography on the basis of travel-time measurements. *Meas. Sci. Technol.*, 15, 1420-1428.

Kaimal, J., Businger, J., 1963: A continuous wave sonic anemometer- thermometer. *Journal of Applied Meteorology*, Vol. 2, No. 1, pp. 156–164.

Kemo Electronic GmbH, 2014: Leher Landstr. 20, 27607 Langen, Germany, http://www.kemo-electronic.de, E-Mail: info@kemo-electronic.de, URL:

http://www.kemo-electronic.de/de/Basteln-Schule/M032S-Universal-Verstaerker-12-W-Plug-Play.php.

Lüke, H. D., 1992: *Korrelationssignale*. Springer.

Masiero, B., Pollow, M., Fels, J., 2011: Design of a fast broadband individual head-related transfer function measurement system. *Proc. Forum Acusticum*, p. 136.

The MathWorks GmbH, 2014: Adalperostraße 45, 85737 Ismaning, Germany, URL: http://www.mathworks.de/products/matlab/.

Möser, M., 2012: *Technische Akustik*. Springer.

Rietschel, H., Fitzner, K.; 2004: *Raumklimatechnik: Band 3: Raumheiztechnik*. Springer.

SONOTEC Ultraschallsensorik Halle GmbH, 2014: Nauendorfer Straße 2, 06112 Halle (Saale), Deutschland, URL: http://www.sonotec.de/

Svensson, P., Nielsen, J. L., 1999: Errors in MLS measurements caused by time variance in acoustic systems. *Journal of the Audio Engineering Society*, Vol. 47, No. 11, pp. 907–927.

Testo AG, 2014: Testo-Straße 1, 79853 Lenzkirch, Deutschland, URL: http://www.testo.de/.

Tervo, S., 2011: Localization and Tracing of Early Acoustic Reflections. *Doctoral Dissertations, Vol. 143/2011, Aalto University publication series.*

Tetzlaff G, Arnold K, Raabe A and Ziemann A 2002 Observations of area-averaged near-surface wind- und temperature-fields in real terrain using acoustic travel time tomography. *Meteorol. Z., N.F.* **11** 273-283

Usher, J., 2010: An improved method to determine the onset timings of re- flections in an acoustic impulse response. *The Journal of the Acoustical Society of America*, Vol. 127, No. 4, pp. EL172–EL177.

Vecherin, S. N., Ostashev, V. E., Wilson, D. K., 2013: Assessment of systematic measurement errors for acoustic travel-time tomography of the atmosphere. *The Journal of the Acoustical Society of America*, Vol. 134, No. 3, pp. 1802–1813.

VISATON GmbH, 2014: Ohligser Straße 29-31, D-42781 Haan, Tel.: 02129/552-0, Fax 02129/552-10, E-Mail: visaton@visaton.com, URL: http://www.visaton.de/de/industrie/breitband/frs5xts_8.html.

Vorländer, M., 1994: Anwendung der Maximalfolgenmeßtechnik in der Akustik. *Fortschritte der Akustik*, Vol. 20, pp. 83–102.

Vorländer, M., Kob, M., 1997: Practical aspects of MLS measurements in building acoustics. *Applied Acoustics*, Vol. 52, No. 3, pp. 239– 258.

Wilson, D.K. und Thomson, D.W., 1994: Acoustic tomographic monitoring of the atmospheric surface layer. J. Atmos. Ocean. Technol., 11, 751-768.

Zuarbeit zum Forschungsbericht 2014
Bearbeitete Forschungsprojekte

Institut für Meteorologie

Direktor
Prof. Dr. M. Wendisch

Allgemeine Meteorologie
AG Atmosphärische Strahlung

Flugzeuggetragene und bodengebundene Messungen von Albedo, BRDF und Schneeeigenschaften in der Antarktis und deren Kopplung zur Verbesserung prognostischer Schneemodelle

Coupling of airborne and in situ ground based measurements of surface albedo, BRDF and snow properties in Antarctica to improve prognostic snow models

T. Carlsen (tim.carlsen@uni-leipzig.de), A. Ehrlich (a.ehrlich@uni-leipzig.de), M. Wendisch (m.wendisch@uni-leipzig.de)

Im Rahmen des Projekts werden die zeitliche und räumliche Variabilität von Oberflächenalbedo, bidirektionaler Reflektivität BRDF und Schneeeigenschaften in der Antarktis untersucht. Das Hauptziel dieses Vorhabens ist eine Verbesserung von prognostischen Schneemodellen und von Parametrisierungen der Schneealbedo, wie sie derzeit in regionalen und globalen Klimamodellen verwendet werden. Diese Parametrisierungen werden in Abhängigkeit von Schneekorngröße, Schneeoberflächenrauigkeit und atmosphärischen Parametern formuliert. Um dieses Ziel zu erreichen, werden bodengebundene in situ Messungen (zeitliche Variabilität) und flugzeuggetragene Fernerkundungsmessungen (räumliche Variabilität) miteinander kombiniert. Die vom Flugzeug erhobenen Daten umfassen die spektrale Bodenalbedo, BRDF, Bodenrauigkeit und Schneekorngröße. Die dazu benötigten Fernerkundungsverfahren werden im Rahmen des Projekts verbessert bzw. entwickelt werden. Die gleichen Größen werden auf dem antarktischen Plateau mittels bodengebundener Messungen an der Kohnen Station erhoben werden. Die bodengebundenen Daten decken dabei die zeitliche Variabilität von Schnee- und Atmosphäreneigenschaften ab, was es ermöglicht, prognostische Schneemodelle zu validieren und zu verbessern, die an ein Strahlungstransfermodel angekoppelt sind. Durch die Einbindung von Messdaten in die Modelle und einem anschließenden Vergleich zwischen simulierter und gemessener Schneealbedo sowie durch Sensitivitätsstudien werden Parametrisierungen der Schneealbedo, wie sie in Strahlungs- und Klimamodellen verwendet werden, validiert und verbessert. Diese Erkenntnisse werden dazu dienen, Unsicherheiten in Vorhersagen der zukünftigen Klimaänderung in der Antarktis zu reduzieren.

Weiterführung: ja

Finanzierung: Uni Leipzig, DFG WE 1900/29-1

Allgemeine Meteorologie
AG Atmosphärische Strahlung

Eine neue Methode zur bodengebundenen Fernerkundung von Profilen mikrophysikalischer Eigenschaften von Wolken mittels abtastender Radiometrie und Lidar

A novel method for ground-based remote sensing of profiles of cloud microphysical properties using scanning radiometry supplemented by Lidar

E. Jäkel (e.jaekel@uni-leipzig.de, M.Wendisch (m.wendisch@uni-leipzig.de)

Mit Hilfe einer neuen bodengebundenen aktiven und passiven Fernerkundungsmethode soll die vertikale Entwicklung der Wolkenmikrostruktur und das Tropfenwachstum in konvektiven Wolken untersucht werden. Für diesen Zweck werden Strahldichtemessungen (passiv) der an den Wolkenrändern reflektierten solaren Strahlung mit Lidarmessungen (aktiv) kombiniert. Die Wolkenseite wird mit beiden Geräten sowohl zeitlich als auch örtlich synchronisiert vermessen. Diese Messungen werden mit neuen Algorithmen zur Gewinnung von wolkenmikrophysikalischen Parametern kombiniert. Aus den analysierten Messungen kann dann ein Vertikalprofil der thermodynamischen Phase, sowie der effektive Wolkenpartikelradius abgeleitet werden. Dabei werden die drei-dimensionalen Strahlungseffekte der räumlich und zeitlich inhomogenen konvektiven Wolke berücksichtigt, was bei dieser Beobachtungsgeometrie unabdingbar ist.

Weiterführung: ja

Finanzierung: DFG JA 2023/2-1

Allgemeine Meteorologie
AG Atmosphärische Strahlung

Flugzeuggetragene Fernerkundung von Wolkenseiten mit abbildenen Spektroradiometern zur bestimmung von Profilen mikrophysikalischer Eigenschaften von konvektiven Wolken

Airborne remote sensing of cloud sides using imaging spectrometers to derive profiles of microphysical properties for deep convective clouds

S. Kanter (sandra.kanter@uni-leipzig.de), E. Jäkel (e.jaekel@uni-leipzig.de, M.Wendisch (m.wendisch@uni-leipzig.de)

Mit Hilfe von Flugzeuggetragenen Messungen an Wolkenseiten reflektierter solar Strahlung sollen vertikale Profile von mikrophysikalischen Wolkeneigenschaften, Wolkenphase und Größe der Wolkenpartikel, abgeleitet werden. Dazu wird eine Kombination zweier abbildender Spektrometer verwendet, die zusammen nahezu den gesamten solaren Spektralbereich abdecken. Die Messungen werden im Rahmen von ACRIDICON aus einem Seitenfenster des Forschungsflugzeuges HALO durchgeführt. Durch Vorbeiflüge an den Wolken können 2-dimensional Abbildungen der Wolken mit voller spektraler Auflösung gewonnen werden.

Insbesondere die spektralen Unterschiede in den Absorptionsbanden von flüssigem Wasser und Eis die mit dem System ausreichend aufgelöst werden, sollen dazu dienen die Phase der Wolkenpartikel in verschiedenen Höhen zu bestimmen. Gleichzeitig könne unter Annahme der Wolkenphase die Größen der Wolkenpartikel bestimmt werden. Durch die Unterschuchung von mehreren Wolken in verschiedenen Wachstumsstadien soll die mikrophysikalische Entwicklung der Wolken besser untersucht werden.

Weiterführung: ja

Finanzierung: MPI-Chemie Mainz

Allgemeine Meteorologie
AG Atmosphärische Strahlung

Räumlich inhomogene Zirren: Einfluss auf die atmosphärische Strahlung
Spatially Inhomogeneous Cirrus: Influence on Atmospheric Radiation
M. Wendisch (m.wendisch@uni-leipzig.de),
F. Finger (f.finger@uni-leipzig.de)

Die Strahlungseffekte durch inhomogene Zirren werden mit Hilfe einer Kombination von Flugzeuggetragenen Messungen (Strahlung und mikrophysikalische Eigenschaften), einem 3D Strahlungsmodell und einem dynamischen wolkenauflösenden Zirrus-Modell untersucht. Ein instrumentiertes Flugzeug (Lear-Jet) misst die spektrale Strahlung über Zirren im Rahmen einer Feldmesskampagne. Daraus werden die mikrophysikalischen Felder der Zirren abgeleitet. Diese werden verglichen mit gleichzeitigen in situ Messungen, welche mit einer Schleppsonde gesammelt werden. Diese wird gleichzeitig vom Flugzeug durch die Zirren gezogen wird. Parallel dazu werden die örtlichen Inhomogenitäten der Zirren Felder mit Hilfe einer abbildenden digitalen CCD Kamera beobachtet. Zusätzlich wird ein wolkenauflösendes Zirren-Modell benutzt zur Berechnung der mikrophysikalischen Zirren-Felder. Die aus den kombinierten in situ und indirekten Messungen abgeleiteten sowie modellierten mikrophysikalischen Zirren-Felder werden als Eingabe für ein 3D Strahlungsmodell benutzt, um die 3D-Effekte inhomogener Zirren zu untersuchen.

Weiterführung: ja

Finanzierung: DFG WE 1900/19-1

Allgemeine Meteorologie
AG Atmosphärische Strahlung

Solare Strahlungsmessungen auf HALO
Solar Radiation Measurements on HALO
C. Fricke (fricke@uni-leipzig.de)
M. Wendisch (m.wendisch@uni-leipzig.de)

HALO (High Altitude and LOng Range Research Aircraft) ist das Synonym für das neue deutsche Forschungsflugzeug mit dem es möglich sein wird, eine Vielzahl von verschiedensten atmosphärischen Parametern bis hin in die untere Stratosphäre zu messen. Aufgrund seiner Reichweite, sowohl in vertikaler als auch in horizontaler Richtung bietet HALO die Möglichkeit großräumige Strahlungsfelder zu erfassen. Während zwei HALO Demo-Missionen kommen dabei neu entwickelte Spektrometersysteme zur spektralen Erfassung solarer Strahlung zum Einsatz. Die dabei ermittelten Messgrößen sind zum einen die (i) spektrale Strahlflussdichte, welche den solaren Strahlungshaushalt der Atmosphäre bestimmt, sowie die (ii) spektrale aktinische Flussdichte, welche photolytische Prozesse innerhalb der Atmosphäre kontrolliert. Die solare spektrale Strahldichte in Nadir-Richtung wird für Fernerkundungsuntersuchungen zusätzlich simultan gemessen. Für die Strahlflussdichten ist es dabei entscheidend, die aufwärts- sowie abwärts gerichteten Flussdichten, welche mittels der Kosinusempfänger oberhalb und unterhalb des Flugzeugs empfangen werden, zu unterscheiden. Hierfür sind Stabilisierungsplattformen vorgesehen, die die Bewegungen des Flugzeuges aufzeichnen und die Position der Empfänger mit hinreichender zeitlicher Verzögerung korrigieren. Bezüglich der aktinischen Flussdichte ist die Kombination aus hoher zeitlicher Auflösung und hoher Genauigkeit innerhalb des UV-B Bereiches die größte Herausforderung. Realisiert wird selbige durch eine entsprechende Kombination aus Monochromatoren und Detektoren. Die aus allen Daten gewonnenen Erkenntnisse sollen zur Modellverbesserung verwendet werden, um sowohl Oxidationsprozesse als auch die mikrophysikalischen Prozesse, welche für die Bildung und zeitlichen Entwicklung von Zirren verantwortlich sind, besser zu verstehen.

Weiterführung: ja

Finanzierung: DFG WE 1900/21-1

Allgemeine Meteorologie
AG Atmosphärische Strahlung

HALO Koordination von “Aerosol, Cloud, Precipitation, and Radiation Interactions and Dynamics of Extra-Tropical Convective Cloud Systems” (ACRIDICON)

HALO coordination of ACRIDICON
D. Rosenow (d.rosenow@uni-leipzig.de)
M. Wendisch (m.wendisch@uni-leipzig.de)

Konvektive Wolken können erheblichen ökonomischen Schaden verursachen aufgrund von starken Windböen, heftigen Schauern und Niederschlagen, welche teilweise mit Hagel, Graupel, und Gewittern verbunden sein können. Die Dynamik und Heftigkeit dieser ausgeprägten Wettererscheinungen werden bestimmt durch mikrophysikalische Prozesse bei der Wolken- und Niederschlagsbildung, welche beeinflusst werden können durch Aerosolpartikel und Wechselwirkungen mit atmosphärischer Strahlung. Weiterhin werden durch konvektive Wolken Spurengase und Aerosolpartikel prozessiert und umverteilt durch vertikalen Transport sowie Ein- und Ausmischen der Wolke mit der Umgebungsluft. Um diese Wechselwirkungen zwischen Spurengasen, Aerosolpartikeln und der Wolken- und Niederschlagsbildung sowie atmosphärischer Strahlung in außertropischen,

konvektiven Wolken zu untersuchen, wurde die HALO Demo-Mission “Aerosol, Wolken, Niederschlag, und Strahlungswechselwirkungen sowie Dynamik von außertropischen, konvektiven Wolkensystemen (ACRIDICON)” vorgeschlagen. ACRIDICON trägt bei zu zwei Schwerpunkten des SPP 1294 bei: „Wolken und Niederschlag“ und „Transport und Dynamik in der Troposphäre und der unteren Stratosphäre“. Der vorliegende Antrag beinhaltet hauptsächlich die Organisation und das Management von ACRIDICON sowie teilweise einen Beitrag zur Analyse und Auswertung der Strahlungsmessungen, welche bei dieser HALO Demo-Mission gesammelt werden.

Weiterführung: ja

Finanzierung: DFG WE 1900/22-1

Allgemeine Meteorologie
AG Atmosphärische Strahlung

Koordination des Schwerpunktsprogramms 1294 "Atmosphären- und Erdsystemforschung mit dem Forschungsflugzeug HALO (High Altitude and Long Range Research Aircraft)"
HALO coordination project
M. Wendisch (m.wendisch@uni-leipzig.de)
D. Rosenow (d.rosenow@uni-leipzig.de)

Das Projekt dient vornehmlich der Kooperation und der Kommunikation unter den Einzelprojekten des Schwerpunktprogramms. Im Rahmen des Projekts werden ein jährliches Statusseminar sowie jährliche Themen-Workshops geplant und durchgeführt. Die drei Koordinatoren vertreten den SPP gegenüber der DFG, dem Wissenschaftlichen Lenkungsausschuss von HALO (WLA), dem HALO Projektteam des Deutschen Zentrums für Luft- und Raumfahrt (DLR) und nach außen. Das Koordinatoren-Team betreibt Maßnahmen zur Nachwuchs- und Gleichstellungsförderung. Zentrale Initiativen wie gemeinsame Sammelveröffentlichungen in einem Sonderband oder die Durchführung von Sitzungen zu Themenschwerpunkten ("special sessions") bei internationalen Konferenzen sowie der Internetauftritt des SPP werden im Rahmen dieses Projekts koordiniert und durchgeführt.

Weiterführung: ja

Finanzierung: DFG WE 1900/24-1

Allgemeine Meteorologie
AG Atmosphärische Strahlung

EUFAR2 - European Facility for Airborne Research in Environmental and Geo-sciences
M. Wendisch (m.wendisch@uni-leipzig.de)
D. Rosenow (d.rosenow@uni-leipzig.de)

Im Rahmen dieses Projektes werden die Expert Working Groups koordiniert. Workshops werden organisiert, und ein Buch wurde geschrieben:

Wendisch, M., and J.-L. Brenguier, Airborne Measurements – Methods and Instruments. In preparation to be published by *Wiley & Sons.*

Weiterführung: ja

Finanzierung: EU

Allgemeine Meteorologie
AG Atmosphärische Strahlung

Spektrale Strahlungsbilanz über dem Atlantik aus Modell und Beobachtung
Spectral radiation budget over the Atlantic Ocean from model and observation
A. Macke (macke@tropos.de)
M. Wendisch (m.wendisch@uni-leipzig.de)
M. Brückner (mbrueck@rz.uni-leipzig.de)
B. Pospichal (bernhard.pospichal@uni-leipzig.de)

Der Stoff- und Energieaustausch zwischen Ozean und Atmosphäre spielt eine entscheidende Rolle für die physikalische, chemische und biologische Entwicklung unseres Klimasystems Erde. Die von den beteiligten Forschungseinrichtungen entwickelten und eingesetzten Technologien zur in-situ Messung im Ozean und zur aktiven/passiven Fernerkundung der Atmosphäre, ermöglichen erstmalig durch eine Kombination dieser Daten eine kontinuierliche Erfassung relevanter Parameter. Im Rahmen des WGL-Verbundprojekts OCEANET wurde in Zusammenarbeit der Forschungseinrichtungen (IFM-GEOMAR, IfT Leipzig, Universität Leipzig, GKSS Geesthacht, AWI) eine autonome Messplattform entwickelt, die langfristig für den operationellen Betrieb an Bord von Fracht- und Forschungsschiffen vorgesehen ist.
Zum Verstehen des Klimasystems Ozean und Atmosphäre spielen Wolken und Strahlung eine wichtige Rolle. Da die Wolkenstrukturen sehr inhomogen sind und damit für Strahlungsübertragungsprozesse entscheidend sind, müssen diese Prozesse in Strahlungsparametrisierungen berücksichtigt werden. Eine Kombination der Beobachtung von physikalischen Eigenschaften und Strahlungseigenschaften von Wolken sind eine Möglichkeit solche Parametrisierungen anzugleichen oder zu validieren. Mithilfe der Erweiterung der breitbandigen Strahlungsflussdichtemessungen auf spektrale Strahldichte- und Strahlungsflussdichtemessungen mit einem bodengebundenem Spektrometer (CORAS) können unterschiedliche Wolkentypen zugeordnet werden. Beobachtete Atmosphärenzustände werden in ein 3D-Monte-Carlo Strahlungstransportmodell eingegeben, sodass die Ergebnisse mit den gemessenen Parametern verglichen werden können. Die Messungen finden weitestgehend auf FS Polarstern statt.

Weiterführung: ja

Finanzierung: Leibniz-Institut für Troposphärenforschung (TROPOS)

****

Allgemeine Meteorologie
AG Atmosphärische Strahlung

Ein Monte Carlo Modell zur Berechnung spektraler atmosphärischer Strahlungsgrößen unter Berücksichtigung von Polarisationsprozessen
A Monte Carlo Model to calculate atmospheric radiation considering polarization
M. Wendisch (m.wendisch@uni-leipzig.de)
A. Macke (macke@tropos.de)

Hierbei wird ein neues Strahlungsübertragungsmodell aufgebaut welches explizit Polarisationseffekte berücksichtigt. Das Modell soll nach Fertigstellung mit ähnlichen Modellen verglichen und durch entsprechende Messungen validiert werden.

Weiterführung: ja

Finanzierung: Leibniz-Doktorandenschule

****

Theoretische Meteorologie
AG Wolken und globales Klima

Evaluierung des Einflusses von kurzlebigen Verschmutzungen der Atmosphäre auf Klima und Luftqualität
Evaluating the climate and air quality impacts of short-lived pollutants (ECLIPSE)

Koordinator: A. Stohl, Norwegian Institute for Air Research (ast@nilu.no)
Beitrag der Universität Leipzig: J. Quaas (johannes.quaas@uni-leipzig.de)
Ribu Cherian (ribu.cherian@uni-leipzig.de)

ECLIPSE hat zum Ziel, effektive Emissions-Reduktions-Strategien für kurzlebige, klimarelevante Verschmutzungsstoffe in der Atmosphäre zu entwickeln und zu evaluieren. Gase und Aerosole wie Stickoxide, Kohlenwasserstoffe, Sulfat und Ruß werden derzeit nicht in klimapolitische Maßnahmen einbezogen. Eine Reduktion kann aber der Abmilderung des Klimawandels dienen und gleichzeitig die Luftqualität verbessern. In ECLIPSE trägt die Universität Leipzig gekoppelte Klimasimulationen mit dem Modellsystem ECHAM6-HAM/MPIOM bei und analysiert Beobachtungen der Klimaänderungen in Osteuropa nach der Wende.

Weiterführung: ja

Finanzierung: EU FP7

Theoretische Meteorologie
AG Wolken und globales Klima

Monitoring von Zusammensetzung der Atmosphäre und Klima – III.
Monitoring atmospheric composition and climate – III (MACC-III)

Koordinator: V.-H. Peuch, Europäisches Zentrum für Mittelfristige Wettervorhersage (Vincent-Henri.Peuch@ecmwf.int)
Beitrag der Universität Leipzig: J. Quaas (johannes.quaas@uni-leipzig.de)

Johannes Mülmenstädt (johannes.muelmenstaedt@uni-leipzig.de)

Im Rahmen des europäischen Beitrags für das globale Monitoring für Umwelt und Sicherheit (Global Monitoring for Environment and Security, GMES), bildet MACC den Vorläufer des operationellen Dienstes für die Atmosphärenkomponente. Dabei wird durch die Assimilation einer Vielzahl von Beobachtungen der Zusammensetzung der Atmosphäre in einer neuen Version des Wettervorhersagemodells des Europäischen Zentrums für mittelfristige Wettervorhersage (EZMW) ein konsistenter Datensatz geschaffen. Beitrag der Universität Leipzig ist es, den Klimaantrieb durch den anthropogenen Beitrag zur Aerosolbelastung aufgrund ihres Einflusses auf die Wolken zu berechnen. Auf Basis des neuen Datensatzes soll ein verbesserter Ansatz entwickelt werden.

Weiterführung: ja

Finanzierung: EU Horizon2020

Theoretische Meteorologie
AG Wolken und globales Klima

High Definition Clouds and Precipitation for Climate Prediction (HD(CP)²) – Teilprojekte
HD(CP)² - O2 Full-domain observations
HD(CP)² - S1 Diagnostics
HD(CP)² - S6 PDF cloud schemes

Koordinator: Bjorn Stevens, Max-Planck-Institut für Meteorologie
(bjorn.stevens@zmaw.de)
Beitrag der Universität Leipzig: J. Quaas (johannes.quaas@uni-leipzig.de)
Christine Nam (christine.nam@uni-leipzig.de)
Odran Sourdeval (odran.sourdeval@uni-leipzig.de)
Matthias Brück (matthias.brueck@uni-leipzig.de)

Ziel von HD(CP)² ist es, Parametrisierungen von Wolken- und Niederschlagsprozessen in Klimamodellen zu verbessern, und die Verbesserung der simulierten Wolken-Klima-Feedbacks nachzuweisen. Dazu wird in den Teilprojekten zur Modellierung eine hochaufgelöste (100 m horizontal) Simulation für mehrere Monate über Mitteleuropa vorbereitet, die als Referenz dienen kann. In den Teilprojekten zur Beobachtung werden Datensätze erstellt, die der Evaluierung dieses Modells und der Erstellung oder Verbesserung und Evaluierung von Klimamodellparametrisierungen dienen. In O2 werden konkret Messnetze (Niederschlagsradar, GPS, Ceilometer) und Satellitendaten für flächige Informationen über dem gesamten HD(CP)²-Gebiet aufgearbeitet. In den Teilprojekten zur Synthese wird darauf hingearbeitet, die sehr großen Datenmengen der geplanten Simulation sinnvoll zu verarbeiten. Konkret werden in Teilprojekt S1 Diagnostiken entwickelt, die relevante Metriken online während der Simulation berechnen, so dass kein Herausschreiben von sehr großen Datensätzen und Postprocessing nötig ist. Im Beitrag der Universität Leipzig werden hier Joint-PDFs konstruiert, die für Wolkenparametrisierungen relevant sind. In Teilprojekt S6 wird die Nutzung dieser PDFs für die Evaluierung von Wolkenparametrisierungen in Klimamodellen, die auf Wahrscheinlichkeitsdichtefunktionen (probability density functions, PDFs) der subskaligen

Verteilung von der Gesamtwasser-spezifischen Feuchte und ggf. anderen Größen basieren, vorbereitet. Dazu werden Sensitivitätssimulationen mit ECHAM6 mit verschiedenen Wolkenparametrisierungen durchgeführt, und eine Evaluierung auf der Basis der HD(CP)²-Beobachtungen vorgenommen.

Weiterführung: ja

Finanzierung: BMBF

Theoretische Meteorologie
AG Wolken und globales Klima

Quantifying Aerosol-Cloud-Climate Effects by Regime

Koordinator: Johannes Quaas, Universität Leipzig (johannes.quaas@uni-leipzig.de)
Beitrag der Universität Leipzig: J. Quaas (johannes.quaas@uni-leipzig.de)
Dipu Sudhakar (dipu.sudhakar@uni-leipzig.de)
Claudia Unglaub (unglaub@rz.uni-leipzig.de)
Karoline Block (karoline.block@uni-leipzig.de)

Ziel von QUAERERE ist die verlässliche Quantifizierung des Strahlungsantriebs von anthropogenen Aerosolen durch ihren Effekt auf Wolken. Aufbauend auf früheren Arbeiten sollen hierzu Satellitendaten verschiedener Instrumente kombiniert und in einem statistischen Ansatz ausgewertet werden. Die Aerosol-Informationen für diese Studie stammen dabei nicht direkt aus Satellitendaten, sondern in wesentlich verbesserter Qualität aus der Reanalyse des MACC-II-Projetks. Die statistische Analyse soll für einzelne Wolken-Aerosol-Regime durchgeführt werden. Neben dieser beobachtungsbasierten Abschätzung sollen Simulationen mit dem regionalen Aerosol-Klima-Modell COSMO-MUSCAT (in Zusammenarbeit mit dem Leibniz-Institut für Troposphärenforschung) durchgeführt werden, die in Sensitivitätsstudien mit abgeschalteten anthropogenen Emissionen dazu dienen können, in den statistischen Korrelationen aus den Satellitendaten Kausalzusammenhänge nachzuweisen. Schließlich soll in Simulationen mit dem globalen Aerosol-Klima-Modell ECHAM6-HAM2 eine globale Abschätzung erzielt werden, die konsistent ist mit der beobachtungsgestützten Abschätzung.

Weiterführung: ja

Finanzierung: Europäischer Forschungsrat (ERC)

****

Theoretische Meteorologie
AG Wolken und globales Klima

Learning about cloud brightening under risk and uncertainty: Whether, when and how to do field experiments (LEAC)

Koordinator: Johannes Quaas, Universität Leipzig (johannes.quaas@uni-leipzig.de)
Beitrag der Universität Leipzig: J. Quaas (johannes.quaas@uni-leipzig.de)
Aswathy Nair (aswathy.nair@uni-leipzig.de)

Im Rahmen des Schwerpunktprojekts „Climate engineering – risks, challenges, opportunitites?“ der Deutschen Forschungsgemeinschaft untersucht das Projekt „LEAC“ den Vorschlag, mit Hilfe des Impfens von marinen Grenzschichtwolken mit Meersalzaerosol diese heller zu machen und so das Klima zu kühlen. Ein möglicher nächster Schritt der Forschung wäre gerade für diesen Vorschlag ein Feldexperiment, das in Raum und Zeit begrenzt sein könnte. Durch Analyse von Satellitendaten und Modellsimulationen wird zunächst untersucht, wie die Unsicherheit bezüglich des zu erreichenden Strahlungsantriebs als Funktion der Größe in Raum und Zeit eines Feldexperiments reduziert werden könnte. Auch mögliche Nebeneffekte werden untersucht. In Zusammenarbeit mit der Arbeitsgruppe Umweltökonomie der Universität Kiel werden sozio-ökonomische Aspekte der Frage beleuchtet.

Weiterführung: ja

Finanzierung: Deutsche Forschungsgemeinschaft (DFG)

****

Hochatmosphäre
Upper Atmosphere

Einfluss der QBO und solarer Variabilität auf stratosphärische Dynamik und Ozongehalt
Influence of the QBO and solar variability on stratospheric dynamics and ozone

Prof. Dr. Christoph Jacobi (jacobi @ rz.uni-leipzig.de), Prof. A.I. Pogoreltsev, E. Rakushina, Russian State Hydrometeorological University

Innerhalb des Projekts sollen die Variabilität stratosphärischer dynamischer Parameter und stratosphärischen Ozons untersucht werden. Insbesondere soll der Zusammenhang des Frühjahrsübergangs mit stratosphärischer Erwärmungen und der Einfluss externer Parameter wie der QBO und solarer Variabilität auf das Verhalten es Polarwirbels untersucht werden.

Weiterführung: nein

Finanzierung: DAAD, Leonhard-Euler-Stipendium

****

Hochatmosphäre
Upper Atmosphere

Großskalige atmosphärische Prozesse
Large-scale atmospheric processes

Prof. Dr. Christoph Jacobi (jacobi @ rz.uni-leipzig.de), Prof. V. Yankovsky, Prof. G. Shved, S. Vasileva, E. Fodotova, St. Petersburg State University

Innerhalb des Projekts sollen einerseits theoretische Methoden erarbeitet und erweitert werden, Eigenschwingungen der Atmosphäre zu beschreiben und ihre Wechselwirkung mit der festen Erde zu erfassen. Andererseits sollen

Kohlenstoffmessungen in der Atmosphäre durchgeführt werden und ihr Ursprung durch Rückwärtstrajektorienrechnung bestimmt werden.

Weiterführung: nein

Finanzierung: DAAD, Leonhard-Euler-Stipendium

****

Hochatmosphäre
Upper Atmosphere

IMF-Einfluss auf die Atmosphäre
IMF-Influence on the atmosphere

Prof. Dr. Christoph Jacobi (jacobi @ rz.uni-leipzig.de), Prof. A.N. Fahrutdinova, M. Elahkov, Kasaner Föderale Universität

Die Dynamik der mittleren und oberen Atmosphäre wird unter anderem auch durch die Polarität des interplanetaren magnetischen Feldes (IMF) beeinflusst. Es soll anhand der Radarwinddaten aus Kasan untersucht werden, inwieweit ein Effekt auf den Wind bei Änderung der Polarität des IMF sichtbar ist.

Weiterführung: ja

Finanzierung: DAAD, Leonhard-Euler-Stipendium

****

Hochatmosphäre
Upper Atmosphere

Untersuchung der Anregungsmechanismen der 8-stündigen solaren Gezeiten in der mittleren Atmosphäre
Analysis of forcing mechanisms of the terdiurnal tide in the middle atmosphere

Prof. Dr. Christoph Jacobi (jacobi @ rz.uni-leipzig.de), F. Lilienthal

Ein nichtlineares mechanistisches Zirkulationsmodell der mittleren Atmosphäre wird verwendet, um die Anregungsmechanismen der 8-stündigen Gezeiten in der mittleren Atmosphäre zu untersuchen. Das verwendete Modell MUAM (Middle and Upper Atmosphere Model) verfügt über Strahlungsroutinen zur selbstkonsistenten Anregung von Gezeiten. Zur Analyse der Gezeitenanregung werden im Modell die potenziellen Anregungsmechanismen einzeln und gemeinsam abgeschaltet. Die zu untersuchenden Anregungsmechanismen sind einerseits die direkte Anregung durch die 8-stündige Komponente im Strahlungsforcing und andererseits die nichtlineare Wechselwirkung der ganz- und halbtägigen Gezeiten, repräsentiert in den Advektionstermen der Bewegungsgleichungen. Durch Vergleich mit Referenzläufen mit vollständiger Gezeitenanregung wird es möglich sein, die Anteile der jeweiligen Anregungsmechanismen am gesamten Wellenforcing zu bestimmen. Die Arbeiten werden komplettiert durch Analyse von Radar- und Satellitendaten.

Weiterführung: ja

Finanzierung: Deutsche Forschungsgemeinschaft (DFG)

****

Allgemeine Meteorologie
AG Bodengebundene Fernerkundung
Ground-based remote sensing

HD(CP)²-High definition clouds and precipitation for advancing climate prediction

Jun.-Prof. Dr. Bernhard Pospichal (bernhard.pospichal@uni-leipzig.de
MSc Andreas Foth (andreas.foth@uni-leipzig.de)

Dieses Projekt beschäftigt sich mit einem sehr relevanten Thema in der aktuellen meteorologischen Forschung, nämlich der Repräsentation von Wolken in Atmosphärenmodellen. Dabei sind noch viele Unsicherheiten, sowohl auf der Beobachtungs- als auch auf der Modellseite zu bemängeln. Im Rahmen von HD(CP)² wird die Expertise zu diesem Themenkomplex deutschlandweit gebündelt. Intensivierte Beobachtungen an verschiedenen Orten, sowie die Kombination verschiedener Messverfahren, soll es u.a. ermöglichen, bessere Parametrisierungen von Wolken in Modellen zu erhalten.
Am LIM soll in diesem Zusammenhang ein neuer Algorithmus zur Bestimmung vertikaler Wasserdampfverteilung aus Fernerkundungsdaten (passive Mikrowellenradiometer und Raman-Lidar) erstellt werden. Dabei werden Daten, die im Rahmen des Projekts bei Messkampagnen in Jülich (HOPE) und Melpitz (HOPE-2) gewonnen wurden, verwendet.

Weiterführung: ja

Finanzierung: BMBF, FKZ: 01LK1209D

****

Allgemeine Meteorologie
AG Bodengebundene Fernerkundung
Ground-based remote sensing

Leibniz Graduiertenschule Wolken-Aerosol-Strahlung *(Leibniz Graduate School Clouds-Aerosol-Radiation)*

Jun.-Prof. Dr. Bernhard Pospichal (bernhard.pospichal@uni-leipzig.de
MSc Daniel Merk (merk@tropos.de)

Im Rahmen der Graduiertenschule Wolken-Aerosol-Strahlung soll im Rahmen von sieben Promotionen der indirekte Aerosoleffekt von verschiedenen Seiten (Mikrophysik, Chemie, Fernerkundung, etc.) betrachtet werden. Die hier vorliegende Arbeit befasst sich mit Fernerkundungsbeobachtungen. Das Besondere daran ist die Verknüpfung von Satellitendaten (SEVIRI sichtbar und nahes Infrarot) und bodengebundener Fernerkundung (Lidar, Radar, Mikrowellenradiometer im Rahmen von LACROS). Daraus soll eine verbesserte Charakterisierung von Flüssigwasserwolken im Hinblick auf deren

mikrophysikalischen Eigenschaften (effektiver Radius, optische Dicke) abgeleitet werden.

Weiterführung: ja

Finanzierung: Leibniz-Gesellschaft (Zusammenarbeit mit TROPOS)
****

Allgemeine Meteorologie
AG Akustik
Acoustics

Sensormodul und Dispatcher-System zur intelligenten und autonomen Überwachung von Umgebungsbedingungen in Rechenzentren und Serverräumen (SenDiServ)
Sensor module and dispatcher system for intelligent and autonomous monitoring of environmental conditions in data centers and server rooms (SenDiServ)

Dr. Armin Raabe (raabe@uni-leipzig.de),Manuela Barth (mbarth@uni-leipzig.de), gemeinsam mit
RÖWAPLAN AG, Brahmsweg 4, 73453 Abtsgmünd
Und
GED Gesellschaft für Elektronik und Design mbH, Pastoratsstraße 3, 53809 Ruppichteroth-Winterscheid

Es wird eine modulare, miniaturisierte Sensorplattform zur Erfassung und Überwachung von über Schallsignalanalysen ermittelte Luftströmungen und Temperaturverteilungen entwickelt. Das Projekt basiert auf Arbeiten zur akustischen Laufzeittomografie, die am LIM durchgeführt wurden. Die Verfahren werden auf Innenräume umgesetzt und sollen so angewendet werden, dass eine Reduzierung des Kühlenergieverbrauchs bei der Klimatisierung von Räumen (u.a. von Rechenzentren und Serverräumen) möglich wird.

Weiterführung: Nein

Finanzierung: BMWi, Zentrales Innvovationsprogramm Mittelstand (ZIM), Förderkennzeichen **AIF FKZ KF2709802DF2**
****

Allgemeine Meteorologie
AG Akustik
Acoustics

Lärm- und Feldlagerschutz der Bundeswehr

Dr. A. Raabe (raabe@uni-leipzig.de), Dipl. Met. Michael Wilsdorf (mwils@uni-leipzig.de), Dipl. Met. Jörg Walter

Die Bewertung von Schallimmissionen, deren Quellen sich in großen Entfernungen (bis zu 15km), aber auch in der näheren Umgebung (weniger als 5km) von

Truppenübungsplätzen, oder auch Feldlagern der Bundeswehr befinden, ist ohne Berücksichtigung der aktuellen Wettersituation nicht möglich. Das heißt, dass die Ausbreitung akustischer Signale über mehrere Kilometer Entfernung wesentlich von der Temperatur- und Windvektorverteilung in dem Teil der Atmosphäre abhängen, durch den sich die Schallwellen ausbreiten. Die bisherige Vorgehensweise bei der Beachtung atmosphärischer Verhältnisse im Zusammenhang mit Schallimmissionen basiert im Wesentlichen auf der Verwendung von Radiosondendaten. Ihr Nachteil besteht darin, dass meist nur wenige Radiosondenaufstiege am Tag (meist 2x) durchgeführt werden und (weltweit) sich nur wenige Stationen über ein riesiges Gebiet verteilen. Deshalb wird der Frage nachgegangen ob Wetter-Modelldaten die Radiosondendaten auf eine solche Weise ersetzen können, dass die auf Basis der Modelldaten abgeleiteten Aussagen bezogen auf die Schallimmissionsverhältnisse weitgehend identisch bleiben.

Weiterführung: Ja

Finanzierung: AGeoBw; M/U2CD/CA277/CA647

****

Allgemeine Meteorologie

Niederschlagsdaten zu historischen Hochwasserereignissen - Orografische Niederschlagsverstärkung
Precipitation data for historical flood events - Orographic precipitation enhancement

Dr. A. Raabe (raabe@uni-leipzig.de), Dipl. Met. Michael Wilsdorf (mwils@uni-leipzig.de), Dr. M. Barth (mbarth@uni-leipzig.de)

Für hydrologische Berechnungen sind für historische Niederschlagsereignisse im Gebiet der Mulde Niederschlagsverteilungskarten notwendig. Mittlerweile gestatten es die meteorlogischen Datenbanken auch historische Ereignisse flächenhaft zu analysieren. Die Beobachtungen werden mit Hilfe eines physikalischen Modelles in Beziehung zu den maximal möglichen Niederschlag gesetzt, was als planungsrelevante Größe für Wassereinzugsgebiete Verwendung findet. Spezielle wird dabei der Effekt der orografischen Niederschlagsverstärkung im Vergleich Modell / Beobachtung untersucht.

Weiterführung: Nein

Finanzierung: Landestalsperrenverwaltung des Freistaates Sachsen (LTV)

****

Allgemeine Meteorologie

Orografische Niederschlagsverstärkung am Erzgebirge
Orographic precipitation enhancement at the Erzgebirge

Dr. A. Raabe (raabe@uni-leipzig.de), Dipl. Met. Michael Wilsdorf (mwils@uni-leipzig.de), Dr. M. Barth (mbarth@uni-leipzig.de)

Für Starkregenereignisse werden die in den Beobachtungen tatsächlich dokumentierten Niederschlagsverstärkungseffekte zwischen dem Vorland des Erzgebirges und dem Erzgebirge selbst analysiert. Diese Niederschlagsverstärkung ergibt sich aus theoretischen Überlegungen, lässt sich aber für spezifische Niederschlagereignisse oft nur schwer deutlich zeigen. Für die extremen Fälle, werden die Wetterbedingungen dokumentiert, bei denen sich solche Niederschlagverstärkungen tatsächlich zeigen.

Weiterführung: Nein

Finanzierung: Landestalsperrenverwaltung des Freistaates Sachsen (LTV)

****

Allgemeine Meteorologie

Abschätzung maximaler Regenmengen für vorgegebene Wiederkehrintervalle unter Berücksichtigung einer Klimaänderung
Estimation of maximum rainfall rates for a given return period under consideration of climate change

Dr. A. Raabe (raabe@uni-leipzig.de), Dr. M. Barth (mbarth@uni-leipzig.de)

Die Wiederkehrzeiten starker Niederschlagmengen können aus Beobachtungen der letzten 100 Jahre auch für das Gebiet des Erzgebirges analysiert werden. Offen bleibt, inwieweit sich diese Wiederkehrzeiten für bestimmte Niederschlagsmengen verändern, wenn sich das Klima verändert. Unter Verwendung von Klimaszenarien wird untersucht, welche Veränderungen es in den nächsten 100 Jahren geben könnte. Diese Angaben gehen in die Planung von wasserwirtschaftlichen Anlagen ein.

Weiterführung: Nein

Finanzierung: Landestalsperrenverwaltung des Freistaates Sachsen (LTV)

****

2. Wiss. Veröffentlichungen Institut für Meteorologie 2014

Hauptautor	Autoren / Herausgeber	Titel, in: Zeitschrift, Ort; Verlag, Jahr, Seite von – bis ….
	Barlakas, V., A. Macke, M. Wendisch, A. Ehrlich	Implementation of polarization in a 3D Monte Carlo Radiative Transfer Model, Wiss. Mitteil. Instit. f. Meteorol. Universität Leipzig Bd. 52, S. 1-14
	Baumgardner, D., R. Newton, M. Krämer, J. Meyer, A. Beyer, M. Wendisch, and P. Vochezer	The Cloud Particle Spectrometer with Polarization Detection (CPSPD): A next generation open-path cloud probe for distinguishing liquid cloud droplets from ice crystals, Atmos. Res. doi:10.1016/j.atmosres.2013.12.010
	Brückner, M., Pospichal, A., Macke, A., and Wendisch, M.	A new multispectral cloud retrieval method for ship-based solar transmissivity measurements. J. Geophys. Res. doi:10.1002/2014JD021775
	Cherian, R.	doi:10.1002/2013GL058715
	Finger, F., F. Werner, M. Klingebiel, M. Wendisch, S. Borrmann	Collocated Airborne Measurements of Radiative Properties of Cirrus LayersWiss. Mitteil. Instit. f. Meteorol. Universität Leipzig Bd. 52, S. 15-24
	Fricke, C. A. Ehrlich, E. Jäkel, B. Bohn, M. Wirth, and M. Wendisch	Influence of local surface albedo variability and ice crystal shape on passive remote sensing of thin cirrus. Atmos. Chem. Phys, doi: 10.5194/acp-14-1943-2014
	Fytterer, T.	doi:10.1186/1880-5981-66-79
	Jacobi, Ch.	doi:10.5194/ars-12-161-2014
	Jacobi Ch.	Zonal prevailing wind trends derived from combined low frequency and VHF meteor radar wind measurements in the lower thermosphere over Collm (51.3°N, 13.0°E). Wiss. Mitteil. Instit. f. Meteorol. Universität Leipzig Bd. 52, S. 35-48.
	Jacobi Ch., Nikutowski, B.; Hein, J.; Unglaub, C.; Erhardt, C.; Brunner, R.; Schmidtke, G.	Solar activity and ionospheric response as seen from combined SolACES and SDO-EVE solar EUV spectra. Wiss. Mitteil. Instit. f. Meteorol. Universität Leipzig Bd. 52, S. 49-56
	Jacobi C.	doi:10.1016/j.jastp.2013.05.009
	Li, L., Zhengqiang L., and M. Wendisch	Stokes parameters calculated from Sun photometer measurements of polarized skylight. J. Quant. Spectr. & Rad. Trans 149, 334-346
	Lilienthal, F.	doi:10.5194/ars-12-205-2014
	Lilienthal, F, Jacobi, Ch.	Comparison of quasi-2-day wave amplitudes and phases over Collm (51.3°N, 13.0°E) based on two different analyses. Wiss. Mitteil. Instit. f. Meteorol. Universität Leipzig Bd. 52, S. 25-34.
	Ma, X.	doi: 10.1002/2014JD021670
	Nam, Ch.	doi: 10.1002/2013MS000277
	Otto, S.	Analytical properties of the radiance in atmospheric radiative transfer theory J. Quant. Spectr. & Rad. Trans. doi:10.1016/j.jqsrt.2013.08.018
	Peters, K.	doi:10.3402/tellusb.v66.24054
	Pospichal, B., Brückner, M., Macke, A., Wendisch, M.	A new multispectral cloud retrieval method for ship-based solar transmissivity measurements. Journal of Geophysical Research: Atmospheres, 119(19), 11-338.
	Berger, T., Amann, C., Formayer, H., Korjenic, A., Pospichal, B., Neururer, C., Smutny, R	Impacts of urban location and climate change upon energy demand of office buildings in Vienna, Austria. Building and Environment, 81, 258-269.

	Berger, T., Amann, C., Formayer, H., Korjenic, A., Pospichal, B., Neururer, C., Smutny, R	Impacts of climate change upon cooling and heating energy demand of office buildings in Vienna, Austria. Energy and Buildings, 80, 517-530.
	Raabe, A.,Wilsdorf, M.; Barth M.	Maximum Possible Precipitation over a low mountain range. Wiss. Mitteil. Instit. f. Meteorol. Universität Leipzig Bd. 52, S. 57-74
	Raabe, A.,Barth, M.; Holstein, P.	Akustische Tomografie und Raumklimatisierung. In: Lärmschutz in Bezug auf Mobilität und regenerative Energien, Wiss. Zeitschr. Hochschule Mittweida, Nr. 5, S.42-43
	Rosenfeld, D.	doi:10.1002/2013RG000441
	Salzmann, M.	doi:10.1002/2014JD021783
	Schmidtke, G.	doi:10.5194/ars-12-251-2014
	Schmidtke, G.	doi: 10.1007/s11207-013-0430-5
	Sourdeval, O.	doi: 10.1002/qj.2405
	Werner, F. F. Ditas, H. Siebert, M. Simmel, B. Wehner, P. Pilewskie, T. Schmeissner, R. A. Shaw, S. Hartmann, H. Wex, G. C. Roberts, M. Wendisch	Twomey effect observed from collocated microphysical and remote sensing measurements over shallow cumulus J. Geophys. Res. doi:10.1002/2013JD020131
	Yano J.-I.	doi: 10.3390/atmos6010088

3. Wissenschaftliche und technische Mitarbeiter am LIM 2014

Name	E-Mail
Barlakas, Vasileios	vasileios.barlakas@uni-leipzig.de
Barth, Manuela	mbarth@uni-leipzig.de
Block, Karoline	karoline.block@uni-leipzig.de
Brück, Matthias	matthias.brueck@uni-leipzig.de
Brückner, Marlen	m.brueckner@uni-leipzig.de
Can, Özge	oezge.can@tropos.de
Carlsen, Tim	tim.carlsen@uni-leipzig.de
Cherian, Ribu	ribu.cherian@uni-leipzig.de
Ehrlich, André	a.ehrlich@uni-leipzig.de
Feck-Yao, Wolfgang	feckyao@uni-leipzig.de
Finger, Fanny	fanny.finger@uni-leipzig.de
Foth, Andreas	andreas.foth@uni-leipzig.de
Gryspeerdt, Edward	edward.gryspeerdt@uni-leipzig.de
Hirsch, Kerstin	khirsch@uni-leipzig.de
Jacobi, Christoph	jacobi@rz.uni-leipzig.de
Jäkel, Evelyn	evi.jaekel@uni-leipzig.de
Kaiser, Falk	fkaiser@rz.uni-leipzig.de
Kanter, Sandra	sandra.kanter@uni-leipzig.de
Krisna, Trismono Candra	trismono_candra.krisna@uni-leipzig.de
Kühne, Philipp	NN
Lilienthal, Friederike	friederike.lilienthal@uni-leipzig.de
Mülmenstädt, Johannes	johannes.muelmenstaedt@uni-leipzig.de
Nair, Aswathy	aswathy.nair@uni-leipzig.de
Pospichal, Bernhard	bernhard.pospichal@uni-leipzig.de
Quaas, Johannes	johannes.quaas@uni-leipzig.de
Quaas, Johannes	johannes.quaas@uni-leipzig.de
Raabe, Armin	raabe@uni-leipzig.de
Rehnert, Jutta	rehnert@uni-leipzig.de
Rosenow, Dagmar	d.rosenow@uni-leipzig.de
Salzmann, Marc	marc.salzmann@uni-leipzig.de
Schäfer, Michael	michael.schaefer@uni-leipzig.de
Seydel, Birgit	birgit.seydel@uni-leipzig.de
Sourdeval, Odran	odran.sourdeval@uni-leipzig.de
Sudhakar, Dipu	dipu.sudhakar@uni-leipzig.de
Tetzlaff, Gerd	tetzlaff@uni-leipzig.de
Unglaub, Claudia	unglaub@uni-leipzig.de
Weiße, Frank	weisse@uni-leipzig.de
Wendisch, Manfred	m.wendisch@uni-leipzig.de
Werner, Frank	f.henrich@uni-leipzig.de
Wilsdorf, Michael	mwils@uni-leipzig.de

4. Immatrikulationen am Institut f. Meteorologie

BSC Meteorologie

Datum	Semester	1.FS	2. FS	3.FS	4.FS	5.FS	6. FS	7.FS	8.FS	9. FS	10.FS	>10.FS	Gesamt
15.10.2014	WS 14/15	35		14		15		3		3		1	71
15.10.2013	WS 13/14	39		23		21		13		4			100
15.10.2012	WS 12/13	60		29	1	22	2	16	1	2			133
15.10.2011	WS 11/12	60		27		26	1	19		1			134
15.10.2010	WS 10/11	64		34		20							118
15.10.2009	WS 09/10	67		21		20							108
15.10.2008	WS 08/09	71		28		12							111
15.10.2007	WS 07/08	98		15									113
13.12.2006	WS 06/07	31											31

MSC Meteorologie

Datum	Semester	1.FS	2. FS	3.FS	4.FS	>=5.FS	Gesamt
15.10.2014	WS 14/15	19		18		16	53
15.10.2013	Ws 13/14	18		16		20	54
15.10.2012	WS 12/13	18		20	1	15	54
15.10.2011	WS 11/12	21		17		10	48
15.10.2010	WS 10/11	20		9		5	34
15.10.2009	WS 09/10	11					11

Diplom Meteorologie

Datum	Semester	1.FS	2. FS	3.FS	4.FS	5.FS	6. FS	7.FS	8.FS	9. FS	10.FS	>10.FS	Meteo_Diplom
15.10.2013	WS 13/14											2	2
17.10.2012	WS 12/13											3	3
16.10.2011	WS 11/12											3	3
15.10.2010	WS 10/11											14	14
15.10.2009	WS 09/10								0	14	0	7	21
15.10.2008	WS 08/09						0	14	0	23	1	25	63
15.10.2007	WS 07/08				0	22	0	26	1	18	2	19	88
13.12.2006	WS 06/07		0	40	0	36	0	24	2	14	1	17	175
15.10.2005	WS 05/06	109	0	49	0	30	2	16	1	17	1	13	237
08.12.2004	WS 04/05	97	0	35	1	20	0	19	0	12	1	15	200
03.12.2003	WS 03/04	68	1	25	0	20	1	13	1	12	1	13	155
14.10.2002	WS 02/03	45	0	19	0	16	0	15	1	12	1	9	118
06.12.2001	WS 01/02	43	0	21	0	16	0	13	0	7	0	5	105
07.12.2000	WS 00/01	41	1	27	0	22	0	8	0	6	1	6	112
01.12.1999	WS 99/00	40	0	24	0	9	0	9	0	6	1	6	95
16.12.1998	WS 98/99	36	0	11	0	17	1	9	1	5	0	8	88
10.11.1997	WS 97/98	29	0	17	0	10	1	8	0	7	0	4	76

4. Abschlussarbeiten Institut für Meteorologie 2013

Promotionen

Christa Engler
Abschluss: 17.02.2014
Meteorologische Einflüsse auf die Konzentrationen feiner und grober atmosphärischer Aerosolpartikel in Deutschland

Timo Hanschmann
Abschluss: 17.02.2014
Unsicherheiten in der Erfassung des kurzwelligen Wolkenstrahlungseffektes

Stefan Bauer
Abschluss: 21.07.2014
Airborne spectral radiation measurements to derive solar radiative forcing of Saharan dust mixed with biomass burning smoke particles

Gionata Biavati
Abschluss: 14.04.2014
On the Retrieval of Mixing Height from Ceilometers

Florian Ditas
Abschluss: 21.07.2014
Microphysical properties of aerosol particles in the trade wind regime and their influence on the number concentration of activated particles in trade wind cumulus clouds

Jeannine Ditas
Abschluss: 19.05.2014
On the small-scale dynamics of cloud edges

Marcel König
Abschluss: 14.04.2014
Large-Eddy Simulation Modelling for Urban Scale

Nicole Niedermeier
Abschluss: 14.04.2014
Experimental determination of the mass deposition flux of mineral dust at the Cape Verde Islands

Sascha Pfeifer
Abschluss: 15.12.2014
Verknüpfung aerodynamischer und optischer Eigenschaften nichtkugelförmiger atmosphärischer Grobstaubpartikel

Frank Werner
Abschluss: 15.12.2014
Thema: Twomey Effect of Trade Wind Cumuli

Diplomarbeiten

Name / Vorname	**Thema**
Igloffstein, Julia (geb. Geisler)	Ableitung der optischen Dicke bei Cirrusbewölkung aus unabhängigen Strahldichte- und Lidar-Messungen

Bachelor- Abschlussarbeiten:

Osterloh, Vistoria	Reasons of Seasonality of the Meteorological Parameters on the Bolivian High Plateau "Altiplano"
Kunz, Clara	Heterogene Eisbildung im Amazonasgebiet
Carlsen, Tim	Simulation von heutigem und glazialem mineralischen Staubtransport im Klimamodell ECHAM5-HAM2
Berger, André	Temperaturprofile aus Mikrowellenradiometer-Beobachtungen am FS Polarstern
Bohlmann, Stephanie	Heterogene Eisbildung über Südostasien
Stapf, Johannes	Wie inhomogen sind subtropische Passatwindwolken-Felder?
Ulrich, Max	Characterization of Mediterranean dust outbreak events
Krug, Amelie	Simulation der achtstündigen Gezeiten
Löffler, Mareike	Types of ENSO in Conjunction with Cloud Feedbacks in Climate Model Simulations
Küchler, Tobias	Charakterisierung der synoptischen Situation während der Messkampange RACEPAC (April/Mai 2014)
Krause, Julia	Hemisphärische Unterschiede in Aerosolen, Wolken und Strahlung
Radenz, Martin	Variabilty of the atmospheric boundary layer assessed by high resolution ground based remote sensing
Faust, Matthias	Untersuchung der partikulären Bildung von Carbonsäuren durch die Oxidation von Isopren
Kretzschmar, Jan	Arktische Erwärmung und ihr Einfluss auf die mittleren Breiten
Kanngießer,Franz	Untersuchung der Strahlungsüberhöhung durch Wolken anhand von Globalstrahlungsmessungen am LI11
Samtleben, Nadja	Temperaturvariationen der oberen Mesosphäre/unteren Thermosphäre
Strehl, Pit	Ist ein Einfluss der Urbanisierung auf Wolken und Strahlung in Satellitendaten erkennbar?

Master-Abschlussarbeiten

Bier, Andreas	Studies on the modelling of the behaviour of liquid particles/droplets below the melting point of water at the Leipzig Aerosol Cloud Interaction Simulator (LACIS) with FLUENT/FPM
Stieger, Bastian	Aerosol- und Wolkenchemie: Kinetische und mechanistische Untersuchungen der Reaktionen von NO3- und SO4-Radikalen mit sauerstoffhaltigen organischen Verbindungen in wässriger Lösung
Rüffelt, Jörg	Statistische Analyse Wolkentemperatur und wolkenthermodynamischen Phase in Mischphasenwolken aus Satellitendaten
Rosch, Jan	Assessment of Climate Model cloud Parameterizations using Cloud Resolving- and Large Eddy Simulations
Kundisch, Marcus	Influence of air mass origin and seasons on aerosol particle size distribution and soot concentration at Chacaltaya (5,421 m ASL), Bolivia 2012
Kanter, Sandra	Untersuchung zum Immersionsgefrierverhalten von Illit und Feldspatpartikeln am Leipziger Aerosol Cloud Interaction Simulator (LACIS)
Hage, Benjamin	Einfluss der Luftmassenherkunft und der Jahreszeit auf die Anzahlkonzentration atmosphärischer Aerosolpartikel im urbanen Hintergrund zentral- und osteuropäischer Städte
Rehn, Johanna	Gewitteraktivität im Freistaat Thüringen und deren Zusammenhang mit der vertikalen Atmosphärenschichtung abgeleitet aus Radiosondenaufstiegen
Herenz, Paul	Investigations corresponding the influence of temporal change of the thermodynamic state on the surface area structure of ice particles
Lange, Stefan	Simulation solarer Variabilität der mittleren Atmosphäre
Kleinelanghorst, Christin	Klimasensitivität in der Region des Indischen Ozeans: Zeitskalen, Feedbacks und die Rolle der Ozeanzirkulation
Kühne, Philipp	Investigation of the feasibility of constraints on fast cloud-climate feedbacks from a regional cloud-resolving simulation
Rau, Andrea	Zeitaufgelöste Messungen kurzkettiger Dicarbonsäuren (DACs) in atmosphärischen Partikeln
Walther, Jonas	Schattenbandradiometer GUVis-3511- Strahlungsmessung und Bestimmung optischer Eigenschaften von Aerosol zu Wasser und Land
Hoffmann, Erik	Modellierung der troposphärischen Multiphasenchemie mit MCM-CAPRAM unter marinen und kontinentalen Hintergrundbedingungen

Wissenschaftliche Mitteilungen aus dem Institut für Meteorologie der Universität Leipzig

Band 1	*A. Raabe, G. Tetzlaff* und *W. Metz* (Edn.), 1995: Meteorologische Arbeiten aus Leipzig I
Band 2	*R. Devantier*, 1995: Wolkenbildungsprozesse über der südwestlichen Ostsee - Anwendungen eines neuen Wolkenschemas in einem mesoskaligen Modell
Band 3	*J. Laubach*, 1996: Charakterisierung des turbulenten Austausches von Wärme, Wasserdampf und Kohlendioxid über niedriger Vegetation anhand von Eddy-Korrelations-Messungen
Band 4	*A. Raabe* und *J. Heintzenberg* (Edn.), 1996: Meteorologische Arbeiten aus Leipzig II
Band 5	Wind- und Seegangsatlas für das Gebiet um Darß und Zingst *D. Hinneburg, A. Raabe* und *G. Tetzlaff*, 1997: Teil I: Windatlas
Band 6	*W. von Hoyningen-Huene* und *G. Tetzlaff* (Edn.), 1997: Sediment and Aerosol Teil I: Beiträge zur Alfred-Wegener-Konferenz, Leipzig 1997 Teil II: Aktuelle Beiträge aus dem Institut für Meteorologie
Band 7	*B.-R. Beckmann*, 1997: Veränderungen in der Windklimatologie und in der Häufigkeit von Sturmhochwassern an der Ostseeküste Mecklenburg-Vorpommerns
Band 8	*P. Posse*, 1997: Bestimmung klimarelevanter Parameter des maritimen Aerosols unter besonderer Berücksichtigung der Nichtkugelform realer Aerosolteilchen
Band 9	*A. Raabe, K. Arnold* und *J. Heintzenberg* (Edn.),1998: Meteorologische Arbeiten aus Leipzig III
Band 10	Wind- und Seegangsatlas für das Gebiet um Darß und Zingst, Teil II, 1998: *D. Hinneburg, A. Raabe* und *G. Tetzlaff*: Vergleich Windatlas –Beobachtungsdaten; *M. Börngen, H.-J. Schönfeldt, F. Riechmann, G. Panin* und *G. Tetzlaff:* Seegangsatlas; *M. Stephan* und *H.-J. Schönfeldt*: Sedimenttransportatlas
Band 11	*J. Rissmann, 1998*: Der Einfluss langwelliger Strahlungsprozesse auf das bodennahe Temperaturprofil
Band 12	*A. Raabe, K. Arnold* und *J. Heintzenberg* (Edn.), 1999*:*Meteorologische Arbeiten aus Leipzig IV
Band 13	*U. Müller, W. Kuttler und G. Tetzlaff (Edn.)*, 1999: Workshop Stadtklima 17. / 18. 02. 1999 in Leipzig
Band 14	*R. Surkow, 1999*: Optimierung der Leistungsverfügbarkeit von Windenergie durch ihre Integration in Wind-Biogas-Hybridanlagen
Band 15	*N. Mölders*, 1999: Einfache und akkumulierte Landnutzungsänderungen und ihre Auswirkungen auf Evapotranspiration, Wolken- und Niederschlagsbildung
Band 16	*G. Tetzlaff* und *U. Grünewald* (Edn.), 1999:2. Tagung des Fachausschusses Hydrometeorologie 15./16. 11. 1999 in Leipzig
Band 17	*A. Raabe* und *K. Arnold* (Edn.), 2000: Meteorologische Arbeiten aus Leipzig V
Band 18	*K. Arnold*, 2000: Ein experimentelles Verfahren zur Akustischen Tomographie im Bereich der atmosphärischen Grenzschicht
Band 19	*A. Ziemann*, 2000: Eine theoretische Studie zur akustischen Tomographie in der atmosphärischen Grenzschicht
Band 20	*Ch. Jacobi*, 2000: Midlatitude mesopause region dynamics and its coupling with lower and middle atmospheric processes
Band 21	*M. Klingspohn*, 2000: Interdekadische Klimavariabilität über dem Nordatlantik – Statistische Analysen und Modellstudien –
Band 22	*A. Raabe* und *K. Arnold* (Edn.), 2001: Meteorologische Arbeiten aus Leipzig VI
Band 23	*K. Arnold, A. Ziemann, G. Tetzlaff, V. Mellert* und *A. Raabe* (Edn.), 2001: International Workshop Tomography and Acoustics: Recent developments and methods 06. - 07.03.2001 in Leipzig
Band 24	*O. Fanenbruck*, 2001: Ein thermophysiologisches Bewertungsmodell mit Anwendung auf das Leipziger Stadtgebiet
Band 25	*M. Lange*, 2001: Modellstudien zum CO_2-Anstieg und O_3-Abbau in der mittleren Atmosphäre und Einfluss des Polarwirbels auf die zonale Symmetrie des Windfeldes in der Mesopausenregion
Band 26	*A. Raabe* und *K. Arnold* (Edn.), 2002: Meteorologische Arbeiten aus Leipzig VII
Band 27	*M. Simmel*, 2002: Ein Modul zur spektralen Beschreibung von Wolken und Niederschlag in einem Mesoskalenmodell zur Verwendung auf Parallelrechnern
Band 28	*H. Siebert*, 2002: Tethered-Balloon Borne Turbulence Measurements in the Cloudy Boundary Layer
Sonderband	*G. Tetzlaff* (Hrsg.), 2002:- Atmosphäre - Aktuelle Beiträge zu Luft, Ozon, Sturm, Starkregen und Klima
Band 29	*U. Harlander*, 2003: On Rossby wave propagation in atmosphere and ocean

Band 30 *A. Raabe* und *K. Arnold* (Edn.), 2003: Meteorologische Arbeiten aus Leipzig VIII

Band 31 *M. Wendisch*, 2003: Absorption of Solar Radiation in the Cloudless and Cloudy Atmosphere

Band 32 *U. Schlink*, 2003: Longitudinal Models in Biometeorology: Effect Assessment and Forecasting of Ground-level Ozone

Band 33 *H. Heinrich*, 2004: Finite barotrope Instabilität unter synoptischem Antrieb

Band 34 *A. Raabe* und *K. Arnold* (Edn.), 2004: Meteorologische Arbeiten aus Leipzig IX

Band 35 *C. Stolle*, 2004: Three-dimensional imaging of ionospheric electron density fields using GPS observations at the ground and on board the CHAMP satellite

Band 36 *A. Raabe* und *K. Arnold* (Edn.), 2005: Meteorologische Arbeiten (X) und Jahresbericht 2004 des Institutes für Meteorologie der Universität Leipzig

Band 37 *A. Raabe* und *K. Arnold* (Edn.), 2006: Meteorologische Arbeiten (XI) und Jahresbericht 2005 des Institutes für Meteorologie der Universität Leipzig

Band 38 *K. Fröhlich*, 2006: The Quasi Two-Day Wave – its impact on zonal mean circulation and wave-wave interactions in the middle atmosphere

Band 39 *K. Radtke*, 2006: Zur Sensitivität von Starkwindfeldern gegenüber verschiedenen meteorologischen Parametern im Mesoskalenmodell LM

Band 40 *K. Hungershöfer*, 2007: Optical Properties of Aerosol Particles and Radiative Transfer in Connection with Biomass Burning

Band 41 *A. Raabe* (Hrsg.), 2007: Meteorologische Arbeiten (XII) und Jahresbericht 2006 des Institutes für Meteorologie der Universität Leipzig

Band 42 *A. Raabe* (Hrsg.), 2008: Meteorologische Arbeiten (XIII) und Jahresbericht 2007 des Institutes für Meteorologie der Universität Leipzig

Band 43 *A. Kniffka, 2008*: Einfluss der Inhomogenitäten von Aerosol, Bodenalbedo und Wolken auf das aktinische Strahlungsfeld der Atmosphäre

Band 44 *M. Barth, 2009*: Akustische Tomographie zur zeitgleichen Erfassung von Temperatur- und Strömungsfeldern

Band 45 *A. Raabe* (Hrsg.), 2009: Meteorologische Arbeiten (XIV) und Jahresbericht 2008 des Institutes für Meteorologie der Universität Leipzig

Band 46 *G. Stober, 2009:* Astrophysical Studies on Meteors using a SKiYMET All-Sky Meteor Radar

Band 47 *A. Raabe* (Hrsg.), 2010: Meteorologische Arbeiten (XV) und Jahresbericht 2009 des Institutes für Meteorologie der Universität Leipzig

Band 48 *A. Raabe* (Hrsg.), 2011: Meteorologische Arbeiten (XVI) und Jahresbericht 2010 des Institutes für Meteorologie der Universität Leipzig

Band 49 *A. Raabe* (Hrsg.), 2012: METTOOLS_VIII Tagungsband

Band 50 *A. Raabe* (Hrsg.), 2012: Meteorologische Arbeiten (XVII) und Jahresbericht 2011 des Institutes für Meteorologie der Universität Leipzig

Band 51 *A. Raabe* (Hrsg.), 2013: Meteorologische Arbeiten (XVIII) und Jahresbericht 2012 des Institutes für Meteorologie der Universität Leipzig

Band 52 *A. Raabe* (Hrsg.), 2014: Meteorologische Arbeiten (XIX) und Jahresbericht 2013 des Institutes für Meteorologie der Universität Leipzig

Band 53 *A. Raabe* (Hrsg.), 2015: Meteorologische Arbeiten (XX) und Jahresbericht 2014 des Institutes für Meteorologie der Universität Leipzig